**Improving Exploration for Geothermal Resources with the Magnetotelluric Method**

by

Benjamin Martin Lee

A thesis submitted in partial fulfillment of the requirements for the degree of

Doctor of Philosophy

in
Geophysics

Department of Physics
University of Alberta

©Benjamin Martin Lee, 2020

## Abstract

This thesis investigates improvements in methods used for exploration for geothermal resources with the magnetotelluric (MT) method. Geothermal energy is a renewable resource that provides heat and electricity with low carbon emissions. Targets in conventional geothermal exploration are geothermal reservoirs, which are underground regions with hot fluids which can be extracted for direct use of heat or electricity production. Geothermal reservoirs are detected by geophysical methods such as MT, a technique utilizing naturally occurring electromagnetic signals to image the subsurface electrical resistivity. MT is useful for locating geothermal reservoirs because high-temperature hydrothermal alteration can make the reservoir relatively resistive. Improvements in the strategy used for MT exploration are needed to make this method more effective. In this thesis two case studies are described where conventional analysis and interpretation of MT data was inadequate for assessing the potential geothermal resource.

The first study considered the Krafla geothermal field in Iceland. Supercritical fluids beneath the geothermal field could increase electric power output by an order of magnitude per well if used instead of steam. The IDDP-1 well was drilled in the year 2009 to reach the supercritical fluids at a depth of 4 to 5 km. However, drilling ended prematurely when magma was unexpectedly encountered at 2.1 km depth. This study investigates why the magma was not imaged with the existing MT data. First, improvements to the 3-D inversion of the Krafla MT data were implemented, including: (1) a 1-D resistivity model as a constraint on the final resistivity model; (2) full impedance tensor data instead of only the off-diagonal elements used by previous authors; and (3) model cells with horizontal dimensions of 100 by 100 m, which is a finer discretization than used by previous authors.

The most prominent feature in the 3-D resistivity model is the low resistivity feature (C3) coincident with the bottom of the IDDP-1 well. The interpretation of C3 includes (1) partial melt, distributed in a dyke and sill complex, and (2) dehydrated chlorite and epidote minerals at temperatures above 500 to 600°C. Sensitivity tests revealed that the MT data were not sensitive to cubic-shaped magma bodies at the bottom of IDDP-1 that were 1 $km^3$ or smaller with a resistivity between 0.1 and 30 Ωm. Therefore the MT data cannot preclude the existence of magma distributed in small pockets, such as the magma body intersected by IDDP-1. This study demonstrates that the limitations of the MT method should be considered before interpreting the deep parts of a resistivity model.

The second study involves the Canoe Reach geothermal prospect located near Valemount, British Columbia. Although this area hosts the Canoe River thermal spring, there is no obvious heat source and it is unclear if the underground fluids represent a viable geothermal reservoir. MT surveys were performed at Canoe Reach to image the distribution of fluids in the Southern Rocky Mountain Trench Fault (SRMTF), which may be a permeable pathway for fluids to reach the Canoe River thermal spring. Careful interpretation of resistivity models is needed because low resistivity features may correspond to fluids or to other conductive materials within a rock such as graphite or sulfides. In addition, the Canoe Reach area contains deformed rocks with anisotropic textures that may be electrically anisotropic. Isotropic and anisotropic inversions of the Canoe Reach North MT data resulted in significantly different resistivity models. The anisotropic resistivity model contains simpler structure and is more consistent with the mapped geology, which shows that misinterpretation can occur if electrical anisotropy is not considered. An anisotropic feature in the SRMTF footwall has a low resistivity in the east-west direction and a high resistivity in

the vertical direction, which is more easily explained by graphite or sulfides than by fluids in the rock. At Canoe Reach South, anisotropic features near the thermal spring with a low resistivity in the vertical direction may correspond to fluids within the SRMTF. The electrical anisotropy of fluids in faults could be explained by a preferred orientation of fractures and/or fault corrugations that increase permeability and decrease resistivity along the fault slip direction. Electrical anisotropy might be common in highly deformed geological settings, and should be routinely investigated with the increasing availability of 2-D and 3-D anisotropic modeling algorithms.

## Preface

Chapter 3 has been published as Lee, B., Unsworth, M., Árnason, K., & Cordell, D. (2020). Imaging the magmatic system beneath the Krafla geothermal field, Iceland: A new 3-D electrical resistivity model from inversion of magnetotelluric data. *Geophysical Journal International*, *220*(1), 541-567. I was responsible for the magnetotelluric data analysis, 3-D inversions, and writing the manuscript. M. Unsworth coordinated the project between the University of Alberta and Iceland GeoSurvey, and helped write the manuscript. K. Árnason provided the 1-D resistivity model, the magnetotelluric, topographic, geologic, and well log data, and contributed to the writing of the manuscript. D. Cordell developed codes to apply the Kolmogorov-Smirnov statistical test to magnetotelluric data, and helped to write the manuscript.

Chapter 4 is a version of a manuscript to be submitted for publication. I was involved in the collection, analysis, and inversion of the magnetotelluric data, as well as completing the manuscript. T. Finley made Figure 4.1 and Figure 4.3, constructed the cross sections in Figure 4.15 , Figure 4.18, and Figure 4.21, and contributed to writing the manuscript. M. Unsworth coordinated the project between the University of Alberta and Borealis GeoPower, contributed to magnetotelluric data collection, and helped write the manuscript. W. Kong provided and helped me use the 3-D anisotropic inversion code.

Figure 1.1 was adapted from figure 1 in C. J. Smith et al. (2018) and reproduced under a Creative Commons Attribution 4.0 International License (http://creativecommons.org/licenses/by/4.0/).

## Acknowledgments

First, I would like to thank my supervisor Martyn Unsworth for his guidance and supervision during the course of my degree. I would also like to thank students in the magnetotelluric research group at the University of Alberta, including Enci Wang, Darcy Cordell, Sean Bettac, Cedar Hanneson, Theron Finley, Brandon Chase, Zoe Vestrum for their advice and support during my Ph.D. I am also very grateful for discussions with visiting scholars who have helped broaden my views as a researcher.

Thanks to the many individuals who contributed to magnetotelluric data collection at Canoe Reach, including Darcy Cordell, Mike Cote, Martyn Unsworth, Craig Dunn, Juliette Murphy, Scott Porter, Shan Xu, Madison Ritchie, Eddie Ronveaux, Sean Bettac, Cody Good, Alana Kent, Craig 2.0, Feng Jiang, Micah Morin, Tariq Mohammed, and Nam Ong. Thanks to Borealis GeoPower for in-field support and for helping to fund this research. Thanks to the community of Valemount for their enthusiastic support and help with field logistics.

Thank you to my supervisory committee members Claire Currie and John Waldron for their constructive comments and guidance throughout my degree. I would also like to thank the examination committee of Stephen Johnston, Vadim Kravchinsky, and Hersh Gilbert for their suggestions that helped improve this thesis.

I would like to thank Landsvirkjun, the National Power Company in Iceland, for making the Krafla magnetotelluric data available. Thanks to Gary McNeice and Alan Jones for providing their tensor decomposition software. I would like to thank Gary Egbert, Anna Kelbert, and Naser Meqbel for providing their ModEM 3-D inversion algorithm. Thanks to Wenxin Kong for providing his 3-D anisotropic modeling algorithm.

Work on the Krafla project was partially funded by a NSERC Discovery Grant to Martyn Unsworth. I would also like to acknowledge funding by Mitacs through the Mitacs Accelerate program.

Finally, thank you to my family and friends for your unwavering support throughout my degree. A very special thanks goes to Taleana Huff for her patience, encouragement, and support during the arduous process of thesis writing.

# Table of Contents

**1. Introduction ..... 1**

1.1. The future of energy systems ..... 1

1.2. Alternative energy sources ..... 2

1.2.1. Solar ..... 4

1.2.2. Wind ..... 5

1.2.3. Biomass ..... 5

1.2.4. Geothermal ..... 5

1.3. Future geothermal energy development ..... 5

1.4. Overview of geothermal energy ..... 8

1.4.1. Convection dominated systems ..... 10

1.4.1.1. Volcanic fields ..... 10

1.4.1.2. Recent plutons ..... 11

1.4.1.3. Extensional/fault-hosted systems ..... 12

1.4.2. Conduction dominated systems ..... 13

1.4.2.1. Hot dry rocks (HDR) ..... 14

1.4.2.2. Sedimentary basins ..... 14

1.5. Overview of exploration for geothermal resources ..... 16

1.5.1. Exploration for convection dominated systems ..... 17

1.5.1.1. Exploration for geothermal resources in volcanic fields and recent plutons ..... 17

1.5.1.2. Exploration for extensional / fault-hosted systems ..... 17

1.5.2. Exploration for conduction dominated systems ..... 18

1.5.2.1. Hot dry rocks ..... 18

1.5.2.2. Sedimentary basins ..... 18

1.6. Geophysical methods for geothermal exploration ..... 19

1.6.1. Geophysical methods ..... 19

1.6.2. Exploration for volcanic/plutonic systems ..... 22
1.6.3. Exploration for extensional / fault hosted systems ..... 24
1.6.4. Exploration for HDR and sedimentary basin geothermal resources (EGS) ..... 25
1.6.5. Exploration of supercritical resources ..... 25
1.6.6. Summary ..... 26
1.7. Areas where improvements are needed in geophysical exploration for geothermal resources 26
1.7.1. Improvements in methods used to obtaining resistivity models from MT data ..... 26
1.7.2. Improvements in resistivity model interpretation ..... 27
1.8. Investigations in this thesis ..... 29
1.8.1. Project 1: Imaging magma beneath the Krafla geothermal field, Iceland ..... 29
1.8.2. Project 2: Fault imaging in the Canoe Reach area of the Rocky Mountain Trench, Canada ..... 30
1.9. Thesis outline ..... 31
**2. Electromagnetic induction of the Earth ..... 32**
2.1. Electrical resistivity ..... 32
2.2. Electromagnetic signal propagation in the Earth ..... 34
2.2.1. Maxwell's equations ..... 34
2.2.2. The electromagnetic skin depth ..... 36
2.3. Interpretable quantities in magnetotellurics ..... 46
2.3.1. Magnetotelluric impedance ..... 46
2.3.1.1. Impedance tensor of a 1-D Earth ..... 49
2.3.1.2. Impedance tensor of a 2-D Earth ..... 49
2.3.1.3. Impedance tensor of a 3-D Earth ..... 51
2.3.2. Apparent resistivity and phase ..... 52
2.3.3. Vertical magnetic field transfer function (tipper) ..... 55
2.4. Dimensionality and distortion ..... 56

2.4.1. Quantifying distortion of the impedance ..... 56
2.4.2. Tensor decomposition ..... 57
2.4.3. The magnetotelluric phase tensor ..... 59
2.5. Synthetic example: 2-D vertical dykes ..... 63
2.5.1. Synthetic example: Apparent resistivity and phase pseudo-sections ..... 64
2.5.2. Synthetic example: Induction arrow pseudo-section ..... 66
2.5.3. Synthetic example: Phase tensor ellipse pseudo-section ..... 67
2.6. Synthetic Example: 3-D conductor ..... 69
2.6.1. Synthetic example: Apparent resistivity and phase maps ..... 70
2.6.2. Synthetic example: Induction arrow maps ..... 75
2.6.3. Synthetic example: Phase tensor maps ..... 78
2.7. Electrical anisotropy ..... 81
2.7.1. Background ..... 81
2.7.2. Impedance tensor of a 1-D anisotropic Earth ..... 83
2.7.3. Synthetic example: MT data for a 1-D anisotropic Earth ..... 84
2.7.4. Detecting anisotropy in MT data ..... 88
2.7.4.1. Analyzing induction arrows ..... 88
2.7.4.2. Out of quadrant phase ..... 89
2.8. Magnetotelluric data collection ..... 90
2.9. Magnetotelluric time series processing ..... 92
2.9.1. Background ..... 92
2.9.2. Removing bias in MT impedances ..... 93
2.9.3. Statistical methods for MT time series processing ..... 94
2.10. Forward modeling of magnetotelluric data ..... 96
2.11. Inversion of magnetotelluric data ..... 97
2.11.1. The inversion objective function ..... 97
2.11.2. Types of inversion algorithms ..... 100

2.12. Summary ..... 101

**3. Imaging the magmatic system beneath the Krafla geothermal field from 3-D inversion of magnetotelluric data ..... 103**

3.1. Introduction ..... 103

3.2. Krafla volcano and geothermal field ..... 105

3.3. Magnetotelluric data at Krafla ..... 109

3.3.1. Background on magnetotellurics ..... 109

3.3.2. Description of Krafla MT data ..... 111

3.4. New approach to the Krafla 3-D magnetotelluric inversion ..... 120

3.4.1. Inversion details ..... 120

3.4.2. Inversion with uniform starting and prior model ..... 123

3.4.3. Inversion with uniform starting model and 1-D prior model constraint ..... 125

3.5. Resistivity model interpretation ..... 126

3.5.1. Resistivity model features ..... 126

3.5.2. Comparison of the unconstrained and constrained 3-D MT inversions ..... 136

3.5.3. Comparison with previous MT inversions ..... 136

3.6. MT data sensitivity to the IDDP-1 rhyolite magma ..... 138

3.6.1. IDDP-1 magma body resistivity ..... 139

3.6.2. Resolution tests ..... 143

3.6.2.1. Resolution test methodology ..... 143

3.6.2.2. Resolution test: thin sill (B1) ..... 148

3.6.2.3. Resolution test: cubic magma bodies (B2 and B3) ..... 153

3.7. Conclusions ..... 155

**4. Magnetotelluric investigations at the Canoe Reach geothermal prospect ..... 159**

4.1. Introduction ..... 159

4.2. Geological setting ..... 166

4.2.1. Regional tectonics ..... 166

4.2.2. Canoe Reach geology ..... 167
4.2.2.1. Stratigraphy ..... 167
4.2.2.2. Structure and metamorphism ..... 168
4.2.3. Canoe River thermal spring ..... 169
4.3. MT data at Canoe Reach ..... 171
4.3.1. Summary ..... 171
4.3.2. Canoe Reach North: MT data from the 2015-2017 grid ..... 172
4.3.3. Canoe Reach North: MT data from the 2016 profile ..... 177
4.3.4. Canoe Reach South: Lines A and B MT Data ..... 182
4.3.5. Canoe Reach South: Lines C and D MT Data ..... 185
4.4. 3-D inversions of the Canoe Reach MT data ..... 189
4.4.1. Summary ..... 189
4.4.2. Canoe Reach North resistivity models ..... 192
4.4.3. Lines A and B resistivity models ..... 199
4.4.4. Lines C and D resistivity models ..... 203
4.5. Discussion ..... 207
4.5.1. Canoe Reach North: resistivity model interpretation ..... 207
4.5.1.1. AF1 and AF4: Lower Miette Group tectonic slices ..... 209
4.5.1.2. AF2 and AF3: Yellowjacket Gneiss offset by the SRMTF ..... 210
4.5.2. Lines A and B: resistivity model interpretation ..... 211
4.5.2.1. AF6, AF7, and AF8: Fluids hosted within the SRMT fault/splay zone ..... 211
4.5.2.2. AF9: Bulldog Gneiss ..... 213
4.5.2.3. AF10: Malton Gneiss or Lower Miette Group tectonic slices ..... 213
4.5.3. Lines C and D: resistivity model interpretation ..... 214
4.5.3.1. AF11 and AF13: Possible fluids in SRMTF fracture zone ..... 214
4.5.3.2. AF12: Fluids within the SRMTF ..... 215
4.5.4. Do these resistivity models help constrain geometry of the SRMTF? ..... 215

4.5.5. Anisotropic resistivity of faults ..... 216
4.5.6. Implications for geothermal exploration at Canoe Reach ..... 218
4.5.7. The value of anisotropic resistivity modeling in structurally controlled geothermal systems ..... 219
4.6. Conclusion ..... 221
4.6.1. Summary ..... 221
4.6.2. Canoe Reach North ..... 221
4.6.3. Canoe Reach South ..... 224
4.6.4. Implications for geothermal exploration ..... 227
**5. Conclusions ..... 229**
5.1. Summary ..... 229
5.2. Results from the Krafla volcanic field, Iceland ..... 229
5.2.1. Results from a new 3-D inversion of the Krafla MT data ..... 229
5.2.1.1. Improvements to the inversion procedure ..... 229
5.2.1.2. Interpretation of the C3 conductor beneath Krafla ..... 231
5.2.2. MT data sensitivity to small rhyolite magma bodies ..... 233
5.3. Results from Canoe Reach area, British Columbia ..... 235
5.3.1. Canoe Reach North ..... 235
5.3.2. Canoe Reach South ..... 238
5.3.3. Implications for geothermal exploration ..... 241
5.4. Opportunities for future work ..... 243
5.4.1. Krafla ..... 243
5.4.2. Canoe Reach ..... 245
5.5. The future of MT in geothermal exploration ..... 246
**Bibliography ..... 249**
**Appendix A : Krafla ..... 267**
**Appendix B : Canoe Reach ..... 268**

Appendix B.1 : 2-D inversion of the Canoe Reach North 2016 profile..... 268

Appendix B.2 : Observed and modeled data from Canoe Reach North 3-D inversions..... 271

Appendix B.3 :Observed and modeled data from the Lines A and B 3-D inversions ..... 279

Appendix B.4 : Observed and modeled data from the Lines C and D 3-D inversions ..... 283

## List of Tables

Table 3.1: p-values returned by K-S tests of the 18 sensitivity tests. ..... 145
Table 3.2: Change in r.m.s. misfit when the inversion resistivity model is edited in each of the 18 sensitivity tests. ..... 145
Table 4.1: Canoe Reach inversion: data parameters ..... 192
Table 4.2: Canoe Reach inversion: model parameters ..... 192

## List of Figures

Figure 1.1: Global temperature change based on different emissions reductions scenarios. ..... 2
Figure 1.2: Global primary energy consumption over the last thirty years, categorized by fuel type. ..... 3
Figure 1.3: Depiction of the United Nations Framework Classification for Resources 2019. ..... 7
Figure 1.4: Conceptual model of a conventional hydrothermal geothermal reservoir. ..... 12
Figure 1.5: Conceptual model of a fault-hosted geothermal system. ..... 13
Figure 1.6: Conceptual diagram of an enhanced geothermal system (EGS) in a sedimentary basin. ..... 16
Figure 1.7: Typical reservoir pressure in a borehole as a function of true vertical depth (TVD). ..... 19
Figure 1.8: Electrical resistivity model through the center of the Rotokawa geothermal field, New Zealand, demonstrating correlation between resistivity and temperature. ..... 23
Figure 1.9: Hypothetical exploration scenario for a blind fault-hosted geothermal reservoir. ..... 28
Figure 2.1: Schematic of electric current flow *I* through a cylinder. ..... 33
Figure 2.2: Electrical resistivity / conductivity of representative Earth materials. ..... 34
Figure 2.3: Contour lines of *N* as a function of conductivity and angular frequency. *N* is an estimate of the relative contribution of conduction and displacement currents to EM signal propagation (Equation 2.19). ..... 41
Figure 2.4: Electric field magnitude as a function of depth ..... 46
Figure 2.5: Example of coordinate system rotation for a 2-D Earth. ..... 50
Figure 2.6: Galvanic effect producing a secondary electric field $E_s$ from surface charge accumulation. ..... 51
Figure 2.7: a) Apparent resistivity and b) phase curves as a function of signal frequency for three synthetic 2-layer models. ..... 54
Figure 2.8: Representation of the phase tensor as an ellipse in the *xy* plane. ..... 61
Figure 2.9: Example phase tensor ellipses for a 1-D, 2-D, and 3-D Earth. ..... 63
Figure 2.10: Synthetic 2-D resistivity model and pseudo-sections of data calculated from the model. ..... 65

Figure 2.11: Pseudo-section of real induction arrows calculated from the 2-D vertical dykes resistivity model in Figure 2.10. ..... 67
Figure 2.12: Phase tensor ellipse pseudo-section calculated from the 2-D vertical dykes resistivity model shown in Figure 2.10. ..... 69
Figure 2.13: Synthetic 3-D resistivity model to demonstrate MT data responses. ..... 70
Figure 2.14: Interpolated map views of apparent resistivity and phase calculated from the synthetic model in Figure 2.13. ..... 75
Figure 2.15: Map view of real induction arrows calculated from the 3-D resistivity model shown in Figure 2.13. ..... 78
Figure 2.16: Map view of phase tensor ellipses calculated from the 3-D resistivity model shown in Figure 2.13. ..... 81
Figure 2.17: a) example of triaxial vertical anisotropy, where the resistivity varies in the $x$, $y$, and $z$ directions. b) three successive Euler rotations by the angles $\alpha_S$, $\alpha_D$, and $\alpha_L$ to define an arbitrary anisotropy coordinate system. ..... 82
Figure 2.18: Examples of electrical anisotropy in uniaxial media. ..... 83
Figure 2.19: Apparent resistivity, phase, and phase tensor data for a simple 1-D anisotropic model. ..... 86
Figure 2.20: Apparent resistivity, phase, and phase tensor data for a 1-D resistivity model containing a layer with a 30° anisotropic strike direction. ..... 88
Figure 2.21: Typical layout of a broadband magnetotelluric station. ..... 91
Figure 3.1: a) Geological map of the Krafla volcanic field; b) location of Krafla with the neo-volcanic zone, which is the region of active volcanism on Iceland, shaded in red. c) Topographic map of the Krafla volcanic field with labelled geothermal fields. ..... 108
Figure 3.2: Map view of the Krafla MT apparent resistivity ($\rho$) and phase ($\varphi$) data at a frequency of 40 Hz. ..... 113
Figure 3.3: Map view of the Krafla MT apparent resistivity ($\rho$) and phase ($\varphi$) data at a frequency of 0.3 Hz. ..... 114
Figure 3.4: Map view of the Krafla MT apparent resistivity ($\rho$) and phase ($\varphi$) data at a frequency of 0.037 Hz. ..... 115
Figure 3.5: Map view of the Krafla MT apparent resistivity ($\rho$) and phase ($\varphi$) data at a frequency of 0.0092 Hz. ..... 116
Figure 3.6: Selected apparent resistivity and phase curves from stations K-81194, K-81794, KMT05, and KMT50. ..... 117

Figure 3.7: Map view of Krafla MT phase tensor ellipses at 4 frequencies. ..... 119
Figure 3.8: Root mean square (r.m.s.) misfit of the measured and calculated MT data from the unconstrained 3-D inversion. ..... 124
Figure 3.9: Northwest to southeast slice through the a) interpolated 1-D prior resistivity model of Árnason et al. (2007); b) 3-D resistivity model from the 3-D MT inversion with a 10 Ωm half-space as the prior model; c) 3-D resistivity model from the 3-D MT inversion using the interpolated 1-D MT model as a prior model. ..... 131
Figure 3.10: Horizontal slices through resistivity models at elevations of -0.4 km, 0.1 km, 0.6 km, 1.1 km, 1.6 km, and 2.1 km below sea level. Left column (a,d,g,j,m,p): unconstrained 3-D inversion resistivity model with a 10 Ωm half-space prior model; center column (b,e,h,k,n,q): constrained 3-D inversion resistivity model with the 1-D prior model; right column (c,f,i,l,o,r): the interpolated 1-D resistivity model of Árnason et al. (2007). ..... 134
Figure 3.11: Integrated conductivity (conductance) in the unconstrained 3-D resistivity model from the surface to 0.2 km b.s.l. ..... 134
Figure 3.12: Map view of well temperature and 3-D model resistivity in the Krafla geothermal field at four depths: a) -0.3 km, b) 0.1 km, c) 0.5 km, and d) 0.9 km b.s.l. ..... 135
Figure 3.13: Contour lines of electrical resistivity as a function of temperature (°C) and %wt $H_2O$ for a rhyolite melt. Resistivity values are calculated from the relation of Guo et al. (2016). ..... 140
Figure 3.14: Logarithmic contours of Krafla rhyolite bulk resistivity as a function of melt fraction and melt resistivity computed from Modified Archie's Law (Glover et al., 2000). ..... 142
Figure 3.15: Outlines of test magma bodies in a) map view and b) vertical slice through A-A'. See Table 3.1 for magma body dimensions and resistivities. ..... 146
Figure 3.16: Comparison of a) apparent resistivity and b) phase data from the station KMT50. The measured data, predicted data from the 3-D inversion, and predicted data from the inversion resistivity model with synthetic sills added are shown. ..... 149
Figure 3.17: Cross-plot of impedance residuals from the unconstrained 3-D inversion resistivity model and the edited resistivity model with a) 3 Ωm (83 S) sill, b) 1 Ωm (250 S) sill, c) 0.3 Ωm (833 S) sill, and d) 0.1 Ωm (2500 S) sill. ..... 150

Figure 3.18: Difference in impedance normalized by error floor for the resolution test with a 0.1 Ωm (2500 S) sill added to the 3-D inversion resistivity model. ..... 152
Figure 3.19: Asymptotic p-values returned by the K-S test at each MT station when comparing impedance residuals of the inversion model and model with a 0.1 Ωm (2500 S) sill. ..... 154
Figure 3.20: Conceptual west-to-east cross section model of the Krafla geothermal system and underlying magmatic system. ..... 158
Figure 4.1: Map of thermal springs in southeast British Columbia, Canada. ..... 160
Figure 4.2: Map of selected magnetotelluric stations collected in the Canadian Cordillera and resistivity model from the ABC-N transect. ..... 162
Figure 4.3: Geological map of the Rocky Mountain Trench area southeast of Valemount. ..... 165
Figure 4.4: Maps of Canoe Reach North apparent resistivity ($\rho$) and phase ($\varphi$) data at four frequencies. ..... 175
Figure 4.5: Phase tensor ellipse and induction arrow maps of Canoe Reach North MT data at four frequencies ..... 177
Figure 4.6: Maps of apparent resistivity ($\rho$) and phase ($\varphi$) data from the 2016 profile at Canoe Reach North. ..... 180
Figure 4.7: Maps of phase tensor ellipses and induction arrows from the 2016 profile in Canoe Reach North. ..... 181
Figure 4.8: Maps of Lines A and B apparent resistivity ($\rho$) and phase ($\varphi$) data shown at four frequencies. ..... 184
Figure 4.9: Maps of Lines A and B phase tensor ellipses at four frequencies. ..... 185
Figure 4.10: Maps of Lines C and D apparent resistivity ($\rho$) and phase ($\varphi$) data shown at four frequencies. ..... 188
Figure 4.11: Maps of Lines C and D phase tensor ellipses at four frequencies. ..... 189
Figure 4.12: Root mean square (r.m.s.) misfit by frequency for the three groups of Canoe Reach 3-D MT inversions ..... 193
Figure 4.13: Change in root mean square (r.m.s.) misfit of combined impedance and tipper data at Canoe Reach North at four frequencies a) to d). Each colored circle represents the difference in r.m.s. misfit between the isotropic and anisotropic inversions at the given frequency for an MT station. ..... 194
Figure 4.14: Horizontal slices through the Canoe Reach North isotropic and anisotropic 3-D resistivity models. ..... 196

Figure 4.15: Geological cross section M-M' through Canoe Reach North and vertical slices through the Canoe Reach North resistivity models. ..... 198
Figure 4.16: Pseudo-sections of r.m.s. misfit as a function of frequency for the Lines A and B 3-D isotropic and anisotropic inversions. ..... 200
Figure 4.17: Horizontal slices through the Canoe Reach South Lines A and B isotropic and anisotropic resistivity models. ..... 202
Figure 4.18: Geological cross section P-P' through Canoe Reach South and vertical slices through the Lines A and B resistivity model. ..... 203
Figure 4.19: Pseudo-sections of r.m.s. misfit as a function of frequency for the Lines C and D 3-D isotropic and anisotropic inversions. ..... 204
Figure 4.20: Horizontal slices through the Canoe Reach South Lines C and D isotropic and anisotropic 3-D resistivity models. ..... 206
Figure 4.21: Geological cross section Q-Q' through Canoe Reach South and vertical slices through the Lines C and D resistivity models. ..... 207
Figure 4.22: 3-D perspective of the Canoe Reach North area with vertical slices from the 3-D anisotropic resistivity model. ..... 223
Figure 4.23: 3-D perspective of the Canoe Reach South area with vertical slices from the 3-D anisotropic resistivity models. Vertical slices through the $\rho_z$ models are shown, which is the resistivity measured in the *z* direction. ..... 225
Figure 4.24: 3-D perspective of the Canoe Reach South area with vertical slices from the 3-D anisotropic resistivity models. Vertical slices through the $\rho_x$ models are shown, which is the resistivity measured in the *x* direction. ..... 226
Figure 5.1: 3-D view of the low resistivity features below the Krafla volcanic field plotted as a 7 Ωm isosurface. ..... 233
Figure 5.2: 3-D perspective of the Canoe Reach North area with vertical slices from the 3-D anisotropic resistivity model. Vertical slices through the $\rho_y$ model are shown, which is the resistivity measured in the *y* direction. ..... 237
Figure 5.3: 3-D perspective of the Canoe Reach South area with vertical slices from the 3-D anisotropic resistivity models. Vertical slices through the $\rho_z$ model are shown, which is the resistivity measured in the *z* direction. ..... 239
Figure 5.4: 3-D perspective of the Canoe Reach South area with vertical slices from the 3-D anisotropic resistivity models. Vertical slices through the $\rho_x$ model are shown, which is the resistivity measured in the *x* direction. ..... 240

Figure A.1: Vertical slice through 3-D resistivity models obtained from unconstrained inversions with different model covariance values. ..... 267
Figure B.1: Pseudo-sections of apparent resistivity ($\rho$) and phase ($\varphi$) data from the preferred 2-D inversion of the Canoe Reach North 2016 profile. ..... 269
Figure B.2: Preferred 2-D resistivity model obtained from inversion of the Canoe Reach North 2016 MT profile. ..... 270
Figure B.3: Maps of Canoe Reach North observed and modeled apparent resistivity ($\rho$) and phase ($\varphi$) data at a frequency of 100 Hz. ..... 271
Figure B.4: Maps of Canoe Reach North observed and modeled apparent resistivity ($\rho$) and phase ($\varphi$) data at a frequency of 10 Hz. ..... 272
Figure B.5: Maps of Canoe Reach North observed and modeled apparent resistivity ($\rho$) and phase ($\varphi$) data at a frequency of 1 Hz. ..... 273
Figure B.6: Maps of Canoe Reach North observed and modeled apparent resistivity ($\rho$) and phase ($\varphi$) data at a frequency of 0.1 Hz. ..... 274
Figure B.7: Maps of Canoe Reach North observed and modeled tipper ($T$) data at a frequency of 100 Hz. ..... 275
Figure B.8: Maps of Canoe Reach North observed and modeled tipper ($T$) data at a frequency of 10 Hz. ..... 276
Figure B.9: Maps of Canoe Reach North observed and modeled tipper ($T$) data at a frequency of 1 Hz. ..... 277
Figure B.10: Maps of Canoe Reach North observed and modeled tipper ($T$) data at a frequency of 0.1 Hz. ..... 278
Figure B.11: Maps of the Lines A and B observed and modeled apparent resistivity ($\rho$) and phase ($\varphi$) data at a frequency of 650 Hz. ..... 279
Figure B.12: Maps of the Lines A and B observed and modeled apparent resistivity ($\rho$) and phase ($\varphi$) data at a frequency of 100 Hz. ..... 280
Figure B.13: Maps of the Lines A and B observed and modeled apparent resistivity ($\rho$) and phase ($\varphi$) data at a frequency of 20 Hz. ..... 281
Figure B.14: Maps of the Lines A and B observed and modeled apparent resistivity ($\rho$) and phase ($\varphi$) data at a frequency of 5 Hz. ..... 282
Figure B.15: Maps of the Lines C and D observed and modeled apparent resistivity ($\rho$) and phase ($\varphi$) data at a frequency of 800 Hz. ..... 283
Figure B.16: Maps of the Lines C and D observed and modeled apparent resistivity ($\rho$) and phase ($\varphi$) data at a frequency of 100 Hz. ..... 284

Figure B.17: Maps of the Lines C and D observed and modeled apparent resistivity ($\rho$) and phase ($\varphi$) data at a frequency of 20 Hz. ..... 285
Figure B.18: Maps of the Lines C and D observed and modeled apparent resistivity ($\rho$) and phase ($\varphi$) data at a frequency of 5 Hz. ..... 286
Figure B.19: Comparison of horizontal slices from the Canoe Reach South Lines C and D anisotropic 3-D resistivity models. The "even" inversion used every second even-numbered MT station and the "odd" inversion used every second odd-numbered MT station. ..... 288

# 1. Introduction

## 1.1. The future of energy systems

Global industrialization has led to a continued increase in global energy consumption in the past decade. According to the International Energy Agency (IEA), yearly global energy consumption in 2018 increased by 2.3%, the highest rate since 2010 (IEA, 2019). In addition to the increasing energy demand, fossil fuels such as coal, oil, and natural gas constituted more than 80% of the consumed energy in 2018 (BP, 2019). Many countries have acknowledged the negative implications of increasing carbon dioxide concentration in the atmosphere from fossil fuel emissions, such as increasing global average surface temperature. The Intergovernmental Panel on Climate Change (IPCC) deemed it "extremely likely" that more than half of the observed increase in global average surface temperature from 1951 to 2010 is due to anthropogenic factors, including greenhouse gas (GHG) emissions (IPCC, 2014). The IPCC (2014) also warned that even if anthropogenic GHG emissions were completely eliminated, it would take centuries for surface temperatures to decrease. Efforts are thus underway to reduce carbon dioxide emissions because (1) it remains in the atmosphere for 5 to 200 years, and (2) it contributes the most radiative forcing (atmospheric warming from sunlight in $W/m^2$) of the known GHGs (P. Forster et al., 2007). However, despite this knowledge and cautioning, the IEA reports that carbon dioxide emissions increased 1.7% in 2018, and global $CO_2$ emissions have increased every decade since the 1940s (Boden et al., 2017).

The global reliance on fossil fuels makes it impractical to immediately halt fossil fuel consumption. Instead, consumption needs to be gradually decreased, and several studies have outlined reduced carbon emissions targets that could be implemented to limit temperature increases to a specified value, relative to pre-industrial levels. However, these plans are challenging and require immediate action. Rogelj et al. (2011) showed that in order to meet the United Nations (UN) Cancun 2010 goal of limiting global temperature increase to 2°C by the year 2100, infrastructure and policy must be put in place immediately. A more ambitious goal to limit warming to 1.5°C by the year 2100 was agreed upon in the UN Paris Agreement of 2015, as nations recognized that some countries are more vulnerable to the adverse effects of climate change, including sea level rise, drought, etc. Rogelj et al. (2015) acknowledged

that while meeting the 1.5°C scenario is possible, it would take a significant change to international climate policy. Smith et al. (2018) proposed that if no more fossil fuel infrastructure was built after 2018, there would be a 64% chance of meeting the 1.5°C goal (Figure 1.1). However, if emissions reductions began in 2030, it would be much more difficult to meet this goal. All of these studies stress the need to immediately develop alternatives to fossil fuel energy.

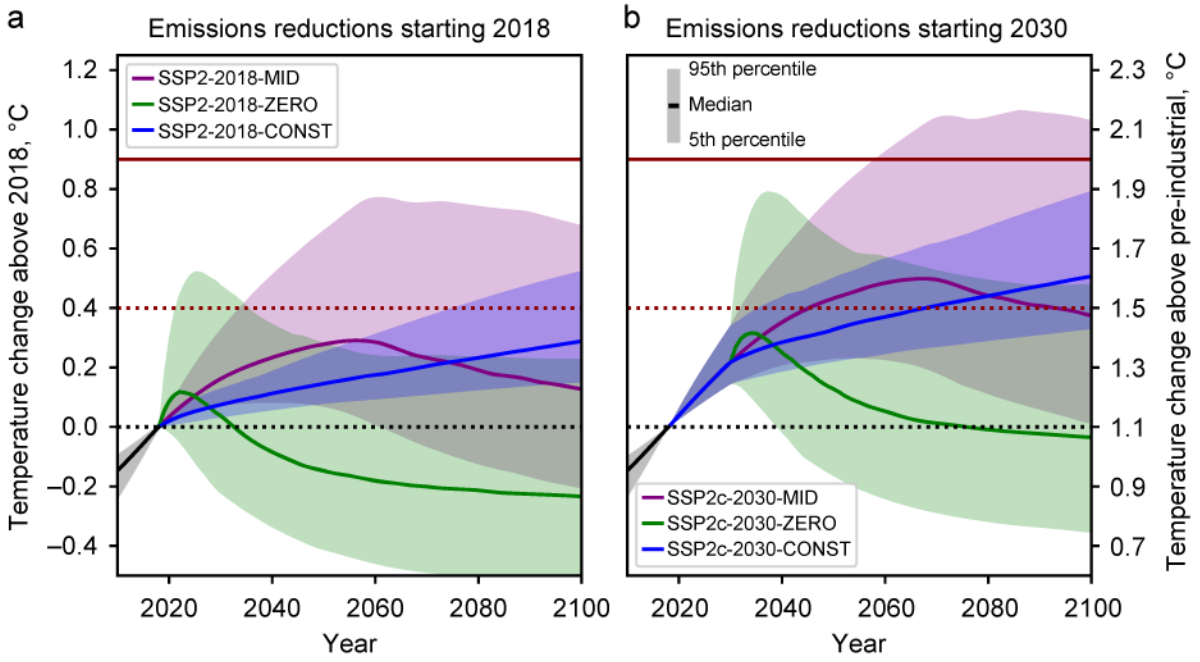


Figure 1.1: Global temperature change based on different emissions reductions scenarios.a) CONST (blue) = constant forcing scenario with atmospheric composition held constant; MID (purple) = scenario with a 40 year phase-out of fossil fuel infrastructure; ZERO (green) = scenario with abrupt end to emissions. Shaded areas indicate the 5-95 percentiles of the responses. b) Same data as a), but with the scenarios beginning in 2030. Adapted from figure 1 in C. J. Smith et al. (2018).

## 1.2. Alternative energy sources

One way to reduce carbon emissions is to replace fossil fuels with alternative energy sources. Figure 1.2 displays the global primary energy consumption since 1990, categorized by fuel type. As previously mentioned, fossil fuels (oil, gas, and coal) have taken a dominant role and accounted for more than 80% of the global energy consumption in 2018. The remaining consumption includes sources like nuclear, hydroelectric, and renewables (solar,

wind, geothermal, and biofuels), which are all promising alternatives to fossil fuels. These alternatives could be developed to capture a larger percentage of global consumption, but each has unique factors that must be considered.

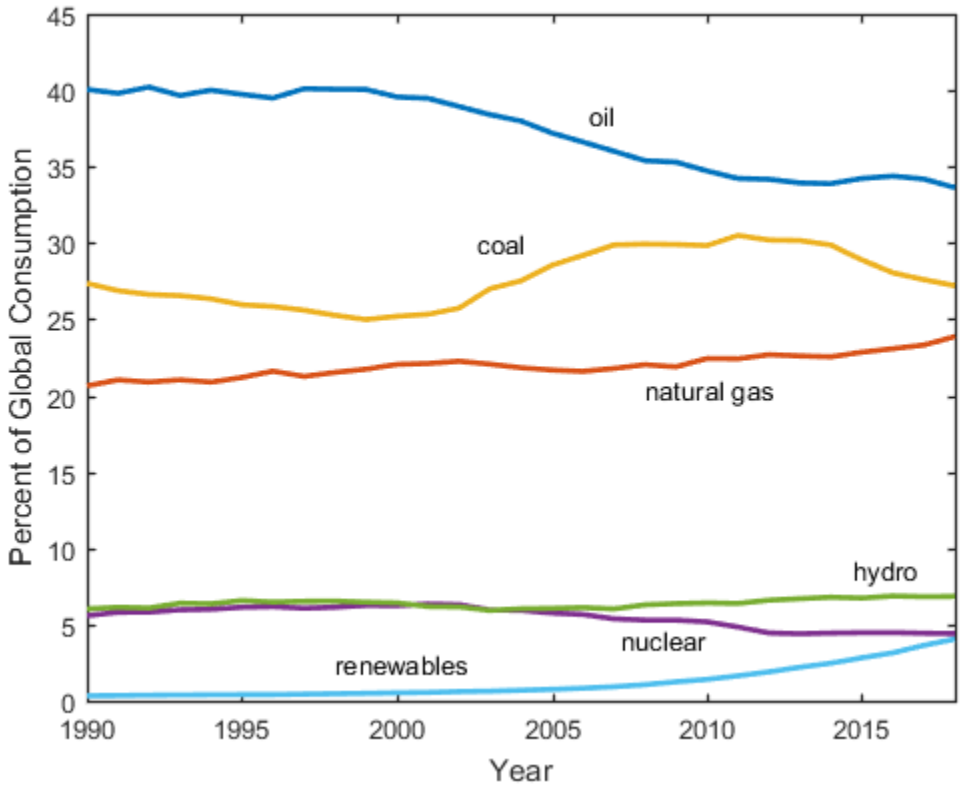


Figure 1.2: Global primary energy consumption over the last thirty years, categorized by fuel type. Fuel consumption is measured in million tons oil equivalent. Renewables include solar, wind, geothermal, and biomass. Data from BP (2019).

In a nuclear power plant, energy is released from the fission of uranium or plutonium isotopes. While nuclear energy has low carbon emissions and is considered to have a small environmental footprint, it is a controversial energy source due to the potentially harmful radioactive by-products that require long-term disposal. Nuclear energy has received some negative attention due to widely publicized accidents, such as the Chernobyl incident in 1986 and the Fukushima incident in 2011. The global average annual change in nuclear energy demand was negative from 2010-2017, largely due to cuts made by two major consumers, Japan and Germany. In contrast, rapidly developing countries such as China and India have more than doubled their nuclear energy consumption since 2008 (BP, 2019).

Hydroelectric power is generated by flowing water and is considered a renewable energy source because it does not consume the water, and the water can be replenished via the global water cycle. Global consumption of hydroelectricity in 2018 ranked above that of nuclear and renewables, but it has remained relatively flat since 1990 (BP, 2019). While the generation of hydroelectricity is a low-carbon process, studies have shown that hydroelectric reservoirs emit GHGs such as carbon dioxide and methane when vegetation decomposes from reservoir flooding (Barros et al., 2011). St. Louis et al. (2000) estimated the total carbon flux into the atmosphere from reservoirs to be $3\times10^{11}$ kg/yr of carbon, or about 4% of known anthropogenic carbon fluxes. A later study by Barros et al. (2011) estimated a total carbon flux of $0.51\times10^{11}$ kg/yr from reservoirs, based on data from 85 reservoirs compared to the 22 reservoirs used by St. Louis et al. (2000). However, these estimates are subject to large uncertainties due to non-standard measurement and assessment methods (Goldenfum, 2012). Hydroelectricity is still expected to play a role in reducing global reliance on fossil fuels, and thus more studies are needed to understand the factors that contribute to GHG emissions from hydroelectric reservoirs (Barros et al., 2011; Deemer et al., 2016).

Other sources of renewable energy that are replenished on a human timescale include solar, wind, geothermal, and biomass. These energy sources have very low carbon emissions, or in the case of biomass, aim to be carbon neutral. Taken together, solar, wind, geothermal, and biomass have increased from less than 1% of global energy consumption in 2007 to 4% in 2018. This is a larger gain than fossil fuels, nuclear, or hydroelectricity (Figure 1.2). These renewable energy sources are summarized below.

### 1.2.1. Solar

Solar power is generated by converting the electromagnetic energy in sunlight to either heat or electrical energy. Two common methods are utilizing the photovoltaic effect (i.e. solar panels) and concentrating solar rays. Solar power consumption is growing rapidly, with an average annual rate of increase of 50% from 2007 to 2017 (BP, 2019). Additional research is required for solar power, with inexpensive solar panels having poor conversion efficiency, and high conversion efficiency panels often requiring exotic materials (Gul et al., 2016). In addition, solar panels are inappropriate for providing base load power due to irregular access to sunlight.

### 1.2.2. Wind

Wind power is generated by air flow that turns air turbines. Wind power consumption also grew at a considerable average annual rate of 21% from 2007 to 2017 (BP, 2019). While a renewable and green energy source, wind intermittency presents a challenge to incorporating wind power into the power grid (Georgilakis, 2008).

### 1.2.3. Biomass

Biomass, and in particular biofuels, are an alternative to fossil fuels that are produced from plants. These fuels may be carbon neutral if planting crops offsets the carbon generated from consumption. However, it can be difficult to correctly budget carbon offsets during every step of the process from planting crops to producing energy (Fargione et al., 2008). Biofuel production (in kilotonnes of oil equivalent) has increased annually an average of 9% from 2007 to 2017.

### 1.2.4. Geothermal

Geothermal energy is produced from heat below the Earth's surface. It has low carbon emissions and the advantage of producing baseload power (Baños et al., 2011). Perhaps the largest limitation of geothermal energy is that the Earth's heat is much more easily accessed in some geographic locations than others. Development of a geothermal power plant is also hindered by the large initial capital investment and uncertainty in the amount of energy that will ultimately be produced (e.g. Williams, 2014). Installed global geothermal capacity (in GW) is increasing steadily every year, but geothermal energy is not experiencing the same boom as solar, wind, and biomass.

## 1.3. Future geothermal energy development

While each renewable energy source has advantages and disadvantages, a combination of energy sources will be needed to replace global dependence on fossil fuels. Geothermal and nuclear power plants are similar in construction / design to coal plants, and are capable of producing baseload power. However, sources such as solar and wind depend on time-varying processes and will have variable power output over the course of a day.

Solar and wind energies can still be implemented into existing power infrastructure with distributed energy storage in a smart grid, a technology that is currently being developed (Roberts & Sandberg, 2011). Geothermal energy also has a place in the future energy systems. While geothermal energy has been exploited in some areas for decades, some future developments could improve efficiency and even allow geothermal energy to be utilized in places with less accessible heat sources.

Despite their potential to reduce global carbon emissions, renewable energy development in the past two decades was hindered by a lack of a standard assessment scheme to accurately report the resource quantity and viability, among other factors. One of these schemes is the United Nations Framework Classification for Resources (UNFC), a classification scheme that provides an evaluation tool for all types of natural resources. The UNFC evaluates a resource in three categories:

- E Axis – Environmental-Socio-Economic Viability
- F Axis – Technical Feasibility and Maturity
- G Axis – Degree of Confidence

These are three independent resource evaluation categories that can be combined to classify a resource. For example, a viable project is one that meets the highest degrees of environmental-socio-economic viability (E1), technical feasibility (F1), and degree of confidence (G1), as seen in Figure 1.3. Some categories contain sub-categories that apply further definitions to the resource. For example, the E1 category is further divided into the sub-categories E1.1 and E1.2. According to the UNFC definitions, a resource can be assigned to the E1.2 category instead of E1.1 if the resource development is not environmentally, socially, or economically viable, but currently made viable through government subsidies or other considerations (UN, 2020).

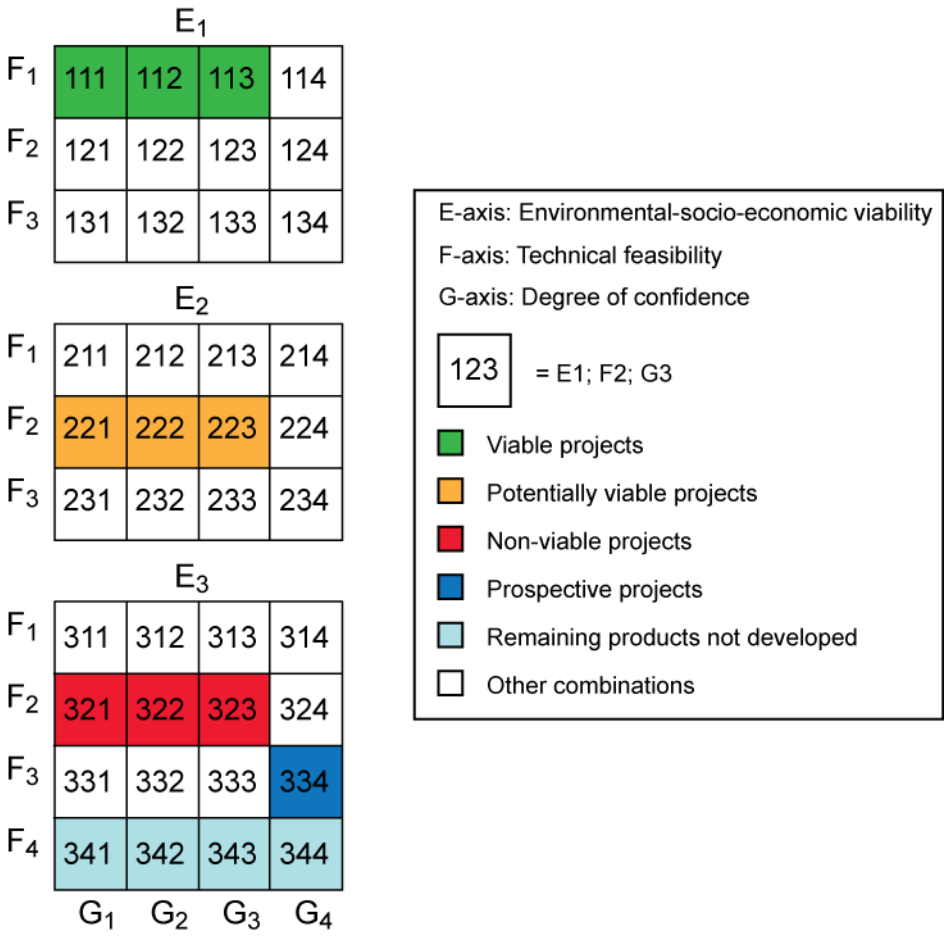


Figure 1.3: Depiction of the United Nations Framework Classification for Resources 2019. Resources are assigned a three-digit classification corresponding to the E, F, and G axes, and subsequently evaluated for their overall viability (see the figure legend) The three grids show, from top to bottom, the possible combinations for an E1, E2, and E3 resource. Only the unproduced quantities at the time of evaluation are shown. After UN (2020).

Prior to the year 2009, renewable resources could not be easily described with the UNFC because its language focused on fossil fuel and mineral resources. An update in the year 2016 included specifications on how to apply the UNFC to renewable resources, thereby providing a common classification framework for both renewable and non-renewable resources (UNECE, 2016). This update may encourage geothermal development in countries such as Canada, where no commercial geothermal power plants exist despite a significant amount of identified geothermal potential.

A report by the United Nations Economic Commission for Europe (UN, 2018) provided examples of how to apply the UNFC to geothermal resources. The Krafla geothermal field, which is the subject of the first case study in this thesis, was included in their publication. The next 30 years of production at Krafla was estimated with a simulation that assumed a maximum production capacity of 63 MWe and that additional production wells would be drilled if economically viable. At the time of evaluation in 2016, the so-called "pessimistic case" of 55.1 PJ of energy over the next 30 years was classified as an E1.1, F1.1, G1 resource. For comparison, the so-called "optimistic case" of 57.5 PJ over 30 years was classified as an E1.1, F1.1, G3 resource due to the lower level of confidence. The examples in the UN (2018) report demonstrate that the UNFC scheme is effective for classifying a range of geothermal resources.

While geothermal energy has not experienced the same rate of growth as solar and wind energy in the past decade, there are still opportunities to develop geothermal power to replace fossil fuels. This thesis focuses on exploration for geothermal resources, which could be improved in order to better locate and characterize potential geothermal resources. The following section gives an overview of the different types of geothermal systems found around the world.

## 1.4. Overview of geothermal energy

Geothermal energy is produced from naturally occurring heat that is found below the Earth's surface. The two sources of heat from inside the Earth are (1) residual heat from planetary accretion and (2) radioactive decay of isotopes such as uranium, potassium and thorium. The total estimated heat flux of the Earth is 47 ± 2 TW (Davies & Davies, 2010). This means that over the course of one year, the Earth emits about $1.5 \times 10^9$ TJ of energy. In 2018, global electricity consumption was about $9.6 \times 10^7$ TJ, which is only about 6% of the Earth's thermal energy emitted over that time period (IEA, 2019). Geothermal energy can also be estimated in terms of a total available resource. For example, Tester et al. (2007) estimated the total geothermal resource of the United States to be $2 \times 10^{11}$ TJ, which is over 2,000 times the global electricity consumption in 2018. Likewise, the Geological Survey of Canada estimated that the potential geothermal energy in Canada was over one million times the electrical consumption of Canada in 2012 (Grasby et al., 2012). Although not all of the

available underground heat can be extracted as energy, it is clear that a great amount of geothermal energy remains to be developed.

In order for geothermal energy to be effectively extracted, a viable geothermal resource requires (1) heat at an accessible depth, (2) fluids to advect the heat to the surface, and (3) sufficient permeability to permit the fluid flow. Geothermal reservoirs may occur naturally where heat, fluids, and permeability are present. These reservoirs are found in regions of high permeability and/or porosity that contain high-temperature fluids that can be extracted to produce electric power – or for direct use in heating homes and growing crops. Reservoir porosity can exist in the form of naturally occurring pore space such as in sedimentary rocks, or as secondary porosity in fractured rocks (Legarth et al., 2005; Zimmermann & Reinicke, 2010). Porosity and permeability are factors related to the fluid storage capacity of a reservoir; however, permeability is also an important control on the reservoir productivity because it determines fluid flow rate (e.g. Eggertsson et al., 2018).

The change in temperature with depth in the Earth is called the geothermal gradient. It is on average 25-30°C/km beneath continents, but can exceed 100°C/km at divergent plate boundaries or close to active volcanoes. However, many wells are not economic to drill with an average geothermal gradient because the price of drilling increases roughly as a power function of depth (Lukawski et al., 2014). Although heat is always present, the presence of fluids and permeability depends on the subsurface structure. Fluids may be naturally occurring or injected into a reservoir to facilitate advection of heat. The degree of permeability depends on the lithology and whether there are any fractures such as brittle faults.

Although every geothermal reservoir occurs in a unique setting, a categorization scheme of reservoir types is important to guide exploration and production strategies. Moeck (2014) classified geothermal play types by their geological controls. The two major categories are (1) convection dominated and (2) conduction dominated systems, and these will be discussed in further detail below. It is important to note that geothermal resources will often have characteristics of both convection and conduction dominated systems, and they may not be perfectly categorized by a single classification scheme.

### 1.4.1. Convection dominated systems

Conventional geothermal energy production has focused on natural hydrothermal systems where (1) high temperatures are present at shallow depth, (2) fluids are naturally present to transport heat to the surface, and (3) natural permeability is high enough to facilitate fluid flow. These systems are called convection-dominated systems because fluid convection occurs naturally due to a heat source and high permeability. Convection dominated systems can be further classified by their heat sources: (1) volcanic fields, (2) recent plutons, and (3) extensional regimes. In all cases, fluids concentrate in the geothermal reservoir from meteoric and, in some cases, magmatic sources. These sub-classifications are discussed below in more detail.

#### 1.4.1.1. Volcanic fields

Volcanoes are commonly formed at convergent and divergent plate boundaries. A common type of convergent plate boundary occurs between continental and oceanic lithosphere, where the denser oceanic lithosphere slides below the continental lithosphere at a subduction zone. Hydrated minerals within the subducting plate release fluids as they are heated at greater depth. In turn, these fluids lower the melting point of rocks and cause partial melting within the mantle wedge beneath the continental lithosphere. A volcanic arc forms where the partial melt is hot and buoyant enough to rise to the surface, occurring typically ~100 km inland from the subduction zone. These volcanic arcs contain volcanoes that can be developed for geothermal power.

Volcanic geothermal reservoirs are typically located above a shallow magma body. Due to the high geothermal gradient near the magma body, nearby fluids are heated and form an up-flow zone above the magma body. In the ideal case, heat is extracted from these circulating fluids, as illustrated in Figure 1.4. As the fluids rise, they advect heat toward the surface and the reservoir forms above the magma body. Unlike low-temperature reservoirs, temperatures under volcanic fields can exceed 300°C, which may be high enough for a two-phase reservoir to form, consisting of both liquid and steam.

As previously mentioned, these systems are often located in subduction zone volcanic arcs. For example, Indonesia has many volcanoes from northward subduction of the Indo-

Australian plate beneath the Eurasian plate. Development of geothermal power from these volcanoes has put Indonesia second in the world with an installed capacity of 1.9 GW in 2018. Another example in the Pacific region is the Taupo Volcanic Zone on the north island of New Zealand, which is the result of the Pacific plate subducting beneath the Australian plate. New Zealand had 1.0 GW installed capacity in 2018, with more than half of that generated from geothermal fields in the Taupo Volcanic Zone.

Iceland also has several examples of volcanic geothermal fields due to its location on the Mid-Atlantic ridge, which is the divergent plate boundary between the North American and Eurasian plates. Iceland has formed under the unique combination of a spreading ridge and an underlying mantle plume (Wolfe et al., 1997). As a result, Iceland has many active volcanoes and easily accessible geothermal resources, with geothermal gradients reaching 200°C locally.

#### 1.4.1.2. Recent plutons

In contrast to volcanic geothermal systems, geothermal systems located above plutons are formed above recent intrusions in the upper crust, and not necessarily connected to ongoing volcanism. "Recent" in this context implies that the plutons can be a few hundred thousand to a few million years old. One example is the Larderello geothermal field in Italy, where extension and associated magmatism began 14 Ma after the collision of the Corsica-Sardinia block and Adriatic micro-plates (Dini et al., 2005). The reservoir at Larderello is located at a depth greater than 3 km within fractured metamorphic rocks that overlie cooling granitic plutons (Bellani et al., 2004). Regions of elevated heat flow (up to 1000 $mW/m^2$) correlate with normal faults imaged by seismic reflection.

The Geysers geothermal field, located in the state of California in the United States, is another example of a system with infrequent volcanic eruptions. The Geysers have the largest installed capacity of any geothermal power plant in the world (~1.5 GWe). The vapour-dominated reservoir lies in fractured metamorphic rocks above a shallow felsite pluton.

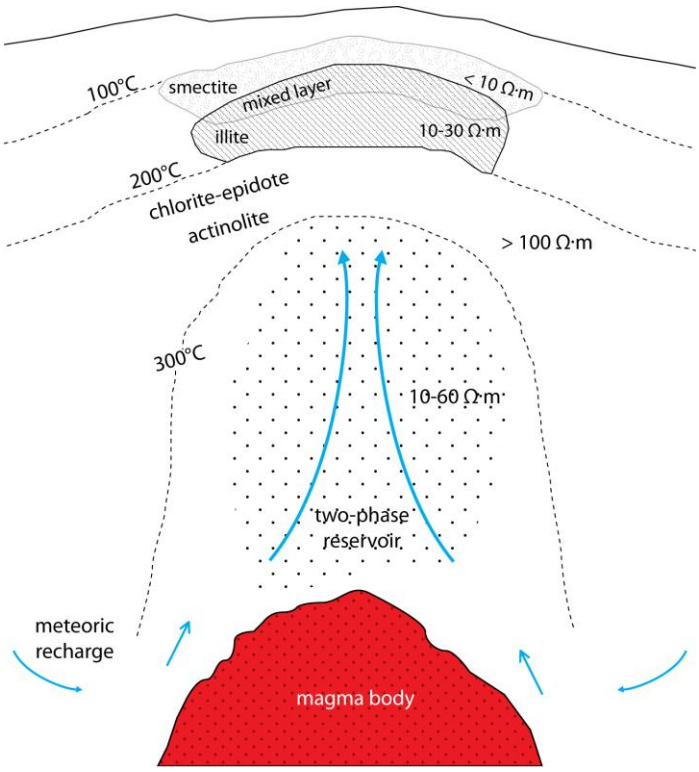


Figure 1.4: Conceptual model of a conventional hydrothermal geothermal reservoir. Heat from the magma body drives the circulation of groundwater, which concentrates in a reservoir above the magma body. Hydrothermal alteration occurs at different temperatures, with typical mineral assemblages shown. The reservoir sits below a relatively conductive layer of clay alteration. Adapted from Muñoz (2014) and Pellerin et al. (1996).

#### 1.4.1.3. Extensional/fault-hosted systems

Non-magmatic fault-hosted geothermal systems are found in tectonically active areas without active volcanism. In the absence of obvious heat sources such as volcanoes, fault-hosted systems can be identified from more subtle surface manifestations such as steam vents or thermal springs. These systems contain permeable pathways for groundwater to rapidly ascend to the surface with minimal heat loss. A conceptual diagram of a fault-hosted geothermal system is shown in Figure 1.5. At a high elevation, meteoric water infiltrates a brittle fault and is heated as it descends into the Earth. If the lithology at depth is permeable and/or naturally occurring fractures exist, the heated water can reside in a potential geothermal reservoir. Figure 1.5 also demonstrates that a hot spring may indicate deep

circulation of meteoric water, but could be located far from the potential reservoir. In this example, the heat source could be a shallow pluton or an elevated regional heat flow.

The Basin and Range province in the western United States contains examples of fault-hosted geothermal systems in an extensional tectonic setting. The underlying heat source for these systems is believed to be magmatic underplating at the base of the crust (Jarchow et al., 1993). Elevated heat flow (>80 $mW/m^2$) and brittle extensional faults contribute to the high geothermal potential of this area (Lachenbruch et al., 1994; Wisian & Blackwell, 2004).

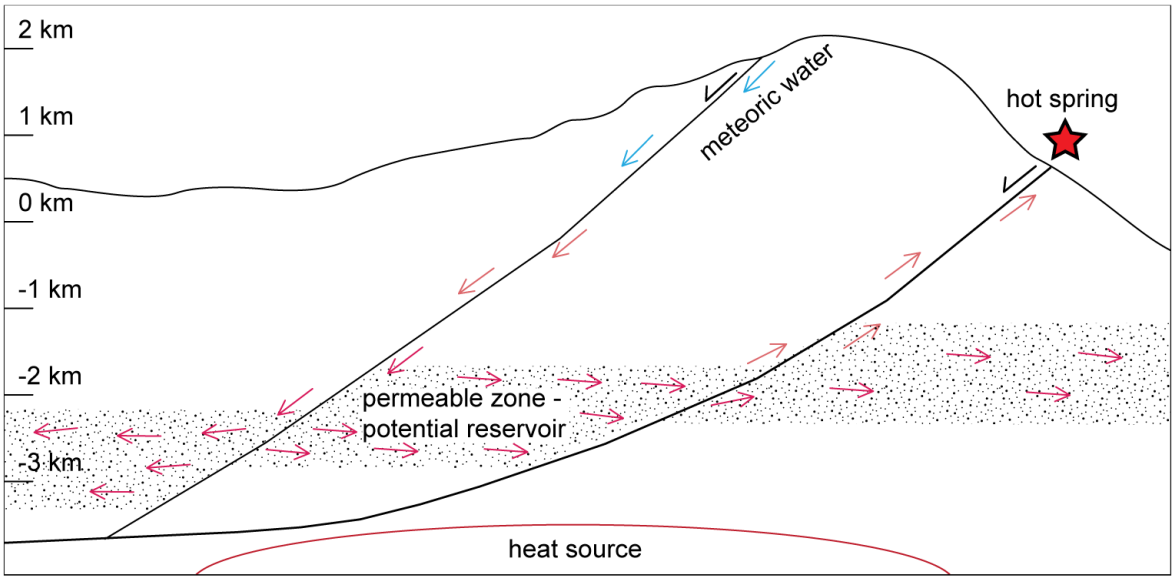


Figure 1.5: Conceptual model of a fault-hosted geothermal system. Meteoric water infiltrates a brittle fault and is heated as it descends into the Earth. A surface hot spring indicates fluid convection but may not be associated with a viable reservoir. The heat source may be a shallow intrusion, or elevated heat flow from an extensional tectonic regime.

### 1.4.2. Conduction dominated systems

The second class of geothermal play type from Moeck (2014) is conduction dominated geothermal systems. Unlike volcanic or fault-hosted geothermal systems, conduction dominated systems do not necessarily occur in tectonically active regions. These systems typically have modest geothermal gradients and may require hydraulic stimulation to

achieve sufficient permeability and porosity for fluid flow. Note that a high porosity is not a necessary indication of a productive reservoir, but the reservoir permeability is a crucial parameter because it determines the flow rate of fluids in the reservoir. In an enhanced geothermal system (EGS), an injection well is used to open fractures in the host rock to create enough permeability to host a reservoir. The injected fluid is heated by the host rock and is pumped out by a production well. These systems can be sub-classified by the reservoir host rock: crystalline (hot, dry rocks) or sedimentary basins.

#### 1.4.2.1. Hot dry rocks (HDR)

Basement igneous rocks emit a large amount of radiogenic heat from naturally occurring radioactive isotopes such as uranium, thorium, and potassium. These elements occur in intrusive rocks such as granite, and can provide heat long after solidification. In addition to a heat source, sufficient permeability is required for economic extraction of geothermal fluids. Crystalline intrusive rocks typically have a low permeability and porosity, and therefore require hydraulic stimulation with EGS so that fluids can exchange heat between injection and production wells (e.g. Tester et al., 2007). One area of study for EGS in HDR is the Cooper Basin in Australia, which has hot Proterozoic granites with estimated temperatures up to 200°C at 3 km depth (Beardsmore, 2004).

#### 1.4.2.2. Sedimentary basins

Sedimentary basins can have significant geothermal potential, even if they have a geothermal gradient close to the continental average of 25 to 30°C/km. Sedimentary rocks typically have a lower thermal conductivity than basement crystalline rocks, effectively creating a "thermal blanket" that helps retain heat in the Earth. Sedimentary basins may already host aquifers with fluid that can be produced; however, if natural permeability does not exist, EGS can be utilized to produce sufficient permeability for fluid flow. A diagram illustrating EGS in a sedimentary basin is given in Figure 1.6. An injection well creates hydraulic fractures by forcing fluid into the sandstone, thereby increasing the formation permeability. With a geothermal gradient of 30°C/km, the fluid is heated to above 100°C and extracted by the production wells for energy production. Note that, assuming a constant vertical heat flow in the sandstone and the basement granite, the geothermal gradient is lower

in the granite due to its higher thermal conductivity. The geothermal gradient in Figure 1.6 also accounts for heat production from radioactive elements in the rock. When the geothermal gradient depends on heat production such as in granite, the geothermal gradient is a parabolic equation.

The Western Canadian Sedimentary Basin (WCSB) in Alberta has been identified as a potential geothermal resource (with EGS applications), due to local temperatures of 120 – 150°C observed in wells 4 – 5 km deep (Majorowicz & Moore, 2014). Grasby et al. (2012) identified regions of the WCSB with potential for electricity production in northwest Alberta and northeast British Columbia with temperatures greater than 150°C at depths of 3.5 to 4.5 km. Banks & Harris (2018) also recently studied data from oil and gas wells in the WCSB and found that about 800 MWe of power could be produced from the resources at temperatures greater than 120°C.

The Gross Schoenebeck geothermal test site in Germany is an example of EGS development within a sedimentary basin. The deep aquifer (>4 km) contains highly permeable, fractured anhydrites at a temperature of about 140°C (Muñoz et al., 2010; Zimmermann & Reinicke, 2010). The Llucmajor aquifer system in Spain is another potential resource without an obvious heat source. This aquifer system was modeled as a shallow unconfined aquifer above a heated confined aquifer. The aquitard between the aquifers is interpreted to allow vertical movement through fractures that brings water from the heated aquifer to the surface (Arango et al., 2009).

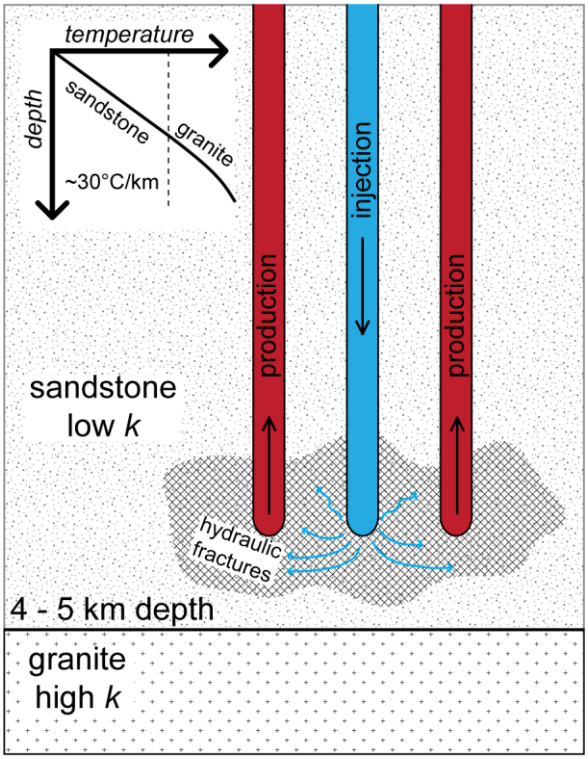


Figure 1.6: Conceptual diagram of an enhanced geothermal system (EGS) in a sedimentary basin. An injection well provides water and creates hydraulic fractures for enhanced permeability. Assuming a constant vertical heat flow in the sandstone and granite, the higher thermal conductivity ($k$) of granite results in a lower geothermal gradient in the granite (see inset graph).

## 1.5. Overview of exploration for geothermal resources

Geothermal resource assessment typically involves a number of branches of geosciences such as: geological surface mapping, geophysical measurements, and geochemical analysis of thermal spring water. Exploration begins with an investigation of the geology and subsurface properties on a regional scale. Geological mapping can identify important tectonic features, such as faults, and can also infer the approximate location of heat sources. Once the geothermal reservoir has been located, high resolution geophysical surveys can be employed to further refine the location. These geophysical methods will be explained in further detail in Section 1.6.

### 1.5.1. Exploration for convection dominated systems

#### 1.5.1.1. Exploration for geothermal resources in volcanic fields and recent plutons

Exploration at volcanic fields typically begins at the surface, where thermal manifestations can reveal information about the underlying geothermal resource. These thermal manifestations are typically a result of water-rock interactions. Hydrothermal alteration, the process by which rock minerals are altered by interaction with hot fluids, is usually visually apparent at the surface. Low temperature alteration products, such as clay and zeolite minerals, occur near the surface and indicate the presence of heated underground fluids. Thermal manifestations such as hot springs and fumaroles can also be used to help identify the underlying reservoir. The chemistry of fluids extracted from thermal manifestations assists in informing on subsurface properties such as reservoir permeability and temperature (Arnórsson, 1995). Geochemistry reveals information on the fluid source, flow direction, and interaction with magmatic fluids, which can lead to a conceptual hydrological model of the underlying reservoir. Together, these types of analyses provide valuable information about a volcanic geothermal resource.

However, geothermal resources associated with recent plutonism may not have the same obvious surface manifestations of volcanic fields. In these instances, heat flow data can be used to locate geothermal anomalies such as in the Larderello geothermal area (Bellani et al., 2004).

#### 1.5.1.2. Exploration for extensional / fault-hosted systems

For exploration in fault-hosted systems, it is especially important to determine the location and orientation of faults controlling fluid flow. An example is the Basin and Range system in the western U.S.A., where analyses comparing fault orientation to directions of geodetic strain show good correlation to geothermal potential (Blewitt et al., 2002; Jolie et al., 2015; Siler & Faulds, 2013). When fluid samples are available from thermal springs or wells, geochemical analyses give insight into the origin, age, composition, and source temperature of geothermal fluids (Ármannsson & Fridriksson, 2009; Haizlip, 2016). Heat flow measurements are also an important indicator of potential geothermal resources, e.g. in western Canada, where there are few surface manifestations (Hickson et al., 2016). From

these observations, smaller regions can be selected where more focused exploration can be performed. For example, when a potential resource is identified on the 1-10 km scale, further geochemical and geophysical studies can define the properties and location of the resource.

Some geothermal resources, such as those in the Basin and Range extensional/transtensional environments, may not contain local surface expressions. A recent study estimated that 39% of the known geothermal systems in the Basin and Range are blind systems, and as much as 75% of the resources in the region may be blind (Faulds & Hinz, 2015). These geothermal systems can be identified with spatial correlation of high temperatures/heat flow with favorable settings such as fault intersections (e.g. Faulds & Hinz, 2015; Faulds et al., 2015).

### 1.5.2. Exploration for conduction dominated systems

#### 1.5.2.1. Hot dry rocks

A successful exploration program for HDR systems must take into account that these reservoirs are typically deep (> 3 km) and relatively impermeable. Thus, geothermal gradient and heat flow mapping are often used to determine the economic parts of the reservoir. The HDR projects at Soultz-sous-Forêts, France (Pribnow & Schellschmidt, 2000) and Cooper Basin, Australia (Hillis et al., 2004) have well-constrained temperature-depth maps from borehole data.

#### 1.5.2.2. Sedimentary basins

Similar to HDR systems, sedimentary basin geothermal resources are generally located at greater depth due to a lower geothermal gradient. Fault-hosted or sedimentary geothermal reservoirs may need to be drilled to a greater depth (2 to 4 km) to achieve a sufficient temperature for electricity production. This is because without hydrothermal circulation, heat is transferred through conduction which is quantified by the geothermal gradient. In non-volcanic settings, the geothermal gradient determines how deep a production well must be drilled to produce electricity. The target depth of a production well is an important economic consideration, as the cost of drilling increases as a power function with depth (Lukawski et al., 2014). Working at shallow depth also avoids complications when the

reservoir is over-pressured, i.e. the pore pressure approaches the lithostatic pressure. This is illustrated in Figure 1.7, which shows a characteristic change in pore pressure with depth. The lithostatic pressure is calculated with an assumed formation density of 2.6 g/cm$^3$. In this example, below 2 km the reservoir pressure begins to deviate from normal hydrostatic pressure, and drilling incidents such as well blowouts, pressure kicks, and fluid influx may occur if the high pressure is unaccounted for (J. Zhang, 2011).

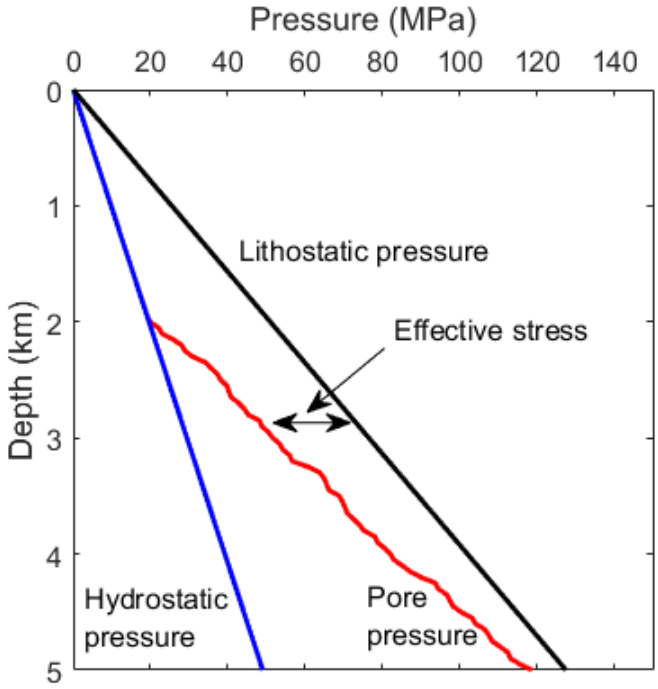


Figure 1.7: Typical reservoir pressure in a borehole as a function of true vertical depth (TVD). At depths above 2 km, the pore pressure is hydrostatic. The reservoir is over-pressured below 2 km, as indicated by the pore pressure rapidly approaching the lithostatic pressure. Modified from J. Zhang (2011).

## 1.6. Geophysical methods for geothermal exploration

### 1.6.1. Geophysical methods

Geophysical exploration infers the physical properties of rocks from surface measurements. Some of the rock properties that can be determined from geophysics include: density, seismic velocity, magnetic susceptibility, and electrical resistivity. Exploration

reveals initial targets for drilling, with drilling providing further physical properties such as temperature, permeability, and heat flow. Commonly used geophysical methods are introduced below, followed by specific applications to different geothermal settings.

- Gravity surveys measure the acceleration due to gravity at the Earth's surface, which is dependent on the density of the rocks below. The density of a rock is controlled by several factors including composition, chemical structure, and porosity. For example, silicate minerals have a large range of density values that are affected by the ratio of interstitial cations to silicate tetrahedra. In addition, a rock's density can be lower if it has an appreciable amount of pore space that is filled with air or fluid. Increasing pressure can also increase density by removing air and/or fluid from the pore space.

- Seismic methods can be classified by the origin of the seismic source. Active seismic methods use human-generated sources while passive seismic utilizes earthquake sources. Active seismic exploration methods such as reflection and refraction measure the time for acoustic waves to travel from a source to receiver. This information can be used to infer the seismic velocity and structure of the Earth below. Passive seismic tomography uses earthquake sources and solves for compressional velocity $v_p$, shear velocity $v_s$, and the ratio $v_p/v_s$.Seismic methods are particularly sensitive to the presence of fluid zones because of a decrease in velocity, and the inability of shear waves to travel through fluid (e.g. Batini & Nicolich, 1985).

- Micro-seismic monitoring is a method that uses data collected from induced seismicity. These data are obtained from down-hole seismometers that measure small earthquakes caused by fluid injection into a reservoir. Micro-seismic data are useful for mapping small earthquakes in reservoir areas that may correspond to brittle cracks or faults. These surveys can show the underground regions that are stimulated by hydraulic fracturing by mapping the location of micro-seismic events (e.g. Sasaki, 1998).

- Magnetic surveys measure the intensity of the Earth's magnetic field on the ground or in the air. These surveys are sensitive to the presence of minerals with high magnetic susceptibility, such as magnetite. Ferrimagnetic minerals such as magnetite become

magnetized under an applied magnetic field and retain a significant magnetic dipole moment even in the absence of an applied field. As a result, the total magnetic field measured in a magnetic survey is due to both induced and remanent magnetization. The induced magnetization in a rock is aligned with the current magnetic field of the Earth. Magnetic minerals develop a remanent magnetization when an igneous rock cools to below its Curie temperature, thus preserving the alignment of the Earth's magnetic field at the time of cooling. Another type of remanent magnetization occurs during sediment deposition, where small grains of magnetic minerals align with the Earth's magnetic field before compaction. The remanent magnetization is erased when a rock is heated above its Curie temperature.

- Electrical resistivity (or its inverse, conductivity) is a measure of a material's ability to conduct electrical current. Two common conduction mechanisms in the Earth are ionic and metallic conduction. Ionic conduction involves the movement of ions that hold a positive or negative electric charge. This type of conduction is observed in materials such as saline water and magma, where mobile ions such as sodium and potassium can transport electric charge under an applied electric field. Metallic conduction involves metals such as copper that have mobile electrons in their valence shell. Under an applied electric field, valence electrons in a metal lattice can move from atom to atom, thereby transporting electrical charge.

The electrical resistivity of the Earth can be determined from direct current (DC) or electromagnetic (EM) induction methods. In the DC method, the simplest layout involves four electrodes, which are typically metal stakes, arranged in a line. In this setup, an instrument injects electrical current into the Earth between the two outer electrodes and measures the resulting voltage between the two inner electrodes. The resistivity is a function of the separation distances, the applied current, and the measured voltage. If the outer electrode separation distance is increased the current flows deeper in the ground, allowing greater depth to be sampled. In a more advanced layout, more than four electrodes can be deployed at once. If there are more than four electrodes, a smart cable system allows the user to make any of the electrodes on the profile as the current and potential electrodes,

simplifying the data acquisition process. However, measurements become logistically difficult with longer dipoles and larger currents.

Geophysical methods involving EM induction have some advantages over the DC resistivity method. EM induction methods such as magnetotellurics (MT) typically have a greater depth of investigation than the DC resistivity method. MT stations are also more compact than DC resistivity deployments, which typically use a large electrode separation (>1 km) during resource exploration. Although EM and DC resistivity methods are both sensitive to electrical resistivity, the techniques are fundamentally different. EM induction involves a primary magnetic field that varies with time and induces electrical currents in the subsurface. These electrical currents generate secondary magnetic fields which are measured at the surface and contain information about variations in the subsurface resistivity.

The following section explains how these geophysical methods are used in detecting different types of geothermal systems.

### 1.6.2. Exploration for volcanic/plutonic systems

Geophysical methods are useful for locating volcanic geothermal reservoirs, although in many cases the reservoir is not directly imaged. Instead, these reservoirs typically have an overlying low permeability clay layer containing hydrothermal alteration products of the host rock at relatively low temperatures (100 to 200°C). The type of alteration is temperature-dependent, with smectite formed at lower temperature, illite at higher temperature, and a layer of mixed clay (smectite and illite) at intermediate temperature. Smectite has a higher cation exchange capacity (CEC) and is generally more conductive than illite (Ussher et al., 2000). Therefore, the resistivity of the clay layer increases at greater depth (e.g. McNamara et al., 2016) as the alteration assemblage transitions to chlorite-epidote minerals formed at higher temperature (Figure 1.4). The clay layer can be readily imaged as a low electrical resistivity zone in geophysical surveys, and it usually lies above the more resistive chlorite-epidote minerals formed at higher temperatures of 200 to 250°C (Árnason et al., 2000; Cumming, 2009). The high resistivity zone containing chlorite-epidote minerals may correspond to a viable geothermal reservoir.

Hydrothermal alteration may also have a magnetic signature because alteration destroys magnetite that may have been present in igneous rocks (e.g. Oliva-Urcia et al.,

2011). This characteristic is useful for mapping hydrothermal alteration zones within volcanic geothermal systems (e.g. Bibby et al., 1992; Pandarinath et al., 2014).

Although clay layers are obvious targets in geothermal exploration, they may indicate the presence of an active or extinct geothermal reservoir as clays are stable at lower temperatures (e.g. Arnason et al., 2008). Nevertheless, the geothermal reservoir can also be directly imaged, with or without a conductive clay layer, because electrolyte-rich reservoir fluids within fractures or faults greatly decrease the bulk resistivity of the host rock.

Heise et al. (2008) presented an example of the alteration-temperature relationships in their resistivity model from the Rotokawa geothermal field in the Taupo Volcanic Zone. As seen in Figure 1.8, low resistivity near the surface (red color) corresponds to smectite alteration. The low resistivity zone appears to be limited to above the 200–250°C isotherms (black lines) which is approximately the highest temperature of smectite alteration. The resistivity is higher in deeper parts of the model, correlating to where the temperature is above 250°C. This agrees with a greater abundance of the more resistive illite and chlorite minerals at this temperature. This example demonstrates an active geothermal field where the current underground temperatures match the expected temperatures from the alteration mineral assemblage.

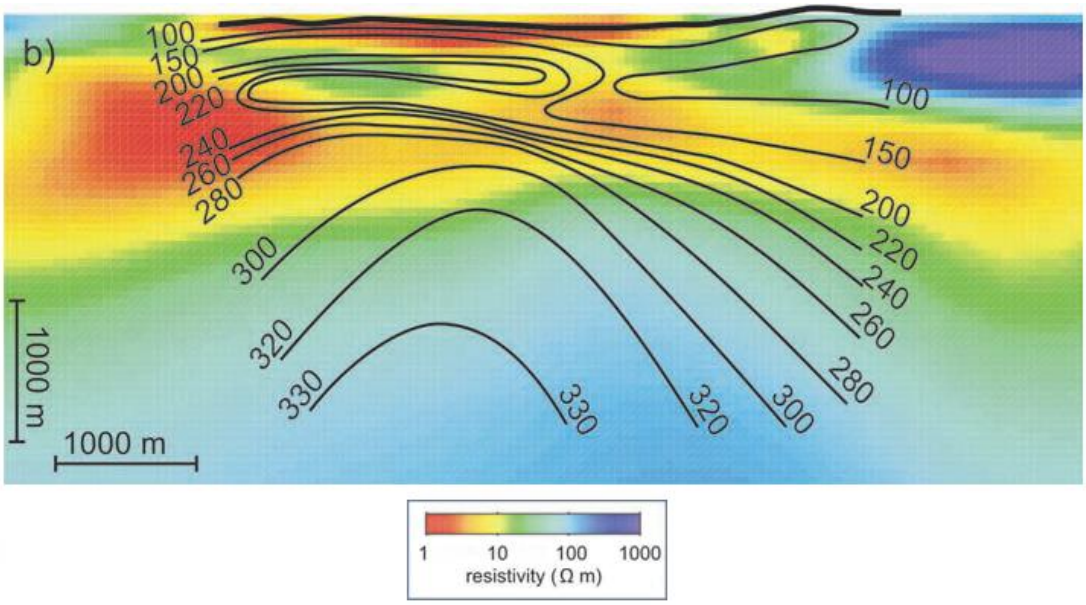


Figure 1.8: Electrical resistivity model through the center of the Rotokawa geothermal field, New Zealand, demonstrating correlation between resistivity and temperature. Red and blue colors

correspond to low and high resistivity, respectively. Black lines are isotherms in °C interpolated from well measurements. Low resistivity associated with smectite clay is seen at shallow depth and temperatures below 200°C. Above 200 to 250°C, the resistivity increases as illite and chlorite minerals are more abundant. Figure adapted from Heise et al. (2008), figure 6.

The DC resistivity technique is also useful for exploration for volcanic geothermal systems. DC resistivity can be used to detect the low resistivity anomaly (< 10 Ωm) produced by clay layers located above geothermal reservoirs, as seen in Bibby et al. (2009). Additionally, EM surveys of the previously discussed Taupo Volcanic Zone in New Zealand detected the clay layers and the underlying reservoirs of several geothermal fields (e.g. Bibby et al., 1995; Heise et al., 2008). MT was also used in the TVZ to resolve deeper hydrothermal circulation above the underlying magmatic source (Bertrand et al., 2012). MT and the time domain EM method (TEM) were also used in a study in Iceland to image the geothermal reservoir and the deeper magmatic heat source below the Hengill volcanic field (Árnason et al., 2010).

Other geophysical methods are useful in detecting magma bodies or plutons that are the heat sources for volcanic and/or plutonic geothermal systems. For example, gravity anomalies may be expected from intrusions if the density is higher than the host rock (e.g. Árnason et al., 2007; Árnason et al., 2010). Magnetic surveys are also useful for mapping the location of freshly solidified intrusions because they generally have a high magnetic intensity due to induced magnetization.

Passive seismic methods use natural earthquakes as sources, and can detect reservoirs and even magma chambers by shear wave attenuation (Einarsson, 1978). This is especially useful in volcanic geothermal systems, where shallow magma bodies display low $v_p$ and $v_s$, and high $v_p/v_s$ (e.g. Jousset et al., 2011; Schuler et al., 2015).

### 1.6.3. Exploration for extensional / fault hosted systems

Typical exploration targets for extensional/fault-hosted systems include fluids in a reservoir or faults, and even the underlying magmatic heat source can sometimes be detected.

In a fault-hosted system, gravity lows may be associated with enhanced porosity and fluid saturation in fault zones, making them suitable for gravity surveys (e.g. Blackwell et al.,

1999; Salem et al., 2005). Fault zones can also be readily imaged by the seismic reflection and refraction techniques, as the discontinuities in fault hosted systems cause anomalies in acoustic wave propagation.

EM methods are a practical choice for fault-hosted systems due to their sensitivity to fluids. MT and time-domain EM have been successfully used in the Basin and Range region in the western United States, imaging low resistivity fluids in faults and even the lower crustal magma that serves as a heat source (e.g. Newman et al., 2008; Wannamaker et al., 2007).

### 1.6.4. Exploration for HDR and sedimentary basin geothermal resources (EGS)

HDR and sedimentary basin geothermal resources require hydraulic stimulation with EGS (see Section 1.4.2 for a review). Micro-seismic data can be obtained from seismic events induced from fluid injection. For example, micro-seismic data collected at the Fenton Hill HDR project revealed the orientation and distribution of cracks in the low-permeability basement rocks (House, 1987). In another example, fluid injection tests at the Soultz-sous-Forêts HDR site showed that fluid migration occurred primarily along hydrothermally altered shear structures within the basement granite (Evans, Genter, et al., 2005; Evans, Moriya, et al., 2005).

The MT method has been used to explore the Llucmajor aquifer system in Spain, which shows anomalously high water temperatures in wells despite a lack of a clear heat source (Arango et al., 2009). An MT survey was used to define a shallow unconfined aquifer, a deeper aquitard, and a lower confined aquifer. Arango et al. (2009) suggest that water was heated by vertical flow where the aquitard was thin.

### 1.6.5. Exploration of supercritical resources

There is interest in developing supercritical fluids that may exist at depths below conventionally exploited geothermal resources, as these have a higher enthalpy than steam. A supercritical fluid exists at a temperature and pressure above its critical point, where it does not behave solely as a liquid or gas. An attractive property of supercritical fluids is their relatively high enthalpy, which could increase the power output of a single geothermal well by one order of magnitude (Fridleifsson & Elders, 2005). The Iceland Deep Drilling Project

(IDDP) is a consortium aiming to produce power from supercritical fluids at depths accessible by deep drilling.

### 1.6.6. Summary

In summary, geophysical methods have been successfully applied to a range of geothermal settings. However, improvements in the exploration techniques are required for geothermal resources at less well-understood settings. This thesis focuses on improvements to exploration with the magnetotelluric method. Areas needing improvements are summarized below.

## 1.7. Areas where improvements are needed in geophysical exploration for geothermal resources

### 1.7.1. Improvements in methods used to obtaining resistivity models from MT data

Although exploration for geothermal resources with MT is a widely used procedure, there is a significant need for improvement in the process of obtaining a resistivity model, i.e. the resistivity of the Earth as a function of space. Obtaining a model of physical properties based on limited information is an example of an inverse boundary value problem, more commonly called an inversion. Inversion of geophysical data such as MT data does not result in a unique solution; i.e. it can be shown mathematically that there are an infinite number of resistivity models that can be fit to a set of observed MT data within some statistical tolerance (Simpson & Bahr, 2005). This non-uniqueness is due to (1) uncertainty in observed MT data from random noise, signal bias, or under-sampling; and (2) the underlying physics of EM induction. The first point involves the quality of MT data, which is more readily addressed during the signal processing phase of exploration and is outside the scope of this thesis. The second point is due to the fact that MT is sensitive to the Earth's conductance, which is a function of a feature's thickness and conductivity. Different combinations of thickness and conductivity can therefore adequately fit the observed MT data. This difficulty can be addressed by incorporating additional data or *a priori* information into the inversion. Geological information or even previously obtained models can be used to constrain the range of models produced by the inversion. When available, additional data may improve the

inversion by providing additional constraints on physical properties. Another approach is the joint inversion of multiple data types, which is becoming more common as more advanced computational algorithms are developed. A common application is joint inversion of seismic and EM data (e.g. Hu et al., 2009; Mackie et al., 2007; Moorkamp et al., 2011).

### 1.7.2. Improvements in resistivity model interpretation

Low resistivity features are often targets of interest in geothermal exploration. However, low resistivity features can often be attributed to more than one material. For instance, some examples of low resistivity materials (typically < 10 Ωm) include: clay, saline fluid, partial melt, and graphite. Note that some of these conductive materials also often exist together in the same geological setting, such as clay, fluids, and partial melt at a hydrothermal geothermal resource. Therefore, a feature with a low resistivity may not correspond to a desirable drill target. One way to improve resistivity model interpretation is to include additional geological and/or geophysical data during interpretation to correctly identify low resistivity features.

Correct resistivity model interpretation is particularly important for geothermal exploration because incorrect interpretation may lead to costly drilling of additional exploratory wells. Cumming (2009) presented a hypothetical example of a geothermal prospect with a low resistivity graphitic schist that was not associated with the geothermal reservoir. In this example, limited information is given about the resistivity and known geology as seen in Figure 1.9. The < 10 Ωm feature at the left of the figure is an attractive anomaly with a low resistivity that may correspond to fluids within a reservoir. However, even without knowing the graphitic nature of this conductor, it can be ruled out as a drill target by inferring the reservoir location from surface geology. The sinter deposit contains siliceous minerals of a previously active fumarole or hot spring, suggesting that subsurface fluid temperatures may have exceeded 100°C. If the system is still active, it is logical to infer that an up-flow zone exists between the fault and the sinter deposit. The low resistivity beneath the observed sediments may correspond to fluids or clay alteration. To continue exploration, the author suggested drilling a shallow slim hole at the proposed drill site to ascertain the lithology and temperature. This example demonstrates how assembling a

reasonable conceptual model based on contextual analysis is more productive than simply drilling low resistivity targets.

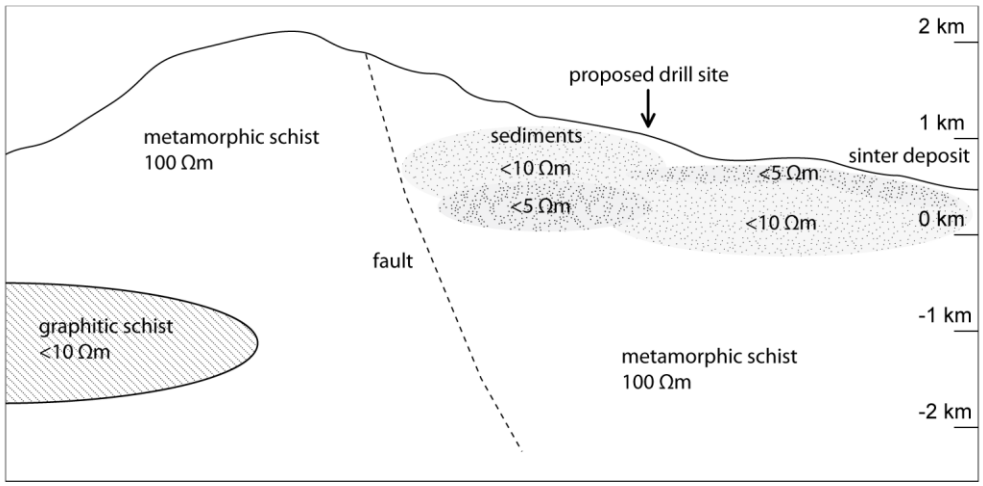


Figure 1.9: Hypothetical exploration scenario for a blind fault-hosted geothermal reservoir. The proposed drill site is inferred from a conceptual model that excludes the conductive graphitic schist as a target. Modified from Cumming (2009).

Another important topic in interpreting resistivity models is quantifying the sensitivity of MT data to particular parts of the resistivity model. Depending on the MT station and frequency distributions, some parts of the resistivity model are better constrained by the MT data than others. To avoid misinterpretation, resistivity features should be interpreted while considering data sensitivity. For example, deep conductors or conductors that appear far from the MT stations should be examined more critically, as these parts of the model are less well-constrained by the MT data. The most direct way to quantify sensitivity is to compute the sensitivity matrix, which describes the sensitivity of each datum to each model cell (Siripunvaraporn, 2012). However, the sensitivity matrix is computationally expensive to compute and is not straightforward to interpret. Many authors have instead run resolution or hypothesis tests to evaluate MT data sensitivity to particular parts of their resistivity models. A common approach is to edit a feature in the resistivity model, calculate the predicted MT data for the edited model, and then compare the two data sets: from the original inversion and from the edited model (e.g. Araya Vargas et al., 2019). If the misfit from the observed MT data worsens after editing the model, then it is inferred that the MT

data are sensitive to the feature in the original inversion model - i.e. the feature was required by the data. This method is a relatively simple and effective way to evaluate the robustness of resistivity model features, as it requires fewer calculations than computing the full sensitivity matrix.

A reader may ask, why is finding a solution to these challenges important in the context of geothermal exploration? As previously mentioned, MT is a common method deployed in geothermal exploration due to its sensitivity to electrically conductive subsurface fluids. Increasing the accuracy, along with improved interpretation of MT-derived resistivity models, would certainly mitigate the cost of follow-up drilling. In addition, although MT is applied throughout the world in geothermal exploration, there are some instances in which conventional methods are insufficient to assess a geothermal resource. This thesis presents two case studies of geothermal exploration with MT that highlight improvements in inversion and interpretation. These two projects are summarized below.

## 1.8. Investigations in this thesis

### 1.8.1. Project 1: Imaging magma beneath the Krafla geothermal field, Iceland

Krafla is a geothermal field located in northeast Iceland, located in the neo-volcanic zone which represents the North America – Eurasia plate boundary in Iceland. The Krafla central volcano is approximately 15 km in diameter and lies along the NE-SW trending fissure swarm of the neo-volcanic zone. Exploration has been performed to understand the distribution of hydrothermal fluids and magma in the subsurface, and to understand a potential deeper supercritical resource (Elders et al., 2014). A supercritical fluid exists at a pressure and temperature above the critical point, where it cannot be distinguished as either a liquid or gas (e.g. Scott et al., 2015, 2016). Finding a shallow supercritical reservoir has large implications for energy production because a geothermal well producing supercritical fluid could output an order of magnitude more electric power than a well producing steam (Fridleifsson & Elders, 2005). This would increase the energy production of a typical geothermal well from on the order of 1 MW to 10 MW. The pilot well of the Iceland Deep Drilling Project (IDDP-1) was drilled in 2009, but did not reach its target depth of 4 km because it unexpectedly intersected rhyolite magma at a depth of 2.1 km.

The rhyolite magma was not previously imaged by geophysical methods including MT. Therefore, new approaches to the inversion of the MT data and interpretation of the resistivity model will be investigated. This approach includes (1) developing an improved methodology for inversion of the MT data, which is inherently non-unique and can provide a range of acceptable resistivity models for interpretation, and (2) understanding why the magma body was not detected geophysically (with either MT or seismic data).

This thesis presents new results from a re-assessment of the Krafla MT data. A new approach to the inversion of the Krafla MT data is presented that uses the full impedance tensor data and a finely discretized mesh to accurately model small, near-surface features. The resulting model notably contains a large low-resistivity feature below the depth that IDDP-1 encountered magma. In accordance with recent laboratory resistivity studies, the decreased resistivity at this depth may correspond to dehydration and decomposition of chlorite and epidote minerals, not necessarily partial melt. In fact, resolution tests with hypothetical magma bodies suggest the MT data would only be sensitive to an unrealistically large sill (2.25 $km^{3)}$ with very low resistivities (0.1 - 0.3 Ωm) at the bottom of IDDP-1. Finally, an improved method to assess MT data sensitivity using the Kolmogorov-Smirnov (K-S) statistical test will be shown that is more objective than only considering r.m.s. misfit.

### 1.8.2. Project 2: Fault imaging in the Canoe Reach area of the Rocky Mountain Trench, Canada

Canoe Reach is a fault-hosted geothermal prospect located in British Columbia, Canada. The Canoe Reach area lies in the Southern Rocky Mountain Trench (SRMT), in the eastern part of the Canadian Cordillera, and is the location of the northernmost thermal spring along the SRMT fault. Although several thermal springs have been observed along the SRMT fault, the Canoe Reach spring is isolated by about 200 km. Other workers have proposed that fault geometry strongly controls the presence of thermal springs in the area, with large offset normal faults associated with many hot springs in the SRMT fault (Grasby & Hutcheon, 2001). The aim of this project is to understand the nature of the Canoe Reach prospect, i.e. what mechanism causes hot fluids to circulate to shallow depth. Resistivity models are presented from two regions of Canoe Reach that intersect the SRMT fault, which is believed to be the conduit for hot, circulating fluids. This study shows that exploration for

this fault-hosted prospect in a structurally complex geological setting requires more care than exploration for a conventional volcanic reservoir. In particular, shallow conductors can be attributed to fluid-filled faults, graphite, or sulfide minerals, and additional information is needed to correctly identify these features. Interpretation of the Canoe Reach resistivity models is also complicated by the possibility of electrical anisotropy, as evidenced by rocks with highly foliated, anisotropic textures visible in outcrop. This study shows an example where 3-D electrical anisotropy must be considered for correct interpretation of the resistivity model.

## 1.9. Thesis outline

- Chapter 2 contains a review of the MT methodology employed in the two case studies of this thesis.

- Chapter 3 presents the MT case study at the Krafla geothermal field in Iceland.

- Chapter 4 is about MT case study at Canoe Reach, located in British Columbia, Canada.

- Chapter 5, the conclusion, summarizes the progress made to MT inversion and interpretation of resistivity models, and highlights implications for geothermal exploration.

# 2. Electromagnetic induction of the Earth

Electromagnetic methods such as magnetotellurics (MT) determine the electric resistivity of the Earth by observing how low frequency electromagnetic signals propagate in the Earth. To fully understand the resolution that is possible with MT, it is important to understand how electromagnetic signals travel in the Earth. This is explained in this chapter, based on Maxwell's equations. This is followed by a discussion of the interpretable quantities used in MT and some aspects of data analysis that include data dimensionality, galvanic distortion, and anisotropy. This chapter concludes with an overview of the procedures used to collect MT data, process raw MT data, and invert MT data to obtain a resistivity model.

## 2.1. Electrical resistivity

Electrical resistivity is a physical property that determines a material's ability to resist the flow of electrical current. Consider the simple case of a copper cylinder with length $L$ and cross-sectional area $A$, as shown in Figure 2.1. The electrical resistivity is defined by:

$$\rho = \frac{RA}{L} \tag{2.1}$$

where $R$ is the material resistance. The SI unit of electrical resistivity is the ohm-meter (Ωm). It is important to distinguish electrical resistivity from resistance. In Figure 2.1 the electric current $I$ flows perpendicular to the exposed cross-sectional area $A$, and therefore the electrical resistance of the copper cylinder can be increased by increasing the length $L$ or by decreasing the cross-sectional area $A$. However, the resistivity of the copper cylinder cannot be changed because it is an inherent property of copper.

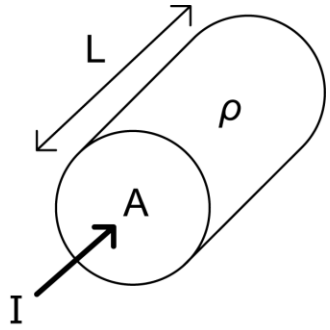


Figure 2.1: Schematic of electric current flow $I$ through a cylinder. The resistance ($R$) can be calculated from the cross-sectional area $A$, length $L$, and resistivity $\rho$.

Resistivity (or its inverse, conductivity) varies by many orders of magnitude for common Earth materials. Representative Earth materials and their resistivity ranges are shown in Figure 2.2. For instance, dry crystalline rocks such as those of the Canadian Shield have a very high resistivity, sometimes greater than 10,000 Ωm. In contrast, partially molten magma bodies beneath active volcanoes may have a resistivity as low as 0.1 Ωm. Due to this large range, resistivity is a useful property to identify materials in the Earth.

Figure 2.2 also illustrates that several Earth materials have overlapping resistivity ranges, which can cause uncertainty in interpreting MT data. In many cases the goal of an exploration project is to map the distribution of fluids in the Earth. The presence of fluids can greatly decrease the bulk resistivity of a rock to < 1 Ωm as seen in Figure 2.2. However, materials such as sulfide minerals, graphite, and partial melt can have a similar resistivity value. Therefore, additional geological information or geophysical data may be required to correctly identify the cause of the low resistivity.

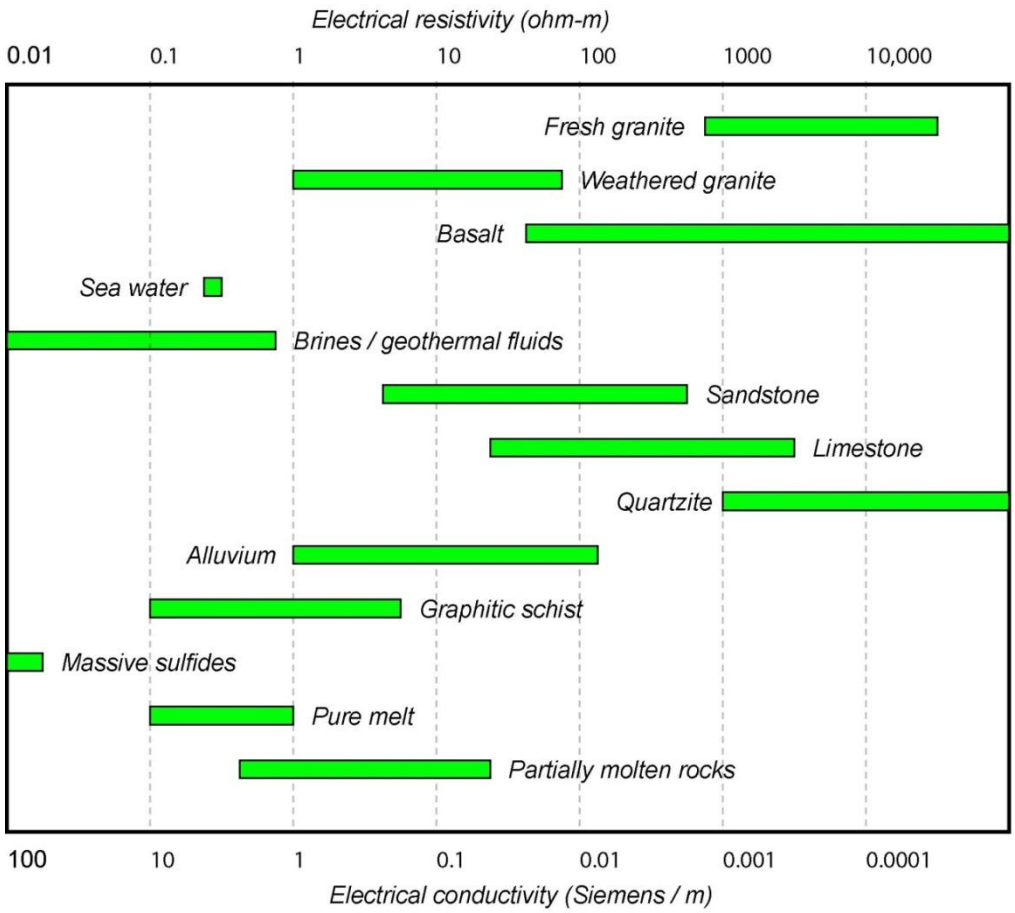


Figure 2.2: Electrical resistivity / conductivity of representative Earth materials. From Unsworth, (2018).

## 2.2. Electromagnetic signal propagation in the Earth

This section describes the physical basis for electromagnetic (EM) signal propagation in the Earth. Starting from Maxwell's equations (Maxwell, 1861), it will be shown that EM signals travel as a wave in the air but by diffusion in the Earth. The skin depth equation, which governs the propagation depth of diffusive EM signals in the Earth, will also be derived.

### 2.2.1. Maxwell's equations

Maxwell's equations describe the behavior of EM signals in matter and are the basis of understanding the signals that are measured with the MT method. Maxwell's equations are:

$$\nabla \cdot \boldsymbol{E} = \frac{Q}{\epsilon} \tag{2.2}$$

$$\nabla \cdot \boldsymbol{H} = 0 \tag{2.3}$$

$$\nabla \times \boldsymbol{E} = -\mu \frac{\partial \boldsymbol{H}}{\partial t} \tag{2.4}$$

$$\nabla \times \boldsymbol{H} = \sigma \boldsymbol{E} + \epsilon \frac{\partial \boldsymbol{E}}{\partial t} \tag{2.5}$$

where $\boldsymbol{E}$ is the electric field strength, $\boldsymbol{H}$ is the magnetic field strength, $Q$ is the volume charge density, $\sigma$ is electrical conductivity (the inverse of resistivity), $\mu$ is the Earth's magnetic permeability, $\epsilon$ is the dielectric permittivity of the Earth, and $t$ is time. $\nabla \cdot$ and $\nabla \times$ are the divergence and curl vector operators, respectively. Equations (2.4) and (2.5) are written as simplified forms assuming that $\mu$ and $\epsilon$ are scalar quantities that are constant in time and space. Note that $\boldsymbol{E}$ and $\boldsymbol{H}$ are functions of space ($x$, $y$, $z$ directions) and time $t$. The coordinate system is right-handed, with positive $x$ as north, positive $y$ as east, and positive $z$ as vertically down.

Equation (2.2) is also known as Gauss' Law, which relates electric field strength to the quantity of electric charge present. To qualitatively understand this law, consider a small volume of material containing a fixed amount of electric charge. The electric flux (i.e. the number of electric field lines) through the volume is proportional to the amount of charge and the volume's dielectric permittivity.

Equation (2.3) is also known as Gauss' Law of Magnetism, which states that the divergence of a magnetic field is zero. While a positive point electric charge radiates an electric field away from it, no similar corollary exists for magnetism; in other words, there are no magnetic monopoles because a point source of a magnetic field implies a non-zero divergence.

Equation (2.4) is also known as Faraday's Law of induction. It states that a time-varying magnetic field results in a spatially-varying electric field.

Equation (2.5) is Ampère's Law with Maxwell's displacement current added. This equation states that a spatially-varying magnetic field can be produced by a static and/or a time-varying electric field.

Three additional relationships are needed to describe the behavior of the electric and magnetic fields in matter. These equations are known as the constitutive equations of electromagnetism, and are listed below:

$$\boldsymbol{B} = \mu \boldsymbol{H} \tag{2.6}$$

$$\boldsymbol{D} = \varepsilon \boldsymbol{E} \tag{2.7}$$

$$\boldsymbol{J} = \sigma \boldsymbol{E} \tag{2.8}$$

where $\boldsymbol{B}$ is the magnetic flux density, $\boldsymbol{D}$ is the displacement field, and $\boldsymbol{J}$ is the current density.

Equations (2.6) and (2.7) are constitutive relations that describe how a material's magnetic permeability and dielectric permittivity modify an applied magnetic or electric field, respectively. These are simplified relations that assume there are no permanently polarized or magnetized (i.e. ferromagnetic) materials in the Earth. It is also assumed that magnetic permeability and dielectric permittivity are scalar quantities linearly related to their respective fields. For the crustal and mantle depths typically sampled by MT, the magnetic permeability of the Earth can be approximated as the free space value $\mu_0$ in the absence of highly magnetic materials such as metallic ore bodies. The dielectric permittivity can also be approximated as the free space value $\varepsilon_0$ in the absence of highly polarisable materials.

Equation (2.8) is a form of Ohm's Law relating current density to the electric field. The current density $\boldsymbol{J}$ appears in the right hand side of Equation (2.5), showing that a static electric field generates a magnetic field.

### 2.2.2. The electromagnetic skin depth

This section applies Maxwell's equations to describe EM signal propagation in the Earth. EM signals travel as waves in the air but by diffusion in the Earth. EM signal diffusion is an important phenomenon that controls the depth at which MT can determine the electrical

resistivity. The depth over which an EM signal is attenuated is called the skin depth, a quantity that will be derived in this section. Here the skin depth is defined as the depth at which the EM signal has attenuated to $1/e$ (~37%) of its magnitude at the surface, where $e$ is the base of the natural logarithm. To understand EM signal propagation in the Earth, first consider the behavior of the electric field in the Earth. Taking the curl of Equation (2.4) and substituting in Equation (2.5) yields:

$$\nabla \times \nabla \times \boldsymbol{E} = -\mu\sigma \frac{\partial \boldsymbol{E}}{\partial t} - \mu\epsilon \frac{\partial^2 \boldsymbol{E}}{\partial t^2} \tag{2.9}$$

where the Earth properties $\mu$, $\sigma$, and $\epsilon$ are assumed to have no time dependence. Now Equation (2.9) is only written in terms of the electric field $\boldsymbol{E}$. Equation (2.9) can be rewritten using the vector identity:

$$\nabla \times \nabla \times \boldsymbol{E} = \nabla(\nabla \cdot \boldsymbol{E}) - \nabla^2 \boldsymbol{E} \tag{2.10}$$

where $\nabla^2$ is the Laplacian operator, as:

$$\nabla(\nabla \cdot \boldsymbol{E}) - \nabla^2 \boldsymbol{E} = -\mu\sigma \frac{\partial \boldsymbol{E}}{\partial t} - \mu\epsilon \frac{\partial^2 \boldsymbol{E}}{\partial t^2} \tag{2.11}$$

In order to simplify Equation (2.11) consider Equation (2.2), which equals zero in the absence of free electric charges ($Q$ = 0). This is equivalent to considering a horizontally layered Earth, where the resistivity is constant within each layer. In a layered Earth, the horizontal electrical fields are parallel to boundaries and thus no free charges exist. Equation (2.11) can be further simplified by considering the EM signal propagating in a halfspace such that:

$$\nabla \cdot \boldsymbol{E} = 0 \tag{2.12}$$

However, in the following sections it will become clear that Equation (2.12) does not hold for 2-D or 3-D resistivity structure, where electric currents cross conductivity boundaries. By

applying Equation (2.12), this derivation ignores the electric fields formed from static (time-invariant) charge accumulation. The time/frequency independent processes are called galvanic effects and are addressed in a Section 2.3. For now, this derivation focuses on the inductive (time/frequency dependent) processes that generate electric fields, i.e. from Equations (2.4) and (2.5).

Continuing with the skin depth derivation, substituting Equation (2.12) into Equation (2.11) yields:

$$\nabla^2 \boldsymbol{E} = \mu\sigma \frac{\partial \boldsymbol{E}}{\partial t} + \mu\epsilon \frac{\partial^2 \boldsymbol{E}}{\partial t^2} \tag{2.13}$$

Note that a similar form of Equation (2.13) can be obtained for the magnetic field $\boldsymbol{H}$ by taking the curl of Equation (2.5) and substituting in Equations (2.3), (2.4), and (2.10). Following this approach results in the expression:

$$\nabla^2 \boldsymbol{H} = \mu\sigma \frac{\partial \boldsymbol{H}}{\partial t} + \mu\epsilon \frac{\partial^2 \boldsymbol{H}}{\partial t^2} \tag{2.14}$$

which is the same form as Equation (2.13). This can be understood because the electric and magnetic fields are the two components of an EM signal and thus are governed by the same propagation equations. The current derivation only considers the $\boldsymbol{E}$ field as in Equation (2.13), but the same result can be obtained from Equation (2.14). Examining the right hand side of Equation (2.13), the first term is a first derivative in time and thus in the form of a conduction equation; the second term is a second derivative in time and thus in the form of a wave equation. These terms are called the conduction current and the displacement current, respectively. If one of these terms is much larger than the other, then that term determines the dominant type of signal propagation. For example, if the conduction term dominates, the EM signal propagates by diffusion. If the displacement current dominates, the EM signal travels as a wave.

Next, in order to simplify Equation (2.13), assume that $\boldsymbol{E}$ varies harmonically in time. With the method of separation of variables, $\boldsymbol{E}$ can be written as:

$$\boldsymbol{E}(x,y,z,t) = \widetilde{\boldsymbol{E}}(x,y,z,\omega)e^{-i\omega t} \tag{2.15}$$

where $\omega$ is the angular frequency and $\widetilde{\boldsymbol{E}}$ is the electric field as a function of $x$, $y$, and $z$, and $\omega$. The angular frequency is related to frequency by:

$$\omega = 2\pi f \tag{2.16}$$

Substituting Equation (2.15) into Equation (2.13) and differentiating with respect to time yields:

$$\nabla^2\widetilde{\boldsymbol{E}} = -i\omega\mu\sigma\widetilde{\boldsymbol{E}} + \omega^2\mu\epsilon\widetilde{\boldsymbol{E}} \tag{2.17}$$

where:

$$i = \sqrt{-1} \tag{2.18}$$

Now it is apparent that the conduction current is a function of conductivity and the displacement current is a function of dielectric permittivity. To understand which term is dominant, we take the ratio of the conduction current and the displacement current:

$$N = \frac{\sigma}{\omega\epsilon} \tag{2.19}$$

As $N$ becomes large, conduction current will become much larger than the displacement current. Figure 2.3 displays values of $N$ for a range of conductivities and angular frequencies. The free space value of dielectric permittivity ($\varepsilon_0$ = $8.85\times10^{-12}$ F/m) is assumed because dielectric permittivity only varies by about two orders of magnitude in the Earth. Note that a larger $\varepsilon$ decreases the value of $N$ as expected from Equation (2.19). Typical operating frequency ranges for ground-penetrating radar (GPR), audio magnetotellurics (AMT), broadband magnetotellurics (BBMT), and long period magnetotellurics (LMT) are outlined

in red, grey, blue, and green boxes, respectively. The GPR method relies on wave propagation and requires a small value of $N$, while MT assumes a diffusive signal and requires a large $N$. Even in the proper operating frequencies for GPR, a high conductivity may lead to a large $N$, and the EM signal propagation cannot be approximated as a wave. Similarly, a low conductivity in BBMT operating frequencies may lead to a small $N$, invalidating the assumption that EM signals propagate by diffusion.

Consider an example calculation of $N$ using typical values for a BBMT survey. Assuming a frequency of 1000 Hz, an Earth conductivity of 0.01 S/m, and the free space value of permittivity $\varepsilon_0$, Equation (2.19) yields $N \approx 180000$. Thus, the conduction current term is much larger than the displacement current term, and therefore the displacement current can be neglected. $N$ is even larger for the lower frequencies that are typically used in broadband and long period MT studies, meaning that for the signals used in MT the displacement current term can be ignored such that Equation (2.17) reduces to:

$$\nabla^2 \widetilde{\boldsymbol{E}} + i\omega\mu\sigma\widetilde{\boldsymbol{E}} = 0 \tag{2.20}$$

Next, Equation (2.20) can be written explicitly for the $x$, $y$, and $z$ directions because $\widetilde{\boldsymbol{E}}(x,y,z,\omega)$ is a function of $x$, $y$, and $z$. To simplify the analysis, assume that the electric field is polarized in the $x$ direction, i.e. $E_y = E_z = 0$. Therefore, Equation (2.20) can be written as:

$$\frac{\partial^2 E_x}{\partial x^2} + \frac{\partial^2 E_x}{\partial y^2} + \frac{\partial^2 E_x}{\partial z^2} + i\omega\mu\sigma E_x = 0 \tag{2.21}$$

Similar equations can be written for $E_y$ and $E_z$ polarizations; however, this derivation only considers $E_x$ because the same result is obtained for the $E_y$ polarization. Additionally, $E_z$ will be ignored because it is typically very small and not measured in an MT survey.

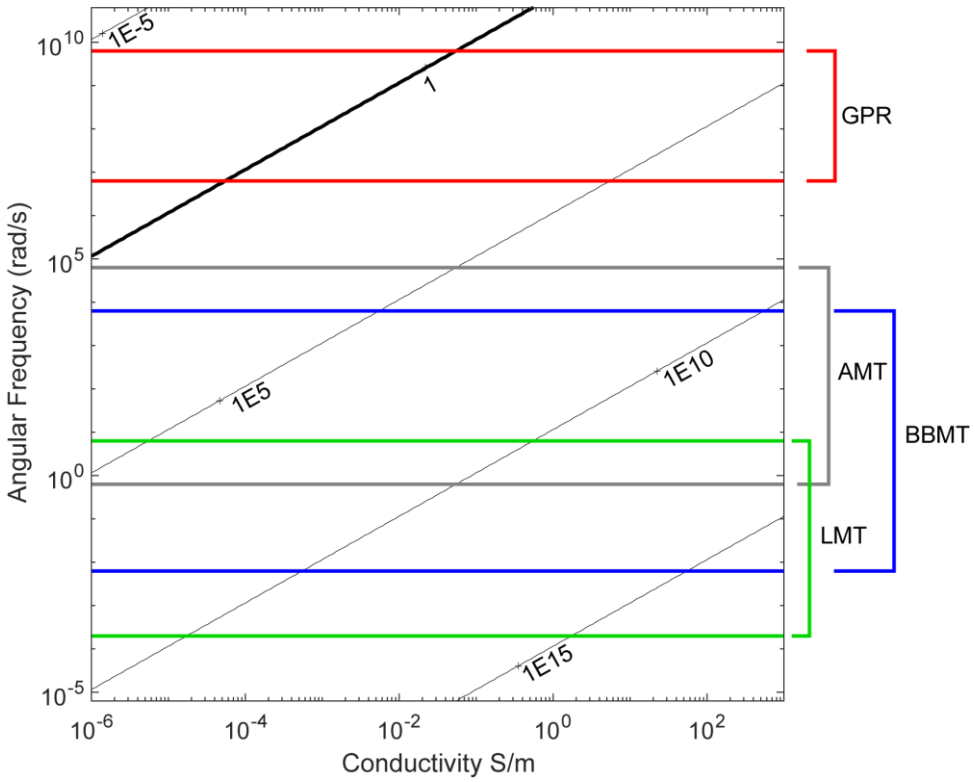


Figure 2.3: Contour lines of *N* as a function of conductivity and angular frequency. *N* is an estimate of the relative contribution of conduction and displacement currents to EM signal propagation (Equation 2.19). Values greater than 1 indicate that the conduction current dominates and the signal propagates by diffusion; values less than 1 indicate a dominant displacement current and thus wave propagation. The dielectric permittivity of free space is assumed. Typical operating frequency ranges for ground-penetrating radar (GPR), audio magnetotellurics (AMT), broadband magnetotellurics (BBMT), and long period magnetotellurics (LMT) are outlined in red, grey, blue, and green boxes, respectively. The GPR method relies on wave propagation and requires a small *N*; MT assumes a diffusive signal and requires a large *N*.

If the signal is a plane wave, then $\widetilde{\boldsymbol{E}}(x,y,z,\omega)$ only varies in the $z$-direction. Thus Equation (2.21) simplifies to:

$$\frac{\partial^2 E_x}{\partial z^2} + i\omega\mu\sigma E_x = 0 \tag{2.22}$$

Equation (2.22) is a homogeneous second-order ordinary differential equation. A trial solution for an equation of this form is:

$$E_x(z) = c_1 e^{r_1 z} + c_2 e^{r_2 z} \tag{2.23}$$

where $c_1$ and $c_2$ are constants to be determined, and $r_1$ and $r_2$ are the roots of:

$$ar^2 + br + c = 0 \tag{2.24}$$

which is the auxiliary equation of Equation (2.22). $a$, $b$, and $c$ are the coefficients of Equation (2.22). Thus $a$ = 1, $b$ = 0, and $c = i\omega\mu\sigma$. The roots of Equation (2.24) are found from the quadratic equation:

$$r = \frac{-b \pm \sqrt{b^2 - 4ac}}{2a} \tag{2.25}$$

where $r$ is a root of Equation (2.24). Solving Equation (2.25) yields:

$$r = \pm\sqrt{-i\omega\mu\sigma} \tag{2.26}$$

Next, the two solutions to Equation (2.26) are:

$$r_1 = \gamma(1 - i) \tag{2.27a}$$

$$r_2 = -\gamma(1 - i) \tag{3.27b}$$

where $r_1$ and $r_2$ are the roots of Equation (2.24), with:

$$\gamma = \frac{\sqrt{2\omega\mu\sigma}}{2} \tag{2.28}$$

Substituting Equations (2.27a) and (3.27b) into Equation (2.23) yields:

$$E_x(z) = c_1 e^{\gamma(1-i)z} + c_2 e^{-\gamma(1-i)z} \tag{2.29}$$

Furthermore, Equation (2.29) can be expanded as:

$$E_x(z) = c_1 e^{\gamma z} e^{-i\gamma z} + c_2 e^{-\gamma z} e^{i\gamma z} \tag{2.30}$$

Now the coefficients $c_1$ and $c_2$ must be determined. The Earth is not a perfect conductor and attenuates the EM signals. Therefore, $E_x \to 0$ as $z \to \infty$. If $c_1 > 0$, the first term on the right hand side of Equation (2.30) approaches infinity as $z$ grows large; if $c_1 < 0$, the same term approaches negative infinity as $z$ grows large. Thus, $c_1$ must equal zero for $E_x$ to be bounded as $z$ increases. Also note that because $E_x = c_2$ at $z = 0$, $c_2$ can be written as $E_x^0$ to represent the value of $E_x$ at the surface of the Earth. Thus Equation (2.30) simplifies to:

$$E_x(z) = E_x^0 e^{-\gamma z} e^{i\gamma z} = E_x^0 e^{-(1-i)\gamma z} \tag{2.31}$$

Note that the term $(1 - i)\gamma$, which was derived in Equation (2.27a), controls the decay of $E_x^0$ in the Earth as a function of $z$. This term is called the wavenumber and is denoted by $k$. An expression for the wavenumber is obtained by substituting Equation (2.28) into Equation (2.27a):

$$k = (1 - i)\gamma = (1 - i)\sqrt{\frac{\omega\mu\sigma}{2}} \tag{2.32}$$

The wavenumber will be further discussed in the next section. In order to study how the complex function $E_x(z)$ changes with depth, consider the modulus of $E_x(z)$. Using Euler's identity:

$$e^{i\theta} = \cos\theta + i\sin\theta \tag{2.33}$$

Equation (2.31) can be rewritten as:

$$E_x(z) = E_x^0 e^{-\gamma z}\cos\gamma z + i(E_x^0 e^{-\gamma z}\sin\gamma z) \tag{2.34}$$

Now it is clear that the first term on the right hand side of Equation (2.34) is the real part of $E_x(z)$ and the second term is the imaginary part. The modulus of a complex number $\xi = a + ib$ is:

$$|\xi| = |a + ib\,| = \sqrt{a^2 + b^2} \tag{2.35}$$

Using terms from Equation (2.34), the modulus of $E_x(z)$ is:

$$|E_x(z)| = \sqrt{(E_x^0 e^{-\gamma z}\cos\gamma z)^2 + (E_x^0 e^{-\gamma z}\sin\gamma z)^2} \tag{2.36}$$

Next, rearranging the right hand side of Equation (2.36) yields:

$$|E_x(z)| = \sqrt{(E_x^0 e^{-\gamma z})^2(\cos^2\gamma z + \sin^2\gamma z)} \tag{2.37}$$

Using the identity:

$$\cos^2\theta + \sin^2\theta = 1 \tag{2.38}$$

Equation (2.37) simplifies to:

$$|E_x(z)| = E_x^0 e^{-\gamma z} \tag{2.39}$$

Note that $|E_x(z)|$ decays monotonically as $z$ increases, and its maximum value occurs at $z = 0$. Returning to the definition of the skin depth, when the exponent $\gamma z$ = 1, $E_x(z)$ has decayed to 1/e of its value at $z = 0$. The depth at which this occurs is called the skin depth and is denoted by $\delta$. Consider the case when $z = \delta$, such that $\gamma z = \gamma\delta = 1$. Substituting this expression into Equation (2.28) yields:

$$\frac{\sqrt{2\omega\mu\sigma}}{2}\delta = 1 \tag{2.40}$$

The final expression for the skin depth equation is obtained by rearranging terms to give:

$$\delta = \sqrt{\frac{1}{\pi\mu f\sigma}} \tag{2.41}$$

The skin depth $\delta$ is thus a function of the signal frequency $f$, the Earth's magnetic permeability $\mu$, and the Earth's conductivity $\sigma$. The magnetic permeability of free space $\mu_0$ is assumed for most Earth materials. Therefore, variations in signal frequency and the Earth's conductivity (or its inverse, resistivity) have the largest impact on the skin depth. Figure 2.4 contains sample skin depth calculations for a halfspace containing an upper boundary but extending to infinity horizontally and in the vertical direction. In this figure, the vertical axis is depth, and the horizontal axis is the electric field magnitude $|E|$ normalized by the magnitude at $z$ = 0, $|E_0|$. Panel a) shows the signal decay with a frequency of 100 Hz and halfspaces of 1, 10, 100, and 1000 Ωm. The solid circle on each curve represents the skin depth for the specified frequency and resistivity. It is clear that for a fixed frequency, the skin depth increases with increasing resistivity. In panel b) the halfspace resistivity is fixed at 10 Ωm and the signal frequencies are 1000, 100, 10, and 1 Hz. Similarly, the solid circle on each curve represents the skin depth for the specified frequency and resistivity. It is evident that decreasing the signal frequency increases the skin depth. Figure 2.4 also demonstrates that different combinations of resistivity and signal frequency can result in the same skin depth.

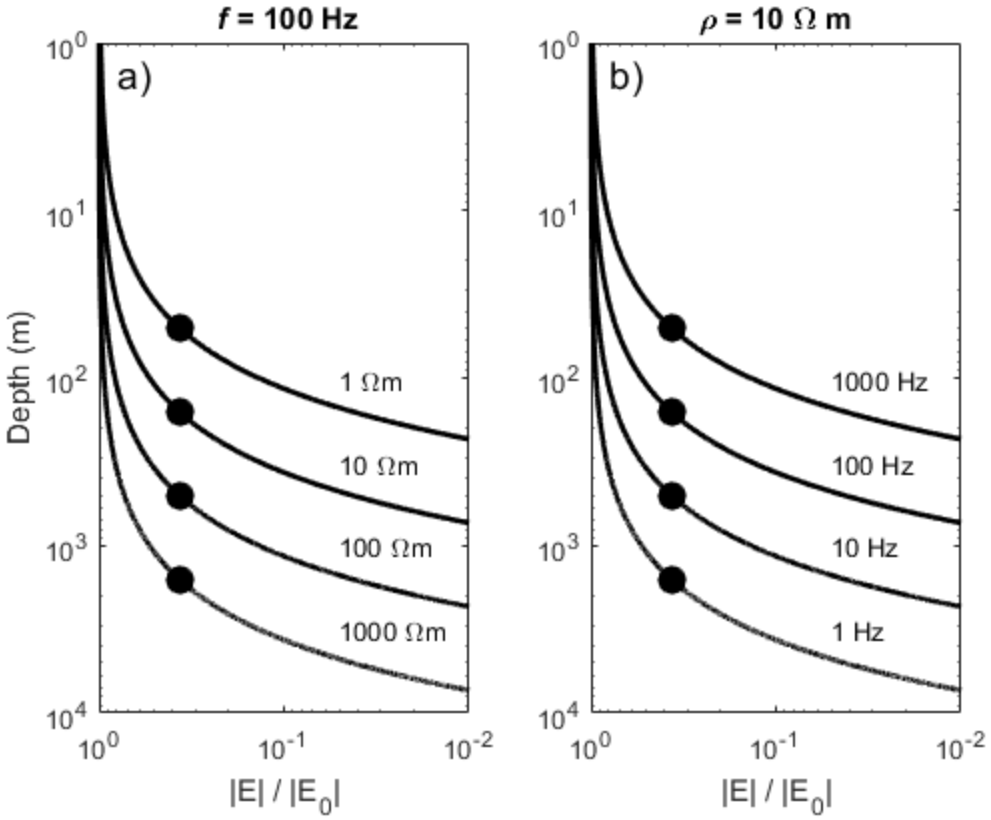


Figure 2.4: Electric field magnitude as a function of depth with a) a fixed signal frequency ($f$) of 100 Hz and halfspace resistivity values of 1, 10, 100, and 1000 Ωm; b) A fixed halfspace resistivity ($\rho$) of 10 Ωm and signal frequencies of 1000, 100, 10, and 1 Hz. The electric field magnitude $|E|$ is normalized to the electric field magnitude at the surface, $|E_0|$. The solid circle on each curve represents the skin depth for the specified frequency and resistivity, i.e. where $|E|/|E_0| = e^{-1}$.

## 2.3. Interpretable quantities in magnetotellurics

The previous section described how EM signals propagate in the Earth. This section describes how the electric and magnetic field components measured at the Earth's surface can be used to determine the Earth's resistivity structure. The following interpretable quantities derived from these EM signals can be analyzed to determine the underlying electrical resistivity structure.

### 2.3.1. Magnetotelluric impedance

MT measures the electric and magnetic field components of EM signals. From Faraday's Law of induction, a time-varying magnetic field induces an electric field that varies

in time and space; thus an oscillating magnetic field at the Earth's surface induces both electric current flow in the Earth along with an associated electric field. The properties of the Earth can be thought of as a filter that determines the amplitude and phase of the induced electric field. In MT this is called the impedance and is represented by a 2 × 2 tensor, $\boldsymbol{Z}$:

$$\begin{bmatrix} E_x(\omega) \\ E_y(\omega) \end{bmatrix} = \begin{bmatrix} Z_{xx}(\omega) & Z_{xy}(\omega) \\ Z_{yx}(\omega) & Z_{yy}(\omega) \end{bmatrix} \begin{bmatrix} H_x(\omega) \\ H_y(\omega) \end{bmatrix} \tag{2.42}$$

where the *x* and *y* subscripts indicate the fields measured in the north-south and east-west directions, respectively. $\boldsymbol{E}$, $\boldsymbol{H}$, and $\boldsymbol{Z}$ are implicitly functions of signal frequency. Determining $\boldsymbol{Z}$ is the goal of MT because $\boldsymbol{Z}$ is a function of the Earth's physical properties, including electrical resistivity. As seen in Equation (2.42), the horizontal components of $\boldsymbol{E}$ and $\boldsymbol{H}$ need to be measured in order to calculate $\boldsymbol{Z}$.

The following is a simple example of how the impedance can be computed from the electric and magnetic field components of an EM wave that enters a homogeneous halfspace. Assuming an incident EM wave that is planar, polarized in the *x* direction, and varies harmonically in time, it can be shown that the electric field of this signal that is transmitted into the Earth can be written as:

$$E_x = E_x^0 e^{-kz} e^{-i\omega t} \tag{2.43}$$

where $E_x^0$ is the value of the electric field at the surface, and $k$ is the wavenumber that describes the signal decay in the Earth. From Equation (2.4), the corresponding magnetic field in the Earth is:

$$H_y = \frac{-kE_x^0 e^{-kz} e^{-i\omega t}}{i\omega\mu} \tag{2.44}$$

Now following Equation (2.42), the impedance of an EM signal polarized in the *x* direction is defined as:

$$Z_{xy} = \frac{E_x}{H_y} \tag{2.45}$$

Substituting Equations (2.43) and (2.44) into Equation (2.45) yields:

$$Z_{xy} = \frac{-i\omega\mu}{k} \tag{2.46}$$

Finally, substituting in the expression for the wavenumber from Equation (2.32) and simplifying yields:

$$Z_{xy} = (1 - i)\sqrt{\frac{\omega\mu}{2\sigma}} \tag{2.47}$$

Equation (2.47) is an expression for the surface impedance of a homogeneous halfspace. This expression contains the conductivity of the Earth, which is the quantity of interest in MT. The impedance can be interpreted by analyzing its magnitude and phase, as seen in Section 2.3.2.

The previous derivation assumed a 1-D Earth, however, in practice the resistivity structure of the Earth is complicated and may be approximated as 1-D, 2-D, or 3-D at different depths. The impedance data are sensitive to different volumes at different frequencies, and therefore the impedance data contain information on the dimensionality of the Earth. It is important to understand the data dimensionality in order to apply the correct type of data analysis. For example, an attempt to model MT data that contain strong indications of 3-D resistivity structure with a 2-D approach will not yield reliable results. However, often a subset of the data (i.e. excluding certain frequencies or stations) can be approximated as 2-D and appropriately modeled with a 2-D approach. The following sections summarize the forms of the impedance tensor in 1-D, 2-D, and 3-D settings.

#### 2.3.1.1. Impedance tensor of a 1-D Earth

MT data analysis is simplified if the Earth's resistivity structure can be approximated as 1-D. In the 1-D case, the resistivity does not vary in the $x$ and $y$ directions and the impedance tensor from Equation (2.42) can be simplified to:

$$\boldsymbol{Z}_{1D} = \begin{bmatrix} 0 & Z \\ -Z & 0 \end{bmatrix} \tag{2.48}$$

Note that the off-diagonal elements of $\boldsymbol{Z}_{1D}$ are equal but opposite in sign. This can be confirmed by replacing $E_x$ with $E_y$ and $H_y$ with $H_x$ in Equations (2.43), (2.44), and (2.45).

#### 2.3.1.2. Impedance tensor of a 2-D Earth

In the case of a 2-D resistivity structure, a coordinate system can be chosen where the resistivity is invariant in one direction. In the simple example depicted in Figure 2.5, the original *xy* coordinate system does not align with the strike direction of the grey prism. The coordinate system can be rotated by the angle $\theta$ to the new *x'y'* system, such that resistivity does not vary in the *x'* direction. In this case, the impedance tensor simplifies to:

$$\boldsymbol{Z}_{2D} = \begin{bmatrix} 0 & Z_{x'y'} \\ Z_{y'x'} & 0 \end{bmatrix} \tag{2.49}$$

and the angle of rotation $\theta$ between the original *xy* coordinate system and the new *x'y'* coordinate system is called the strike angle. The impedance tensor can also be rotated to the angle $\theta$ + 90° such that there are no resistivity variations in the *y'* direction, and the tensor has the form:

$$\boldsymbol{Z}_{2D} = \begin{bmatrix} 0 & Z_{y'x'} \\ Z_{x'y'} & 0 \end{bmatrix} \tag{2.50}$$

The impedance tensor in Equation (2.49) is aligned to the strike direction and the tensor in Equation (2.50) is aligned 90° to the strike direction. When analyzing field MT data where

the Earth's structure is unknown, the geologic strike angle cannot be uniquely determined between $\theta$ and $\theta$ + 90°. Additional data such as tipper and induction arrows discussed in Section 2.3.3 are needed to solve the ambiguity.

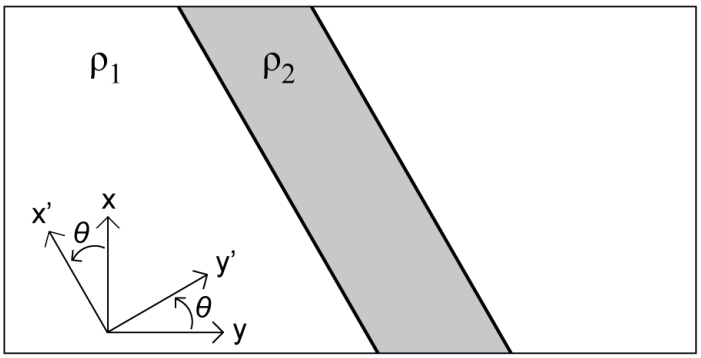


Figure 2.5: Example of coordinate system rotation for a 2-D Earth. The figure shows a map view of a prism with resistivity $\rho_2$ embedded in a background resistivity of $\rho_1$. In the original coordinate system *xy*, resistivity varies in the *x* and *y* directions if $\rho_1 \neq \rho_2$. The coordinate system can be rotated by the angle $\theta$ to the new *x'y'* system in order to align with the geologic strike direction, resulting in resistivity not varying in the *x'* direction.

When aligned with the strike direction, $Z_{x'y'}$ is called the transverse electric (TE) mode, and $Z_{y'x'}$ is called the transverse magnetic (TM) mode. In the TE mode, the electric field is polarized in the strike direction such that the electric current does not cross any resistivity boundaries. Therefore, the TE mode is sensitive to changes in resistivity caused by induction, i.e. frequency-dependent variations in the electric and magnetic fields governed by the skin depth. Conversely, the TM mode electric field is polarized perpendicular to the strike direction and crosses resistivity boundaries. In addition to the inductive effect, the TM mode contains a galvanic (frequency-independent) effect due to electric charge accumulation on resistivity boundaries. The galvanic effect is a result of Gauss' Law (Equation 2.2) which states that electric fields can be generated by static (time invariant) electric charges. Figure 2.6 contains a simple illustration of the galvanic effect. In panel a) a conductive cube in the Earth is subject to a primary electric field $E_p$. In this geometry, it can be shown with Gauss' Law that the surface charge is negative when current flows from a resistor to a conductor, and positive when current flows from a conductor to a resistor. The resulting surface charges

create a secondary dipole field $E_s$ that opposes $E_p$ directly above the cube. In panel b), the charges on the surface of the resistive cube generate an $E_s$ that reinforces $E_p$ above the cube. The inductive and galvanic effects cause the TE and TM modes to have different sensitivity to resistivity structure, an effect which will be demonstrated with synthetic examples in Section 2.5.

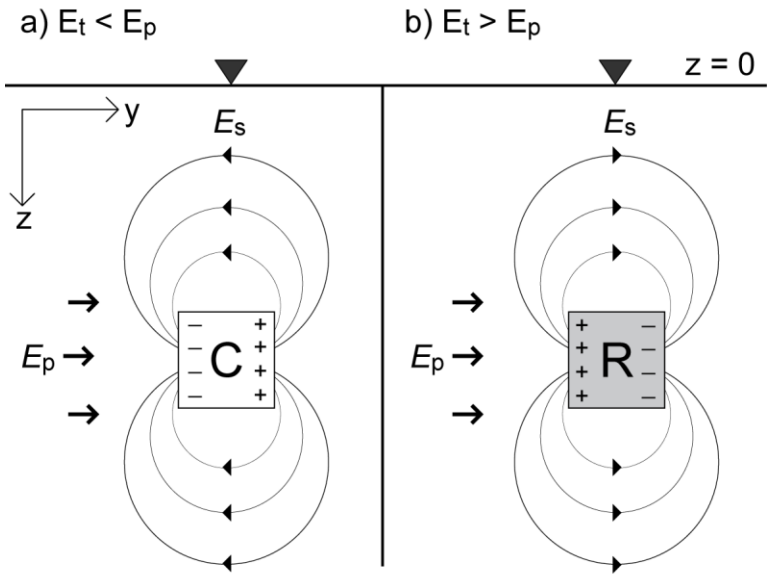


Figure 2.6: Galvanic effect producing a secondary electric field $E_s$ from surface charge accumulation. Assume a primary field $E_p$ directed in the positive *y*-direction. a) buried cube with higher conductivity than the surrounding Earth. The surface charges produce a secondary field $E_s$ that opposes the primary field $E_p$; therefore the vector field sum $E_t$ measured above the cube is lower than $E_p$. b) buried cube with lower conductivity than the surrounding Earth. In this case $E_t > E_p$ when measured above the cube. Black inverted triangles are the measurement points at $z = 0$.

#### 2.3.1.3. Impedance tensor of a 3-D Earth

In the general case of a 3-D resistivity model, the impedance tensor elements are non-zero for all azimuths. In practice, measured impedance data never match the anti-diagonal form of Equations (2.48) or (2.49) due to measurement noise and the fact that the Earth has a 3-D resistivity structure. 3-D MT data are typically more difficult to interpret than 1-D or 2-D MT data, and can only be accurately modeled with 3-D algorithms. Some examples of 3-D MT data are shown in Section 2.6.

### 2.3.2. Apparent resistivity and phase

The impedance tensor can be more easily interpreted by analyzing quantities derived from its magnitude and phase, which include the apparent resistivity and phase. These quantities are calculated because they are more intuitive representations of the impedance. For simplicity, the apparent resistivity and phase will be derived from the halfspace impedance shown in Equation (2.47). The magnitude of this expression, following Equation (2.35), is:

$$|Z_{xy}| = \sqrt{\frac{\omega\mu}{\sigma}} \tag{2.51}$$

Rearranging Equation (2.51) gives an expression for the apparent conductivity:

$$\sigma = \frac{\omega\mu}{|Z_{xy}|^2} \tag{2.52}$$

or its inverse, the apparent resistivity:

$$\rho = \frac{|Z_{xy}|^2}{\omega\mu} \tag{2.53}$$

Note that this quantity is called an apparent resistivity because it is the volume-averaged resistivity over a hemisphere of radius $\delta$ (one skin depth). The apparent resistivity only equals the true resistivity when the sampled hemisphere has a uniform resistivity.

The phase ($\varphi$) of $Z_{xy}$ is the phase difference between $E_x$ and $H_y$. It is computed by taking the complex argument of $Z_{xy}$, i.e.

$$\varphi = \tan^{-1}\left(\frac{Im(Z_{xy})}{Re(Z_{xy})}\right) \tag{2.54}$$

where $Im$ denotes the imaginary part and $Re$ denotes the real part of the quantities in parentheses. Substituting the halfspace impedance from Equation (2.47) into Equation (2.54) yields:

$$\varphi = \tan^{-1}(-1) = -45° \tag{2.55}$$

Thus the magnetic field lags the electric field by 45° in a halfspace. For simplicity, the phase angle is usually plotted in the first quadrant, between 0 and 90°.

When the sampled portion of the Earth is not a uniform halfspace, the phase angle will not be 45°. This is because the impedance is no longer a simple function of a single wavenumber as in Equation (2.46). If the resistivity increases with depth (i.e. decreasing frequency) then the phase angle will be less than 45°. Alternatively, if resistivity decreases with depth the phase angle will be greater than 45°. In most cases the phase angle is in the range 0° and 90°, however special cases are discussed in Section 2.7.4.

Figure 2.7 illustrates the apparent resistivity and phase data calculated for a set of 1-D, two layer resistivity models. The three models contain a 1000 Ωm layer in the upper 3 km, underlain by a more conductive layer of 100, 10, or 1 Ωm extending to infinite depth. A diagram illustrating the resistivity models is given in panel c). The calculated apparent resistivity and phase curves for the three models are shown in the panels a) and b). At frequencies greater than 100 Hz the skin depth is small and the signal only samples the upper layer; thus the apparent resistivity equals the resistivity of the upper layer. Correspondingly, the phase angle equals 45° as expected for a homogenous Earth. At intermediate frequencies between 100 and 0.01 Hz, the signal samples both layers and the apparent resistivity is a value between the resistivities of the two layers. The phase angle is greater than 45°, indicating a decrease in resistivity with depth. At low frequencies less than 0.01 Hz the signal predominantly samples the lower layer. Thus, the apparent resistivity approaches the resistivity of the lower layer, and the phase angle approaches 45°.

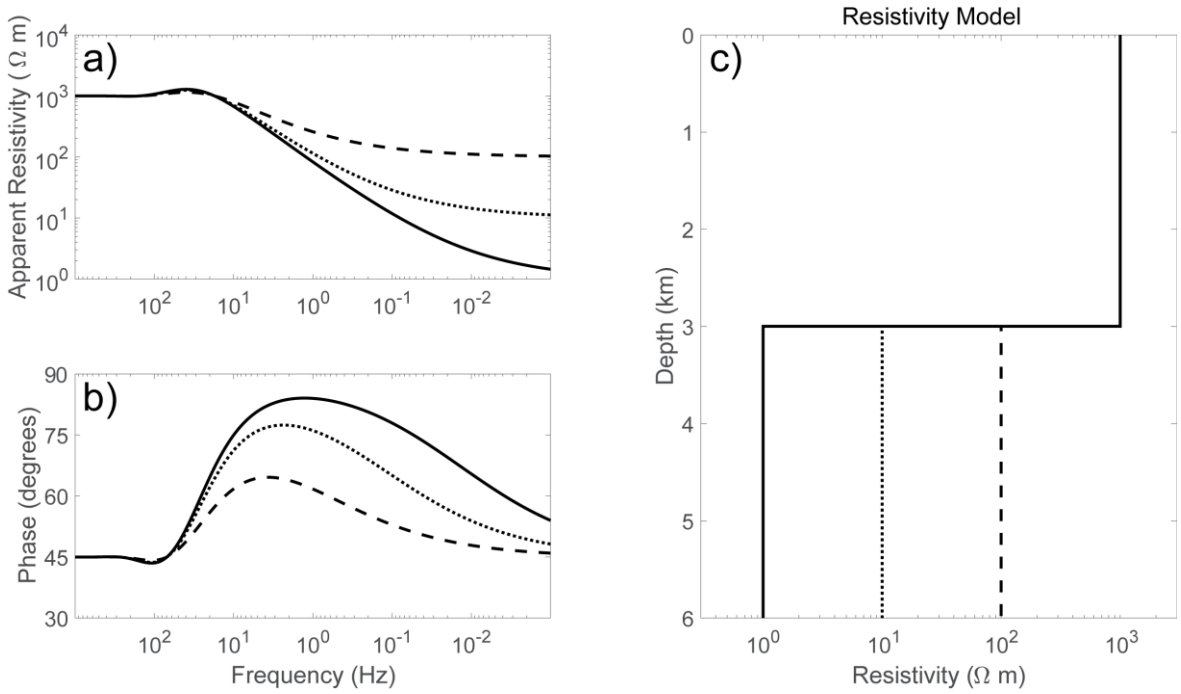


Figure 2.7: a) Apparent resistivity and b) phase curves as a function of signal frequency for three synthetic 2-layer models. All models contain a 1000 Ωm layer from the surface to 3 km depth, underlain by a layer of 100, 10, or 1 Ωm (as seen in panel c). Different dashed lines in a, b) correspond to the resistivity shown in the given 2-layer model in c). At frequencies greater than 100 Hz, the apparent resistivity equals the resistivity of the upper layer and the phase angle is 45° as expected for a homogeneous Earth. At frequencies in the range 100 – 0.01 Hz, the data are sensitive to both layers and the apparent resistivity is a value between the resistivities of the two layers, while the phase angle is greater than 45° indicating a decrease in resistivity with depth. At frequencies less than 0.01 Hz, the apparent resistivity approaches the resistivity of the lower layer and the phase angle approaches 45° as the lower layer resistivity dominates the response.

The example data shown in Figure 2.7 were calculated for a simple 1-D geometry where the resistivity only changes in the vertical direction. However, it is an instructive example that highlights that exploration depth is controlled by signal frequency, and that phase angle can be used as an indicator for changes in apparent resistivity with frequency. The apparent resistivity and phase data are more complicated for 2-D or 3-D resistivity structures where there are resistivity variations in one or both horizontal directions, requiring more care for their analysis. Examples of data for 2-D and 3-D resistivity structures are shown in Section 2.5 and Section 2.6.

### 2.3.3. Vertical magnetic field transfer function (tipper)

It was shown in Section 2.3.1 that the impedance tensor relates the horizontal (*x* and *y)* components of the electric and magnetic fields. Additional information can be obtained about subsurface resistivity structure by analyzing the vertical component of the magnetic field. The vertical magnetic field transfer function, also called the tipper (***T***), relates the vertical magnetic field to the horizontal magnetic field components with the following relation:

$$H_z(\omega) = [T_{zx}(\omega) \quad T_{zy}(\omega)] \begin{bmatrix} H_x(\omega) \\ H_y(\omega) \end{bmatrix} \tag{2.56}$$

The tipper components $T_{zx}$ and $T_{zy}$ are dimensionless because they are ratios of magnetic field components. Note that as a consequence of Faraday's Law (Equation 2.4), a vertical magnetic field $H_z$ is nonzero if the electrical resistivity varies in the *x* or *y* directions. Thus $H_z$ and the tipper components $T_{zx}$ and $T_{zy}$ are zero for a 1-D layered Earth. In a 2-D Earth, when the coordinate system is aligned with the geologic strike (as in Figure 2.5), $T_{zy} \neq 0$ if resistivity varies in the *y* direction, but $T_{zx} = 0$ because there are no resistivity variations in the *x* direction.

Tipper data are sensitive to horizontal changes in resistivity structure in a 2-D or 3-D Earth where the resistivity varies in the *x* or *y* directions. Tipper data are more sensitive to horizontal resistivity gradients than the absolute values of subsurface resistivity because the tipper is not computed from the electric field. In contrast, impedance data are calculated from the electric field and are therefore sensitive to absolute values of the subsurface resistivity.

A common way to display tipper data is to plot induction arrows which point towards or away from lateral resistivity variations, depending on the plotting convention used (Parkinson, 1959; Wiese, 1962). Induction arrows are calculated from the tipper components $T_{zx}$ and $T_{zy}$. Examples are shown in Section 2.5 and Section 2.6.

## 2.4. Dimensionality and distortion

### 2.4.1. Quantifying distortion of the impedance

Distortion describes a broad class of physical phenomena that affect measured MT impedance data. This excludes measurement noise, which is usually dealt with prior to computation of the impedance tensor. Historically, distortion includes any physical effects in the data that were non-negligible but which could not be modeled with the available methods. For example, a 1-D analysis of MT data cannot be accurately performed if the measured impedance tensor contains non-zero diagonal elements, which does not match the expected 1-D form in Equation (2.48). One plausible explanation may be that the Earth is in fact layered, but contains small 3-D resistivity structures that are also detected by the MT data. In this example, the user must remove the 3-D effects from the measured impedance data in order to model the Earth as 1-D.

As in the previous hypothetical example, the distortion problem has commonly been expressed as removing 3-D effects from a 1-D or 2-D regional impedance tensor. For several decades, MT data were collected with the intention of modeling the data in the form of the 1-D or 2-D impedance tensors (Equations 2.48 and 2.49) because modeling was computationally limited to 1-D or 2-D. However, measured impedances might show significant 3-D effects, such as nonzero diagonal components, due to small 3-D heterogeneities in the Earth. Many methods were devised to identify and possibly remove the 3-D distortion from the measured impedances. One way to express 3-D distortion is with a 2 × 2 tensor $\boldsymbol{C}$ that modifies the underlying 2-D regional impedance (e.g. Bahr, 1988; Groom & Bailey, 1989):

$$\boldsymbol{Z}_{obs} = \boldsymbol{C}\boldsymbol{Z}_{2D} \tag{2.57}$$

where $\boldsymbol{Z}_{\text{obs}}$ is the measured impedance, $\boldsymbol{Z}_{\text{2D}}$ implies that the tensor is rotated to an appropriate 2-D coordinate system, and:

$$\boldsymbol{C} = \begin{bmatrix} c_{11} & c_{12} \\ c_{21} & c_{22} \end{bmatrix} \tag{2.58}$$

Note that the elements of $\boldsymbol{C}$ are real and frequency independent. This type of distortion is termed galvanic because it is frequency independent. In addition, $\boldsymbol{C}$ only describes distortions of the electric field components. Magnetic field distortion can also be modeled, but is generally assumed to be small because the magnetic field is more spatially continuous than the electric field (Chave & Smith, 1994). In this example, if an estimate of $\boldsymbol{C}$ is obtained, then the user can proceed with a 2-D inversion using $\boldsymbol{Z}_{2D}$, which is the impedance of the undistorted 2-D Earth. The following section describes a commonly used method to obtain estimates for $\boldsymbol{C}$ and $\boldsymbol{Z}_{2D}$.

### 2.4.2. Tensor decomposition

As previously shown, the distortion matrix $\boldsymbol{C}$ is a mathematical expression of the electric field distortion. In order to understand the physical nature of the distortion, $\boldsymbol{C}$ can be factorized by decomposing the measured impedance tensor from Equation (2.57) into discrete components. One of the most widely used factorizations of $\boldsymbol{C}$ was described by Groom & Bailey (1989). In their scheme, the $\boldsymbol{C}$ matrix was written as:

$$\boldsymbol{C} = g\boldsymbol{TSA} \tag{2.59}$$

where $g$ is a real scalar called the gain, and $\boldsymbol{S}$, $\boldsymbol{T}$, and $\boldsymbol{A}$ are the shear, twist, and anisotropy matrices, respectively. These four distortion parameters can be estimated with the algorithm described by Groom & Bailey (1989). These four parameters can be subdivided into those that affect the orthogonality of the electric fields, and those that modify the electric field amplitudes (i.e. Ogawa, 2002).

The parameters that affect electric field amplitudes are the gain scalar and the anisotropy matrix. The anisotropy matrix $\boldsymbol{A}$ contains the anisotropy factor which scales the electric field amplitudes. When $\boldsymbol{Z}_{2\mathrm{D}}$ is multiplied by g$\boldsymbol{A}$, the impedance amplitudes are changed but their phase angles are preserved. The anisotropy scales the difference between $Z_{xy}$ and $Z_{yx}$, hence the term "anisotropy", while $g$ scales both impedance components by a constant value. The net effect of $g$ and $\boldsymbol{A}$ is a subset of galvanic distortion often called static shifts, which only affect the amplitudes of the off-diagonal impedance elements (Jones, 1988).

The parameters that affect electric field orthogonality (i.e. changing amplitude and phase) are the twist, $\boldsymbol{T}$, and the shear, $\boldsymbol{S}$. $\boldsymbol{T}$ and $\boldsymbol{S}$ contain the twist and shear angles, respectively, which are angles that modify the direction of the electric field. $\boldsymbol{T}$ can be considered a rotation matrix and $\boldsymbol{S}$ can be considered a shear matrix, with both parameters affecting the impedance amplitude and phase. In addition, because $\boldsymbol{T}$ and $\boldsymbol{S}$ affect the diagonal impedance elements, they can make the measured impedance $\boldsymbol{Z}_{obs}$ appear 3-D in nature.

These distortion parameters can be determined with the tensor decomposition algorithm of Groom & Bailey (1989), a widely used method to decompose an observed impedance tensor into a regional 2-D impedance tensor $\boldsymbol{Z}_{2D}$, the four distortion parameters contained in Equation (2.59), and a strike angle. Similar to previous approaches, this method assumes that the underlying resistivity distribution is 2-D and that the distortion is frequency-independent and only observed in the electric field components. For each MT station frequency, there are 9 parameters to be determined: the off-diagonal elements of $\boldsymbol{Z}_{2D}$ (two real and two imaginary parts), the four distortion parameters (the gain, anisotropy factor, twist angle, and shear angle), and the strike angle $\theta$. However, this problem is under-determined because the observed impedance tensor only contains eight parameters: i.e. the four complex tensor elements. This problem is solved by absorbing $g$ and $\boldsymbol{A}$ into $\boldsymbol{Z}_{2D}$ because the parameters $g$ and $\boldsymbol{A}$ have a similar effect of scaling the impedance element amplitudes. In effect, this means that the twist, shear, and strike angles, as well as $\boldsymbol{Z}_{2D}$, can be determined except for the amplitude distortion (static shifts) resulting from $g$ and $\boldsymbol{A}$. Therefore, the amplitude-distorted 2-D impedance tensor recovered by tensor decomposition can be written as:

$$\boldsymbol{Z'}_{2D} = g\boldsymbol{A}\boldsymbol{Z}_{2D} \tag{2.60}$$

The tensor decomposition algorithm of McNeice & Jones (2001) is an extension to the Groom & Bailey (1989) approach that implements a decomposition for a range of frequencies and set of MT stations. This tensor decomposition algorithm allows users to determine which MT stations and frequencies have a 2-D regional impedance. MT data that do not satisfy this assumption may be poorly fit by the tensor decomposition and may need to

be excluded from subsequent 2-D analysis. If the shear angle and twist angle are large, the user can choose to work with $\boldsymbol{Z'}_{2D}$, i.e. the amplitude-distorted impedance recovered from the tensor decomposition. Although $\boldsymbol{Z'}_{2D}$ may contain amplitude distortions, the effects of the twist and shear distortions are removed and $\boldsymbol{Z'}_{2D}$ follows the expected form of a 2-D impedance tensor (Equation 2.49).

In addition, tensor decomposition allows the user to determine the strike angle $\theta$ (or $\theta$ + 90°) that will allow for 2-D analysis (Figure 2.5). Another difficulty may arise if the MT data do not have the same strike angle for all stations and frequencies. A subset of the MT data with a consistent strike angle must be selected because 2-D analysis assumes a single strike angle for the whole dataset. Using 3-D MT data or a dataset with more than one well-defined strike angle may result in inaccurate 2-D modeling.

The tensor decomposition scheme is useful in the case of 3-D distortion of a 2-D impedance tensor, but is limited by the assumption of an underlying 2-D resistivity distribution. The next section describes the phase tensor, another tool for analyzing data dimensionality that does not require the 2-D assumption.

### 2.4.3. The magnetotelluric phase tensor

As mentioned in the previous section, the MT impedance tensor is characterized with a 1-D, 2-D, or 3-D form that will determine the type of analysis that is required to correctly analyse the data. The phase tensor is a useful tool to determine the dimensionality of MT data because it does not require the assumption of an underlying 2-D resistivity structure, as in tensor decomposition (Caldwell et al., 2004). The phase tensor is easily calculated from the observed impedance and no assumptions about the underlying resistivity distribution are required. Consider the real and imaginary parts of the impedance tensor:

$$\boldsymbol{Z} = \boldsymbol{X} + \boldsymbol{Y}i \tag{2.61}$$

where $\boldsymbol{X}$ and $\boldsymbol{Y}$ are the real and imaginary parts of the impedance tensor, respectively. The phase tensor $\boldsymbol{\Phi}$ is defined as:

$$\boldsymbol{\Phi} = \boldsymbol{X}^{-1}\boldsymbol{Y} = \begin{bmatrix} \Phi_{11} & \Phi_{12} \\ \Phi_{21} & \Phi_{22} \end{bmatrix} \tag{2.62}$$

where $\boldsymbol{X}^{-1}$ denotes the inverse of the tensor $\boldsymbol{X}$ and $\Phi_{11}$, $\Phi_{12}$, … are the elements of the phase tensor. It can be shown that the phase tensor is unaffected by the galvanic distortion matrix $\boldsymbol{C}$ and thus is an undistorted representation of the regional impedance.

The phase tensor can be described with four parameters: the maximum phase value $\Phi_{\max}$, the minimum phase value $\Phi_{\min}$, the skew angle $\beta$, and a rotation angle $\alpha$. $\Phi_{\max}$ and $\Phi_{\min}$ are functions of phase tensor coordinate invariants and are therefore also coordinate invariants (Caldwell et al., 2004). The skew angle $\beta$ is calculated with:

$$\beta = \frac{1}{2}\tan^{-1}\left(\frac{\Phi_{12} - \Phi_{21}}{\Phi_{11} + \Phi_{22}}\right) \tag{2.63}$$

and the rotation angle $\alpha$ is calculated with:

$$\alpha = \frac{1}{2}\tan^{-1}\left(\frac{\Phi_{12} + \Phi_{21}}{\Phi_{11} - \Phi_{22}}\right) \tag{2.64}$$

The skew angle is a measure of the tensor's asymmetry and the rotation angle places the tensor in the measurement coordinate system. These four parameters are used to plot a graphical representation of the phase tensor in the *xy* plane as illustrated in Figure 2.8. The $\Phi_{\max}$ and $\Phi_{\min}$ values determine the lengths of the major and minor axes, respectively. The angle $\alpha$ - $\beta$ defines the ellipse's orientation relative the measurement coordinate system.

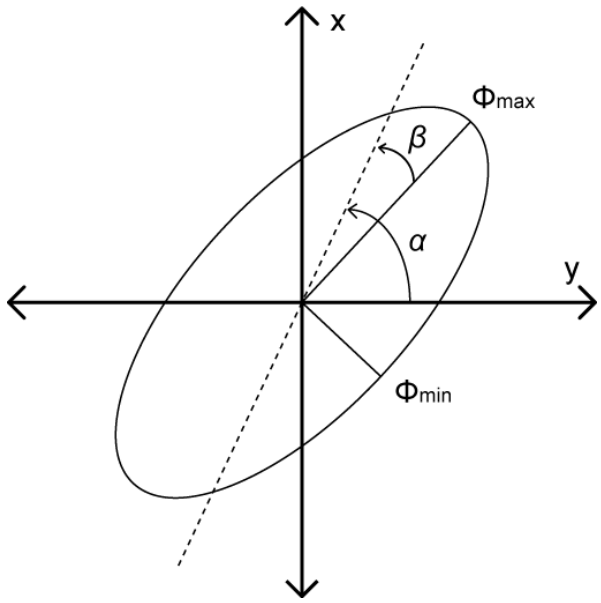


Figure 2.8: Representation of the phase tensor as an ellipse in the *xy* plane. After Caldwell et al. (2004).

The phase tensor is a useful tool for assessing the dimensionality of MT data because it has unique properties in 1-D, 2-D, and 3-D resistivity distributions. If the Earth has a 1-D resistivity structure, the phase tensor will be symmetric with the following simple form:

$$\boldsymbol{\Phi}_{1D} = \begin{bmatrix} \Phi_{1D} & 0 \\ 0 & \Phi_{1D} \end{bmatrix} \tag{2.65}$$

where $\Phi_{1D}$ is the phase calculated from the 1-D impedance in Equation (2.48). Examining the 1-D phase tensor it is clear from Equation (2.63) that $\beta = 0$ and $\alpha$ is undefined (from Equation 2.64). It is clear that $\Phi_{\max} = \Phi_{\min}$, and therefore the phase tensor ellipse is a circle and the angle $\alpha$ is meaningless (see Figure 2.9). In other words, there is no defined strike direction because there are no resistivity variations in the *x* and *y* directions.

If the Earth has a 2-D resistivity structure, when the impedance is rotated to the strike direction as in Equation (2.49), the phase tensor will have the form:

$$\boldsymbol{\Phi}_{2D} = \begin{bmatrix} \Phi_{2D}^{yx} & 0 \\ 0 & \Phi_{2D}^{xy} \end{bmatrix} \tag{2.66}$$

where $\Phi_{2D}^{yx}$ is calculated from the real and imaginary parts of $Z_{yx}$. When the impedance is rotated 90° to the strike direction, $\Phi_{2D}^{yx}$ and $\Phi_{2D}^{xy}$ are swapped in Equation (2.66). As in the case of the 1-D phase tensor, $\beta = 0$. The angle $\alpha$ equals the strike angle and is found by using Equation (2.64) with the unrotated impedance tensor. In general, $\Phi_{2D}^{yx} \neq \Phi_{2D}^{xy}$, and therefore the phase tensor is plotted as an ellipse with $\Phi_{\max} \neq \Phi_{\min}$ as in Figure 2.9. In the unrotated coordinate system, the major and minor ellipse axes (which correspond to $\Phi_{\max}$ and $\Phi_{\min}$), are aligned either parallel or perpendicular to the regional strike direction. This is because the phase tensor only identifies the direction of maximum inductive current, but this could be aligned either parallel or orthogonal to the strike direction. The phase tensor ellipse major axis is oriented in the direction of the magnetic field that results in the maximum phase. This principle is illustrated with the synthetic example in Section 2.5.

If the Earth has 3-D resistivity structure, the phase tensor generally does not have the simple symmetric form of $\boldsymbol{\Phi}_{1D}$ and $\boldsymbol{\Phi}_{2D}$, and consequently, $\beta \neq 0$. The phase tensor is plotted as an ellipse where the major axis is aligned to the direction $\alpha$ - $\beta$ (see Figure 2.8). The angle $\alpha$ - $\beta$ can be considered a generalization of the 2-D strike concept in a 3-D situation. The principal axes of the phase tensor ellipse therefore still correspond to the directions of maximum and minimum induced current, as in the 2-D case.

When plotted in map view at a single frequency, the phase tensor ellipses provide information about the underlying resistivity structure. Figure 2.9 shows simple examples of phase tensor ellipses for Earth structures where resistivity varies in 1-D, 2-D and 3-D. As previously mentioned, the 1-D phase tensor ellipse will be a circle with $\beta = 0$ that is easily distinguished from the 2-D and 3-D ellipses. The 2-D phase tensor ellipse can be distinguished by $\Phi_{\max} \neq \Phi_{\min}$ and $\beta = 0°$. Finally, the 3-D phase tensor ellipse is similar to the 2-D ellipse but with $\beta \neq 0$. This is often illustrated by plotting a color-filled ellipse with the fill color corresponding to the value of $\beta$. In practice, real MT data are noisy and the $\beta \neq 0°$ criterion is not useful for distinguishing a 2-D phase tensor from a 3-D phase tensor. Instead, many studies have justified the application of a 2-D analysis on the basis of low values of $|\beta|$. However, it is impossible to choose the maximum value of $|\beta|$ that permits a 2-D analysis. Caldwell et al. (2004) imply that $|\beta| < 3°$ are acceptable, although Booker (2014) mentions that some studies have tried to justify 2-D analysis with considerably larger values

up to $|\beta| = 10°$. A consistent alignment of phase tensor principal axes in space may be a more robust indicator of a 2-D Earth (Caldwell et al. 2004).

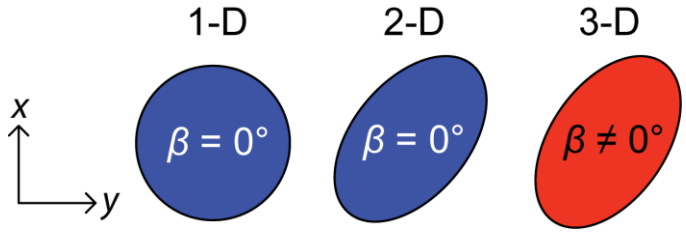


Figure 2.9: Example phase tensor ellipses for a 1-D, 2-D, and 3-D Earth. The ellipses are plotted in map view with the *xy* coordinate system shown. In a 1-D Earth the major and minor ellipse axes are equal in length and the phase tensor is symmetric. In a 2-D or 3-D Earth the major and minor ellipse axes are generally not equal in length, and the phase tensor has a coordinate system dependence defined by the angle $\alpha$ - $\beta$ which is not necessarily equal to zero. The major and minor ellipse axes are aligned with the maximum and minimum directions of inductive current flow. In a 3-D Earth the phase tensor is asymmetric and thus the skew angle $\beta \neq 0°$. The skew angle can be shown with a color-filled ellipse. In this example, the red fill corresponds to $\beta \neq 0°$.

In summary, measured MT impedance data are analyzed to determine whether the underlying resistivity distribution most closely matches a 1-D, 2-D, or 3-D geometry. The tensor decomposition algorithm allows users to quantify distortion, but is only valid for a 2-D regional impedance tensor affected by 3-D distortion. The phase tensor ignores distortion and allows users to identify the dimensionality of the data, which determines the appropriate types of modeling that can be applied to the data. In principle, a 1-D Earth can be appropriately modeled with 1-D, 2-D, or 3-D algorithms, but a 3-D Earth cannot be accurately modeled with 1-D or 2-D algorithms. The following sections contain synthetic data examples to convey characteristics of MT data observed with 1-D, 2-D, and 3-D resistivity structures.

## 2.5. Synthetic example: 2-D vertical dykes

This section presents examples of MT data calculated from a simple 2-D resistivity model. In this example, 61 MT stations with an inter-station spacing of 0.5 km are located at the surface. The MT data at these stations were calculated with the 2-D modeling algorithm

of Rodi & Mackie (2001). Figure 2.10a shows the 2-D model with a 1 Ωm vertical dyke at $y$ = 10 km and a 1000 Ωm vertical dyke at $y$ = 20 km. Both dykes are buried at a depth of 2 km and extend to the bottom of the model at 200 km depth. The remainder of the model has a resistivity of 100 Ωm. Note that no resistivity variations exist in the $x$ direction because the dykes extend infinitely in the $x$ direction (i.e. perpendicular to the $yz$ plane).

### 2.5.1. Synthetic example: Apparent resistivity and phase pseudo-sections

Figure 2.10 shows pseudo-sections of apparent resistivity and phase data calculated from the 2-D vertical dykes resistivity model. A pseudo-section shows the data as a function of station location and frequency. The coordinate system is aligned to the strike direction such that $\rho_{xy}$ and $\rho_{yx}$ correspond to the TE and TM mode apparent resistivities, respectively.

The $\rho_{xy}$ data are plotted in Figure 2.10b. At frequencies greater than 10 Hz the data only sample shallow depths and therefore $\rho_{xy}$ equals the 100 Ωm background resistivity. At frequencies less than 10 Hz $\rho_{xy}$ decreases due to the inductive response of the 1 Ωm dyke at $y$ = 10 km. At frequencies less than 0.01 Hz the apparent resistivity increases because the 1 Ωm dyke becomes small compared to the overall volume sampled at these low frequencies.

The $\varphi_{xy}$ data in Figure 2.10c are consistent with the $\rho_{xy}$ data. At frequencies greater than 10 Hz the phase angle is 45° because the data are not sensitive to the two dykes. At frequencies less than 10 Hz the 1 Ωm dyke is clearly imaged; the phase angle is greater than 45° at frequencies in the range 10 to 0.01 Hz because the 1 Ωm dyke decreases the apparent resistivity. At frequencies less than 0.01 Hz the phase angle is less than 45° which is consistent with the increase in apparent resistivity at these low frequencies. Notice that the inductive effect of the 1 Ωm dyke is observed at all stations, but the response occurs at lower frequencies for stations farther away from the dyke. The 1000 Ωm dyke located at $y$ = 20 km is not easily detected in $\rho_{xy}$ or $\varphi_{xy}$ because this dyke is more resistive than the background, resulting in a small inductive response.

Figure 2.10d shows the $\rho_{yx}$ data. Once again, these data are not sensitive to the two dykes at frequencies greater than 10 Hz. Below a frequency of 10 Hz the 1000 Ωm dyke is clearly imaged as an increase in $\rho_{yx}$ centered at $y$ = 20 km. The large anomaly is caused by the fact that $E_y$ crosses resistivity boundaries and the resulting surface electric charges

increase the resistivity above the 1000 Ωm dyke (as demonstrated in Figure 2.6). The 1 Ωm dyke also has a small response at $y$ = 10 km, however it is clear that the induction in the $xy$ component is more effective at detecting the conductive dyke. The $\varphi_{yx}$ data in Figure 2.10e are consistent with the $\rho_{yx}$ data; below 10 Hz a large phase anomaly less than 45° is centered at the 1000 Ωm dyke. Due to the minimal $\rho_{yx}$ response of the 1 Ωm dyke at $y$ = 10 km, the corresponding $\varphi_{yx}$data are approximately 45° at $y$ = 10 km.

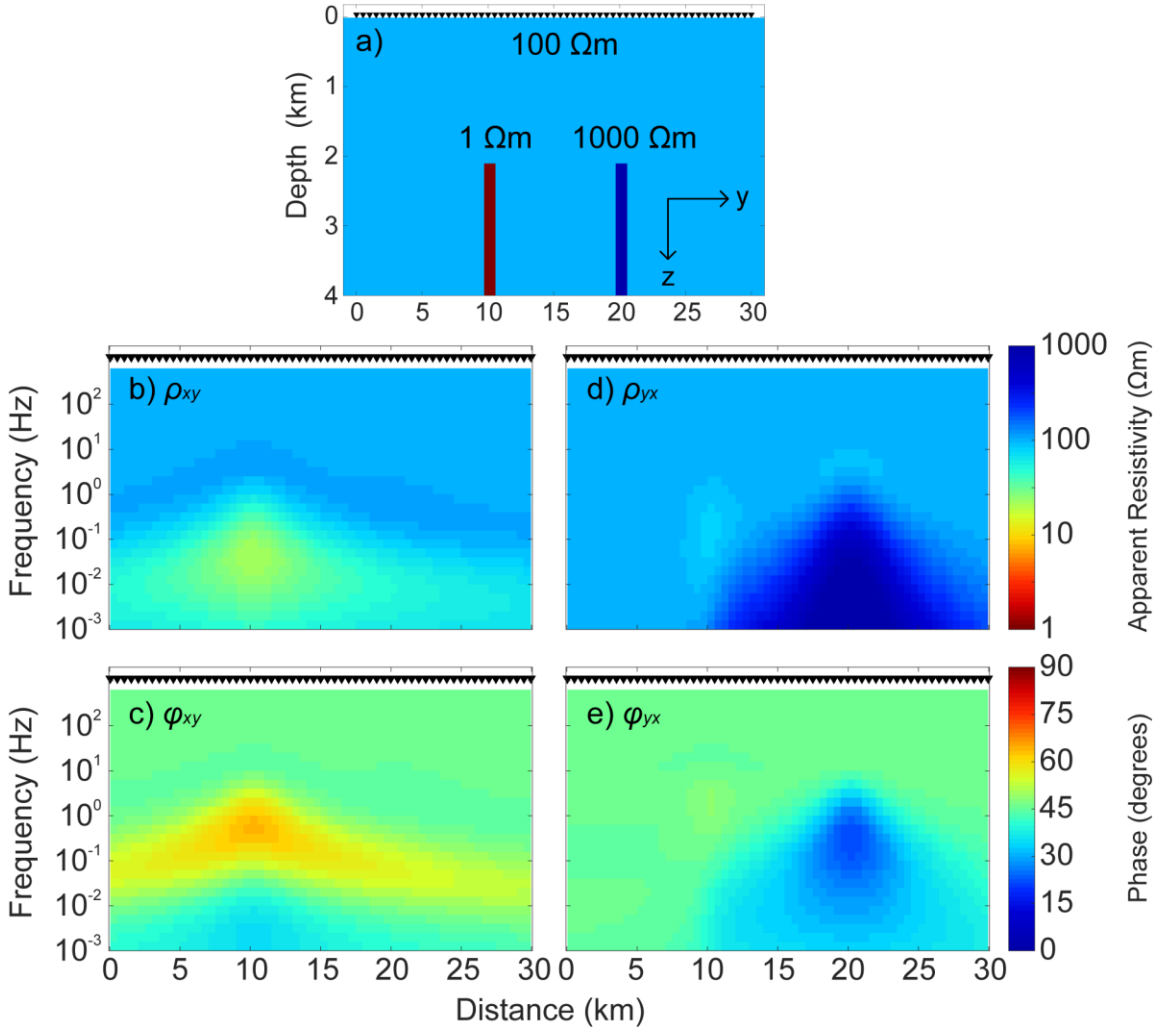


Figure 2.10: Synthetic 2-D resistivity model and pseudo-sections of data calculated from the model. a) resistivity model containing two vertical dykes embedded in a 100 Ωm halfspace. The dykes extend to the bottom of the model at > 200 km depth (not shown). The dyke at $y$ = 10 km has a resistivity of 1 Ωm and the dyke at $y$ = 20 km has a resistivity of 1000 Ωm. V.E. = 5. b) $xy$ component

apparent resistivity; c) *xy* component phase; d) *yx* component apparent resistivity; e) *yx* component phase. Black triangles show the locations of MT stations.

### 2.5.2. Synthetic example: Induction arrow pseudo-section

Induction arrows calculated from the tipper are used to constrain lateral resistivity variations. The synthetic data in this section were calculated from the 2-D vertical dykes model in Figure 2.10. The induction arrows at every second MT station are plotted in Figure 2.11 as a pseudo-section, where a decreasing frequency corresponds to a greater model depth. Each row can be considered a map view at one frequency in the *xy* plane, with positive *x* upward and positive *y* to the right. In this 2-D example resistivity only varies in the *y* direction; thus all induction arrows have an *x* component equal to zero. The induction arrows with a low magnitude (< 0.01) are plotted as small black dots to improve the clarity of the figure. The induction arrows are plotted in the Parkinson convention so that they point toward conductors.

At high frequencies greater than 10 Hz the data are only sensitive to the shallow parts of the model above the dykes where no resistivity variations exist; therefore, the induction arrows have zero magnitude. At lower frequencies in the range 1 to 0.001 Hz the data are sensitive to the 1 Ωm dyke at *y* = 10 km. The induction arrows decrease in magnitude at the lowest frequencies due to decreased induction in the 1 Ωm dyke. Note that the induction arrows reverse directions on either side of the 1 Ωm dyke at *y* = 10 km because $H_z$ changes from positive to negative. At *y* = 10 km the induction arrows at all frequencies have a very small magnitude because $H_z = 0$ directly above the conductor. Therefore, the 1 Ωm dyke at *y* = 10 km is easily located due to the induction arrow reversal and small magnitude above the conductor. The 1000 Ωm dyke at *y* = 20 km is difficult to perceive from the induction arrows because it does not localize current flow in the *x* direction (i.e. perpendicular to the *yz* plane) due to its high resistivity.

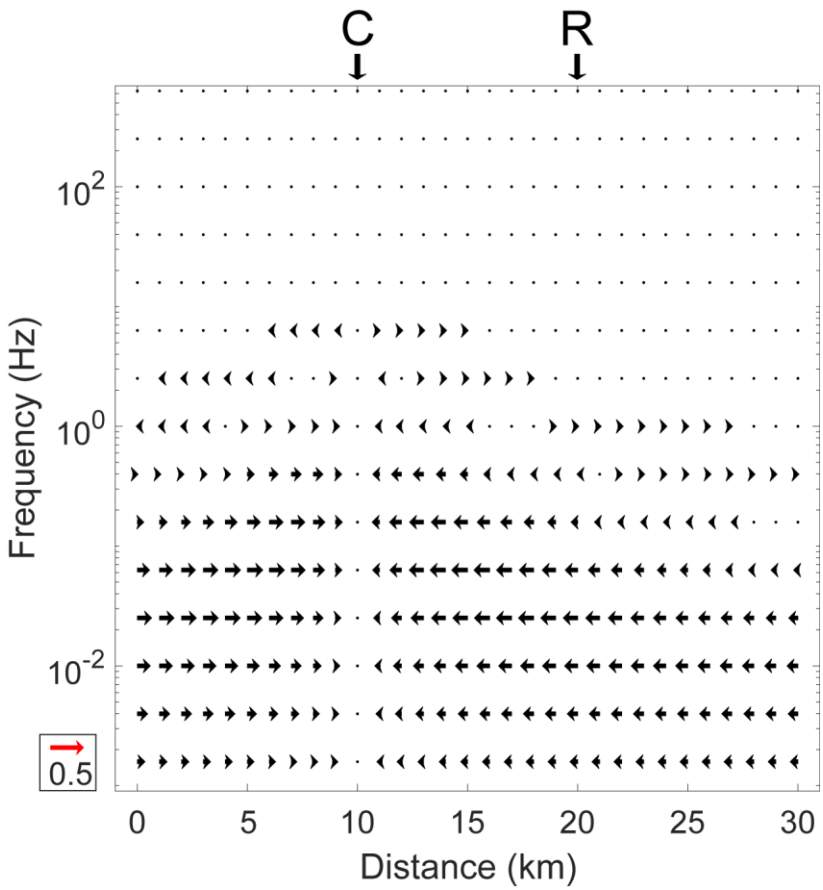


Figure 2.11: Pseudo-section of real induction arrows calculated from the 2-D vertical dykes resistivity model in Figure 2.10. For clarity, only arrows for every second MT station are shown. The 1 Ωm dyke at $y$ = 10 km (labeled C) is easily located, but the 1000 Ωm dyke at $y$ = 20 km (labeled R) has a very small tipper response. Induction arrows with magnitude < 0.01 are plotted as black dots. The red arrow is magnitude 0.5 for scale. Arrows are plotted in Parkinson convention (pointing toward conductors).

### 2.5.3. Synthetic example: Phase tensor ellipse pseudo-section

The phase tensor was introduced in Section 2.4.3 and contains information about the MT data dimensionality. This section contains a synthetic example displayed as a pseudo-section. Figure 2.12 shows the phase tensor ellipses calculated from the 2-D vertical dykes model shown in Figure 2.10. In this pseudo-section, each row corresponds to the phase tensor ellipses at a single frequency. A single row of ellipses can be considered a map view with positive $x$ upward and positive $y$ to the right. Therefore, from top to bottom, each row is a map view of the ellipses at successively lower frequencies. Recall that the 1 Ωm dyke is

located at $y$ = 10 km, the more resistive 1000 Ωm dyke is located at $y$ = 20 km, and both dykes are buried at a depth of 2 km. At frequencies > 10 Hz, the data are only sensitive to the 100 Ωm background resistivity above the dykes. Therefore, the phase tensor ellipses are circles that correspond to 1-D structure (see Figure 2.9).

At frequencies less than 10 Hz, the data are sensitive to the vertical dykes. First, consider the data at stations between $y$ = 0 km and $y$ = 15 km, where the response to the 1 Ωm dyke dominates. At these stations, the major axes of the ellipses are aligned parallel to the $y$ axis in the frequency range 10 and 0.1 Hz. Recall that the phase tensor ellipse major axis is aligned parallel to the magnetic field that produces the maximum phase angle. In this case, $\rho_{xy}$ (i.e. the TE mode) contains a strong inductive response from the 1 Ωm dyke that decreases $\rho_{xy}$ and increases $\varphi_{xy}$ to above 45° (see Figure 2.10). However, $\rho_{yx}$ (i.e. the TM mode) does not contain a strong response ($\varphi_{yx} \approx 45°$). Therefore, the maximum phase is $\varphi_{xy}$, and the phase tensor ellipse major axes are aligned with the corresponding magnetic field $H_y$.

Below a frequency of 0.1 Hz, the phase tensor major axes from $y$ = 5 km to $y$ = 10 km change from being parallel to the $y$ direction, to being parallel to the $x$ direction at the lowest frequencies. This is a consequence of the 1 Ωm dyke contributing very little to $\rho_{xy}$ at low frequencies, where a larger volume is sampled and the apparent resistivity is dominated by the 100 Ωm background. As a result, $\rho_{xy}$ increases and $\varphi_{xy}$ is less than 45° at frequencies below 0.01 Hz. On the other hand, $\varphi_{yx} \approx 45°$ and is greater than $\varphi_{xy}$ because the $yx$ component shows very little response to the 1 Ωm dyke. Therefore, the phase tensor major axes are parallel to the $H_x$ magnetic field associated with $\varphi_{yx}$. This example shows that the ellipse major axes are parallel or orthogonal to the strike direction.

Next, consider stations from $y$ = 15 km to $y$ = 30 km where the data are most sensitive to the 1000 Ωm dyke. Below a frequency of 10 Hz, these stations have phase tensor major axes parallel to the $y$ direction, which is in response to the 1000 Ωm dyke. The alignment in the $y$ direction can be understood by examining Figure 2.10, where $\rho_{yx}$ increases and $\varphi_{yx}$ is less than 45° in response to the 1000 Ωm dyke. In contrast, the $xy$ component shows little response to the 1000 Ωm dyke such that $\varphi_{xy} \approx 45°$. Consequently, the maximum phase is $\varphi_{xy}$ and the phase tensor major axes are parallel to the corresponding $H_y$ magnetic field.

In this section, all phase tensors have a skew angle $\beta = 0°$ because the 2-D vertical dykes resistivity model only produces 1-D and 2-D impedance data. The following section contains a 3-D resistivity model where some phase tensors have $\beta \neq 0°$.

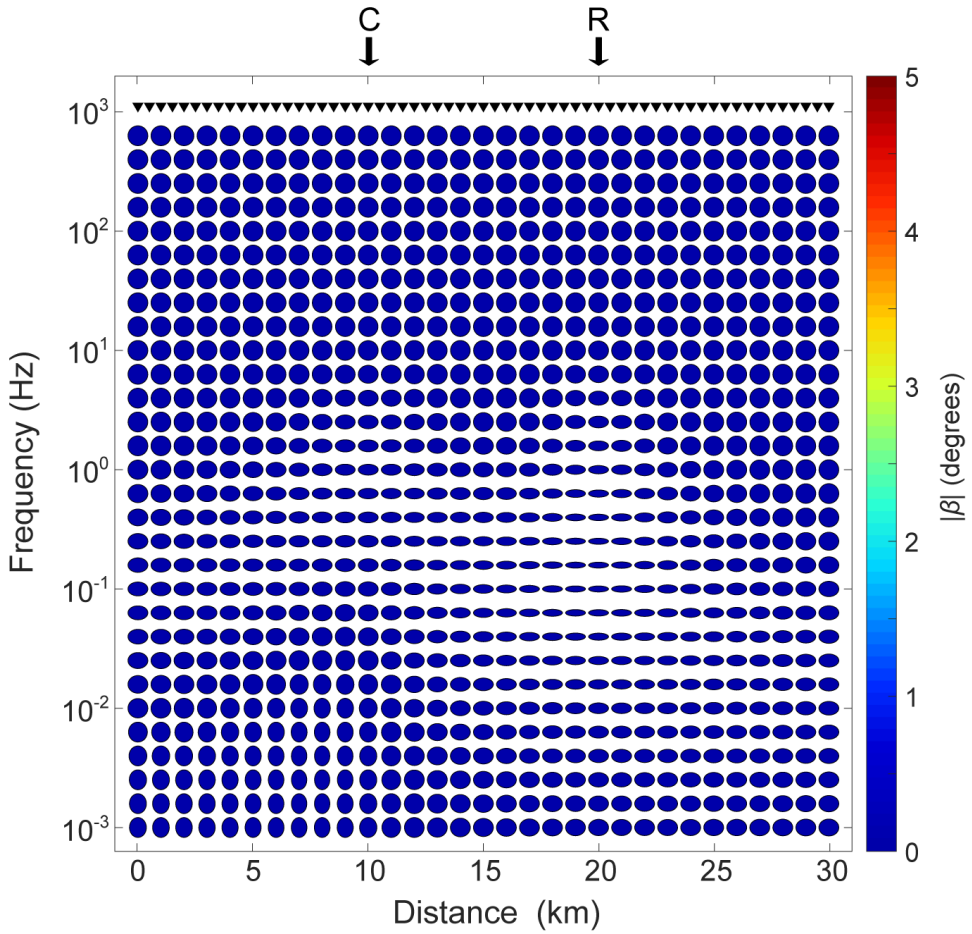


Figure 2.12: Phase tensor ellipse pseudo-section calculated from the 2-D vertical dykes resistivity model shown in Figure 2.10. For clarity, only the ellipses from every second MT station are shown. The ellipse size is normalized to the major axis length. Black triangles show the locations of MT stations.

## 2.6. Synthetic Example: 3-D conductor

To better understand the behavior of MT data for a 3-D resistivity model, this section shows MT data calculated for a synthetic resistivity model with a buried 3-D conductor shown in Figure 2.13. The vertical slice in (a) contains a 10 Ωm layer in the upper 0.3 km (yellow). A 3-D feature with a resistivity of 1 Ωm is buried between 1 and 5 km depth (red).

As shown in (b), the feature contains a prism with dimensions of 400 km in the *x* direction and 12 km in the *y* direction. The feature also contains a diagonal extension 10 km wide that terminates at approximately *x* = -5 km, *y* = 20 km. The remainder of the model has a resistivity of 100 Ωm. The data in the following sections were calculated with the 3-D algorithm of Kelbert et al. (2014).

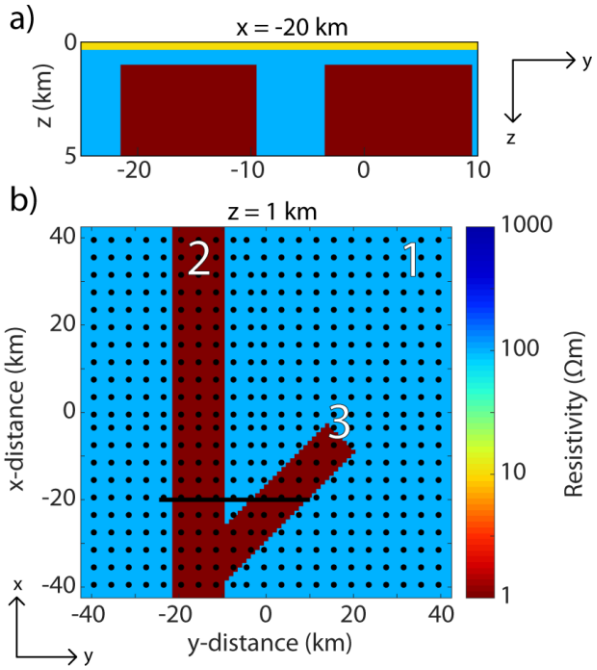


Figure 2.13: Synthetic 3-D resistivity model to demonstrate MT data responses. (a) Vertical slice through the model at *x* = -20 km (profile cross section marked in b). The upper 0.3 km is a 10 Ωm layer (yellow). A 3-D structure with a resistivity of 1 Ωm is buried between 1 and 5 km depth (red). Vertical exaggeration = 2. (b) Horizontal slice through the model at 1 km depth. The 3-D structure consists of a prism extending from *x* = -200 km to *x* = 200 km (not shown), and *y* = -21.5 km to *y* = -9.5 km. The structure also contains a diagonal extension that terminates at approximately *x* = -5 km, *y* = 20 km. The remainder of the model has a resistivity of 100 Ωm. Black points show the locations of MT stations, and locations labeled 1, 2, and 3 are discussed as features of interest in the text.

### 2.6.1. Synthetic example: Apparent resistivity and phase maps

Figure 2.14 shows synthetic apparent resistivity and phase data calculated at the MT stations in the frequency range 1000 to 0.001 Hz (see Figure 2.13 for station locations). The synthetic data were interpolated onto grids with 2 km x 2 km cells shown in Figure 2.14. $\rho_{xy}$

and $\varphi_{xy}$ are the apparent resistivity and phase data calculated from the electric field polarized in the $x$ direction. $\rho_{yx}$ and $\varphi_{yx}$ are the apparent resistivity and phase calculated from the electric field polarized in the $y$ direction. Each column corresponds to a different data component; for example, the left column shows the $\rho_{xy}$ data at 6 frequencies. A lower frequency corresponds to a larger skin depth, i.e. greater investigative depth. The outline of the buried conductor is shown for reference.

The data descriptions focus on three locations marked in Figure 2.13. These locations are marked because at particular frequencies, the data at these locations are representative examples of 1-D, 2-D, and 3-D data. For example, location 1 is located far from the buried conductor and therefore exhibits 1-D data. Location 2 is directly above the buried prism and, because the coordinate system is aligned with the strike, exhibits 2-D data. Location 3 is above the end of the diagonal structure and therefore exhibits 3-D data. Each row (frequency) in Figure 2.14 is examined in detail below.

- Frequency = 100 Hz

  The maps of $\rho_{xy}$ and $\rho_{yx}$ show the same 10 Ωm apparent resistivity at all locations because the data are only sensitive to the 10 Ωm layer. Correspondingly, the $\varphi_{xy}$ and $\varphi_{yx}$ data are 45°, which is the expected value for a halfspace. The responses at frequencies up to 1000 Hz were also calculated but not shown because they are identical to the response at 100 Hz.

- Frequency = 10 Hz

  Stations away from the buried conductor, such as those in location 1, are sensitive to the 100 Ωm background resistivity. This is clear from the apparent resistivity values greater than 10 Ωm and phase angles less than 45° for stations not above the buried conductor. Stations above the buried conductor, such as those at location 2, begin to show sensitivity to the conductor. These stations have a higher phase angle than stations at location 1, as expected for a conductive feature.

- Frequency = 1 Hz

  Stations at location 1 are mostly sensitive to the 100 Ωm background resistivity, and thus the apparent resistivity for both modes approaches 100 Ωm and the phase angles are less than 45°. Stations at location 2 are sensitive to the buried conductor, with their measured apparent resistivity lower than was observed for 10 Hz. The phase angles are greater than 45° because apparent resistivity is decreasing with increasing frequency,

- Frequency = 0.1 Hz

  The response from the buried conductor can clearly be seen as a low apparent resistivity at stations above the conductor. Interestingly, the low $\rho_{xy}$ can be seen for stations near to, but not directly above, the prism; however, the low $\rho_{yx}$ is confined to stations directly above the prism. In other words, the low apparent resistivity response is narrower above the prism in $\rho_{yx}$ than for $\rho_{xy}$. This can be explained by the fact that $\rho_{xy}$ is only sensitive to inductive effects because $E_x$ does not cross any resistivity boundaries below location 2, where the situation is approximately 2-D. $E_y$ crosses resistivity boundaries at the prism, and therefore $\rho_{yx}$ is affected by inductive and galvanic effects. The galvanic effect causes electric charge to collect on the edge of a conductor, therefore increasing $E_y$ and $\rho_{yx}$ locally (see Figure 2.6).

  The phase angles are greater than 45° for stations directly above the buried conductor because the apparent resistivity is decreasing with frequency. Stations such as those at location 1 are not sensitive to the buried conductor. These stations show an increase in apparent resistivity below 1 Hz and, correspondingly, phase angles less than 45°. Stations at location 3 begin to sense the edge of the diagonal extension of the conductor, with the effect becoming more obvious at lower frequencies.

- Frequency = 0.01 Hz

  At this frequency, stations at location 1 are still not sensitive to the buried conductor. The apparent resistivity still approaches 100 Ωm and the phase angles approach 45° as the background resistivity dominates the response. The data at

location 2 are strongly influenced by the buried conductor; both $\rho_{xy}$ and $\rho_{yx}$ are less than 10 Ωm, but the phase angles show different responses. $\varphi_{xy}$ is less than 45° meaning that the apparent resistivity is increasing with lower frequency. This indicates that the *xy* component data are sensitive to the 100 Ωm background below the conductor, and the inductive response of the conductor is becoming smaller with decreasing frequency. $\rho_{yx}$ remains low (near 1 Ωm) due to charges on the boundaries of the conductor, even though the inductive effect of the conductor is small at this frequency. The values of $\varphi_{yx}$ approach 45° because $\rho_{yx}$ is stabilizing to a value determined by the galvanic effect.

At location 3, the structure is clearly 3-D because resistivity varies in the *x* and *y* directions. Near location 3, the electric field is not polarized in the *x* or *y* directions because the electric field is deflected around finite 3-D bodies. Complex geometries such as the 90° corners on the buried conductor deflect electric fields and produce local anomalies in apparent resistivity and phase. The dipolar appearance of high/low apparent resistivity and phase anomalies at location 3 is due to the fact that large charge accumulation occurs at points on conductors, such as the 90° corners. Therefore, a larger electric field is locally observed at these points.

- Frequency = 0.001 Hz

Stations at location 1 are still mostly sensitive to the 100 Ωm background. As a result, the apparent resistivity and phase for both modes approach 100 Ωm and 45°, respectively. At location 2, the apparent resistivity and phase data behave similarly to the 0.01 Hz case. The inductive response of the buried conductor is apparently small at 0.001 Hz because $\rho_{xy}$ is increasing, approaching the background resistivity of 100 Ωm, and $\varphi_{xy}$ remains below 45°. Conversely, $\rho_{yx}$ is still low due to the galvanic effect, which will be present at all frequencies down to 0 Hz. $\varphi_{yx}$ continues to approach 45° as inductive effects become negligible at low frequencies.

At location 3, a dipolar high/low apparent resistivity pattern persists to low frequencies due to the galvanic effect at the buried conductor's diagonal extension. The phase angles approach 45° at low frequencies as inductive effects become negligible.

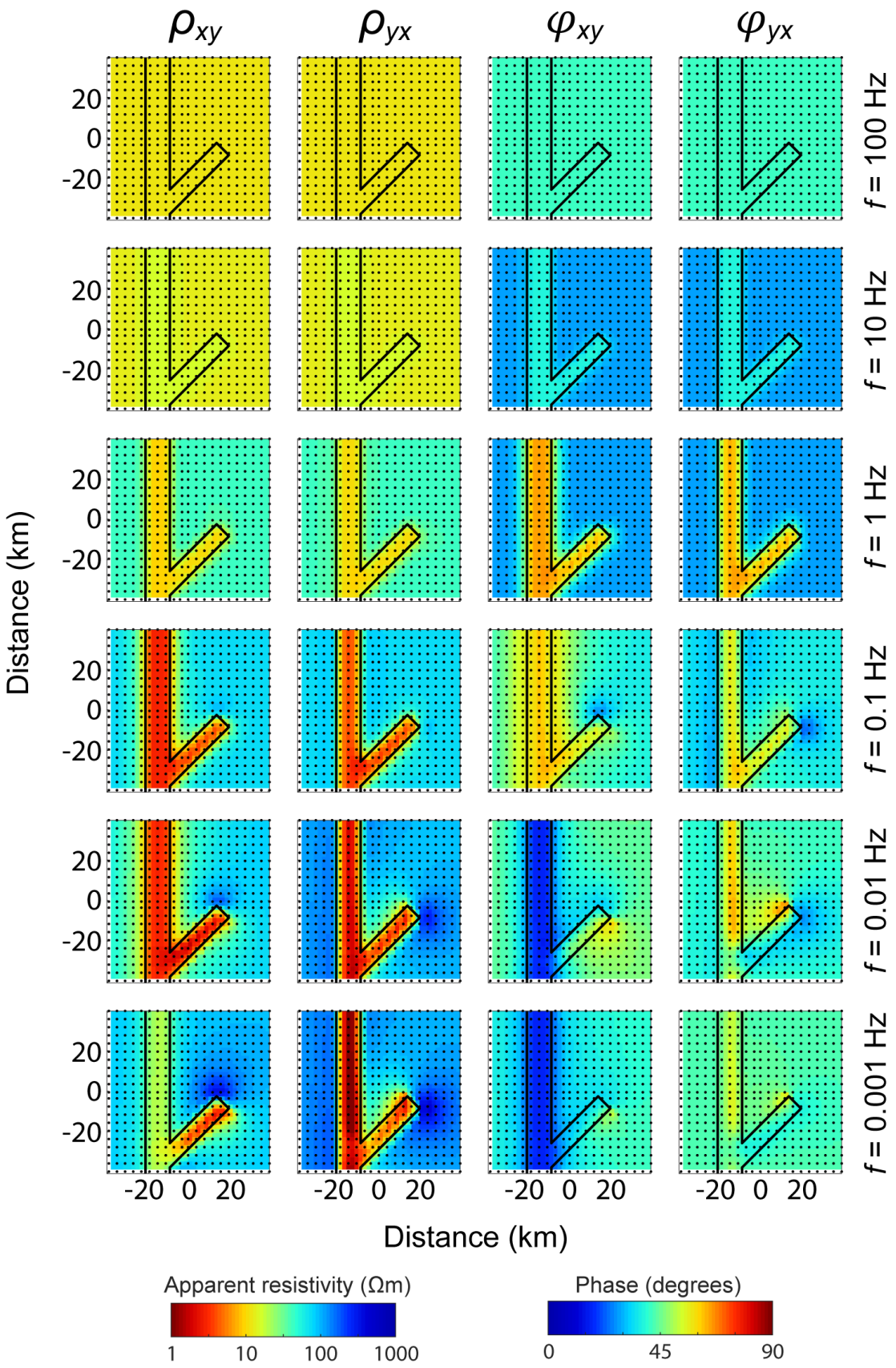
ρxy
ρyx
φxy
φyx
f = 100 Hz
f = 10 Hz
f = 1 Hz
f = 0.1 Hz
f = 0.01 Hz
f = 0.001 Hz
Distance (km)
Distance (km)
20
0
-20
Apparent resistivity (Ωm)
1
10
100
1000
Phase (degrees)
0
45
90

Figure 2.14: Interpolated map views of apparent resistivity and phase calculated from the synthetic model in Figure 2.13. Data were calculated at MT stations (black points) and interpolated onto a grid with 2 km x 2 km cells. $\rho_{xy}$ and $\varphi_{xy}$ are the apparent resistivity and phase calculated from the electric field polarized in the *x* direction. $\rho_{yx}$ and $\varphi_{yx}$ are the apparent resistivity and phase calculated from the electric field polarized in the *y* direction. Each row corresponds to data at a different frequency. The outline of the buried conductor at 1 to 5 km depth is shown for reference.

### 2.6.2. Synthetic example: Induction arrow maps

Induction arrows are computed from the magnetic field components and are sensitive to lateral resistivity variations (see Section 2.3.3). Figure 2.15 shows induction arrows calculated at the MT stations in the frequency range 1000 to 0.001 Hz (see Figure 2.13 for station locations). Each panel corresponds to data at a single frequency, where a lower frequency corresponds to a larger skin depth i.e. greater depth. The outline of the buried conductor is shown for reference. The data at each frequency are described in detail below.

- Frequency = 100 Hz and 10 Hz

  The data at these frequencies are only sensitive to the 10 Ωm and 100 Ωm layers above the buried conductor. Therefore, no vertical magnetic field is observed and the induction arrows have zero magnitude.

- Frequency = 1 Hz

  At this frequency some stations are sensitive to the top of the buried conductor and have small induction arrows. Stations farther from the buried conductor still do not detect it at these relatively high frequencies.

- Frequency = 0.1 Hz

  Stations farther from the buried conductor show a response as the skin depth increases with lower frequency. The induction arrows point toward the conductor as expected in the Parkinson convention. Stations directly above the conductor have small induction arrow magnitudes because a 2-D resistivity model predicts that the vertical magnetic field component should be zero directly above a conductor.

- Frequency = 0.01 Hz

  All stations are sensitive to the buried conductor and have induction arrows greater than 0.05 in magnitude. Stations close to (but not directly above) the buried conductor have the largest induction arrow magnitudes. Induction arrows near the conductor's diagonal extension show a more complicated pattern. These data are sensitive to both the conductive prism and its diagonal extension, thus the induction arrow direction is influenced by both conductors and may not point directly at either one.

- Frequency = 0.001 Hz

  At this frequency the inductive response of the buried conductor is small as the frequency is low and the skin depth is very large. As a result, induction arrows magnitudes are smaller than at 0.01 Hz. At even lower frequencies, the magnitudes approach zero as the inductive response of the conductor becomes negligible.

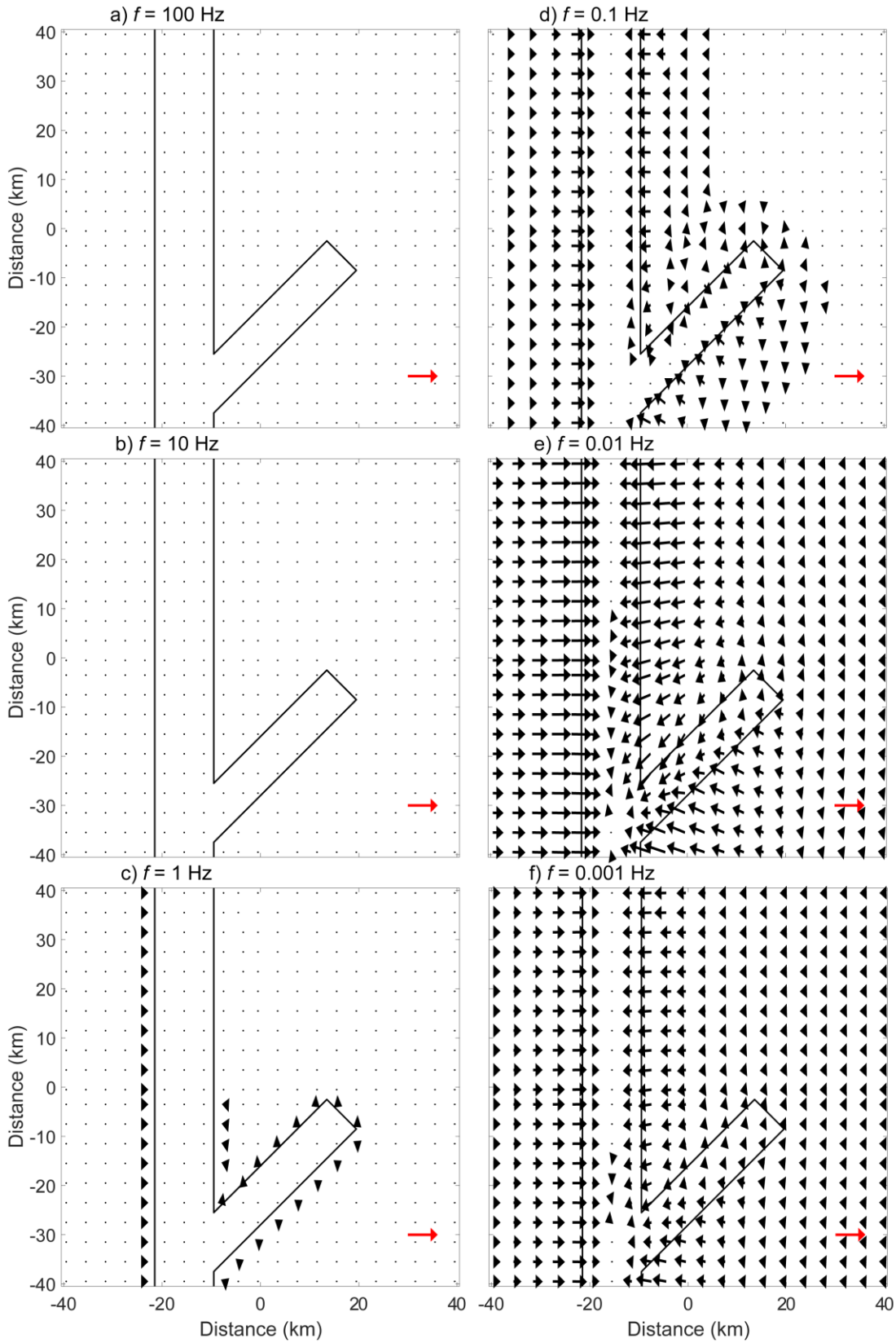
a) f = 100 Hz
d) f = 0.1 Hz
b) f = 10 Hz
e) f = 0.01 Hz
c) f = 1 Hz
f) f = 0.001 Hz
Distance (km)
Distance (km)
40
30
20
10
0
-10
-20
-30
-40

Figure 2.15: Map view of real induction arrows calculated from the 3-D resistivity model shown in Figure 2.13. The arrows are plotted in the Parkinson convention such that they point toward conductors. Induction arrows with magnitude < 0.05 are plotted as small points for clarity. The red arrows show induction arrows with a length of 1 for scale.

### 2.6.3. Synthetic example: Phase tensor maps

The phase tensor (introduced in Section 2.4.3) is a quantity used to estimate the dimensionality of MT data. Figure 2.16 shows map views of the phase tensors calculated from the 3-D model shown in Figure 2.13. Refer to Figure 2.13 for the positions of locations 1, 2, and 3, which are referred to in this section. Each panel, as with the prior maps, corresponds to a single frequency. The outline of the buried conductor is shown for reference. The data behavior at each frequency is described below.

- Frequency = 100 Hz and 10 Hz

  As seen in the apparent resistivity, phase, and induction arrow plots, data at these frequencies are only sensitive to the 10 Ωm and 100 Ωm layers above the buried conductor. These layers represent a 1-D resistivity structure; therefore the phase tensor ellipses at all stations are circles with $|\beta| = 0°$ (see Figure 2.9).

- Frequency = 1 Hz

  At this frequency, the stations above the buried conductor have non-circular phase tensor ellipses. Note that phase tensor ellipses at the boundaries of the conductor have major axes aligned perpendicular to the boundary. This is because the main inductive current runs parallel to the strike of the conductor (i.e. the TE mode, if in the 2-D case). The corresponding magnetic field is perpendicular to the inductive current, which is indicated by the ellipse orientation. However, the situation is not purely 2-D in this example. Some ellipses near the conductor corners have $|\beta|$ greater than 0°, corresponding to local 3-D structure.

- Frequency = 0.1 Hz

  The phase tensor ellipses follow a similar pattern as the 1 Hz data. Stations at locations 1 and 2 still have $|\beta| = 0$, indicating 1-D and 2-D structure at these locations, respectively. However, $|\beta|$ is notably larger near location 3, where there is an obvious 3-D geometry.

- Frequency = 0.01 Hz

  Stations at location 1 still have nearly circular ellipses, but the fact that they are not circles indicates that the data are sensitive to the buried conductor at this frequency. At location 2, the ellipse major axes now align in the *x* direction instead of the *y* direction. This makes sense because the major axes align to the magnetic field that produces the maximum phase, and Figure 2.14 shows a higher $\varphi_{yx}$ at this frequency. The data at location 2 are predominantly 2-D, as evidenced by the elongated ellipses and small values of $|\beta|$. However, the non-zero values of $|\beta|$ indicate that the data are sensitive to the conductor's 3-D diagonal extension. Stations at location 3 have high values of $|\beta|$, some greater than 5°, with these high values indicating they are substantially sensitive to the 3-D geometry of the buried conductor. Following the suggestion of Caldwell et al. (2004), the fact that the ellipse major axes change orientation by about 90° on either side of the diagonal extension may be a more robust indication of 3-D structure than examining the value of $|\beta|$ alone.

- Frequency = 0.001 Hz

  Stations at location 1 still have a nearly circular ellipse with small values of $|\beta|$ consistent with a 1-D resistivity structure. Stations at location 2 also have small values of $|\beta|$, but the major axes of the ellipses are parallel to the *x* direction as $\varphi_{xy}$ is less than $\varphi_{yx}$ as seen in Figure 2.14. Stations at location 3 have smaller values of $|\beta|$ because the conductor's inductive response is small at low frequencies, and the 3-D geometry scale is very small compared to the skin depth.

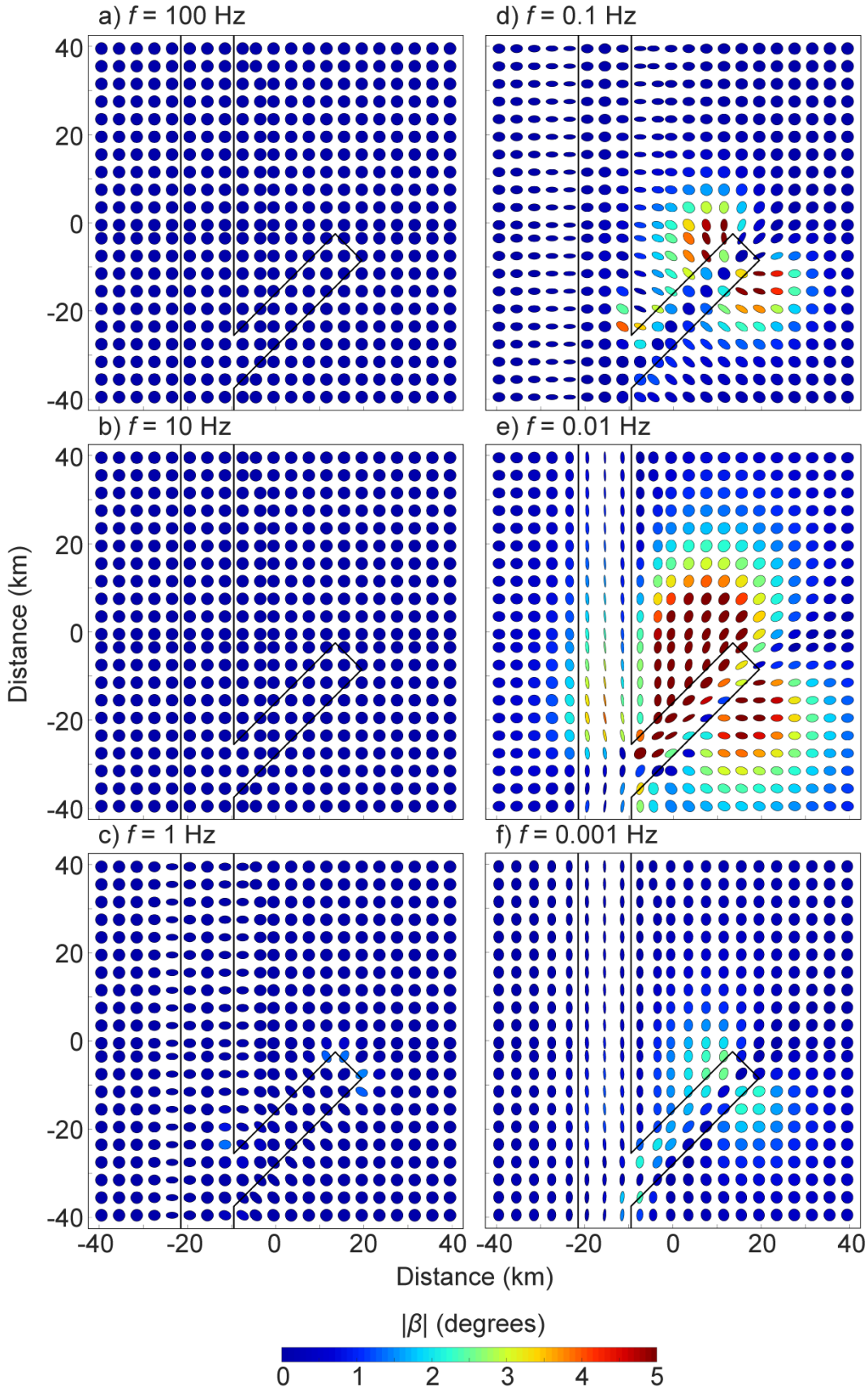
a) f = 100 Hz
d) f = 0.1 Hz
b) f = 10 Hz
e) f = 0.01 Hz
c) f = 1 Hz
f) f = 0.001 Hz
Distance (km)
Distance (km)
40
20
0
-20
-40
|β| (degrees)
0
1
2
3
4
5

Figure 2.16: Map view of phase tensor ellipses calculated from the 3-D resistivity model shown in Figure 2.13. The fill color corresponds to the skew angle, $\beta$. Ellipse radius is normalized to the value of $\Phi_{max}$.

## 2.7. Electrical anisotropy

### 2.7.1. Background

So far, this thesis has treated electrical resistivity as a scalar quantity that does not depend on the measurement direction. However, this is an approximation that may not be valid for all cases. Due to heterogeneity in the Earth (at all length scales), resistivity varies with direction. In many geological settings, the electrical anisotropy is minor and can be ignored. However, recent studies have revealed examples of anisotropy in the Earth's crust with consequences for MT modeling. For example, graphite has often been interpreted as a conductive phase in the Earth's mid to lower crust, and may cause electrical anisotropy if metamorphosed rocks contain graphite in a predominant foliation direction (i.e. Heise & Pous, 2003). Anisotropy can also be observed at a larger scale, such as in a series of sub-vertical conductive dykes in the resistive crust (Eisel & Haak, 1999; Patro et al., 2005). Modeling electrical anisotropy with MT data is now feasible with the availability of 2-D and 3-D forward modeling algorithms (e.g. Pek & Verner 1997; Kong et al. 2018). In order to model electrical anisotropy with MT data, electrical resistivity must be considered a 3 × 3 tensor that depends on the *x*, *y*, and *z* coordinate system:

$$\rho(x,y,z) = \begin{bmatrix} \rho_{xx} & \rho_{xy} & \rho_{xz} \\ \rho_{yx} & \rho_{yy} & \rho_{yz} \\ \rho_{zx} & \rho_{zy} & \rho_{zz} \end{bmatrix} \tag{2.67}$$

If conduction only depends on the electric field, the resistivity tensor is symmetric and can be described by a simpler form involving only three principal resistivities and three rotation angles (Martí, 2014). The rotation angles are commonly called $\alpha_S$, $\alpha_D$, and $\alpha_L$, corresponding to the anisotropic strike, dip, and slant, respectively. The three rotation angles $\alpha_S$, $\alpha_D$, and $\alpha_L$ are defined by three successive Euler rotations (e.g. Pek & Santos 2002), as

shown in Figure 2.17. When the coordinate system is rotated to align with the anisotropic axes, the resistivity tensor takes on the simpler form:

$$\rho(x,y,z) = \begin{bmatrix} \rho_{xx} & 0 & 0 \\ 0 & \rho_{yy} & 0 \\ 0 & 0 & \rho_{zz} \end{bmatrix} \tag{2.68}$$

where the diagonal elements, abbreviated as $\rho_x$, $\rho_y$, and $\rho_z$, are the principal resistivity values. The six parameters $\rho_x$, $\rho_y$, $\rho_z$, $\alpha_S$, $\alpha_D$, and $\alpha_L$ can be modeled in a 1-D, 2-D, or 3-D Earth. In the triaxial case $\rho_x \neq \rho_y \neq \rho_z$, as seen in Figure 2.17. However, the number of parameters can be reduced if two or more of the principal resistivity values are equal. For example, the uniaxial case has two equal principal resistivity values. These simplifications can be made if additional information such as geological observations suggests that the anisotropy can be simplified.

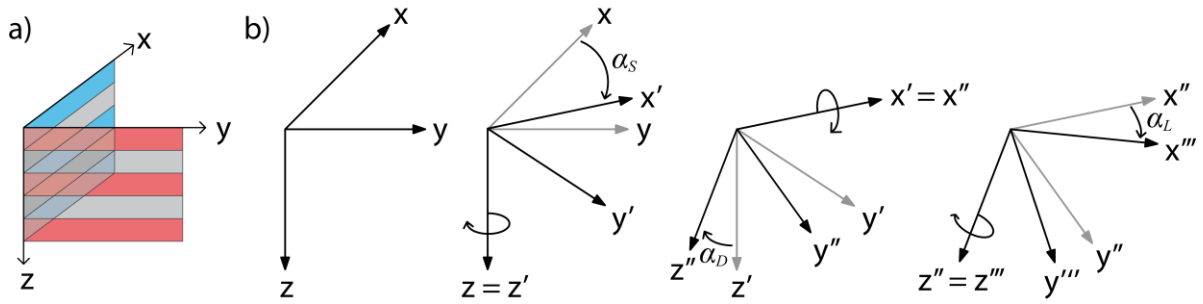


Figure 2.17: a) example of triaxial vertical anisotropy, where the resistivity varies in the *x*, *y*, and *z* directions. b) three successive Euler rotations by the angles $\alpha_S$, $\alpha_D$, and $\alpha_L$ to define an arbitrary anisotropy coordinate system. After Martí et al. (2010).

Figure 2.18 illustrates simple examples of anisotropy in uniaxial media. In these examples the coordinate system is aligned with the anisotropy axes such that the resistivity tensor is the form in Equation (2.68). Each panel shows an anisotropic medium composed of two materials with different resistivity values, $\rho_1$ and $\rho_2$. Due to different alignments of materials with respect to the coordinate system, each medium has a different resistivity tensor, each with one unique principal resistivity. In Figure 2.18a the unique principal resistivity is $\rho_x$; in Figure 2.18b, it is $\rho_y$; and in Figure 2.18c, it is $\rho_z$.

For applications of MT, the Earth is electrically anisotropic if resistivity varies on a scale smaller than the EM inductive scale, i.e. the skin depth of a particular frequency (e.g. Wannamaker, 2005). The effect of anisotropy on measured MT data cannot be uniquely determined because inductive effects cannot be uniquely differentiated from effects of anisotropy (Martí, 2014). In order to demonstrate the effects of anisotropy on MT data, the following sections discuss examples of MT data for a 1-D anisotropic Earth.

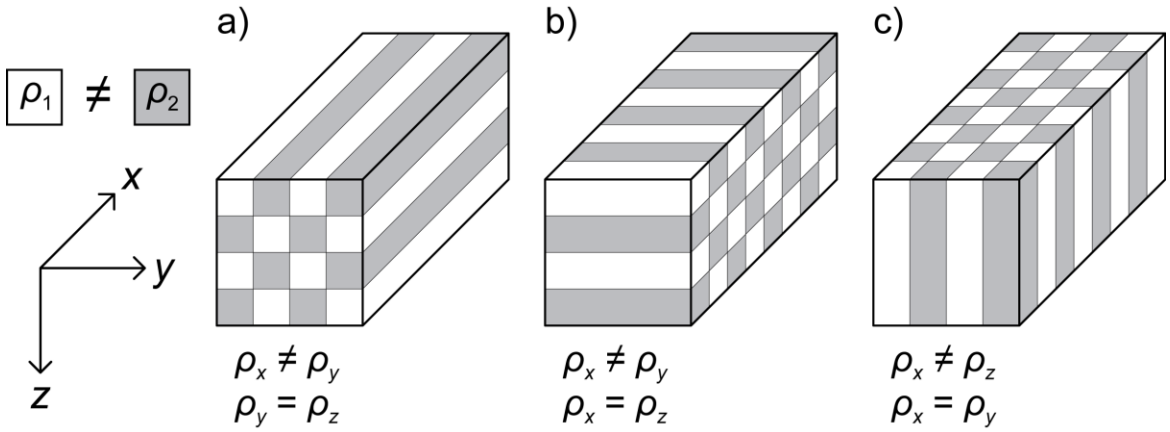


Figure 2.18: Examples of electrical anisotropy in uniaxial media. The medium in each example is composed of two materials of unequal electrical resistivity ($\rho_1 \neq \rho_2$). $\rho_x$, $\rho_y$, and $\rho_z$ are the principal resistivity values (see Equation 2.68). The unique principal resistivity in each example is a) $\rho_x$; b) $\rho_y$; and c) $\rho_z$.

### 2.7.2. Impedance tensor of a 1-D anisotropic Earth

Recall from Equation (2.48) that the impedance tensor of a 1-D isotropic Earth is anti-diagonal with the off-diagonal elements equal but of opposite sign. The impedance tensor of a 1-D anisotropic Earth is different than that of a 1-D isotropic Earth:

$$\boldsymbol{Z}_{1D}^{aniso} = \begin{bmatrix} Z_{xx} & Z_{xy} \\ Z_{yx} & -Z_{xx} \end{bmatrix} \tag{2.69}$$

In fact, the 1-D anisotropic impedance tensor bears some resemblance to the 2-D isotropic impedance tensor. However, unlike the 2-D impedance tensor in Equation (2.49), $\boldsymbol{Z}_{1D}^{aniso}$ cannot necessarily be rotated to an angle such that its diagonal elements equal zero for

all frequencies. This rotation angle only exists if there is only one anisotropic layer, or if all anisotropic layers have the same anisotropic axes (e.g. Jones, 2012).

Note that in most cases, $Z_{xy} \neq Z_{yx}$ in Equation (2.69). Therefore, MT data for a 1-D anisotropic Earth may appear similar to that of a 2-D isotropic Earth, i.e. with distinct responses for the *xy* and *yx* apparent resistivity and phase data (see Figure 2.10 for the 2-D isotropic example of two vertical dykes). This is demonstrated with synthetic examples in the following section.

### 2.7.3. Synthetic example: MT data for a 1-D anisotropic Earth

This section presents synthetic examples of apparent resistivity and phase data for two simple 1-D anisotropic models. The purpose is to demonstrate that these data behave differently than data for a 1-D isotropic resistivity model, and also have similar characteristics as data observed for a 2-D isotropic Earth. A simple 1-D anisotropic resistivity model is shown in Figure 2.19. In this example the anisotropic axes are aligned with the *xyz* coordinate system, and thus the anisotropy is defined by the three principal resistivity values in Equation (2.68). Figure 2.19a shows the principal resistivity values as a function of depth. The top layer is isotropic, 10 Ωm, and has a thickness of 0.25 km. The second layer is 1 km thick, with $\rho_x$ = 1 Ωm and $\rho_y = \rho_z$ = 100 Ωm. The bottom layer is isotropic, with a resistivity of 100 Ωm, and extends infinitely downward. Note that $\rho_y = \rho_z$ for the entire model. Figure 2.19b shows the anisotropic angles as a function of depth. The anisotropic axes are aligned with the measurement coordinate system, and therefore the strike, dip, and slant angles are 0° for the entire model. Note that the anisotropic layer is uniaxial with $\rho_x$ as the unique principal resistivity, which is the case illustrated in Figure 2.18a.

The 1-D anisotropic modeling algorithm of Pek & Santos (2002) was used to calculate MT data for the model. The calculated apparent resistivity and phase data are shown as functions of frequency in Figure 2.19c and Figure 2.19d, respectively. As in previous sections, the *xy* component corresponds to data calculated from the electric field polarized in the *x* direction and the magnetic field polarized in the *y* direction. The data here are clearly different than data for a 1-D isotropic model, where the *xy* and *yx* component data are identical at all frequencies. In order to understand why this is the case, the following paragraphs explain the behavior of the data at different frequencies.

First, Figure 2.19 shows that the *xx* and *yy* apparent resistivities and phases are zero for all frequencies. This is due to the fact that the curves are plotted for the angle that the anisotropic and measurement axes are aligned. Examining the non-zero data at frequencies above 100 Hz, the *xy* and *yx* apparent resistivities equal 10 Ωm and the phases are 45° because the data are only sensitive to the isotropic 10 Ωm layer. At about 30 Hz the data are sensitive to the anisotropic layer at 0.25 km depth, with the *xy* and *yx* components sensitive to different principal resistivities of the anisotropic layer. The *xy* component (electric field polarized in the *x* direction) is sensitive to the $\rho_x$ principal resistivity (1 Ωm), causing a decrease in *xy* apparent resistivity and a phase greater than 45°. The *yx* component (electric field polarized in the *y* direction) is sensitive to the $\rho_y$ principal resistivity (100 Ωm), causing an increase in *yx* apparent resistivity and a phase less than 45°. At about 0.3 Hz the data become sensitive to the isotropic 100 Ωm layer. Correspondingly, the *xy* apparent resistivity approaches 100 Ωm and the *xy* phase is less than 45° at the lowest frequencies. However, the *yx* component cannot differentiate between the anisotropic layer with $\rho_y$ = 100 Ωm and the underlying 100 Ωm isotropic layer because the resistivity in the *y* direction is equal in both layers. Therefore, at frequencies below 30 Hz the *yx* apparent resistivity approaches 100 Ωm and the *yx* phase is less than 45°. The *yx* apparent resistivity and phase curves effectively behave as if the isotropic 10 Ωm layer is underlain with a 100 Ωm isotropic halfspace.

Figure 2.19e shows a pseudo-section of phase tensor ellipses plotted in the frequency range 1000 to 0.001 Hz (see Section 2.4.3 for a review of the phase tensor). Recall that each ellipse is a map view at a particular frequency. Similar to a model with a 2-D isotropic resistivity structure, the phase tensor skew angle ($\beta$) is 0° for a 1-D anisotropic Earth. Here the ellipses are instead filled with a color corresponding to $\Phi_{min}$, the minimum phase tensor value at a particular frequency. In this example, because the anisotropic and measurement axes are aligned and the resistivity distribution is 1-D, $\Phi_{min}$ at a particular frequency is either the *xy* or *yx* phase, whichever is smaller. At frequencies above 100 Hz the data only detect the 10 Ωm layer, and the phase tensor ellipses are circles. Below a frequency of 100 Hz, the anisotropic layer causes different responses in the *xy* and *yx* modes, and therefore the ellipses are not circles. In the frequency range 100 and 0.3 Hz, the ellipses are elongated in the *y* direction because the maximum phase occurs in the *xy* component. Below a frequency of 0.3 Hz, the maximum phase occurs in the *yx* component and therefore the ellipses are aligned in

the *x* direction. This 90° change in ellipse azimuth is similar to the behavior of the phase tensor ellipses of the 2-D conductive dyke in Section 2.5.3. In fact, 1-D anisotropic data appear similar to 2-D isotropic data due to (1) non-circular phase tensor ellipses and (2) beta skew angle equal to zero at all locations and frequencies. In practice, this ambiguity is resolved by analyzing tipper data, a method that is discussed in the following section.

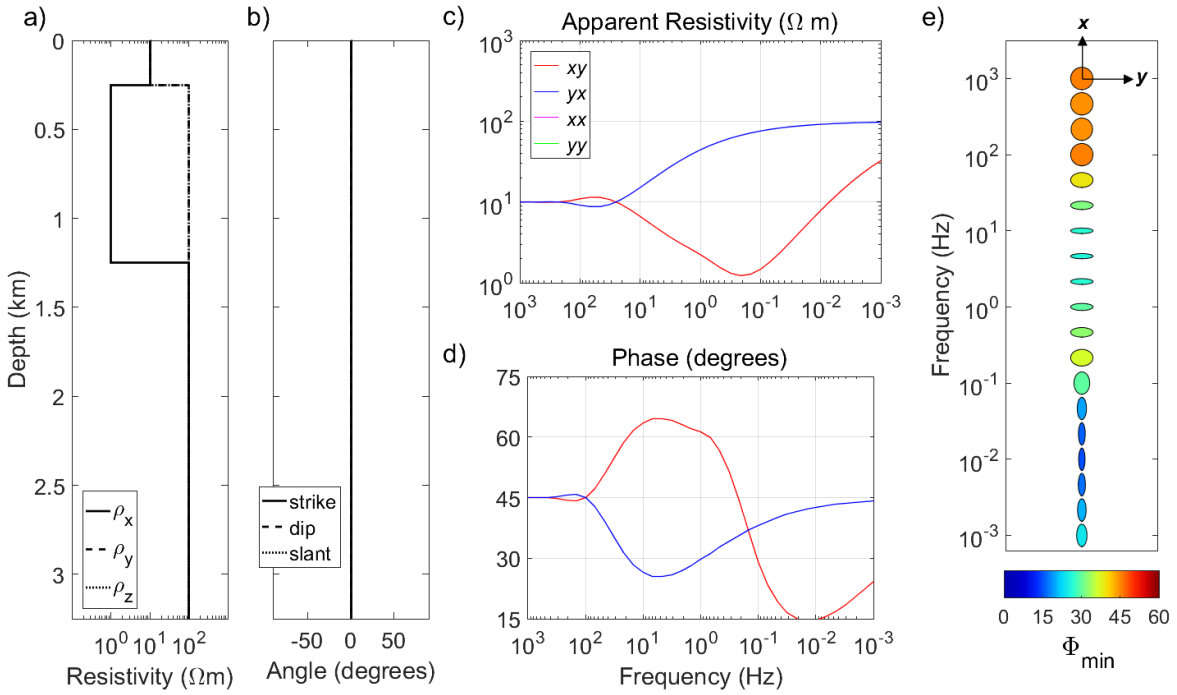


Figure 2.19: Apparent resistivity, phase, and phase tensor data for a simple 1-D anisotropic model. a) principal resistivity values as a function of depth; note that $\rho_y = \rho_z$ for the entire model. The top layer is isotropic, 10 Ωm, and 0.25 km thick. The second layer is 1 km thick, with $\rho_x = 1$ Ωm and $\rho_y = \rho_z = 100$ Ωm. The bottom layer is isotropic, 100 Ωm, and extends infinitely downward. b) anisotropic angles as a function of depth; note that the strike, dip, and slant angles are zero for the entire model. c) calculated apparent resistivity as a function of frequency. The *xx* and *yy* apparent resistivities are both zero for all frequencies. d) calculated phase data as a function of frequency. The *xx* and *yy* phase are both zero for all frequencies. e) phase tensor ellipse pseudo-section. Each ellipse is a map view at a particular frequency; the *x* and *y* directions are shown for clarity. The fill color corresponds to the minimum phase tensor value at each frequency. Note that the skew angle $\beta = 0°$ for all frequencies. Induction vectors have zero magnitude for all frequencies.

Figure 2.19 featured a 1-D anisotropic resistivity model with anisotropic axes aligned to the measurement coordinate system. The measured MT data are more difficult to interpret if the anisotropic axes are not aligned to the measurement coordinate system. Figure 2.20 shows data calculated for a 1-D anisotropic model similar to the one shown in Figure 2.19, except that the anisotropic strike angle is 30° in the anisotropic layer (0.25 to 1.25 km depth).

Figure 2.20c shows the apparent resistivity as a function of frequency for the 1-D anisotropic model, where *xy* corresponds to data calculated from the electric field polarized in the *x* direction and the magnetic field polarized in the *y* direction. At frequencies above 100 Hz, where the data are only sensitive to the top layer, the *xy* and *yx* apparent resistivities are 10 Ωm and the phases are 45° (Figure 2.20d). Between 100 and 0.3 Hz, the apparent resistivity and phase data are different than in Figure 2.19. Unlike the previous example, the *xx* and *yy* apparent resistivity and phase data are not zero at all frequencies because the anisotropy axes are not aligned with the measurement coordinate system. As predicted from Equation (2.69), the *xx* and *yy* apparent resistivities are equal, and therefore their curves coincide in Figure 2.20c. In addition, because the anisotropic strike angle is not zero, the *xy* and *yx* components differ from the previous example because they are sensitive to a mixture of the $\rho_x$ and $\rho_y$ principal resistivities. The phase tensor ellipses in Figure 2.20e are similar to those in Figure 2.19e except that at frequencies sensitive to the anisotropic layer, their principal axes are aligned with the anisotropic strike of 30°.

The 1-D anisotropic MT data presented in Figure 2.20 are similar to the impedance tensor of a 2-D isotropic Earth that is not rotated to the strike angle. If the impedance tensor calculated for the model in Figure 2.20 is rotated by 30° to align with the anisotropic strike, the resulting rotated impedance tensor is equivalent to the one obtained for the 1-D anisotropic model in Figure 2.19.

The MT data for the 1-D anisotropic models shown in Figure 2.19 and Figure 2.20 have some similarities to data observed for a 2-D isotropic Earth. The next section discusses how to use induction arrows to distinguish 1-D anisotropic data from 2-D isotropic data.

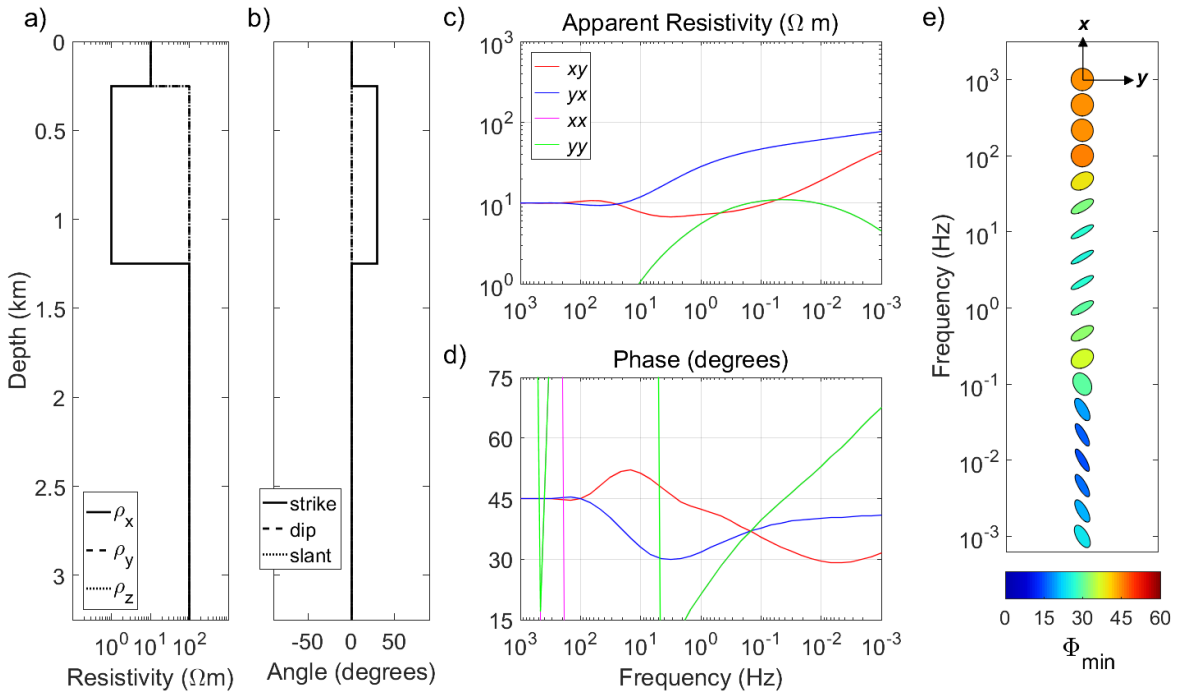


Figure 2.20: Apparent resistivity, phase, and phase tensor data for a 1-D resistivity model containing a layer with a 30° anisotropic strike direction. a) principal resistivity values as a function of depth; note that $\rho_y = \rho_z$ for the entire model. The top layer is isotropic, 10 Ωm, and 0.25 km thick. The second layer is 1 km thick, with $\rho_x$ = 1 Ωm and $\rho_y = \rho_z$ = 100 Ωm. The bottom layer is isotropic, 100 Ωm, and extends infinitely downward. b) anisotropic angles as a function of depth; note that both the dip and slant angles are zero for the entire model. The anisotropic strike is 30° in the second layer (0.25 to 1.25 km depth). c) calculated apparent resistivity as a function of frequency. The *xx* and *yy* apparent resistivities are equal. d) calculated phase data as a function of frequency. e) phase tensor ellipse pseudo-section. Each ellipse is a map view at a particular frequency; the *x* and *y* directions are shown for clarity. The fill color corresponds to the minimum phase tensor value at each frequency. Note that the skew angle $\beta$ = 0° for all frequencies. Induction vectors have zero magnitude for all frequencies.

### 2.7.4. Detecting anisotropy in MT data

#### 2.7.4.1. Analyzing induction arrows

As previously mentioned, tipper data and therefore induction arrows are zero for a model where the resistivity is 1-D and isotropic. This property also holds for a 1-D anisotropic Earth, even if $Z_{xy} \neq Z_{yx}$. Therefore, the dimensionality of the Earth may be

distinguished by the absence or presence of induction arrows. For a 2-D Earth such as the vertical dykes in Figure 2.10, induction arrows have non-zero magnitudes near lateral resistivity boundaries (see Figure 2.11).

Another characteristic indicative of MT data affected by anisotropy is the deflection of induction arrows, which is best understood in the case of a 2-D resistivity model. If the Earth is isotropic, in the Parkinson convention induction arrows point perpendicular to the geoelectric strike direction, i.e. toward conductive bodies. However, 2-D cases have been illustrated where an anisotropic layer deflects induction arrows almost parallel to the regional strike direction that was determined from the impedance tensor. This is due to the net induction in both the isotropic and anisotropic layers (Heise & Pous, 2001, 2003; Pek & Verner, 1997).

#### 2.7.4.2. Out of quadrant phase

Anisotropy can also lead to anomalous inductive effects, similar to those of 3-D features. Recall that the impedance phase angle is the phase lag between electric and magnetic fields of the EM signal. In 1-D, 2-D, and simple 3-D geometries, the phase angle for $E_x$ and $E_y$ polarizations is expected to be between 0° and 90° for $E_x$, and between -90° and -180° for $E_y$. Out of quadrant phase (OOQP) has been observed for isotropic 3-D resistivity models. Examples include an L-shaped conductor in a resistive background (Ichihara & Mogi, 2009), thin conductors sub-parallel to a larger 2-D conductor such as the ocean (Lezaeta & Haak, 2003), highly conductive ring structures (Pous et al. 2002; Weckmann et al., 2003), and complicated arrangements of 3-D conductors (Ichihara et al., 2013; Piña-Varas & Dentith, 2018). In these cases 3-D conductive bodies cause significant changes in electric current direction, leading to the observed OOQP (Egbert 1990; Chouteau & Tournerie, 2000).

OOQP can also be caused by anisotropy, with it deflecting the direction of regional current flow. For example, out of quadrant phase can be demonstrated in 2-D anisotropic models with large resistivity contrasts and/or anisotropic strikes at oblique angles to the measurement coordinate system (i.e. Heise & Pous, 2001).

## 2.8. Magnetotelluric data collection

Magnetotellurics (MT) has many applications due to its ability to image the resistivity of the Earth from the surface to depths of a few hundred kilometers. MT instruments measure natural electromagnetic waves at the surface of the Earth and the exploration depth depends on the measured signal frequency through the skin depth equation (Equation 2.41). High frequency signals (>1 Hz) typically originate in distant lightning strikes and low frequency (<1 Hz) signals are due to interactions of the solar wind with the Earth's magnetosphere. Several types of MT systems have been developed for particular applications. These systems are listed below.

- Audio magnetotelluric (AMT) instruments are designed to explore shallow depths, typically the upper kilometer. These systems have a high sampling rate (> 20 kHz) to record high frequency signals that penetrate to shallow depths. A controlled source variant (CSAMT) utilizes a transmitter to boost the signal strength in the so-called "dead band" (~1 to 5 kHz) where natural EM signal amplitude is low (Garcia & Jones, 2002).

- Broadband magnetotelluric (BBMT) instruments are used to explore shallow to moderate depths, typically ~1 to 50 km. This broad depth range makes these instruments useful for resource exploration, as well as regional crustal studies. BBMT systems have been designed with variable sampling rates (~1 Hz to 20 kHz) that make them versatile for different types of surveys.

- Long period magnetotelluric (LMT) instruments are used for imaging into the upper mantle. In areas with a thick lithosphere, these instruments can resolve structures at > 250 km depth. LMT systems typically have a low sampling rate (1 to 10 Hz) to record low frequency signals that penetrate deep into the Earth.

The following description of field operation focuses on BBMT because this is the type of data predominantly studied in this thesis. A typical broadband MT station layout is shown in Figure 2.21. As previously mentioned, the orthogonal electric and magnetic fields are measured in order to calculate the full impedance tensor. In the field, the data are

measured as a time series with multiple recording bands with different sampling rates. For example, the Phoenix Geophysics V5-2000 instrument records a continuous 15 Hz time series and two discontinuous time series with higher sampling rates of 150 Hz and 2400 Hz. The electric field components are measured with two orthogonal sets of non-polarizing electrodes. The magnetic fields components are measured with three magnetic induction coils. Recall that the vertical magnetic field is not used in the impedance calculation, but used to calculate the tipper. All instruments are buried approximately 30 cm below the surface to prevent noise from mechanical motion and to ensure thermal stability.

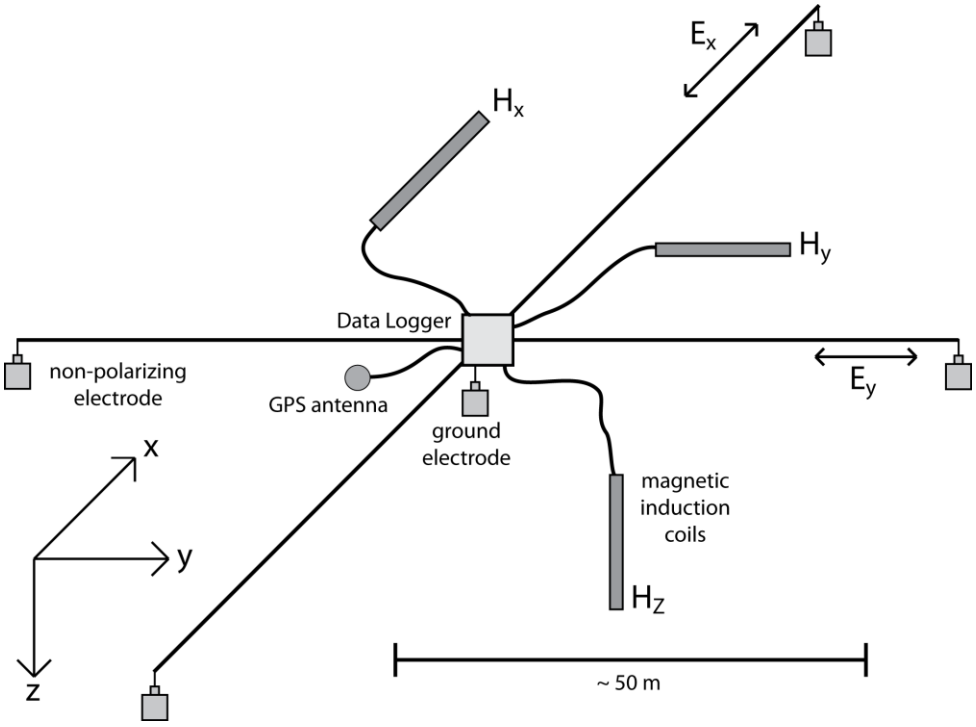


Figure 2.21: Typical layout of a broadband magnetotelluric station. Instruments not to scale.

A typical recording time for a broadband MT station is about 12 to 24 hours. The recording time depends on the target depth of investigation and the signal quality. Recall that the skin depth equation (Equation 2.41) controls the propagation depth of an EM signal. Lower frequency signals propagate deeper into the Earth and therefore are sensitive to deeper resistivity structure. However, it takes more time to measure a full period of a low frequency signal. For example, a signal with a frequency of 0.001 Hz has a period of 1000 s or about 16.7 min. Ideally, many samples of this 0.001 Hz signal should be recorded to allow random

measurement noise to be averaged out during processing. Another reason to measure a longer time series is the fact that the naturally-occurring signals measured by broadband and long period MT stations are transient and vary in strength over time. For the case studies in this thesis, where the target depth is < 10 km, an overnight recording of 12 to 24 hours is usually sufficient. The following section summarizes data processing methods to convert the recorded MT time series to impedance data.

## 2.9. Magnetotelluric time series processing

### 2.9.1. Background

Raw magnetotelluric (MT) data consist of electric and magnetic field measurements where the total recording time ranges from several minutes (AMT) to several weeks (LMT). The time series provide limited information for interpretation since the measured fields are not the final quantity of interest. Instead, the impedance transfer function $Z_{ij}$ that relates the measured electric and magnetic fields and contains the response of the Earth is calculated:

$$E_x(\omega) = Z_{xx}(\omega)H_x(\omega) + Z_{xy}(\omega)H_y(\omega) \tag{2.70}$$

$$E_y(\omega) = Z_{yx}(\omega)H_x(\omega) + Z_{yy}(\omega)H_y(\omega) \tag{2.71}$$

where the electric field $E$, magnetic field $H$, and impedance $Z_{ij}$ are functions of angular frequency $\omega$. Note that Equation (2.70) and Equation (2.71) are computed from Equation (2.42).

MT data undergo a large reduction in the number of data points when transformed from the time series to estimates of the impedance tensor at discrete frequencies. First, the raw time series is inspected and segments with obvious noise (e.g. instrument failure) are removed. Next, assuming the signal has a harmonic time dependence, the time series is divided into smaller windows for discrete Fourier transforms. For example, if the sampling rate is 0.5 Hz (2 s) and a time window consists of 512 data points, then the lowest frequency signal that can be recovered is about 0.02 Hz (50 s), assuming 20 samples are necessary. If the user is interested in deep resistivity structure, then it is important to obtain as low a frequency as possible. The minimum frequency can be decreased by a process called

decimation. With this method, the time series is sub-sampled by taking, for example, only every fourth data point. In this example, the effective sampling rate is then 0.125 Hz (8 s) and a time window with 512 data points can be processed to recover frequencies as low as 0.005 Hz (200 s). The Nyquist frequency, defined as the highest-frequency signal that can be fully reconstructed at a particular sampling rate, is equal to half of the sampling rate. Therefore, in this example the Nyquist frequency is 0.0625 Hz (16 s), which is half of the effective sampling rate. The decimated time series is low-pass filtered to remove any signal with a frequency above the new Nyquist frequency. The resulting spectra are evaluated at frequencies regularly spaced on a logarithmic scale to obtain complex Fourier coefficients. This process is performed for each measurement channel, i.e. $E_x$, $E_y$, $H_x$, $H_y$, and $H_z$. The auto and cross-powers of each channel are then computed from the Fourier coefficients and stacked over multiple time windows. Simpson & Bahr (2005) show eight equations relating the impedance tensor components to the electric and magnetic power spectra (their Equations 4.16a – h). These equations are obtained by multiplying Equations (2.70) and (2.71) by the complex conjugates of the electric and magnetic field spectra. It is clear from Simpson and Bahr's Equations (4.16a – h) that there is more than one equation to calculate each impedance component, $Z_{ij}$. In the absence of measurement noise, different equations for a particular $Z_{ij}$ yield the same solution. However, due to measurement noise in electric and magnetic fields, the auto-power terms in these equations amplify noise since any component is coherent with itself. As a result, some of these equations result in estimates that are (1) biased upward by random noise in the electric field, or (2) biased downward by random noise in the magnetic field (Sims et al., 1971; Swift, 1967). The following sections describe some methods to minimize or remove this bias.

### 2.9.2. Removing bias in MT impedances

When calculating the impedance tensor for a single MT station, auto-correlated terms of the electric and magnetic fields are biased in the presence of measurement noise. Early approaches to minimize the bias focused on manipulating the spectra prior to calculating the impedance components. Kao & Rankin (1977) developed a cyclic operation to improve the signal-to-noise ratio and eliminate bias from the auto-power terms. However, this approach only improved impedance estimates when the cross-power terms were free of noise. Goubau

et al. (1978) described two methods to rewrite the impedance estimates in terms of the averaged cross-power terms. However, these methods fail for the 1-D case and the 2-D case when one electrode is aligned with the strike direction. Sims et al. (1971) calculated the mean of the downward biased impedance and the upward biased impedance and suggested that the mean estimate would result in smoother data than just one of the biased estimates alone.

The remote reference method is a widely implemented approach to overcome the bias in the auto-power terms. Time series processing with the remote reference method requires synchronous measurements at two MT stations. The impedance data at one MT station (designated as the local station) are computed using the locally measured fields and the electric and/or magnetic fields from the second (remote) MT station. Goubau et al. (1978) were the first to suggest using simultaneous local and remote electric or magnetic field measurements to calculate the impedance components. The remotely measured field must be correlated to the field measured at the local station, which means that the two synchronous MT stations must be spatially close enough to measure the same signals. Therefore, the remote magnetic field is usually preferred because the electric field is more sensitive to the local geology while the magnetic field can be uniform over many kilometers (Zelwer & Morrison, 1972). With two additional channels of magnetic field measurements, Simpson and Bahr's Equations (4.16a – h) can be rewritten in terms of cross-powers (Gamble et al., 1979). When rewritten, each cross-power term contains one term from the local site and one term from the remote site. If the noise measured by the local and remote stations is uncorrelated, then each cross-power term will be unbiased by noise. Gamble et al. (1979) showed that estimates of the impedance components using a remote reference resulted in unbiased and smoother apparent resistivity curves compared to curves derived by earlier least-square methods. An issue with this method was ensuring that the distance between the local and remote stations was large enough to remove coherent noise from the time series. This issue was solved by development of accurate and transportable GPS antennas, removing the need for a cable connection between MT stations.

### 2.9.3. Statistical methods for MT time series processing

Least-square and robust methods are examples of techniques to remove noise from processed MT data. The least-square method minimizes the sum of squares misfit for

estimated impedance components while assuming a Gaussian distribution of noise. However, this approach is inaccurate if (1) error is dependent on the signal power, (2) noise distribution is non-Gaussian, or (3) noise is time-dependent (Egbert & Booker, 1986). Robust processing techniques (e.g. Chave et al., 1987; Egbert & Booker, 1986) were developed to systematically reduce the influence of particularly noisy data points (known as outliers) when calculating the impedance components. Outliers may be due to natural signal that violates the MT plane-wave source approximation, such as magnetic storms or auroral jets occurring near the MT station. MT data contaminated by these signals have been observed at mid-latitudes (e.g. Egbert & Booker, 1986) and further north in auroral zones (e.g. Lezaeta et al., 2007). Cultural noise such as power stations, substations, or direct current train signals may also violate the plane-wave approximation (e.g. Egbert et al., 2000; Pádua et al., 2002). In general, any noise that is not random (i.e. not a Gaussian distribution) may systematically affect all measurement channels, and is therefore more difficult to remove when calculating the MT impedance components.

The robust processing scheme of Egbert & Booker (1986) used an iterative scheme that reduces the weight of data points with large deviations from their expected least-squares values. The goal is to down-weight the outliers so that they have minimum influence when stacking the data. However, it is important to consider that one outlier can still affect the computation of impedance components since the time window contains many (e.g. 512) data points. When the time window is Fourier transformed, the power from the outlier will be averaged with the rest of the data in the time window. Thus, Egbert & Booker (1986) suggest using a short time window for robust processing so that the effect of outliers can be more readily detected and removed.

Jones et al. (1989) compared the results from least-square and robust processing techniques. They showed that the robust processing techniques resulted in smoother apparent resistivity curves and smaller uncertainties. Robust processing is also useful because it automates the procedure of removing poor data points from the time series. These data are removed on a statistical basis, whereas simple visual inspection could be more arbitrary. The remote reference method should also be utilized whenever possible to reduce bias errors. The use of robust processing and a remote reference has greatly increased the quality of processed MT impedance data.

## 2.10. Forward modeling of magnetotelluric data

The forward problem in geophysics involves calculating geophysical data for a given model. In the case of MT, the EM fields for a given resistivity model are calculated by solving Maxwell's equations. For simple geometries, such as 1-D resistivity models, the EM fields can be solved analytically. For 3-D resistivity models, where the fields cannot be solved analytically, the most common methods to solve the forward problem are finite-difference (FD), finite-element (FE), and integral equation (IE) methods (Avdeev, 2005). These methods use a resistivity model that is discretized into cells, and solve the EM fields at discrete points in the resistivity model. The FD method is the most commonly used method in 3-D MT forward modeling. Therefore, the FE and IE methods will not be discussed here.

A brief overview of the FD method is given below. For a more detailed introduction see J. T. Smith (1996), Mackie et al. (1994), and Börner (2010). The FD method solves the EM fields at discrete points on a rectilinear grid of cells. The staggered FD grid is commonly used to define the electric and magnetic fields at different locations on each cell (Siripunvaraporn et al., 2002). For example, the electric field can be computed on cell faces while the magnetic field is computed on the cell edges (Madden & Mackie, 1989). To set up the FD forward problem, consider Maxwell's equations under the same assumptions used in Section 2.2. These assumptions are (1) the conduction current is much larger than the displacement current; (2) EM fields vary harmonically with time; (3) the magnetic permeability of the Earth is approximated as its free space value, and is constant in time and space; (4) electrical resistivity is isotropic and does not vary with time. Under these assumptions, a second-order partial differential equation can be obtained by substituting Equation (2.5) into the curl of Equation (2.4):

$$\nabla \times \nabla \times \boldsymbol{E} = i\omega\mu_0\sigma\boldsymbol{E} \tag{2.72}$$

Alternatively, Equation (2.4) can be substituted into the curl of Equation (2.5) to obtain:

$$\nabla \times \rho\nabla \times \boldsymbol{H} = i\omega\mu_0\boldsymbol{H} \tag{2.73}$$

Using the FD discretized mesh, Equation (2.72) or Equation (2.73) can be rewritten in the form:

$$\boldsymbol{Ax} = \boldsymbol{b} \tag{2.74}$$

where $\boldsymbol{A}$ is a matrix of coefficients, $\boldsymbol{x}$ is a vector containing the electric (or magnetic) field at discrete points on the mesh, and $\boldsymbol{b}$ is a vector containing the boundary conditions. The matrix $\boldsymbol{A}$ must be inverted to solve for the unknown fields in $\boldsymbol{x}$; however, this is computationally prohibitive for a 3-D model and iterative solvers must be used.

If solving for the electric fields on the staggered FD grid with Equation (2.74), it is practical to define the electric fields on cell edges and the magnetic fields on cell faces. In this case, it is natural to define $\boldsymbol{H}$ on the cell faces because once Equation (2.74) is solved for $\boldsymbol{E}$, the values of $\boldsymbol{E}$ are known on the four edges surrounding any cell face. Then using Equation (2.4) the curl of $\boldsymbol{E}$ can be approximated at points around the face to obtain $\boldsymbol{H}$.

In the case of electrical anisotropy, the forward problem is more complicated because electrical resistivity is a tensor as in Equation (2.67). Kong et al. (2018) provide an example of a FD scheme for arbitrary 3-D anisotropy. Martí (2014) gives a review of electric and magnetic field derivations for 1-D and 2-D anisotropic resistivity models.

## 2.11. Inversion of magnetotelluric data

### 2.11.1. The inversion objective function

This section provides a brief overview of inverting MT data. An inversion algorithm uses geophysical data to obtain a resistivity model of the Earth that satisfies some specified requirements. Usually, these requirements are that (1) the MT data predicted from the resistivity model fits the measured MT data to a specified statistical level; (2) the resistivity model is spatially smooth, i.e. contains minimum structure. These requirements can be implemented as an objective function, which the inversion algorithm seeks to minimize. The objective function may have a form such as:

$$\phi(\boldsymbol{d},\boldsymbol{m}) = (\boldsymbol{d}-\boldsymbol{F}(\boldsymbol{m}))^T \boldsymbol{C_d^{-1}}\big(\boldsymbol{d}-\boldsymbol{F}(\boldsymbol{m})\big) + \lambda(\boldsymbol{m}-\boldsymbol{m}_0)^T \boldsymbol{C_m^{-1}}(\boldsymbol{m}-\boldsymbol{m}_0) \quad (2.75)$$

where:

$\boldsymbol{d}$ is a vector containing the measured MT data,

$\boldsymbol{m}$ is the resistivity model at a particular iteration,

$\boldsymbol{m}_0$ is a prior resistivity model,

$\boldsymbol{F}$ is the forward modeling operator,

$\boldsymbol{C_d}$ is the data covariance matrix,

$\boldsymbol{C_m}$ is the model covariance matrix,

$\lambda$ is a scalar trade-off parameter,

$U^T$ is the transpose of an arbitrary matrix $U$, and

$U^{-1}$ is the inverse of an arbitrary matrix $U$.

Equation (2.75) is the form of the objective function used in many MT inversion algorithms (Siripunvaraporn, 2012), and can be simplified as:

$$\phi(\boldsymbol{d},\boldsymbol{m}) = \phi_{\boldsymbol{d}} + \lambda\phi_{\boldsymbol{m}} \quad (2.76)$$

with:

$$\phi_{\boldsymbol{d}} = (\boldsymbol{d}-\boldsymbol{F}(\boldsymbol{m}))^T \boldsymbol{C_d^{-1}}\big(\boldsymbol{d}-\boldsymbol{F}(\boldsymbol{m})\big) \quad (2.77)$$

$$\phi_{\boldsymbol{m}} = (\boldsymbol{m}-\boldsymbol{m}_0)^T \boldsymbol{C_m^{-1}}(\boldsymbol{m}-\boldsymbol{m}_0) \quad (2.78)$$

Equation (2.77), which is the first term on the right hand side of Equation (2.76), contains terms pertaining to the MT data. $\phi_{\boldsymbol{d}}$ is a measure of the data misfit, i.e. how closely the predicted data, $\boldsymbol{F}(\boldsymbol{m})$, fit the measured data, $\boldsymbol{d}$. The predicted MT data are expressed as $\boldsymbol{F}(\boldsymbol{m})$ to denote the forward modeling operator acting on the resistivity model to calculate the predicted data. $\boldsymbol{C_d}$ is the data covariance matrix, which contains the uncertainties associated with each datum.

Equation (2.78), which appears in the second term on the right hand side of Equation (2.76), contains parameters pertaining to the resistivity model. $\phi_{\boldsymbol{m}}$ is commonly called the model norm and is a measure of the model roughness. The model norm contains the term $\boldsymbol{m} - \boldsymbol{m}_0$, which is the difference between resistivity values of the resistivity model $\boldsymbol{m}$ and the prior model $\boldsymbol{m}_0$. $\boldsymbol{C}_{\boldsymbol{m}}$ is the model covariance matrix, which contains the user-imposed smoothing constraints on the model. For example, $\boldsymbol{C}_{\boldsymbol{m}}$ can be adjusted to impose a greater degree of smoothing in the *x*, *y*, or *z* directions. If $\phi_{\boldsymbol{m}}$ is large, the model is "rough", which may be due to large differences from the reference model, or large spatial variations in resistivity.

Many inversion algorithms require the user to specify $\boldsymbol{m}_0$ and an initial $\boldsymbol{m}$ at the start of the inversion. For example, the ModEM 3-D inversion algorithm of Kelbert et al. (2014) requires the user to specify the prior model, $\boldsymbol{m}_0$. If the user does not specify an initial model, $\boldsymbol{m}_0$ is used as the initial model by default. In order to constrain the possible resistivity models obtained by the inversion, a prior model can include constraints from other types of data, e.g. geophysical or petrophysical data. If no *a priori* information is known, a homogeneous halfspace prior model can be used. However, it should be noted that the magnitude of resistivity values in the prior and initial models can influence the magnitude of resistivity values in the final resistivity model. In systematic tests by Robertson et al. (2020), the authors varied the resistivity of their halfspace prior model by two orders of magnitude (3 to 1000 Ωm). When the prior model was also used as the initial model, Robertson et al. (2020) found that the averaged resistivity values from the final model were clearly dependent on the prior/initial model resistivity. Therefore, several resistivity values should be tested and the preferred prior/initial model should be a reasonable estimate of the subsurface resistivity.

In Equation (2.76) it is clear that the trade-off parameter $\lambda$ controls the relative weights of the data misfit $\phi_{\boldsymbol{d}}$ and the model norm $\phi_{\boldsymbol{m}}$ in the objective function. For example, if $\lambda$ is large, $\lambda\phi_{\boldsymbol{m}}$ has a relatively large contribution to $\phi(\boldsymbol{d}, \boldsymbol{m})$, and therefore the inversion preferentially seeks to minimize $\phi_{\boldsymbol{m}}$. If $\lambda$ is small, then $\phi_{\boldsymbol{d}}$ is relatively large and the inversion preferentially seeks to minimize the data misfit. Some inversions allow $\lambda$ to decrease as the inversion progresses, which might decrease computation time by allowing for large changes to the model in early inversion iterations.

The trade-off between data misfit and model norm is an example of non-uniqueness in the inversion process. Depending on the value of $\lambda$, a range of inversion solutions can be obtained that exist on a spectrum between (1) low data misfit and a spatially rough model, and (2) high data misfit and a spatially smooth model. In case (1), the predicted MT data closely fit the measured MT data, but the resulting resistivity model is unrealistically rough. In case (2), the resistivity model is smooth, but at the expense of a poor fit to the measured MT data. The preferred inversion solution should be a trade-off between these two cases.

It is important to note the differences in the objective function between isotropic and anisotropic inversions because both types of inversions are used in this thesis. First, the forward modeling operator for an anisotropic inversion is different than for an isotropic inversion. This is because a more general form of Maxwell's equations is used where the electrical resistivity is treated as a tensor instead of a scalar. Therefore, the forward modeling operator $\boldsymbol{F}$ represents a different forward modeling algorithm for the isotropic and anisotropic cases. The parameters $\boldsymbol{m}$ and $\boldsymbol{m}_0$ must also be different for isotropic and anisotropic inversions because the anisotropic inversion contains a greater amount of model parameters, i.e. more than one resistivity per cell. In an isotropic inversion $\boldsymbol{m}$ is a vector containing the resistivity of each model cell and $\boldsymbol{m}_0$ is a vector of the same size containing the resistivity of each cell in the reference model. In the arbitrary anisotropic inversion, because the six parameters $\rho_x$, $\rho_y$, $\rho_z$, $\alpha_S$, $\alpha_D$, and $\alpha_L$ are needed to describe the anisotropy, $\boldsymbol{m}$ and $\boldsymbol{m}_0$ each contain six times the number of entries as in the isotropic inversion.

### 2.11.2. Types of inversion algorithms

The most widely used MT inversion algorithms are deterministic algorithms that are designed to iteratively converge to the final solution. That is, the inversion begins with an initial resistivity model and iteratively updates the resistivity model until the inversion is finished. On the other hand, stochastic inversion algorithms obtain a range of models that can be evaluated with summary statistics (e.g. Buland & Kolbjørnsen, 2012; Chen et al., 2012). A stochastic algorithm draws models randomly from a probability distribution, where the distribution can be gradually updated to constrain the possible models. An advantage of stochastic algorithms is that they provide more robust measures of the model uncertainty than deterministic algorithms (Trainor-Guitton & Hoversten, 2011). However, because a

stochastic algorithm must run the forward modeling operator for a large number of randomly generated models, stochastic inversions are currently not computationally feasible for 3-D inversion of MT data.

The work in this thesis utilized deterministic 3-D MT inversion algorithms. The deterministic inversions can be further classified by the techniques used to determine how to update the resistivity model in order to further decrease the objective function. A few examples include Occam's inversion (e.g. Siripunvaraporn et al., 2005; Siripunvaraporn & Egbert, 2000), the Gauss-Newton method (e.g. Farquharson et al., 2002; Haber et al., 2004; Y. Sasaki, 2004), and the non-linear conjugate gradient method (e.g. Kelbert et al., 2014; Newman & Alumbaugh, 2000; Rodi & Mackie, 2001). Each inversion algorithm has a different approach to minimization of the objective function that results in different computational requirements. In most cases the final interpretation of a resistivity model should not depend on choosing one inversion over another. Miensopust et al. (2013) presented results from a 3-D MT inversion workshop showing that different inversion algorithms produced qualitatively similar results, and that differences can be attributed to the user's choice of inversion parameters. Therefore, the choice of inversion algorithm does not affect the quality of the result as much as correct implementation of the inversion algorithm.

## 2.12. Summary

The MT method is based on the propagation of electromagnetic signals in the Earth. In this chapter an equation for EM signal propagation in a 1-D Earth was derived, based on several assumptions including (1) a plane wave source, (2) harmonic time variance of the signal, (3) no free charges in the Earth, (4) the magnetic permeability of free space in the Earth, and (5) propagation in the Earth by diffusion. This equation is called the skin depth, which governs the propagation depth of EM signals as a function of the signal frequency and the Earth's electrical resistivity. The EM signals contain electric and magnetic field components which are measured at the Earth's surface and used to calculate the main interpretative quantities in MT: impedance, apparent resistivity, phase, and the tipper. Apparent resistivity and phase are expressions of the impedance magnitude and phase, and are often viewed as functions of frequency to study resistivity variations with depth. The

tipper is calculated from the magnetic field components and reveals horizontal spatial variations in resistivity.

The form of the measured MT impedance tensor is indicative of a 1-D, 2-D, or 3-D resistivity distribution in the Earth. In practice, the dimensionality of the data is extremely important to understand because it determines the lowest dimensionality of analysis that is valid for a dataset. For example, a 1-D Earth can be accurately modeled in 1-D, 2-D, or 3-D; but a 3-D Earth cannot be accurately modeled in 1-D or 2-D. The tensor decomposition algorithm of McNeice & Jones (2001) and the magnetotelluric phase tensor (Caldwell et al., 2004) are examples of tools used to identify the dimensionality of MT data. The tensor decomposition also allows for identification of galvanic distortion, which superimposes 3-D inductive effects on lower dimensionality data. Distortion can be a major problem in analysis of a 2-D Earth and must be identified and possibly removed for accurate modeling.

Electrical anisotropy is another complication in modeling the resistivity of the Earth. Anisotropy affects the measured impedance data when the Earth's resistivity varies on a scale much smaller than the MT skin depth, usually on a microscopic scale. Unfortunately, the effect of anisotropy on the MT data cannot be uniquely determined from 3-D distortion.

MT equipment is available in configurations suitable for different applications. Audio magnetotelluric (AMT) equipment is suitable for shallow (~ 1 km) depths, long period (LMT) equipment is suitable for crustal and mantle studies, and broadband (BBMT) equipment is suitable for a large depth range (~ 1 to 50 km). Electric field data are typically measured with non-polarizing electrodes and magnetic fields are measured with either induction coils or a three-component magnetometer. The measured data are converted to the frequency domain in order to calculate impedance as a function of frequency. The remote reference method and robust processing techniques are widely used to remove noise from the processed impedance data.

Inversion algorithms are used to obtain a resistivity model from observed MT data. These algorithms work by iteratively minimizing an objective function, which is a measure of the data misfit and the model smoothness. There are many published inversion algorithms that use different mathematical approaches; however, the choice of inversion algorithm usually does not significantly impact the final interpretation of the resistivity model.

# 3. Imaging the magmatic system beneath the Krafla geothermal field from 3-D inversion of magnetotelluric data

## 3.1. Introduction

Recent studies have investigated the properties of supercritical geothermal reservoirs which are sometimes found at the base of conventional geothermal reservoirs (Fridleifsson & Elders, 2005; Scott et al., 2015; Watanabe et al., 2017). The supercritical fluids found in these reservoirs contain significantly more heat than the steam used in conventional geothermal plants. Fridleifsson et al. (2003) reported that at the same volumetric flow rate, a geothermal well producing supercritical fluids could generate an order of magnitude more electrical power than a conventional well producing steam. The Iceland Deep Drilling Project (IDDP) is a government-industry consortium that has drilled two wells to reach supercritical fluids beneath two operating geothermal fields: the IDDP-1 well at Krafla (2009), and the IDDP-2 well at Reykjanes (2017). Drilling of the IDDP-1 well at Krafla ended prematurely at a vertical depth of 2.1 km when the drill head encountered a layer of rhyolitic melt (Elders et al., 2014). Although subsequent flow tests produced superheated steam at 450°C, the pressure was still subcritical at a depth of 2.1 km. The IDDP-2 well at Reykjanes successfully reached supercritical fluid at a total vertical depth of 4.5 km with fluid temperature of 426°C and a pressure of 34 MPa (Fridleifsson et al., 2017).

Prior to the IDDP project, extensive geophysical exploration had taken place at Krafla. An upper crustal magma body at Krafla was first inferred from the shear wave shadows observed by (Einarsson, 1978). Subsequent studies of seismic refraction (Brandsdóttir et al., 1997) and seismic tomography (e.g. Arnott & Foulger, 1994; Schuler et al., 2015) imaged low P-wave velocity anomalies but no low S-wave anomaly was imaged which would indicate a magma body. Extensive magnetotelluric (MT) exploration has also taken place at Krafla by groups from Moscow State University and Duke University (Onacha, 2006). Árnason et al. (2007) used a one-dimensional (1-D) joint inversion of MT and time domain electromagnetic (TEM) data to obtain a 1-D model of subsurface resistivity. This model imaged an electrically conductive layer in the depth range 2 to 4.5 km depth below the geothermal field that was interpreted as being due to partial melt (Árnason et al., 2007). Two vertical peaks of low resistivity extended upwards from the inferred magma body

in this model (Fridleifsson et al., 2014). IDDP-1 was located between these two peaks with the intention of avoiding regions of partial melt. However, 1-D inversion of MT data is an approximation and does not always yield a correct model of the subsurface resistivity. To validate the 1-D models, three-dimensional (3-D) inversions of the Krafla MT data set were later implemented by a range of authors. Rosenkjaer et al. (2015) compared the resistivity models from three different 3-D inversion algorithms and reported that these models had significant differences despite recovering the same main features. These variations are to be expected due to the different inversion algorithms and the fact that inversions are non-unique and many resistivity models can fit the observed MT data to a given statistical level (e.g. Siripunvaraporn, 2012). In order to assess if 3-D MT inversion provides an improved resistivity model, this paper will compare a new 3-D resistivity model to the 1-D resistivity model of Árnason et al. (2007).

Despite failing to reach supercritical conditions at Krafla, the drilling of the IDDP-1 well gave the opportunity to address important questions about the presence of magma in the crust at shallow depths and the processes that occur as it crystallizes. Although extensive geophysical exploration had been performed at the Krafla geothermal field, the magma body intersected at a depth of 2.1 km had not been imaged geophysically and the well was originally planned to extend to a depth of 4.5 km. Since MT data are sensitive to the presence of aqueous fluids or interconnected melt, it was a surprise to some that the magma body was not detected prior to drilling.

In this paper, we re-examine the Krafla MT dataset by performing a systematic 3-D inversion study. Additional datasets and other constraints can be incorporated into the MT inversion in order to reduce the number of resistivity models that will fit a given MT dataset to a specified statistical tolerance. A range of approaches were investigated, including inversions that started from the 1-D resistivity model of Árnason et al. (2007), in order to include features that have been corroborated by other geophysical methods and drill cuttings from IDDP-1 (Mortensen et al., 2014). In particular three possible reasons for the magma body to go undetected will be investigated in this paper:

(1) the location of the rhyolitic magma beneath a low resistivity clay alteration layer in the geothermal field makes it difficult to be resolved with the MT method;

(2) the rhyolitic magma body intersected by IDDP-1 has a relatively high resistivity and/or is relatively small and does not produce an obvious anomaly in the resistivity model.
(3) the magma body was not detected due to limitations of the 1-D inversion.

A key part of the analysis was to undertake resolution tests to evaluate the sensitivity of the MT data to the size, location and resistivity of the upper crustal magma body. Deeper parts of a resistivity model derived from MT inversion are often less constrained by the data than shallower features. Previous studies have sought to evaluate MT data sensitivity to model features by (1) comparing the calculated data between a preferred resistivity model and an edited model (e.g. Campanyà et al., 2018; Piña-Varas et al., 2018) or; (2) comparing the data misfit of the preferred resistivity model to the data misfit of the edited resistivity model (e.g. Becken et al., 2008; Cordell et al., 2018; Hill et al., 2009). In the first method, if the difference between the two sets of calculated MT data is greater than the data error, then it is assumed that the measured MT data can distinguish between the two models. If the difference is smaller than the data error, then the measured MT data cannot distinguish between the two models, and either model can be considered plausible. However, this method only compares the model responses with no direct reference to the MT data itself. In the second method, the data misfit summary statistics are compared but this method fails to distinguish between up-biasing and down-biasing. As a result, the two misfit values could be similar (or identical) while the two model responses are significantly different from one another. We improve upon both these approaches by applying the two sample Kolmogorov-Smirnov (K-S) statistical test to compare the two sets of residuals (Massey Jr, 1951; Miller & Kahn, 1962). This is another way to compare the data fit between two resistivity models, and is more quantitative than simply comparing the overall r.m.s. (root mean square) misfit of the models.

## 3.2. Krafla volcano and geothermal field

Iceland is located on the mid-Atlantic Ridge between the North American and Eurasian tectonic plates. The tectonic activity and volcanism in Iceland is attributed to the combination of the spreading of the mid-Atlantic Ridge with enhanced melt production that results from interactions of the ridge with a mantle plume (e.g. Allen et al., 1999; Foulger &

Anderson, 2005; Wolfe et al., 1997). The volcanic and rifting activity on Iceland is mostly confined to the neo-volcanic zone, which is a corridor crossing the island in a southwest-to-northeast direction (Figure 3.1). Several studies suggest that there is an anomalous layer with low electrical resistivity, low seismic velocity, and high temperature gradient beneath much of Iceland (Björnsson et al., 2005; Flóvenz & Gunnarsson, 1991; Flóvenz & Saemundsson, 1993). This layer is less than 10 km deep beneath active rift zones, including the Krafla volcanic field, and 20-25 km deep beneath other parts of Iceland (Björnsson et al., 2005). It has been interpreted as a layer of 5-10% mafic melt that accumulates at the base of the crust (Björnsson et al., 2005). Recent laboratory measurements of electrical resistivity show that rocks containing the alteration minerals chlorite and epidote can decrease in resistivity by more than 3 orders of magnitude when heated to above 500°C (Manthilake et al., 2016; Nono et al., 2020). This large decrease in resistivity is due to the destabilization of chlorite and epidote, resulting in the release of conductive aqueous fluids and the formation of interconnected magnetite. Though the cause of this anomalous layer is still under investigation, it seems to be spatially related to the active rift zones in Iceland.

More detailed geophysical studies have taken place at individual volcanic centers in Iceland, including Krafla. The Krafla volcanic field contains a ~10 km diameter caldera that has an age of 110 ka and which is bisected by a NNE-SSW trending fissure swarm (Figure 3.1). The rim is discontinuous and separated by about 3 km east to west due to the spreading of the North American and European plates (~1.9 cm/yr; DeMets et al., 1990) and burial over time (Árnason et al., 2007). Gravity data show an inner caldera, now buried and filled with hyaloclastites (Árnason et al., 2007). The calderas and enclosed fissure swarm represent the Krafla central volcano, the focal area of frequent eruptions. The distribution of volcanic rocks at Krafla is strongly bimodal, with felsic rocks (rhyolites) confined to the central volcano (Gudmundsson, 1998; Jónasson, 2007). Fissure eruptions in the last 3000 years with a recurrence time of approximately 100 to 300 yr have filled the central volcano with basaltic lavas and hyaloclastites, which are porous lavas formed from sub-glacial eruptions (Sæmundsson, 1991). Two major episodes of basaltic fissure eruptions have occurred in recorded history. The first was the 1724-1729 Mývatn Fires and the most recent was the 1975-1984 Krafla Fires (Sæmundsson, 1991). The total horizontal extension in the fissure swarm during the Krafla Fires was about 9 m (E. Tryggvason, 1994). The Krafla central

volcano has also produced occasional silicic eruptions in the last ~100 ka. For example, the outer caldera formation was related to a rhyolite dome and composite welded tuff that erupted 110 ka (Sæmundsson, 1991) and the inner caldera was formed after subglacial eruptions outside the older caldera (Árnason et al., 2007). The origin of bimodal assemblages of rhyolite and basalt at Krafla and across Iceland is unclear; but recent geochemical studies show that Krafla rhyolites form from re-melt of hydrothermally altered basaltic crust (e.g. Elders et al., 2011; Jónasson, 1994; Sigmarsson et al., 1991). The reheating and re-melting of the crust could occur when basaltic melt ascends below Krafla. Einarsson (1978) found areas of high shear wave attenuation (S-wave shadows) below the Krafla volcanic field that were interpreted as a shallow magma body at 3 to 7 km depth. Subsequent seismic tomography studies have shown low P-wave velocity anomalies within the caldera, but no low S-wave anomaly which would indicate a magma body (e.g. Brandsdóttir et al., 1997; Kim et al., 2017; Schuler et al., 2015).

Krafla is well known for its geothermal field characterized by high temperatures (>200°C) at shallow depth. Geophysical exploration at Krafla began in the 1970's in order to understand the structure of the underlying geothermal reservoirs. The Krafla geothermal power station began operation in 1977 and has a current capacity of 60 MWe with 19 production wells as of 2015. The Krafla geothermal field is divided into several subfields based on location, thermo-hydraulic conditions, fluid chemical composition and isotopic content of the thermal water. In this study we will focus on the subfields within the central caldera: the Leirbotnar, Vitismor, Vesturhlidar, and Sudurhlidar subfields (Figure 3.1). In the northern part of Krafla, the Hveragil fault system divides the Vitismor and Leirbotnar fields in the west from the Sudurhlidar field to the east. Vesturhlidar is located in the northern part of Hveragil, east of the Viti crater. The Hveragil fault system appears to be a boundary between distinct thermal conditions and alteration to the east and west. The chlorite-epidote zone is relatively shallow beneath Sudurhlidar (0.2 – 0.3 km a.s.l.), whereas it is 0.2 to 0.3 km b.s.l. beneath Leirbotnar and Vitismor. Temperatures beneath Sudurhlidar and Vesturhlidar at shallow depths (above 0.4 km b.s.l.) are generally higher than those in Leirbotnar and Vitismor (Weisenberger et al., 2015). Temperatures are high enough for a two-phase system beneath Sudurhlidar and Vesturhlidar at shallow depths (~0.2 km b.s.l.) However, beneath Leirbotnar and Vitismor there are two distinct reservoirs: a shallow,

almost isothermal (~200°C) liquid reservoir above ~0.5 km b.s.l., and a deeper two-phase reservoir. Chlorite-epidote alteration in the upper reservoir indicates that a two-phase system existed there in the past. Data from over 40 wells have contributed to the understanding of this complex geothermal field.

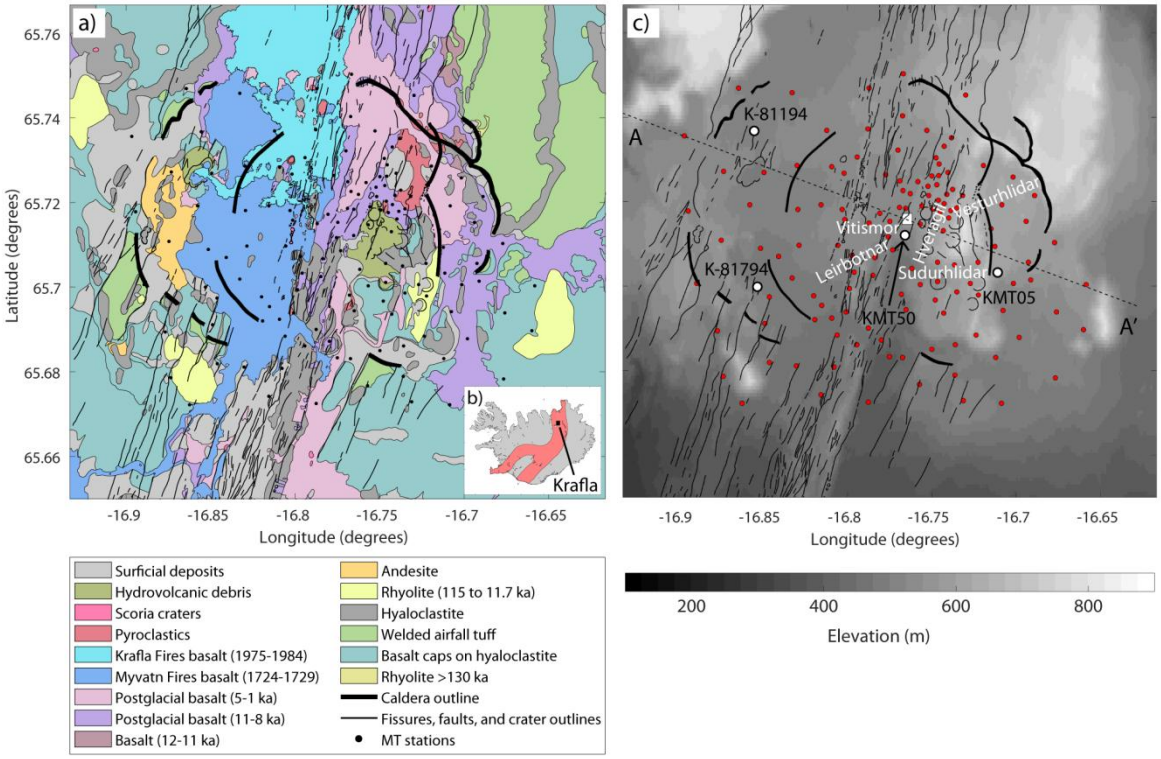


Figure 3.1: a) Geological map of the Krafla volcanic field; b) location of Krafla with the neo-volcanic zone, which is the region of active volcanism on Iceland, shaded in red. c) Topographic map of the Krafla volcanic field with labelled geothermal fields. Thick black lines show fissures and the caldera rims. The outer caldera formed about 110 ka and is ~10 km in diameter, while the inner caldera formed about 80 ka and is filled with hyaloclastites. Red circles are locations of MT stations, and the white square is the location of the IDDP-1 well. White circles are MT stations mentioned in text. A-A' is the profile shown in Figure 3.9. Geological data provided by Iceland GeoSurvey (ÍSOR).

Supercritical fluids may exist at the base of geothermal systems such as Krafla. The Iceland Deep Drilling Project (IDDP) group considered searching for supercritical fluids beneath Krafla partly due to the high temperatures (>300°C) encountered at relatively shallow depth (2 km) (Fridleifsson et al., 2003; Fridleifsson & Elders, 2005). The IDDP

group drilled the exploratory IDDP-1 well in 2009 with the goal of reaching supercritical fluids approximately 4 km below the Krafla geothermal field. However, drilling was prematurely stopped when a layer of rhyolitic magma was encountered at 2.1 km depth (Fridleifsson et al., 2014). The bottom-hole temperature was estimated to be as high as 500°C, corresponding to a superheated reservoir. The recovered cuttings consisted of basaltic lavas and hyaloclastites to a depth of 1.36 km, an intrusive complex of basaltic dykes and dolerite from 1.36 km to 2 km depth, and granophyres and felsites below 2 km (Mortensen et al., 2014).

Prior to drilling IDDP-1, magma was not expected to be found at such a shallow depth, although it was considered a possibility after the nearby well K-39 intersected rhyolitic magma at a total vertical depth of about 2.6 km (Mortensen et al., 2010). Previous 1-D modeling of magnetotelluric (MT) data predicted a low resistivity zone at about 4.5 km depth below Krafla, interpreted as partial melt or aqueous fluids (Árnason et al., 2007; Fridleifsson et al., 2014). It is important to investigate why the 1-D MT modeling did not predict the presence of magma at 2.1 km below Krafla. In the following sections we will use a different approach than previously published work (Árnason et al., 2007; Gasperikova et al., 2015; Rosenkjaer et al., 2015) to model and analyze the Krafla MT data.

## 3.3. Magnetotelluric data at Krafla

### 3.3.1. Background on magnetotellurics

Electrical resistivity (DC) and electromagnetic (EM) methods such as the time domain electromagnetic method (TEM) and magnetotellurics (MT) are used to map variations in electrical resistivity. MT is distinct from other EM methods because it is able to measure signals in a broad frequency range of the EM spectrum (~$10^4$ - $10^{-5}$ Hz). The exploration depth of MT data depends on the signal frequency. Audio (high) frequency MT equipment is suitable for shallow surveys, and long period (low frequency) MT is suitable for deeper exploration. Broadband MT equipment measures signals in the intermediate frequencies and can be used effectively in both cases. MT is particularly useful in volcano and geothermal studies because it can detect resistivity variations due to water content, low temperature (< 220°C) alteration and partial melt that typically have a low resistivity

compared to the host rock (e.g. Árnason et al., 2010; Bibby et al., 2009; Cumming & Mackie, 2010). The MT method measures naturally-occurring EM signals to image the electrical resistivity of the Earth. High frequency signals (>1 Hz) originate from worldwide lightning storms, and low frequency signals (<1 Hz) are derived from interactions of the solar wind with the Earth's magnetosphere. When an EM wave reaches the surface of the Earth, it is refracted vertically downward, diffuses into the ground, and decays as a function of the signal frequency $f$ and the resistivity of the Earth ($\rho$). A proxy for the depth of investigation is given by

$$\delta \approx 503 \sqrt{\frac{\rho}{f}} \tag{3.1}$$

where δ is the so-called skin depth in metres, $\rho$ is the Earth resistivity in Ωm, and $f$ is signal frequency in Hz. Each MT station records time series with five channels of data: two orthogonal electric field components ($E_x$, $E_y$) and three orthogonal magnetic field components ($H_x$, $H_y$, $H_z$), where the $x$, $y$, and $z$ directions are geographic north, geographic east, and vertically downward, respectively. The Fourier transformed horizontal components of the electric and magnetic fields are used to calculate the impedance tensor, $Z$ as function of frequency or period which is defined as:

$$\begin{bmatrix} E_x \\ E_y \end{bmatrix} = \begin{bmatrix} Z_{xx} & Z_{xy} \\ Z_{yx} & Z_{yy} \end{bmatrix} \begin{bmatrix} H_x \\ H_y \end{bmatrix} \tag{3.2}$$

The impedance contains information about the spatial distribution of electrical resistivity in the Earth. In the 3-D case the electrical resistivity varies in the $x, y, z$ directions and the four components of the impedance tensor are non-zero. The complex impedance tensor is commonly expressed in terms of apparent resistivity and phase angle. The apparent resistivity, $\rho_{ij}$, is calculated with:

$$\rho_{ij} = \frac{\left|Z_{ij}\right|^2}{2\pi f \mu_0} \tag{3.3}$$

where $\mu_0$ is the magnetic permeability of free space, and $i, j$ are the components of the impedance tensor, $Z$. Apparent resistivity is a volume-averaged resistivity in Ωm; the lower the frequency, the greater the depth that is sampled. The phase, $\varphi_{ij}$, is defined as:

$$\varphi_{ij} = \tan^{-1}\left[\frac{Im(Z_{ij})}{Re(Z_{ij})}\right] \tag{3.4}$$

where $Im(Z_{ij})$ and $Re(Z_{ij})$ are the imaginary and real parts of $Z_{ij}$, respectively. The phase angle is commonly expressed in the first quadrant ($0° \leq \varphi \leq 90°$) such that it indicates whether apparent resistivity increases ($\varphi_{ij} < 45°$) or decreases ($\varphi_{ij} > 45°$) as frequency decreases. Apparent resistivity and phase, when viewed over a range of frequencies, are useful to study resistivity changes due to changes in geology and rock properties.

Vertical magnetic field transfer function (tipper) data relate the vertical magnetic field $H_z$ to the two horizontal magnetic field components. Tipper data contain information about spatial resistivity variations but electric field data are needed to constrain absolute resistivity values. These tipper data provide complementary information to the impedance data, but were not used in this study due to the reasons discussed below.

### 3.3.2. Description of Krafla MT data

A total of 163 MT stations were collected at the Krafla volcanic field during campaigns conducted by Duke University (2004-2005) and Moscow State University and Iceland GeoSurvey (ÍSOR; 2006 and 2008). The data consist of broadband MT soundings in the frequency ranges of 320 – 0.001 Hz. Time domain electromagnetic (TEM) data were also collected to correct galvanic distortion caused by localized, near-surface resistivity anomalies. We used 133 of the original 163 MT stations in our 3-D inversion due to practical considerations that will be described in detail in the next section. The selected stations are shown in Figure 3.1. Tipper data were available for 35 out of the 133 selected MT stations. However, we did not include these data in our inversion because many of these stations had significant noise in the tipper in the 10 - 0.001 Hz range. Although we do not have access to the MT time series data, we believe that signals from the nearby Krafla power plant infrastructure may have contaminated the vertical magnetic field data. In future work it may

be useful to reprocess the tipper data because they provide information on lateral resistivity variations.

Prior to inverting the data, it is useful to analyze qualitative trends in the measured MT data. Figure 3.2, Figure 3.3, Figure 3.4, and Figure 3.5 show map views of the apparent resistivity and phase data ($xy$ component, $yx$ component, and computed from determinant of impedance) over a range of frequencies. In Figure 3.2 data at 40 Hz is shown, and at this high frequency, the data are sensitive to the near-surface ( < 1 km) resistivity structure of the Krafla volcanic field. Areas with low apparent resistivity correspond to the shallow clay layer (smectite/zeolite), and areas with higher apparent resistivity ( >100 Ωm) correspond to basalt and hyaloclastites (e.g Árnason et al., 2010). At 40 Hz most of the phase data outside of the clay layer is greater than 45°, corresponding to a decrease in apparent resistivity with depth as the data begin to image structure below the resistive surface basalt.

Figure 3.3 shows the same quantities at a frequency of 0.3 Hz. Data at this frequency have similar spatial variations as in Figure 3.2; however, the phases are lower which indicates that resistivity is no longer decreasing as a function of (decreasing) frequency (increasing period). At frequencies of 40 and 0.3 Hz the outline of the inner caldera appears as an abrupt resistivity contrast. Low resistivity inside the inner caldera corresponds to subglacial hyaloclastite, and high resistivity outside the inner caldera corresponds to basaltic lava filling in the outer caldera.

Figure 3.4 shows a map view of the apparent resistivity and phase data at a frequency of 0.037 Hz, which corresponds to the upper few kilometres below the volcanic field. At 0.037 Hz the low apparent resistivity beneath the shallow clay cap is likely associated with a magmatic heat source and/or elevated concentrations of aqueous fluids. The high apparent resistivity within the geothermal field inside the inner caldera corresponds to chlorite-epidote alteration minerals stable at 220 to 500°C. The phase data are mostly greater than 45°, indicating that the apparent resistivity is decreasing with depth.

Figure 3.5 shows the apparent resistivity and phase for a frequency of 0.0092 Hz which show a deep conductor below Krafla. Most stations have a low apparent resistivity and phase greater than 45° at this frequency. This may correspond to the regional conductor beneath Iceland observed by Björnsson et al. (2005).

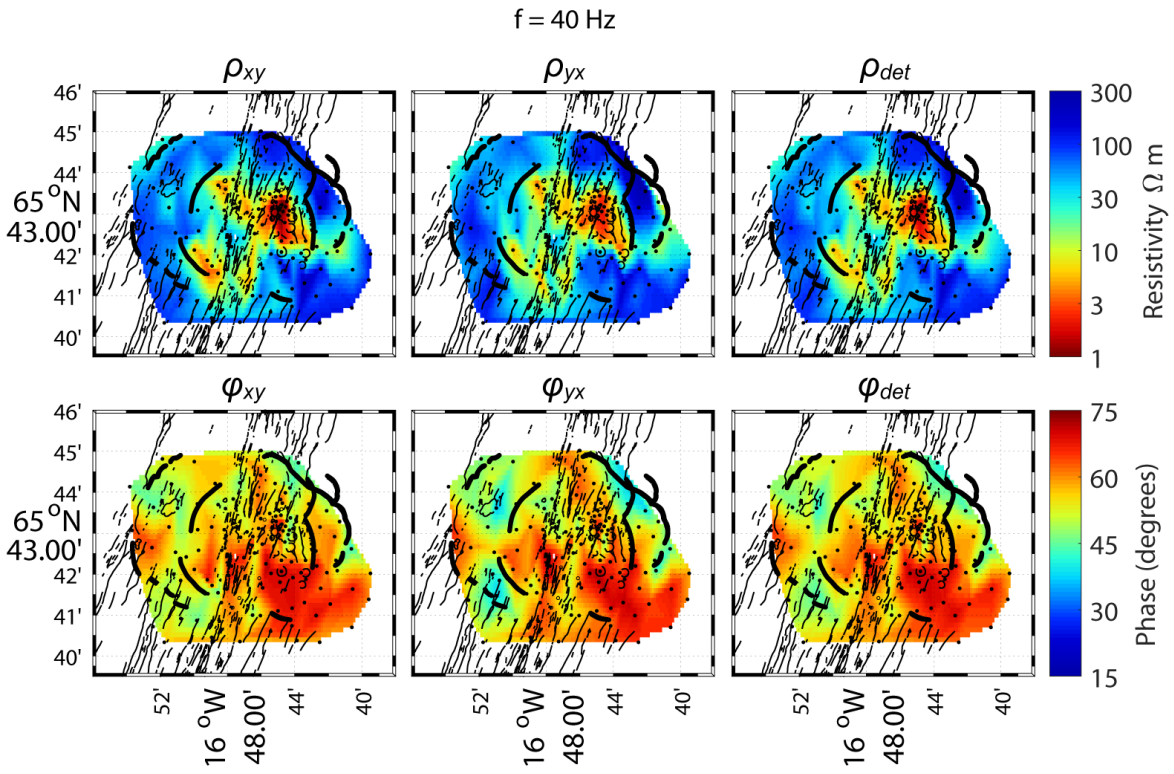


Figure 3.2: Map view of the Krafla MT apparent resistivity ($\rho$) and phase ($\varphi$) data at a frequency of 40 Hz. $xy$ = electric field oriented geographic north and magnetic field oriented geographic east; $yx$ = electric field oriented geographic east and magnetic field oriented geographic north; $det$ = quantity derived from determinant of MT impedance data. These data are sensitive to the near-surface ( <1 km) and reveal lateral variations in resistivity in the Krafla volcanic field. The apparent resistivity data show low resistivity areas that correspond to the shallow clay layer (smectite/zeolite) and high apparent resistivity ( >100 Ωm) areas of near-surface basalt and hyaloclastites. The phase data show a more complicated pattern; but the phase across most of the volcanic field is greater than 45°, corresponding to a decrease in resistivity as the data begin to probe the underlying geothermal reservoirs. Thick black lines = outline of inner and outer caldera; thin black lines = fissures and craters; filled black circles = MT stations with data at this frequency; open circles = MT stations with no data at this frequency.

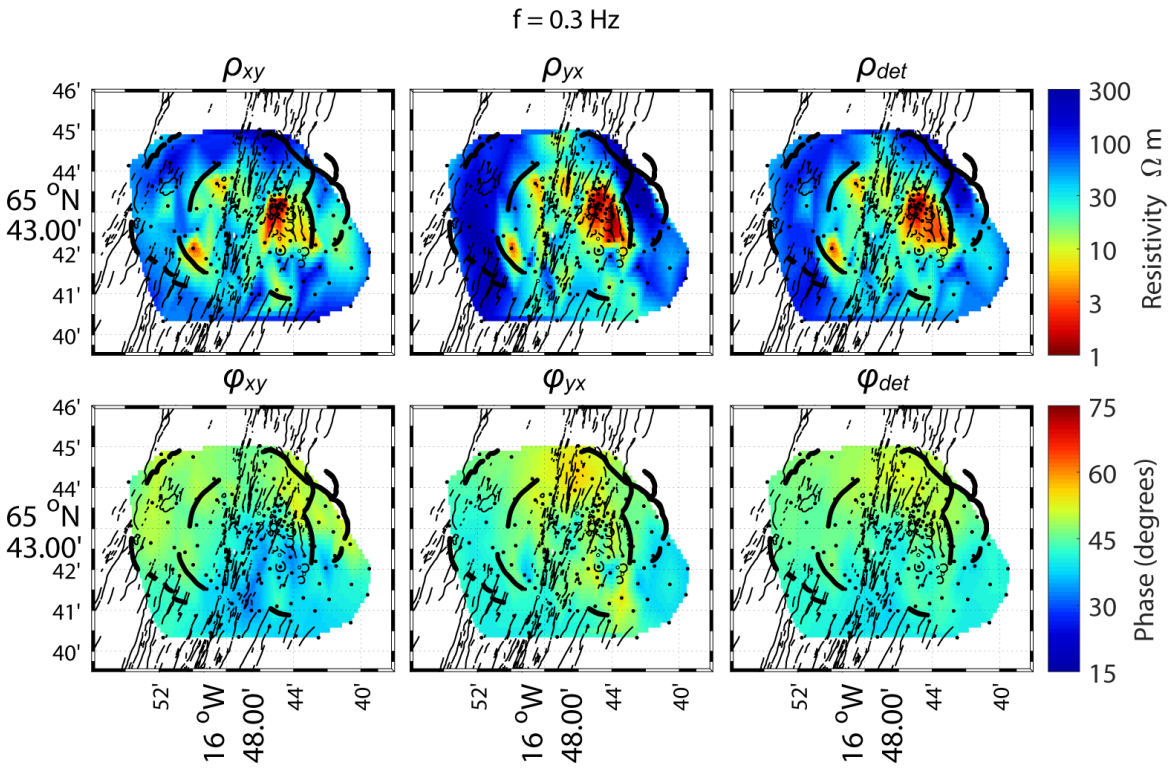


Figure 3.3: Map view of the Krafla MT apparent resistivity ($\rho$) and phase ($\varphi$) data at a frequency of 0.3 Hz. $xy$ = electric field oriented geographic north and magnetic field oriented geographic east; $yx$ = electric field oriented geographic east and magnetic field oriented geographic north; $det$ = quantity derived from determinant of MT impedance data. Data at this frequency has similar spatial variations as in Figure 3.2; however the phases are lower which indicates that resistivity is no longer decreasing as a function of frequency. The inner caldera outline separates low resistivity in the subglacial hyaloclastite fill from high resistivity basaltic subaerial lavas in the outer caldera. Thick black lines = outline of inner and outer caldera; thin black lines = fissures and craters; filled black circles = MT stations with data at this frequency; open circles = MT stations with no data at this frequency.

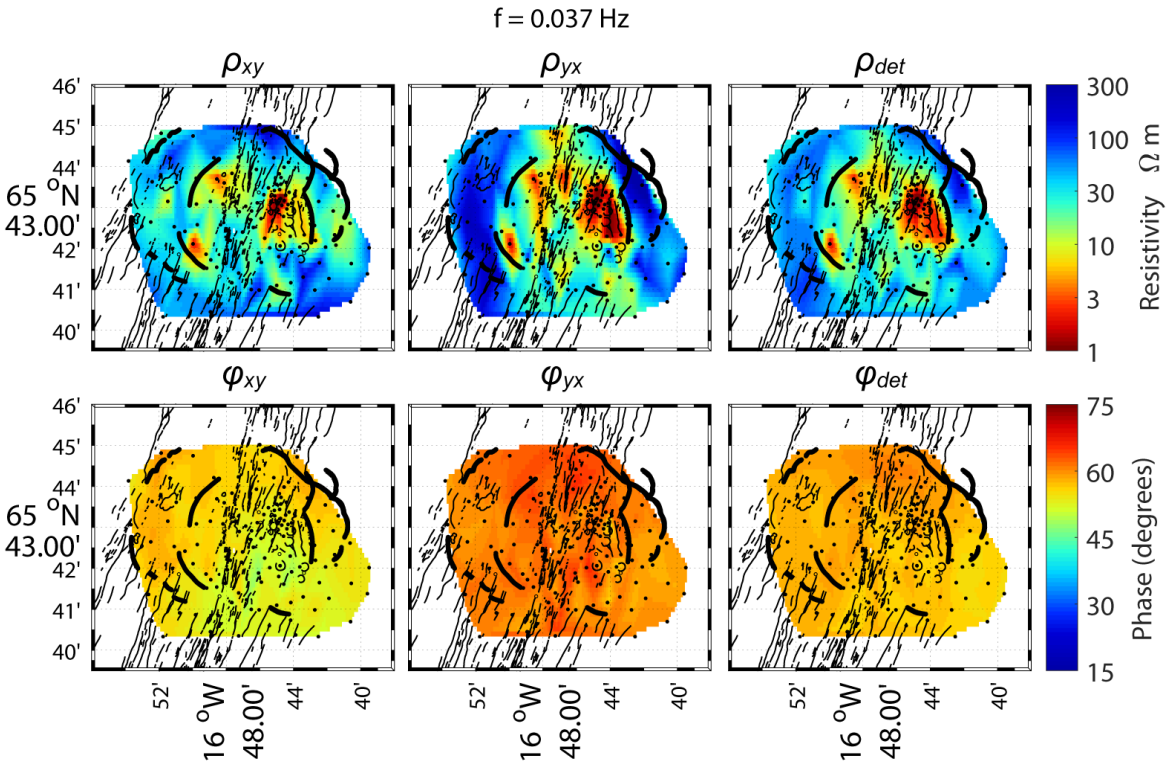


Figure 3.4: Map view of the Krafla MT apparent resistivity ($\rho$) and phase ($\varphi$) data at a frequency of 0.037 Hz. $xy$ = electric field oriented geographic north and magnetic field oriented geographic east; $yx$ = electric field oriented geographic east and magnetic field oriented geographic north; $det$ = quantity derived from determinant of MT impedance data. These data are sensitive to the upper few km below the Krafla volcanic field. The apparent resistivity data show a low resistivity feature beneath the east part of the inner caldera and a high resistivity beneath the middle of the inner caldera. The phase data are mostly greater than 45°, indicating that the apparent resistivity is decreasing with depth as most MT stations begin to detect a conductor at the root of the geothermal system. Thick black lines = outline of inner and outer caldera; thin black lines = fissures and craters; filled black circles = MT stations with data at this frequency; open circles = MT stations with no data at this frequency.

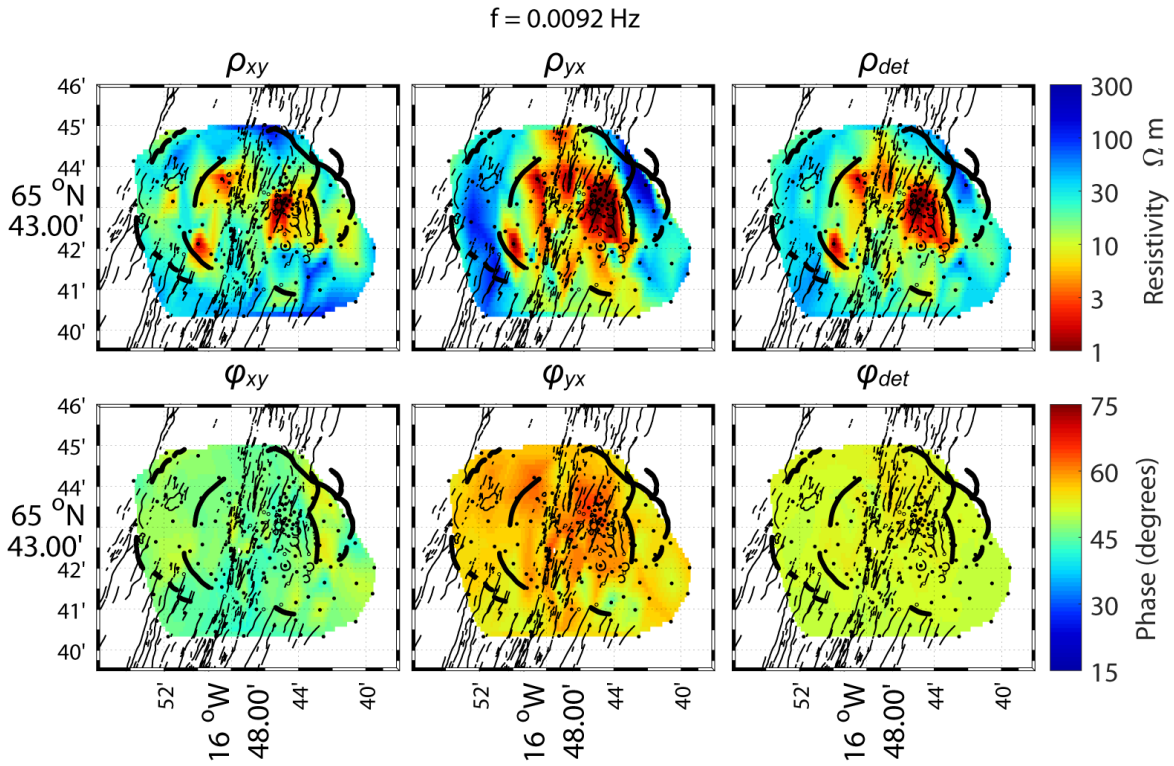


Figure 3.5: Map view of the Krafla MT apparent resistivity ($\rho$) and phase ($\varphi$) data at a frequency of 0.0092 Hz. $xy$ = electric field oriented geographic north and magnetic field oriented geographic east; $yx$ = electric field oriented geographic east and magnetic field oriented geographic north; $det$ = quantity derived from determinant of MT impedance data. Most stations have a low apparent resistivity and phase greater than 45°. This may correspond to the deep regional conductor beneath Iceland observed by Björnsson et al., (2005). Thick black lines = outline of inner and outer caldera; thin black lines = fissures and craters; filled black circles = MT stations with data at this frequency; open circles = MT stations with no data at this frequency.

Figure 3.6 shows examples of apparent resistivity and phase curves for four stations at Krafla (see Figure 3.1 for station locations). Stations K-81194 and K-81794 are located in the outer caldera in the west part of the Krafla volcanic field. These two stations exhibit similar apparent resistivity and phase curves. At high frequencies the slightly decreasing apparent resistivity indicates shallow moderately low resistivity. 1-D inversion of TEM data (Árnason et al., 2007) shows much higher resistivity in this area than inside the inner caldera. Stations KMT05 and KMT50 are located on the eastern and central parts of the calderas, respectively. These stations exhibit a more dramatic decrease in apparent resistivity at high

frequencies, corresponding to a thicker clay layer. At intermediate frequencies, all four stations increase in apparent resistivity with decreasing frequency as the data are sensitive to the resistive chlorite-epidote alteration products. At low frequencies the data show a decrease in apparent resistivity which may be a deeper magma body or regional conductor beneath Krafla.

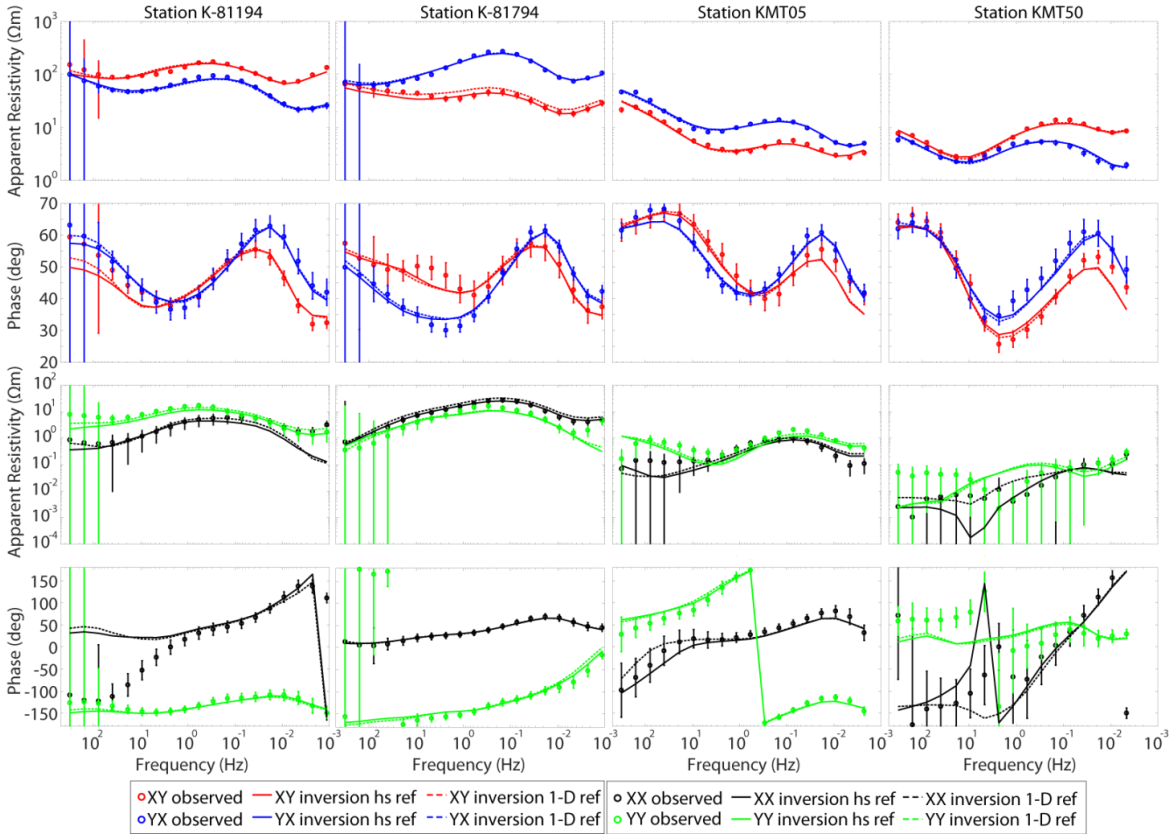


Figure 3.6: Selected apparent resistivity and phase curves from stations K-81194, K-81794, KMT05, and KMT50. See Figure 3.1 for station locations. Symbols with error bars are the measured MT data and solid lines represent the unconstrained inversion response. Red= $xy$ component data; blue = $yx$ component data; black = $xx$ component data; green = $yy$ component data.

The phase tensor, which is independent of local distortions of the electric field, is also a useful tool in evaluating MT data because it can estimate the data dimensionality and direction of the geoelectric strike (Caldwell et al., 2004). The minimum phase tensor value, maximum phase tensor value, and skew angle are three coordinate invariants of the phase tensor that can be represented as a colored ellipse. When shown in map view, a predominant geoelectric strike direction can be inferred from the elongated ellipses that align to the

preferred flow direction of electric current. The skew angle ($\beta$) represents the asymmetry of the phase tensor due to a 3-D resistivity distribution. Large skew angles are indicative of a 3-D resistivity distribution; however, small skew angles do not necessarily preclude one (Booker, 2014). Here we show maps of phase tensors to help understand the directionality and dimensionality of resistivity structures at Krafla. Figure 3.7 shows a map view of phase tensor ellipses at four frequencies. For each frequency, each station is represented by a colored ellipse. The ellipse axes are proportional to the maximum and minimum values of the phase tensor, and the color indicates the absolute value of the skew angle. Note that the size of each ellipse is normalized by its maximum phase tensor value. A polar histogram that shows the major axis direction for each station is also shown for each frequency. At 40 Hz the data at each station are sensitive only to near surface structure and there is some variation in strike direction from station to station. However, many stations have a strike direction of approximately N20°E at this frequency, which agrees with the direction of the fissure swarm. At a frequency of 0.3 Hz there is no clear predominant strike direction, and many stations have a skew angle greater than 3° which is indicative of 3-D resistivity structures at this frequency. At frequencies of 0.037 Hz and 0.0092 Hz the alignment of the ellipses with the NNE-SSW direction of the fissure swarm and low skew angles suggest that the MT data are relatively 2-D at lower frequencies. Note that in the 2-D case the phase tensor major axes are aligned either parallel or perpendicular to the strike direction. At low frequencies, the phase tensor major axes align in the direction of the rifting at Krafla because the phase data begin to detect a resistive feature beneath the deep conductor (e.g. station data curves in Figure 3.6). Overall the phase tensors and apparent resistivity indicate a relatively complicated resistivity structure beneath Krafla that requires a 3-D approach to model the 3-D resistivity structure at intermediate frequencies.

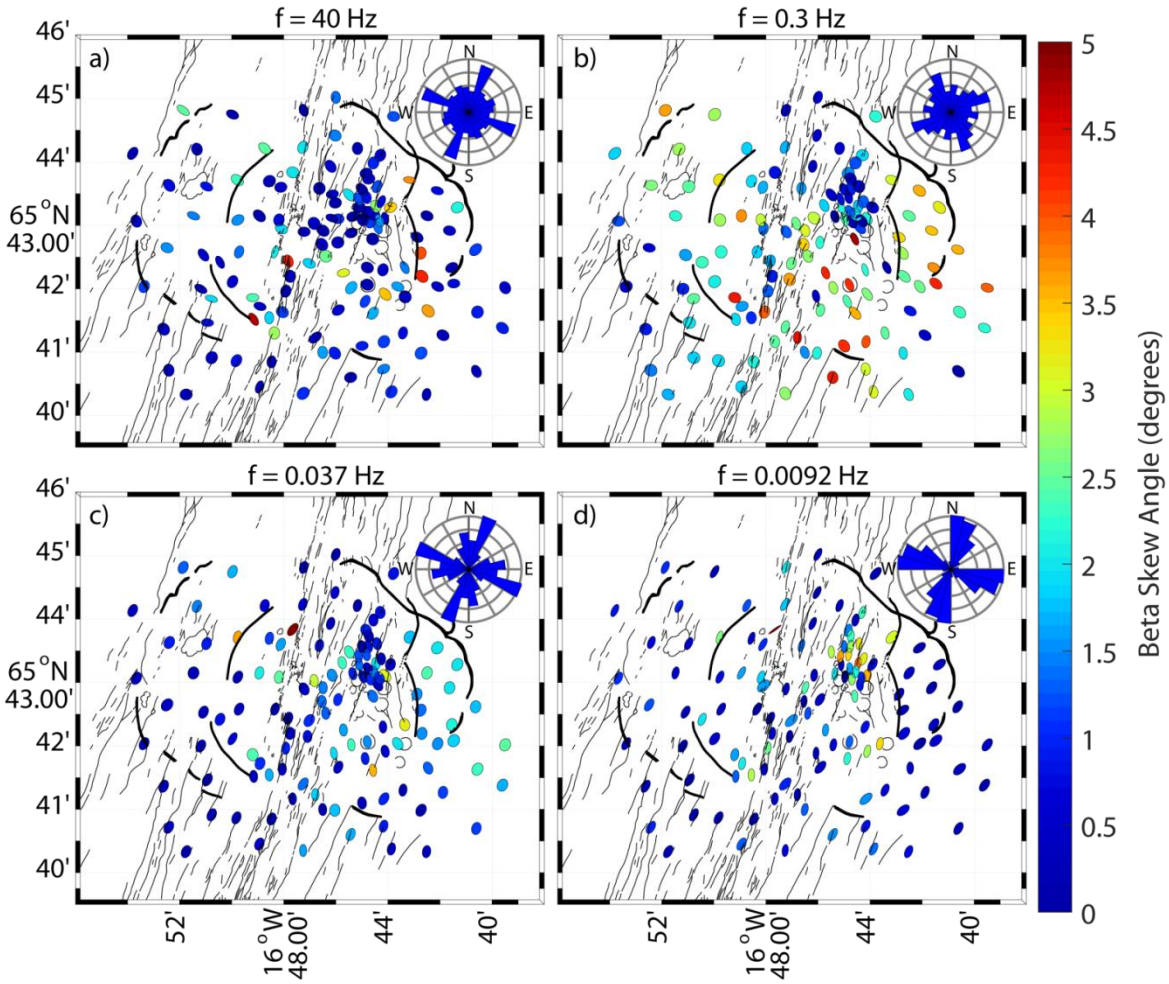


Figure 3.7: Map view of Krafla MT phase tensor ellipses at 4 frequencies. Inset polar histograms show the major and minor axis directions of phase tensor ellipses for all stations. Grey circles in the histograms are increments of 10 stations, with the largest circle for 40 stations. The major axis direction indicates the strike direction, i.e. the preferred direction of electric current flow. At 40 Hz there is some variation in strike direction from station to station because the data are only sensitive to shallow depths, yet there is a pronounced N20°E strike direction that agrees well with the mapped fissures. At a frequency of 0.3 Hz there is no clear predominant strike direction. Many stations have a skew angle greater than 3° which is indicative of 3-D resistivity structure at this frequency. At frequencies of 0.037 Hz and 0.0092 Hz the alignment of the ellipses with the NNE-SSW direction of the fissure swarm and low skew angles suggest that the data are relatively 2-D at lower frequencies.

As described in the previous section, Árnason et al. (2007) performed joint 1-D TEM-MT inversions on 125 MT stations that were corrected by nearby TEM soundings and presented the resulting resistivity model as interpolated horizontal and vertical cross sections.

In this paper we show selected slices through the interpolated 1-D resistivity model in Figure 3.9 and Figure 3.10. A 1-D inversion only accounts for resistivity variations with depth at each MT station and may be inaccurate in more complex geological settings. A 3-D inversion does not require any assumptions about the subsurface resistivity distribution. However, in consideration of the large amount of data and model parameters, along with numerous settings that control the inversion algorithm, some care is required in order to obtain a satisfactory result (e.g. Miensopust, 2017; Siripunvaraporn, 2012). In practice, a different resistivity model can be obtained from the inversion simply by choice of data frequencies or size of the cells in the model, among other parameters. Many inversion settings and parameters should be tested to understand the consistency and reliability of the inversion results. In the case of the Krafla MT dataset, Gasperikova et al. (2015) and Rosenkjaer et al. (2015) presented resistivity models obtained from three 3-D inversion algorithms. The three models contained the same main features but had significant differences. The main features of the resistivity models are:

At shallow depths (< 2 km below surface) resistivity values agree well with the expected alteration mineralogy. High resistivity values (>1000 Ωm) are correlated with unaltered basalt that fills the Krafla outer caldera and low resistivity values in the inner caldera are associated with a shallow clay layer.

Smectite alteration occurs in the temperature range 100 to 220°C and results in a low resistivity (<10 Ωm) clay layer in the upper 500 m.

At the base of the clay layer, relatively resistive (100 – 1000 Ωm) chlorite and epidote alteration minerals stable at temperatures of 220 to 500°C.

A conductive (<10 Ωm) domed feature at a depth of ~2.5 km beneath the Krafla caldera was interpreted as a magma body/intrusion.

## 3.4. New approach to the Krafla 3-D magnetotelluric inversion

### 3.4.1. Inversion details

Unlike 1-D and 2-D MT inversion algorithms, 3-D inversion algorithms do not require assumptions about the dimensionality of the Earth's electrical resistivity. 1-D and 2-D inversions are computationally inexpensive and provide valuable information, but may not

be appropriate for complex geological settings. Apparent resistivity and analysis of phase tensors in the previous sections suggest that a 3-D inversion is appropriate for the Krafla MT dataset.

Our first step in the process of inverting the MT data was to select a subset of the data for inversion. Ideally, the inversion needs a set of MT stations that are uniformly distributed on the surface and that sample the entire area of interest. In model discretization there should not be more than one MT station in each model cell, and there should be a few model cells between each pair of MT stations. This ensures that the inversion is able to place resistivity variations between stations, particularly when there are small, near-surface features. There is a trade-off between including more data/model cells and incurring a higher computational cost because the computational cost of an inversion depends on the number of data points and model cells. At Krafla the distance between neighboring MT stations ranges from 100 m to more than 1 km. In the case of two stations that were less than about 300 m apart, we excluded the station with lower-quality MT data in order to remove redundant data and to minimize the number of model cells. Our model mesh includes topography and contains 119 cells in the north-south direction, 142 in the east-west direction, and 84 in the vertical direction. Layers above sea level have a thickness of 40 m, and the first layer beneath sea level has a thickness of 30 m that increases by a factor of 1.1 for each subsequent layer. The core mesh contains 100 m by 100 m horizontal cells to allow room for multiple model cells between each station.

In addition to spatial sampling, data frequency selection is an important step prior to the inversion. We selected 19 frequencies, logarithmically spaced, from 320 to 0.00114 Hz. The highest and lowest frequencies will determine the smallest and largest resolvable depths, respectively. For example, following Equation (3.1), in a 10 Ωm half-space the highest frequency of 320 Hz will penetrate about 90 m into the subsurface, and the lowest frequency of 0.00114 Hz will sample to a depth of 46 km. We included 19 frequencies in order to accurately represent the smooth variations of impedance as a function of frequency.

Each datum in the inversion must be assigned an error (uncertainty) estimate. This value is important as the inversion seeks a solution to minimize the misfit of each datum. Large error estimates may cause the inversion to inadequately fit the measured data; error estimates that are too small may cause noise to be fit and result in a rough model. The

standard impedance errors obtained from time-series processing may be very small compared to the impedance values (<1 %) and it may be necessary to apply an error floor in order to obtain a satisfactory inversion result. In our inversion we applied an error floor equal to 5% of $\sqrt{|Z_{xy}Z_{yx}|}$.

It is important to consider the effects of galvanic distortion on the measured MT data. Galvanic distortion is caused by local distortions of electrical current from either (1) near-surface features smaller than the resolvable limit of the MT data, or (2) extreme topographic relief. Several methods to determine galvanic distortion in the electric field define a 2 x 2, frequency independent distortion tensor (e.g. Bahr, 1988; Groom & Bailey, 1989). The Groom & Bailey (1989) tensor decomposition method factors the distortion tensor into four components: (1) the twist and (2) shear tensors that modify impedance amplitudes and phases, (3) the anisotropy tensor that modifies amplitudes, and (4) the scalar gain that modifies amplitudes. When the Earth has a 2-D regional geologic strike and 3-D distorting bodies, the twist and shear tensors can be solved but anisotropy and gain (together commonly called "static shift") cannot be uniquely determined. In a 3-D Earth where all elements of the impedance tensor are significant, different approaches must be used. There has been some debate about how to handle galvanic distortion in the 3-D inversion of MT data (Miensopust, 2017). The unknown scalar shifts at each MT station can be solved by jointly inverting MT and TEM data (e.g. Árnason et al., 2010). Alternatively, the distortion tensor can be simultaneously inverted with the MT impedance (e.g. Avdeeva et al., 2015; Y. Sasaki & Meju, 2006; Usui et al., 2016). Even if distortion is not explicitly handled in the inversion, Patro & Egbert (2011) found that for moderately distorted data (e.g. no out-of-quadrant phases or mode splits of several orders of magnitude) the 3-D inversion placed small, near-surface features into the model to accurately reproduce distortion in the MT data. We chose to implicitly allow distortion in our model by designing our mesh to contain 2 to 3 small (100 m by 100 m) cells between each MT station. These small cells allow the inversion to place small, distorting features into the resistivity model.

A number of inversions were undertaken to determine the optimal regularization parameters, starting model and prior model. The ModEM 3-D inversion algorithm that we used contains a model covariance matrix that controls the change in resistivity (spatial

smoothing) between neighboring model cells (Kelbert et al., 2014). This allows the user to specify the smoothing constraints in three spatial directions. We varied the degree of smoothing in test inversions, but in every inversion we applied the same model covariance length scale value in each spatial direction. The ModEM algorithm attempts to minimize differences in resistivity between the recovered model and the prior model. In this section we test if the recovered resistivity model is dependent on our choice of prior models with two representative inversions:

- A uniform starting and prior model
- A uniform starting model with interpolated 1-D prior model.

### 3.4.2. Inversion with uniform starting and prior model

This inversion used a 10 Ωm half-space starting and prior model. We tested other resistivity values and found that the inversion with the 10 Ωm halfspace resulted in good data fit and a model with reasonable structure at all depths. We used the ModEM code of Kelbert et al. (2014) to invert the full impedance tensor (8 components). After 98 iterations the inversion converged to an overall r.m.s. misfit of 1.04. Figure 3.6 shows the measured and calculated data for 4 selected stations (see Figure 3.1). The data fit was relatively uniform for all stations and frequencies with no significant outliers (see Figure 3.8). In particular, the low r.m.s. misfit at high frequencies suggests that the inversion adequately fit the MT data with static shifts. Figure 3.9 and Figure 3.10 show selected slices through the resistivity model; we will discuss model interpretation in the next section.

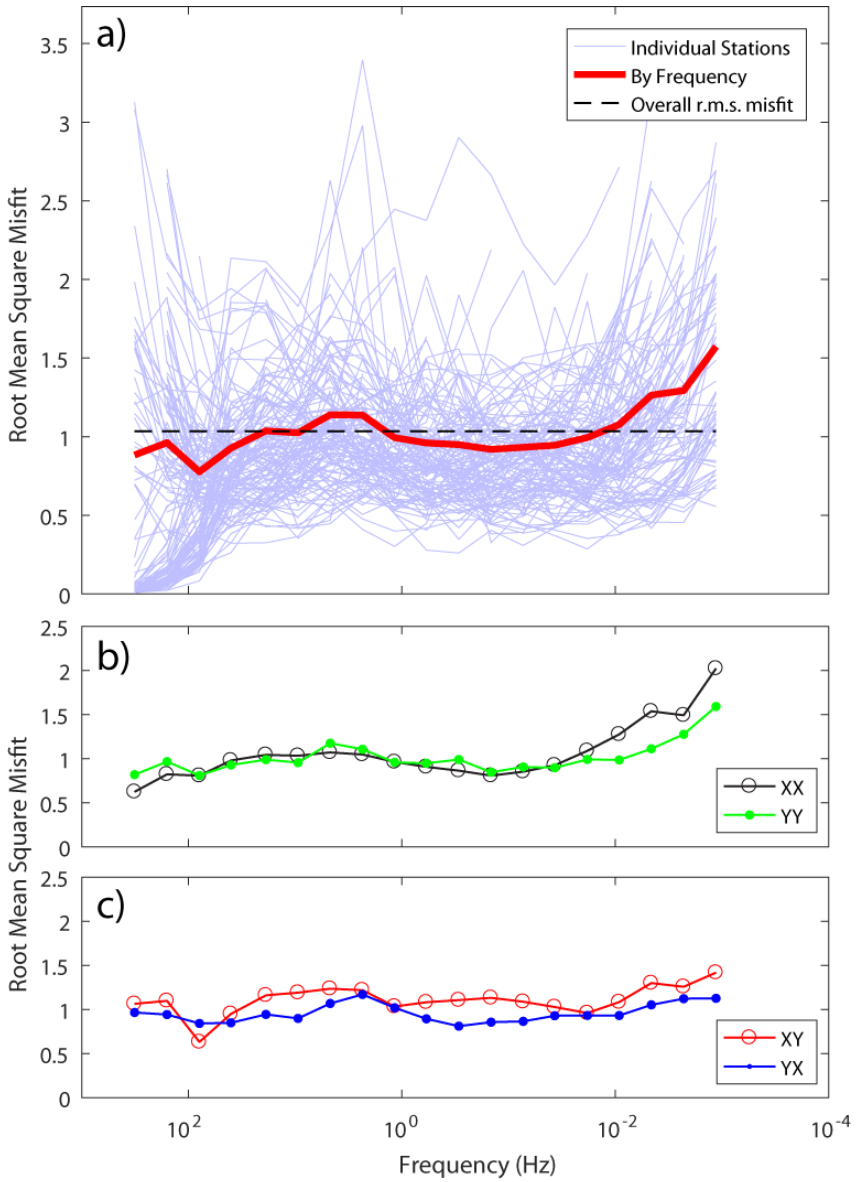


Figure 3.8: Root mean square (r.m.s.) misfit of the measured and calculated MT data from the unconstrained 3-D inversion. a) r.m.s. misfit by frequency for each individual station; the overall misfit for each frequency and the overall inversion misfit are shown in red and dashed black lines, respectively. b) diagonal and c) off-diagonal impedance components r.m.s. misfit by frequency.

We performed different inversions to test whether or not the main resistivity features in the model were strongly dependent on the inversion settings. If the resistivity and spatial extent of a model feature greatly varies from changing one setting, then it may not be well-constrained by the MT data. In these tests we considered the inversion that used a 10 Ωm half-space starting and prior model. We tried changing the model covariance setting to see if

any model features would significantly change. Figure A.1 shows the diagonal slice A-A' through the unconstrained inversion resistivity models with covariance length scale values of 0.1, 0.3, and 0.5. Note that the effect of changing the model covariance values, which control the smoothing between neighboring model cells, depends on the size of cells in the mesh. Slezak et al. (2018) tested multiple covariance length scale values in their ModEM MT inversions and found that values that were too small resulted in resistivity models that only contained heterogeneities near the surface. We observed a similar effect in the Krafla MT inversion, where the resistivity model obtained from a covariance value of 0.1 did not contain much detail at greater depth. It is clear from Figure A.1 that the covariance setting of 0.1 is not within the optimal range for our data and mesh. Thus it is important to test a range of model covariance values to find an optimal value for a particular set of data and mesh. The optimal model covariance (smoothing) parameter was set to 0.3 in each direction ($x$, $y$, and $z$) and used for all inversions.

### 3.4.3. Inversion with uniform starting model and 1-D prior model constraint

The inversion of MT data is inherently non-unique. By changing the inversion parameters and regularization, a broad range of models can be obtained that all fit the measured data. In the absence of any *a priori* geological information, the resulting 3-D resistivity model can also be influenced by the choice of the starting model. For example, if a half-space of constant resistivity is chosen as the starting model to emphasize model smoothness, the inversion is free to fit the observed MT data with resistivity structure that may not be geologically reasonable. In the case of Krafla, there is a significant amount of geophysical and geological information that can help to constrain the 3-D MT inversion toward a more reasonable result. Gravity, shear wave attenuation, seismic tomography, and MT studies at Krafla have all given evidence for a magma body located at about 3 km depth beneath the Krafla central volcano. The presence of the magma body is confirmed by several methods and can be included as *a priori* information in the 3-D MT inversion. We chose to incorporate the deep magma body and other features such as the shallow clay layer, in the form of the 1-D MT models presented by Árnason et al. (2007). Although few geological environments can truly be considered 1-D, the 1-D analysis provides information about how resistivity varies with depth. We interpolated the 125 1-D resistivity models onto a 3-D mesh

to create a prior model for the 3-D MT inversions. A slice through the prior model is shown in Figure 3.9. The r.m.s. misfit between the measured MT data and the MT data calculated from the interpolated 1D resistivity model is 7.55. This is a relatively high misfit which shows that the interpolated 1-D model does not fit the MT data when considering three spatial dimensions. However, the 1-D prior model can be a useful constraint by limiting deviations in the model from known structures such as the shallow clay layer and deeper conductor.

Apart from the change in prior model, the inversion used identical parameters to the unconstrained inversion discussed in Section 3.4.2. The r.m.s. misfit between the observed and calculated data converged to a value of 1.05. Even with the interpolated 1-D model as the prior model, the constrained inversion recovered a very similar model to the unconstrained inversion. The differences between the two models will be discussed in the next section.

## 3.5. Resistivity model interpretation

The unconstrained and constrained inversion models in Figure 3.9 and Figure 3.10 contain similar features, which are summarized below.

### 3.5.1. Resistivity model features

*C1: Shallow low resistivity layer*

The low resistivity layer C1 is a prominent feature in the two inversion models. Clay minerals such as smectite are common low-temperature (100 to 220°C) hydrothermal alteration products and are the cause of the low resistivity of this feature. Smectite has a very high cation exchange capacity (CEC) and as a result, a low resistivity. The smectite zone (or smectite/chlorite mixed layer) in our model appears as a low resistivity layer that extends to a depth of about 0.3 km a.s.l., which is coincident with the depth where chlorite was first observed in the IDDP-1 log (Mortensen et al., 2014).

Due to the diffusive nature of the EM signals measured by MT, there is non-uniqueness in resolving multiple low-resistivity layers (Simpson & Bahr, 2005). In our model, C1 could prevent the detection of deeper features because it is a low resistivity clay layer with a thickness of a few hundred meters and a resistivity of 1 – 10 Ωm. We can estimate the integrated conductivity (i.e. conductance) of C1 to find the minimum

conductance a deeper conductor would need in order to be resolved. Figure 3.11 shows the conductance from the surface of the model to an elevation of 0.2 km b.s.l. (about 0.6 km beneath the IDDP-1 well pad). The conductance map shows a high conductance ( > 300 S) within the inner caldera that coincides with the conductive clay layer. The conductance varies laterally because C1 does not have a uniform thickness. From this map we can estimate that a deeper low resistivity feature needs a conductance greater than 300 S to be resolved in the resistivity model.

*R1: High-temperature reservoir/ chlorite-epidote alteration zone*

This feature extends from a depth of about 0.1 to 1 km below sea level beneath the Vitismor field. Temperature logs of wells in the Vitismor field reveal that the current reservoir temperature at depths 0.1 to 0.7 km b.s.l. is isothermal and about 200°C (Figure 3.12). Analysis of drill cuttings performed by Mortensen et al. (2014) indicates that the top of R1 coincides with the transition into the chlorite-epidote alteration zone where the formation temperature once exceeded 220°C. Although high temperature fluids may be attributed to high resistivity (e.g. Ucok et al., 1980; Ussher et al., 2000) this cannot be the case here because the upper reservoir temperature of Vitismor is only about 200°C. This observation is consistent with the pattern that resistivity in geothermal fields in Iceland is mainly controlled by alteration mineralogy, as opposed to permeability. In addition to R1, high resistivity in Sudurhlidar corresponds to resistive epidote-actinolite alteration, and high resistivity in Leirbotnar corresponds to chlorite-epidote alteration.

*C2: Low resistivity chimney*

This moderately conductive feature appears to connect the deeper conductor (C3) to the surface. A similar feature was observed in the 1-D resistivity models of Árnason et al. (2007) and the 3-D models of Gasperikova et al. (2015) and Rosenkjaer et al. (2015). There are two vertical low resistivity anomalies that flank the path of IDDP-1 and merge with the conductor C3 at a depth of approximately 1.5 km below sea level. The location of C2 agrees well with the Hveragil fault system, which divides the Vitismor and Leirbotnar fields from the Sudurhlidar field. As previously mentioned, increased porosity within the Hveragil fault system can host aqueous fluids that could significantly decrease resistivity. Weisenberger et

al. (2015) also reported a major feed zone in Sudurhlidar associated with a felsic intrusion complex from 0.2 to 0.6 km b.s.l., coinciding with the elevation of C2. C1 and C2 appear connected due to the fact that MT has a limited ability to resolve the lower boundary of conductors. However, the chlorite-epidote zone beneath Sudurhlidar is observed at 0.3 to 0.2 km a.s.l. which effectively constrains the lower elevation of the clay layer C1 (Weisenberger et al., 2015). Thus, the low resistivity of C2 is not due the clay layer and can instead be attributed to aqueous fluids within the permeable Hveragil fault system.

Pope et al. (2016) analyzed isotope ratios of geothermal fluids form Krafla. Their hydrogeological model of Krafla describes the same meteoric source for Leirbotnar and Sudurhlidar, but with different degrees of phase separation and mixing with magmatic gases. In our resistivity model, a low to intermediate resistivity zone (C2) between Leirbotnar and Sudurhlidar matches the location of the Hveragil fault system, which agrees with their interpretation of Hveragil as an upflow zone separating these two subfields. Hveragil appears as a low resistivity feature because it is a sub-vertical pathway for hot geothermal fluid and magmatic gas ascending from the two-phase reservoirs below Sudurhlidar, Vitismor, and Leirbotnar.

*C3: Upper crustal conductor*

Feature C3 is an extensive low resistivity zone beneath the northern part of the inner caldera. Its lateral dimensions are approximately 5 km by 5 km; however, the northern edge is not well-constrained because it extends outside of the MT survey area. C3 domes upward to a depth of about 1.6 km b.s.l., and appears to extend to greater than 5 km b.s.l., although the lower limit is not well-constrained by the MT data. In Figure 3.9 and Figure 3.10 the bottom of IDDP-1 intersects a low resistivity zone that connects features C2 and C3. We believe the feature C3 has two possible interpretations:

(1) A zone of partial melt

(2) A zone of dehydrated chlorite and/or epidote alteration minerals that have formed magnetite (H. Hu et al., 2017; Manthilake et al., 2016; Nono et al., 2020).

It is unclear if C3 is due to just one, or a combination of the two interpretations stated above. If C2 is an up-flow zone of two-phase geothermal fluid ( >340°C) related to the permeable Hveragil fault system, then it makes sense that it would be connected to a deeper magmatic heat source. However, it is unlikely that the top of C3 corresponds to the top of a large, homogeneous magma body. Einarsson (1978) inferred a 3 km depth to the top of the magma body from shear wave attenuation, which is about 1 km deeper than the bottom of IDDP-1. C3 is also mostly to the north of the S-wave shadows from Einarsson (1978) at 1.6 to 2.1 km b.s.l. (see Figure 3.10). Although the spatial correlation is not exact, it must be noted that the seismic study had limited resolution and different station coverage to the MT survey. Einarsson (1978) stated that the southern boundaries of the S-wave shadows are better constrained than the northern ones. Only one of the three seismic stations in the study (station SN) was located to the north of the caldera and would receive many ray paths passing under the north caldera. Most of the arrivals were critically refracted and may not have sampled a deep attenuating magma body. Seismic tomography by Schuler et al. (2015) revealed a low $v_p/v_s$ ratio anomaly at the bottom of IDDP-1 that they interpreted as a zone of superheated steam above the rhyolitic magma body. This effectively rules out an expansive zone of partial melt at 1.6 km b.s.l., which would require an elevated $v_p/v_s$ ratio. However, we cannot eliminate the possibility that IDDP-1 intersected a small magma body (dyke or sill), which would not provide as strong of a geophysical anomaly as a larger magma body. We will assess the MT data response to synthetic smaller magma bodies in the next section.

Recent work has shown that dehydration of chlorite and epidote alteration minerals leads to decreased rock resistivity at high temperatures and pressures (H. Hu et al., 2017; Manthilake et al., 2016; Nono et al., 2020). Nono et al. (2018) performed resistivity measurements on Icelandic rocks at high temperature (200 to 700°C) and pressure (70 MPa) and showed that destabilization of the chlorite and epidote alteration minerals above 500 to 600°C resulted in an irreversible resistivity decrease from about 1000 - 100,000 Ωm to about 3 - 30 Ωm. The resistivity of C3 falls within this resistivity range. Mortensen et al. (2014) estimated that the formation temperature at the bottom of IDDP-1 is about 500°C, which agrees with the onset temperature of chlorite/epidote destabilization reported by Nono et al. (2018). This suggests that destabilization of the alteration minerals may occur below the bottom of IDDP-1. Note that the pressure at the bottom of IDDP-1 is between hydrostatic and

lithostatic pressures (21 to 51 MPa; Elders et al., 2011) which is lower than the experimental 70 MPa pressure of Nono et al. (2018). However, at these conditions temperature has a much larger impact on electrical resistivity than pressure (e.g. H. Hu et al., 2017; Manthilake et al., 2016).

Upper crustal conductors have been observed beneath other geothermal fields in Iceland. Large low resistivity (< 10 Ωm) zones have been detected 4 km b.s.l. at Hengill (Árnason et al., 2010) and about 3 km b.s.l. at Námafjall (Karlsdóttir et al., 2015). Seismic tomography at Hengill did not reveal a velocity anomaly consistent with the presence of partial melt (A. Tryggvason et al., 2002). Destabilization of chlorite and epidote may explain the conductors below these geothermal fields.

Other studies at Krafla have proposed more complicated geometries for the magmatic system. Schuler et al. (2015) imaged a low $v_p/v_s$ ratio anomaly at the depths that IDDP-1 and K-39 intersected rhyolitic magma. They suggested that the anomaly was due to a region of superheated steam overlying a region of melt. Although our resistivity model contains a moderately low resistivity zone at the bottom of IDDP-1, a zone of superheated steam would not be expected to produce a low resistivity anomaly (e.g. Ussher et al., 2000). Their vertical grid spacing of 0.5 km is about twice as large as the cell size used in our inversions, so it is possible that the low $v_p/v_s$ ratio anomaly is not coincident with the top of C3 in our resistivity model. Axelsson et al. (2014) modeled the possibility that a small magma intrusion was emplaced during the Krafla Fires of 1975 to 1984 that was later intersected by IDDP-1. Though they were unable to confirm or disprove the idea, deformation-induced melt segregation could be a mechanism of transporting relatively viscous, immobile rhyolitic melt (Jónasson, 2007).

The origin of rhyolite melt beneath Krafla was confirmed by studies of recovered silicic glass. Hydrogen and oxygen isotope analysis of the IDDP-1 rhyolite showed that the rhyolite was formed by re-melt of hydrothermally altered basalt (Elders et al., 2011; Zierenberg et al., 2013). Well K-39, about 2 km to the southeast of IDDP-1, intersected a thin sill (~20 m) of rhyolite melt at approximately 2.1 km b.s.l. Major element analysis of the quenched silicic glass recovered by well K-39 suggested that the melt also formed by partial melting of hydrothermally altered basalt (Mortensen et al., 2010). Jónasson (2007) suggested that the rhyolite magma forms an intrusive complex beneath a central volcano, rather than a

single, large magma chamber. Thus, IDDP-1 and K-39 may have intersected an intrusive complex with a number of small, rhyolite magma bodies that overlie the basaltic magma body inferred at about 3 km depth (Figure 3.9 and Figure 3.10).

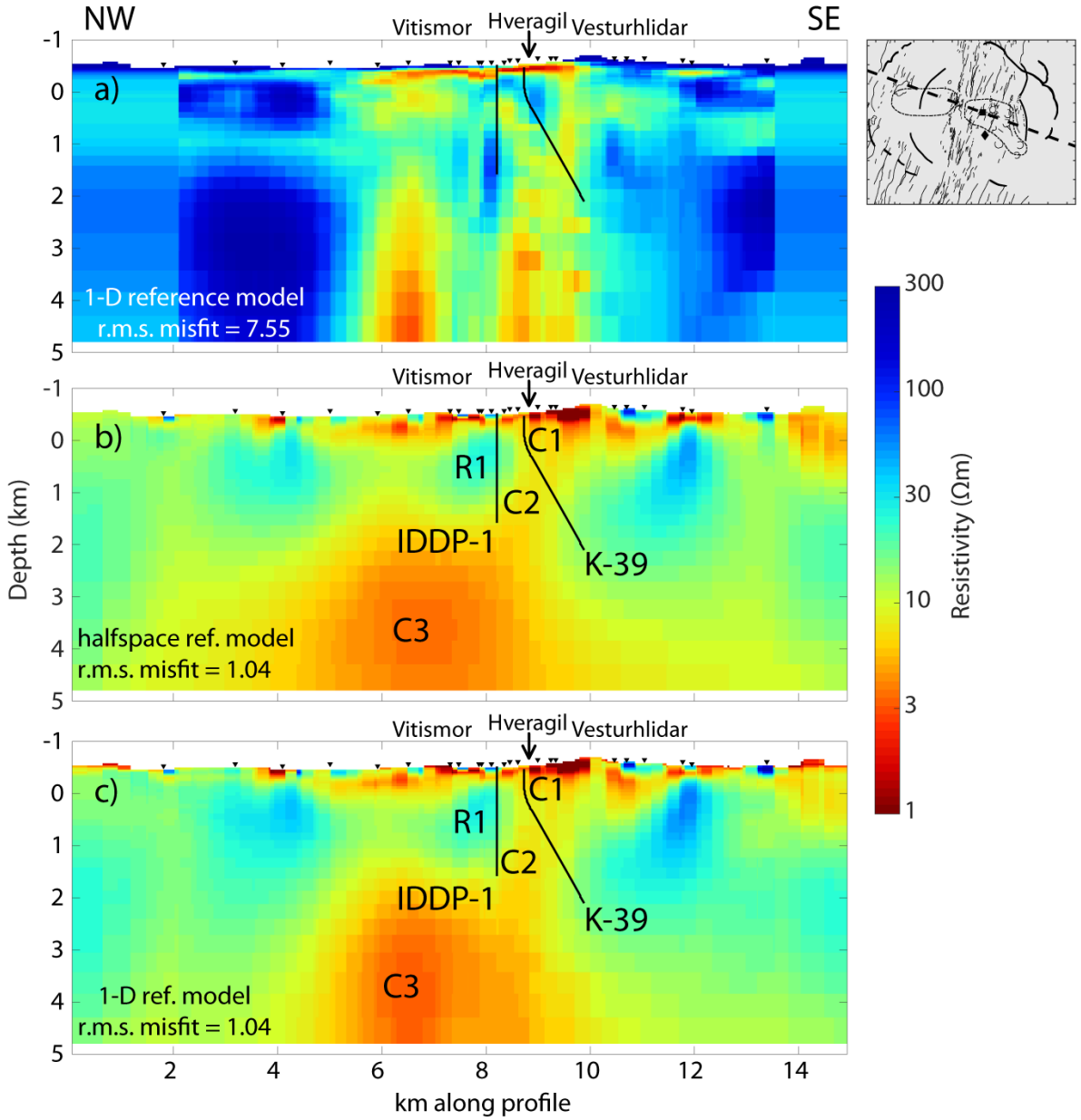


Figure 3.9: Northwest to southeast slice through the a) interpolated 1-D prior resistivity model of Árnason et al. (2007); b) 3-D resistivity model from the 3-D MT inversion with a 10 Ωm half-space as the prior model; c) 3-D resistivity model from the 3-D MT inversion using the interpolated 1-D MT model as a prior model. See inset map and Figure 3.1 for the location of profile trace A-A'. Note that the 1-D model in a) has been interpolated onto the 3-D mesh used in our inversions. The path of

the two wells that intersected rhyolite magma, IDDP-1 and K-39, are shown in black. The path of K-39 is projected onto the profile from about 1 km to the south.

These models with multiple, small magma bodies are inconsistent with the feature C3 in the resistivity model shown in Figure 3.9 and Figure 3.10. A key issue to understand is the resolution of the MT method. It can be difficult to distinguish relatively small bodies at depth because the MT method uses signals that diffuse in the Earth. The fact that the rhyolite sill intersected by well K-39 was about 20 m thick suggests that rhyolite magma bodies beneath Krafla are too small to be resolved at such depth by the MT method. In addition, well K-25 is located 200 m southwest of IDDP-1 but did not encounter rhyolite magma at its total depth of 1.55 km b.s.l. The inability of MT to detect such small-scale bodies may explain why the bottom of K-39 does not coincide with a low resistivity feature in the model (Figure 3.9 and Figure 3.10). The next section will address this issue with a set of resolution tests to quantify the size and resistivity of possible magma bodies at Krafla.

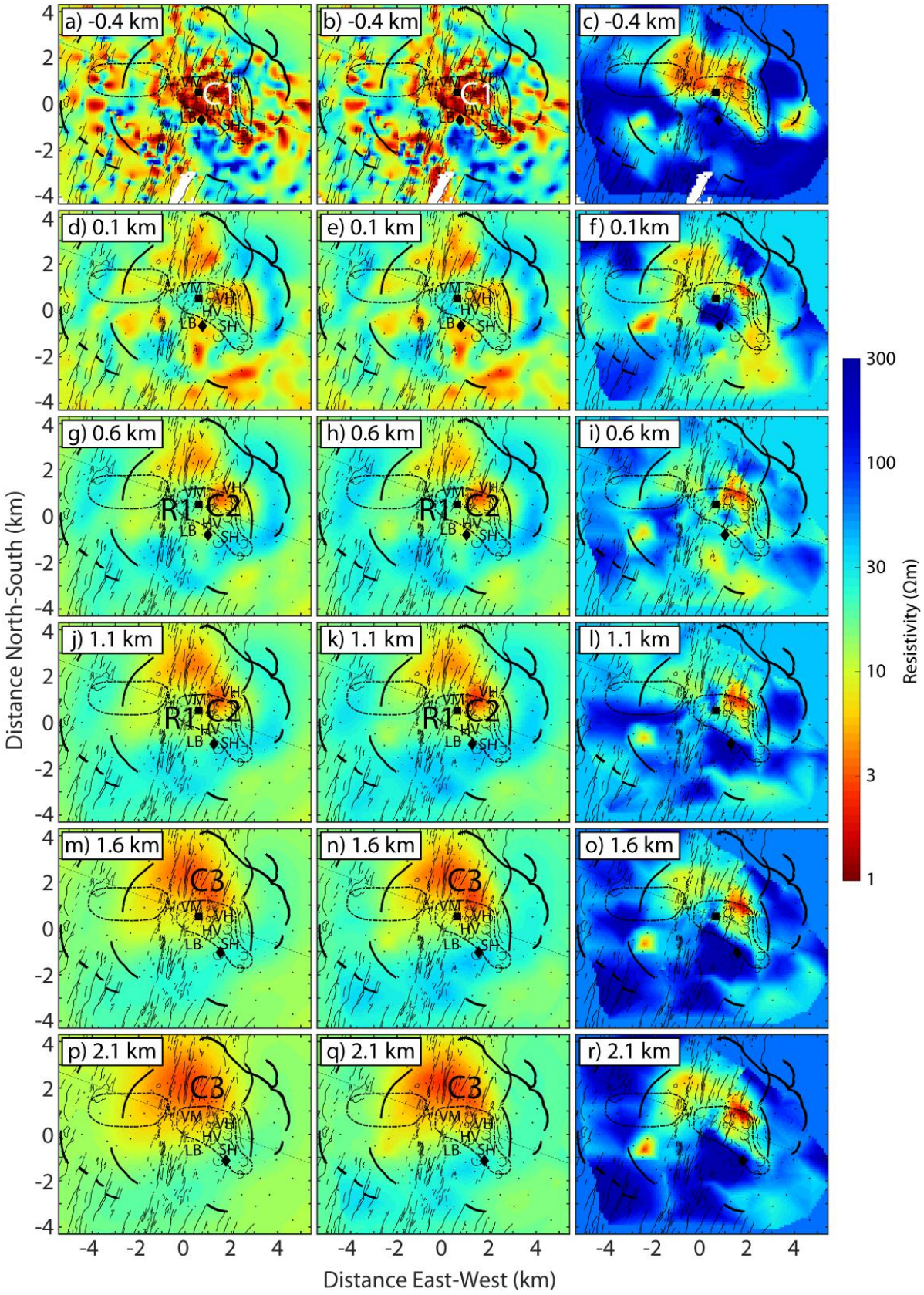
a) -0.4 km
b) -0.4 km
c) -0.4 km
d) 0.1 km
e) 0.1 km
f) 0.1km
g) 0.6 km
h) 0.6 km
i) 0.6 km
j) 1.1 km
k) 1.1 km
l) 1.1 km
m) 1.6 km
n) 1.6 km
o) 1.6 km
p) 2.1 km
q) 2.1 km
r) 2.1 km
C1
R1
C2
C3
VM
VH
HV
LB
SH
Distance North-South (km)
Distance East-West (km)
Resistivity (Ωm)
300
100
30
10
3
1

Figure 3.10: Horizontal slices through resistivity models at elevations of -0.4 km, 0.1 km, 0.6 km, 1.1 km, 1.6 km, and 2.1 km below sea level. Left column (a,d,g,j,m,p): unconstrained 3-D inversion resistivity model with a 10 Ωm half-space prior model; center column (b,e,h,k,n,q): constrained 3-D inversion resistivity model with the 1-D prior model; right column (c,f,i,l,o,r): the interpolated 1-D resistivity model of Árnason et al. (2007). The slices at 1.6 km and 2.1 km elevation correspond to the depths that the IDDP-1 and K-39 wells intersected rhyolitic magma, respectively. Thick black lines are the inner and outer calderas, thin lines are faults and fissures; dashed shapes are the shear wave shadows from Einarsson (1978), the black square is IDDP-1, the black diamond is well K-39. VM = Vitismor; LB = Leirbotnar; HV = Hveragil; SH = Sudurhlidar; VH = Vesturhlidar. See main text for interpretation of the resistivity features R1, C1, C2, and C3.

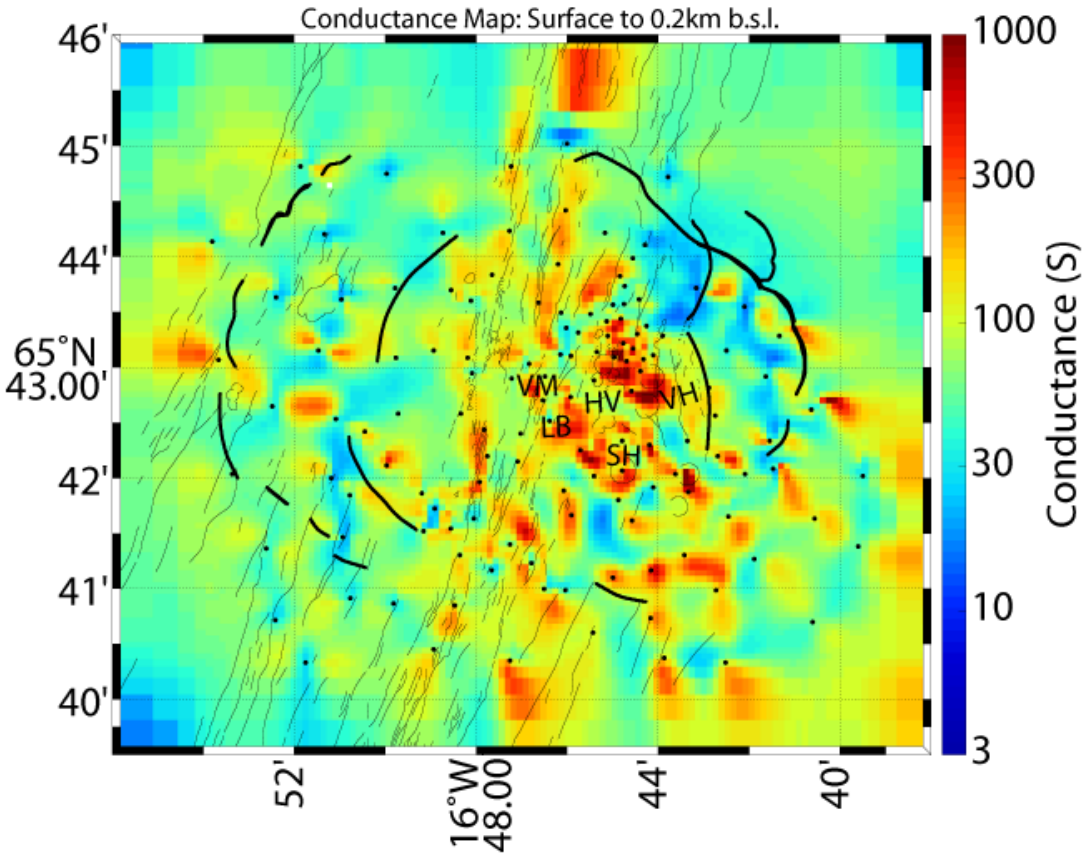


Figure 3.11: Integrated conductivity (conductance) in the unconstrained 3-D resistivity model from the surface to 0.2 km b.s.l. A high conductance ( >300 S) in the inner caldera coincides with the shallow clay layer. VM = Vitismor; LB = Leirbotnar; HV = Hveragil; SH = Sudurhlidar; VH = Vesturhlidar.

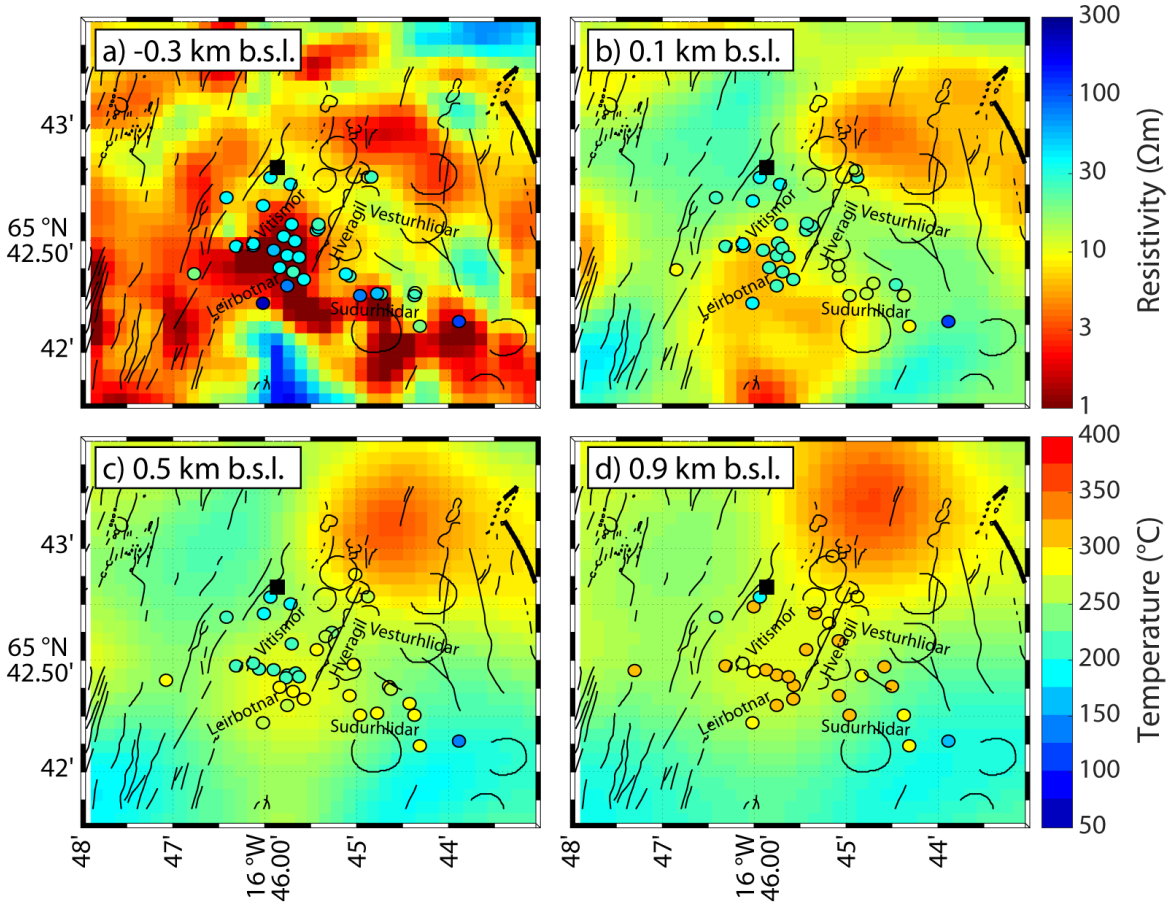


Figure 3.12: Map view of well temperature and 3-D model resistivity in the Krafla geothermal field at four depths: a) -0.3 km, b) 0.1 km, c) 0.5 km, and d) 0.9 km b.s.l. Note the resistivity color bar corresponds to the model resistivity (background shading) and the temperature color bar corresponds to the well temperatures (colored circles). Each colored circle is the location of a well track at the specified depth. In a) temperatures below 200°C correspond to the shallow, two-phase reservoirs. The well temperatures below 200°C correlate with the low resistivity clay layer. At intermediate depths in b) and c) temperatures in the Leirbotnar and Sudurhlidar fields are greater than 225°C corresponding to the superheated reservoir, but only about 200°C in the Vitismor field. This corresponds to the nearly isothermal reservoir beneath Vitismor. Below 900 m in d) most well temperatures are above 300°C, corresponding to superheated reservoirs. Higher resistivity is due to chlorite and epidote alteration minerals formed above 220°C. Black square indicates the location of IDDP-1 (no temperature log available). Black lines are faults, fissures, and craters.

### 3.5.2. Comparison of the unconstrained and constrained 3-D MT inversions

Figure 3.9b shows the vertical slice A-A' through the 3-D resistivity model from the unconstrained inversion (same uniform starting and prior models). Figure 3.9c shows the same slice through the 3-D resistivity model from the constrained inversion (uniform starting model with 1-D prior model). It is clear that with no *a priori* information, the resulting resistivity model is quite similar to the one obtained with the interpolated 1-D model as a prior model. Compared to the inversion with the interpolated 1-D prior model (Figure 3.9), the inversion with no *a priori* information is smoother at depths below 1 km (depths are below sea level). In the constrained model (Figure 3.9c), the conductor C3 below 1 km depth has a more limited lateral extent, as seen in the 1-D prior model (Figure 3.9a). Horizontal slices through the two inversion models also show very similar resistivity structures (Figure 3.10). The constrained inversion model appears to keep high resistivity structures such as R1 from the 1-D prior model at elevations of 1.1 km and 1.6 km b.s.l. (Figure 3.10), which is expected of the high-temperature geothermal reservoirs at those depths. The slices at 1.6 km and 2.1 km b.s.l. coincide with the depths that the IDDP-1 and K-39 wells intersected rhyolitic magma, respectively.

### 3.5.3. Comparison with previous MT inversions

The resistivity models of the Krafla volcanic field presented in this paper share a number of features with the 3-D models published by Gasperikova et al. (2015) and Rosenkjaer et al. (2015). These include:

- Resistive, unaltered basalt and low resistivity clay layers (C1) near the surface
- A resistive chlorite-epidote core (R1) at depths of -0.5 to 2 km b.s.l.
- Sub-vertical, low resistivity feature (C2) flanking IDDP-1 to the northwest and east
- A low-resistivity feature (C3) at 3 km b.s.l. below the northern part of the inner caldera

Although our resistivity model contains the same major features as the previous authors' model, there are some notable differences. In the models of Gasperikova et al. (2015) and Rosenkjaer et al. (2015), IDDP-1 is flanked by low-resistivity structures to the west and northwest, and the bottom of IDDP-1 is located in a resistive feature interpreted as the chlorite-epidote core. Their interpretation was that IDDP-1 intersected a small magma body that was too small to be resolved with MT. However, in our model the bottom of IDDP-1 intersects a low resistivity region where the features C2 and C3 meet. We have interpreted this region as a zone of high permeability where primary aquifer fluids mix with magmatic fluids and gas from the deeper magma body (C3). There are a few differences in our inversion strategies that might help explain the disparity in our models. Rosenkjaer et al. (2015) summarized the inversion parameters used to obtain the resistivity models in their paper and in Gasperikova et al. (2015). A significant difference from our model is the minimum cell size; in their inversions the smallest cell size varied from 250 x 250 x 50 m to 300 x 300 x 8 m compared to our 100 x 100 x 30 m cells. This results in our model containing over twice as many cells in the horizontal directions (north-south and east-west). The 100 m cell width is close to the estimated 90 m skin depth of the highest frequency signals (320 Hz) in a 10 Ωm halfspace. Therefore, improved spatial resolution is not expected if cells smaller than 100 m in width were used.

Due to the non-linearity of the inversion process, and the fact that different inversion algorithms were used, it is difficult to determine if the difference in cell size would lead to differences in our models at about 2 km depth. However, we believe that the 100 m horizontal cells are required to model near-surface resistivity variations between MT stations that are only about 300 m apart. While we are not explicitly solving for galvanic distortion, the small cells between MT stations allow the inversion to fit distorted MT data by placing small features near the surface. The low r.m.s. misfit at high frequencies suggests that the model surface is sufficiently discretized to fit the distortion in the MT data (Figure 3.8).

The resistivity models presented in Gasperikova et al. (2015) and Rosenkjaer et al. (2015) were derived from inversion of the off-diagonal impedance elements, while our inversions used the full impedance tensor. The diagonal impedance elements in many MT datasets are at least an order of magnitude smaller than the off-diagonal elements; thus their importance in 3-D inversion is still under debate (Miensopust, 2017). For example, Newman

et al. (2008) justified omitting the diagonal elements because of their low magnitude, and thus low signal-to-noise ratio. Lindsey & Newman (2015) inverted the Krafla MT data to demonstrate their sequenced inversion workflow. They justified neglecting the diagonal impedance elements because only 15% of the data had a diagonal to off-diagonal ratio greater than 0.1. Additionally, because 80% of these data were below 0.1 Hz, they claimed that the off-diagonal elements were sufficient for imaging the upper ~3 km below Krafla. However, we believe that the diagonal elements should be inverted because the data below 0.1 Hz are sensitive to the deep conductors in the vicinity of IDDP-1. This can be seen in the map view of MT data in Figure 3.2 to Figure 3.5 and the data curves in Figure 3.6 that show a decrease in apparent resistivity at frequencies below 0.1 Hz. We have inverted the Krafla MT data using only off-diagonal elements and found that the main interpreted features (R1, C1, C2, and C3) are still present in the resistivity model. Although a qualitative interpretation of the resistivity model might remain unchanged, we note that the full impedance tensor data calculated from the off-diagonal derived resistivity model (1) poorly fit the observed diagonal impedance components; and (2) did not reproduce the high ( >3°) beta skew angles at intermediate frequencies. Other authors have presented benefits of inverting the full tensor (e.g. Kiyan et al., 2013; Patro & Egbert, 2011).

Besides the differences in model discretization and choice of impedance tensor elements, our choice of data frequencies, number of frequencies, number of stations, and uniform initial starting model vary slightly from those of Gasperikova et al. (2015) and Rosenkjaer et al. (2015). However, these choices are dependent on the individual user and available software, and a more rigorous study is required to determine their exact effects on the inversion resistivity model.

## 3.6. MT data sensitivity to the IDDP-1 rhyolite magma

In this section we will assess why MT did not detect the presence of rhyolite melt prior to drilling IDDP-1. Our resolution tests will address two possibilities: (1) the location of the rhyolitic magma directly beneath the clay layer makes it difficult to be resolved with the MT method; and (2) the rhyolite magma body has a relatively high resistivity and/or is relatively small and does not appear as an anomaly in the resistivity model. First we use petrological information about the IDDP-1 rhyolite and relations from laboratory melt studies

to constrain a range of possible resistivity values, assuming a homogeneous magma body. Next we add anomalies into our 3-D inversion model to simulate rhyolite magma bodies with a range of simple geometries. We tested anomalies with three different geometries and six resistivity values, for a total of 18 resolution tests. In each test, we calculated the predicted MT data for the edited model and compared this with the response of the MT inversion model. We use two approaches to quantify the difference between the two sets of data: (1) the change in r.m.s. misfit, and (2) an asymptotic p-value from the two-sample Kolmogorov-Smirnov (K-S) statistical test. To our knowledge, this is the first published use of the K-S test to judge a change in MT data fit between two resistivity models.

### 3.6.1. IDDP-1 magma body resistivity

An important part of this modelling study is to estimate the expected resistivity of the rhyolite melt. This is required to determine whether the contrast between the magma body and the host rock is sufficient for an MT survey to detect the magma body as a zone of low resistivity. Gibert et al. (2017; published in: Levy (2019) measured the electrical resistivity of melted rhyolite from the Hrafntinnuhryggur, an obsidian ridge produced by subglacial fissure eruption, southeast of the southern slopes of Mt. Krafla (labeled in Figure 3.1 as Rhyolite 115 to 11.7 ka). The rhyolite resistivity was measured to be 0.8 to 1.2 Ωm at temperatures of 900 to 1000°C. We further investigate the Krafla rhyolite resistivity using data from additional lab experiments.

We can estimate the resistivity of the IDDP-1 magma body in order to understand whether or not it could be detected by the MT data. As seen in Figure 3.9 and Figure 3.10, the region at the bottom of IDDP-1 has a resistivity of about 7 Ωm, which is relatively resistive. Following the relation of Guo et al. (2016), a pure rhyolite melt can be relatively resistive (> 1 Ωm) under particular conditions such as low water content, low melt fraction, or limited connectivity.

We estimated the resistivity range of the rhyolitic magma encountered by IDDP-1 using the experimental melt relations of Guo et al. (2016) and petrological analyses by Elders et al. (2011) and Zierenberg et al. (2013) in order to provide an input for the resolution tests. Figure 3.13 shows values of electrical resistivity of pure rhyolite melt for varying temperature and %wt $H_2O$. The figure demonstrates that increasing temperature and/or %wt

$H_2O$ decreases the melt resistivity. Additionally, it is possible that a rhyolite melt with a high %wt $H_2O$ at a low temperature could have the same resistivity as a melt with lower %wt $H_2O$ at a higher temperature. Note that the pressure at the bottom of IDDP-1 is between hydrostatic and lithostatic (Elders et al., 2011) and its influence on electrical resistivity is negligible in the range ~20 to 50 MPa. The dashed rectangle denotes the possible range of resistivity for the rhyolite melt based on temperature and %wt $H_2O$ estimates by Elders et al. (2011) and Zierenberg et al. (2013). This gives a minimum of 0.6 Ωm (black circle) and a maximum of 0.9 Ωm (black square) for the melt resistivity. Our calculated pure rhyolite melt resistivity values agree with the 0.8 to 1.2 Ωm measured by Gibert et al. (2017). If possible, a direct resistivity measurement of the rhyolite recovered from IDDP-1 would eliminate the need to use empirical relations to estimate the resistivity.

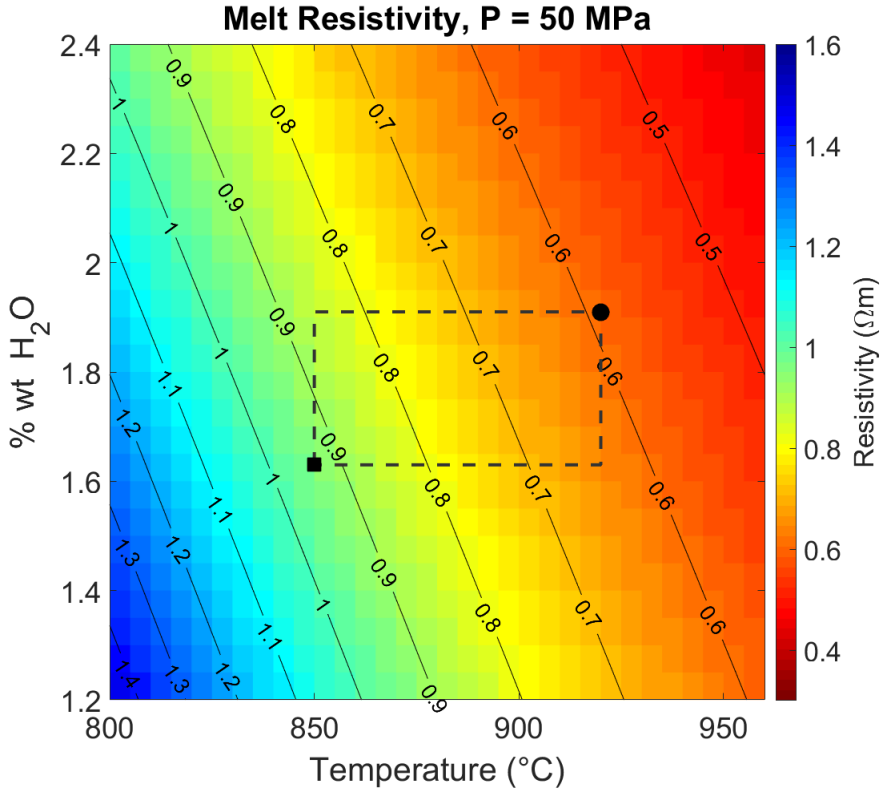


Figure 3.13: Contour lines of electrical resistivity as a function of temperature (°C) and %wt $H_2O$ for a rhyolite melt. Resistivity values are calculated from the relation of Guo et al. (2016). Dashed line shows ranges of temperature from Zierenberg et al. (2013) and % wt $H_2O$ from Elders et al. (2011). The black square is the maximum resistivity from these bounds; black circle is the minimum resistivity.

Once the melt resistivity has been calculated, it is necessary to estimate the bulk resistivity of the rock, which is a mixture of melt and crystals. The bulk resistivity can be estimated using the empirical Modified Archie's Law (Glover et al., 2000) to relate melt and bulk resistivity to melt fraction. The bulk conductivity $\sigma_b$ is related to the rock matrix conductivity $\sigma_r$ and melt (fluid) conductivity $\sigma_f$ by:

$$\sigma_b = \sigma_r(1-\phi)^p + \sigma_f\phi^m \tag{3.5}$$

where $m$ is the cementation factor, $\phi$ is the melt fraction, and

$$p = \frac{log(1-\phi^m)}{log(1-\phi)} \tag{3.6}$$

The cementation factor $m$ defines the connectivity of the melt and is a function of pore geometry, distribution, and dihedral (wetting) angle (e.g. Yoshino et al., 2010). Commonly $m$ is in the range of 1 (well connected) to 2 (poorly connected). Some studies suggest that silicate melt is relatively well-connected at intermediate melt fractions. Rosenberg & Handy (2005) found that melted granite was well-connected at melt fractions greater than 0.07. ten Grotenhuis et al. (2005) observed that basaltic melt occupied grain boundary layers as opposed to only triple junctions as melt fraction increased from 0.01 to 0.1. We use $m$ = 1.5 assuming a moderate degree of interconnected melt. However, we found that choosing a value of $m$ in the range 1 to 2 does not affect the resistivity enough to change our interpretation. Figure 3.14 shows contours of bulk resistivity computed from Modified Archie's Law for a range of melt resistivity and melt fraction. We used a rock matrix conductivity ($\sigma_r$) of 0.001 S/m for these calculations, though we observe negligible differences in bulk resistivity when the rock matrix is at least 3 orders of magnitude more resistive than the melt (i.e. $\sigma_r << \sigma_f$). A low melt fraction might be expected for Krafla rhyolite due to inferred high viscosity and a near-solidus state (Jónasson, 2007). However, the recovered IDDP-1 rhyolite was a nearly aphyric glass (Elders et al., 2011; Zierenberg et al., 2013) which indicates a high melt fraction. In our analysis we make no assumption about

melt fraction and consider the range from 0.1 to 0.9. The range of rhyolite melt resistivity constrained from Guo et al. (2016) is 0.6 to 0.9 Ωm. These minimum and maximum estimates of melt fraction and melt resistivity are shown in Figure 3.14 as dashed lines. Using these bounds on melt resistivity, and considering a melt fraction range of 0.1 to 0.9, the rhyolite encountered by IDDP-1 has a maximum bulk resistivity of about 30 Ωm and a minimum of about 0.7 Ωm. In the next section we will test if the MT data are sensitive to magma bodies in this resistivity range.

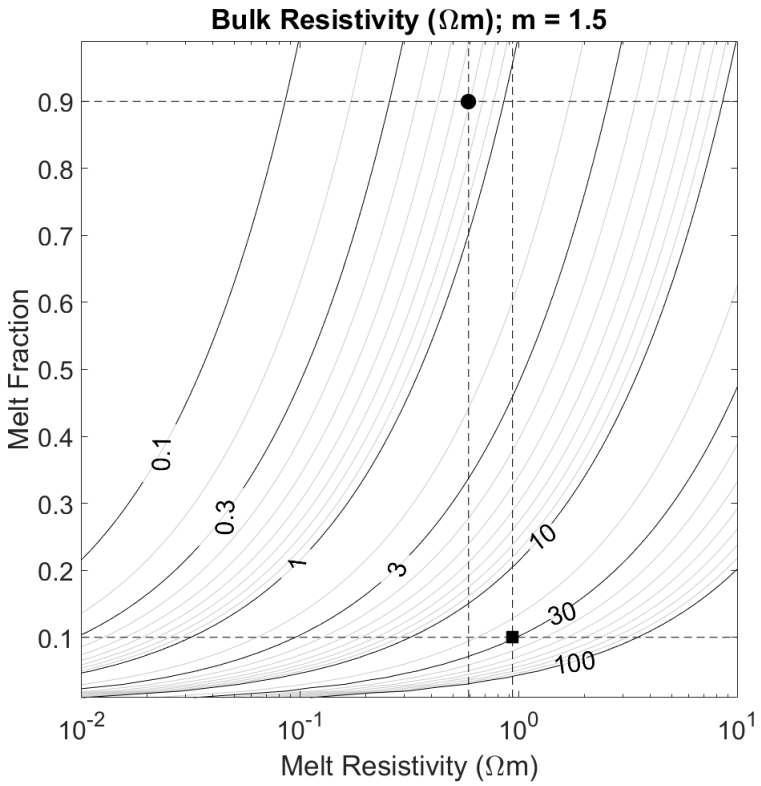


Figure 3.14: Logarithmic contours of Krafla rhyolite bulk resistivity as a function of melt fraction and melt resistivity computed from Modified Archie's Law (Glover et al., 2000). Vertical dashed lines: minimum and maximum resistivity of the Krafla rhyolite computed from relation of Guo et al. (2016); horizontal dashed lines: range of melt fraction (0.1 to 0.9) considered in our synthetic tests. Black square and black circle denote maximum and minimum estimated bulk resistivity of Krafla rhyolite, respectively.

This resistivity range is higher than resistivity estimates of silicic magma reservoirs such as those of the New Zealand Taupo Volcanic Zone (Heise et al., 2010) and the Laguna del Maule volcanic field in Chile (Cordell et al., 2018). Heise et al. (2010) estimated a

resistivity of ~ 0.3 Ωm and a melt fraction of ~50% for a silicic plume beneath the Taupo Volcanic Zone, and Cordell et al. (2018) estimated a resistivity of ~1 Ωm and a melt fraction of <35% for a long-lived silicic magma chamber below Laguna del Maule. In particular, the relatively low 1.77 %wt $H_2O$ of the IDDP-1 rhyolite contributes significantly to its higher resistivity (Elders et al., 2011). Note that due to the difference in size, temperature, depth, and water content, it is impossible to directly compare these melt fraction estimates to that of the of the IDDP-1 rhyolite. These silicic magma chambers are long-lived features that may be close to a crystal mush state with a low to intermediate melt fraction. However, Elders et al. (2011) and Zierenberg et al. (2013) noted that the recovered IDDP-1 rhyolite was aphyric, which indicates a high melt fraction. This comparison demonstrates how a wet magma with low melt fraction can have a similar resistivity as a dry magma with high melt fraction (i.e. Figure 3.14).

### 3.6.2. Resolution tests

These tests are needed because it is possible that the conductor caused by the magma body is not being correctly imaged. This can occur for a number of reasons:

(1) the presence of C1, a high conductance ( > 300 S) layer that screens the EM signals, and
(2) the magma body is relatively resistive and/or has a small resistivity contrast from the surrounding rock. The diffusive physics of MT means that a small, low resistivity anomaly can go undetected. The approach used in the inversion assumes diffusive signal propagation and generates a smooth resistivity model with minimum structure.

#### 3.6.2.1. Resolution test methodology

To implement the resolution tests, the unconstrained resistivity models in Figure 3.9 and Figure 3.10 were edited to include different geometries of a low resistivity zone which represents a crustal magma body. These low resistivity zones (i.e. magma bodies) were added at a depth of 1.6 km b.s.l. based on the depth at which IDDP-1 well intersected magma. This corresponds to the upper edge of the conductive feature C3. Figure 3.15 shows the outlines of the three magma bodies considered in these tests. The three magma bodies were designed to represent a thin sill (B1), a small cubic magma body (B2), and a larger cubic magma body

(B3). In the previous section we determined that the magma body encountered by IDDP-1 has a resistivity between 0.7 to 30 Ωm with a melt fraction of 0.1 to 0.9. To investigate this resistivity range each of the 3 magma body geometries was assigned 6 different bulk resistivity values between 0.1 and 30 Ωm. The 18 combinations of geometry and resistivity that were tested are listed in Table 3.1. Table 3.1 also lists the conductance for each test magma body. The conductance of an arbitrarily-shaped body can be calculated with the relation

$$C = \frac{\sigma A}{L} \qquad (3.7)$$

where A is the cross-sectional area and L is the body length (e.g. Yoshino, 2018). In a 1-D layered Earth, where conductivity only varies in the z-direction, Equation (3.7) simplifies to the conductivity multiplied by the thickness of the feature (e.g. Bai et al., 2010; Yang et al., 2015). However, in the 3-D case the spatial dimensions of the body may be different in 3 directions. We can calculate the conductance of the B1, B2, and B3 test anomalies by considering electrical current flow in the north-south direction, and using the dimensions from Table 3.1. Using Equation (3.7), the conductances of the thin sill, small magma cube, and large magma cube range from 8.3 to 2500 S, 16.7 to 5000 S, and 33.3 to 10,000 S, respectively (see Table 3.1 and Table 3.2). The same values can be obtained for current flow in the east-west direction. Note that we have considered test magma bodies with conductances greater than and less than the 300 S conductance of C1.

Table 3.1: p-values returned by K-S tests of the 18 sensitivity tests. Red shading: statistically significant p-values.

| p-values for test magma bodies, alpha = 0.05 | | | | |
|---|---|---|---|---|
| Resistivity (Ωm) | Conductance (S) B1, B2, B3 | B1: Thin sill 3 km x 3 km x 0.25 km | B2: Small cube 0.5 km x 0.5 km x 0.5 km | B3: Large cube 1 km x 1 km x 1 km |
| 30 | 8.3, 16.7, 33.3 | 1 | 1 | 1 |
| 10 | 25, 50, 100 | 1 | 1 | 1 |
| 3 | 83, 167, 333 | 1 | 1 | 1 |
| 1 | 250, 500, 1000 | 8.2E-1 | 1 | 1 |
| 0.3 | 833, 1667, 3333 | **6.1E-3** | 1 | 1 |
| 0.1 | 2500, 5000, 10000 | **1.3E-5** | 1 | 1 |

Table 3.2: Change in r.m.s. misfit when the inversion resistivity model is edited in each of the 18 sensitivity tests. Pink shading corresponds to features with statistically significant p-values from Table 3.1. Note that a value of 0 indicates a change in r.m.s. misfit less than 0.01.

| r.m.s. misfit change for test magma bodies (inversion r.m.s. misfit = 1.04) | | | | |
|---|---|---|---|---|
| Resistivity (Ωm) | Conductance (S) B1, B2, B3 | B1: Thin sill 3 km x 3 km x 0.25 km | B2: Small cube 0.5 km x 0.5 km x 0.5 km | B3: Large cube 1 km x 1 km x 1 km |
| 30 | 8.3, 16.7, 33.3 | 0 | 0 | 0 |
| 10 | 25, 50, 100 | 0 | 0 | 0 |
| 3 | 83, 167, 333 | 0 | 0 | 0 |
| 1 | 250, 500, 1000 | 0.02 | 0 | 0 |
| 0.3 | 833, 1667, 3333 | **0.08** | 0 | 0 |
| 0.1 | 2500, 5000, 10000 | **0.15** | 0 | 0 |

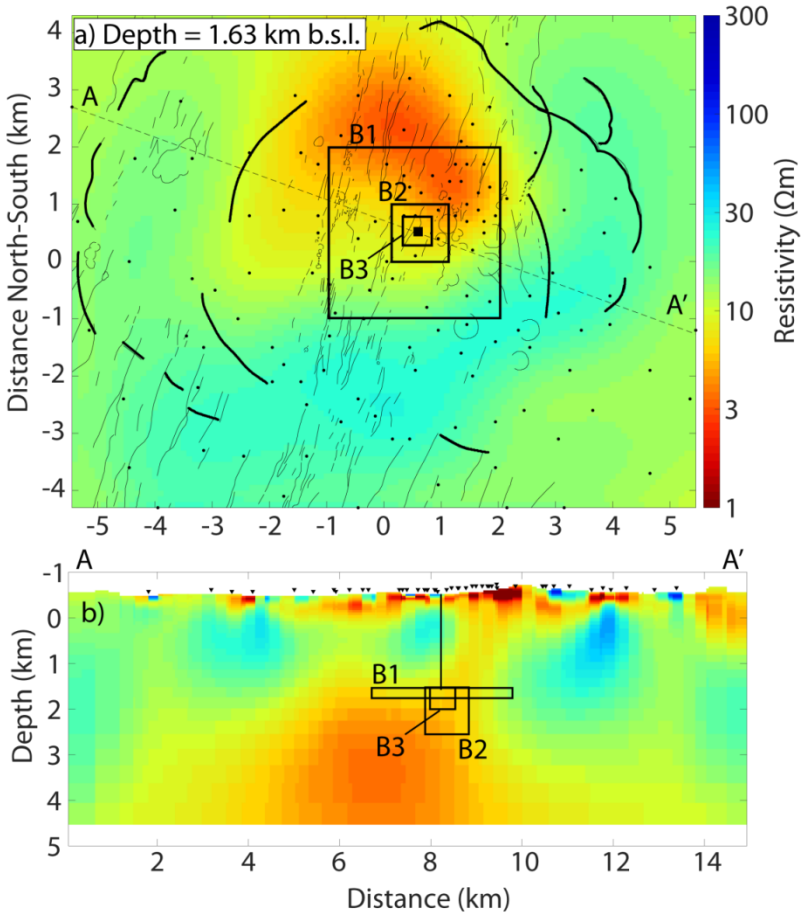


Figure 3.15: Outlines of test magma bodies in a) map view and b) vertical slice through A-A'. See Table 3.1 for magma body dimensions and resistivities.

We use two methods to quantify whether or not the edited resistivity model differs from the preferred inversion model: the Kolmogorov-Smirnov (K-S) test and the change in r.m.s. misfit. The two sample K-S test is a nonparametric hypothesis test that determines whether two populations are from the same continuous distribution within some significance level (Massey Jr, 1951; Miller & Kahn, 1962). If the asymptotic significance, or p-value, is larger than the significance level, then we accept the null hypothesis that the two populations are from the same distribution. A p-value less than the significance level is statistically significant and indicates that the null hypothesis can be rejected and the distributions are different.

We perform the K-S test with the function *kstest2* in MATLAB. The test considers two populations $x_1$ and $x_2$, with $n_1$ and $n_2$ samples, respectively. Let $D$ represent the

maximum difference between their empirical distribution functions, $F_1$ and $F_2$. If $D$ is greater than some critical value, then the null hypothesis is rejected. Instead of computing the critical value, *kstest2* accepts or rejects the null hypothesis by computing the asymptotic p-value and comparing it with the significance level.

In these resolution tests we are interested in whether or not the MT data are sensitive to the added anomalies in the edited models. We compare the residuals (normalized by error) from the original model to the residuals (normalized by error) of the calculated response of the edited model. In our case, the two populations $x_1$ and $x_2$ are the two sets of normalized residuals. If the null hypothesis is accepted (p-value greater than significance level), then we cannot conclusively determine if the two sets of residuals are drawn from the same or different distributions. If the null hypothesis is rejected (p-value less than significance level), we conclude that the two sets of residuals are distinct and thus the added anomaly has a statistically significant impact on the inversion response. In these resolution tests we are interested in whether or not the MT data are sensitive to anomalies in the edited models. We determined if the change in the MT data is statistically significant by comparing the MT data residuals (normalized by error) of each model. We will consider the anomaly in the edited model as "detected" by the MT data if the K-S tests returns a statistically significant p-value (null hypothesis is rejected). It should be emphasized that the significance level is arbitrary and does not influence the calculated p-value. In this paper we used a significance level of 0.05 for all K-S tests.

The change in r.m.s. misfit between an inversion model and an edited model has also been used to assess the sensitivity of MT data to a test anomaly (e.g. Cordell et al., 2018; Hill et al., 2009). While an increase or decrease in r.m.s. misfit suggests that the MT data are sensitive to a test anomaly, the threshold of detection is somewhat arbitrary and it is unclear how large of a change in r.m.s misfit is significant. In addition, because the r.m.s. misfit is calculated from squared residuals, it only represents a relative difference between the two sets of residuals (i.e. no information on positive or negative bias). The K-S test has the benefit of giving a summary statistic that is sensitive to a positive or negative difference between residuals. A third method to assess sensitivity follows the method of Piña-Varas et al. (2018). They added test magma bodies to their resistivity model of the Teide volcano and calculated the percent change in apparent resistivity. The MT data were considered to be

sensitive to the test anomaly if the change in apparent resistivity was greater than the error floor used in the MT inversion. We use the same approach to consider if the MT data are sensitive to an added anomaly. This method is visually helpful to identify data points with large changes but does not provide any summary statistic for the dataset as a whole.

#### 3.6.2.2. Resolution test: thin sill (B1)

The first test (B1) modelled a thin sill of magma located at a depth of 1.6 km. The sill extends 3 km in the north-south and east-west directions, and has a thickness of 0.25 km. In the first test the sill has a resistivity of 30 Ωm (conductance of 8.3 S), which is the upper end of the resistivity range calculated in the previous section. Table 3.2 shows the change in r.m.s. misfit from the inversion model when the sill is assigned the chosen resistivity value. The r.m.s. misfit changes by less than 0.01 when the 30, 10, and 3 Ωm sills are added to the model. These sills have conductances of 8.3, 25, and 83 S, respectively. It is also useful to examine changes at individual stations because overall r.m.s. misfit considers the entire dataset. In general, stations close to the sill such as KMT50 (0.4 km from IDDP-1) exhibit larger changes in their data. Figure 3.16 shows the off-diagonal apparent resistivity and phase curves for station KMT50 when the test sills are edited into the model. Figure 3.16 also shows the observed and calculated inversion data for comparison. This is a qualitative way to examine the change in MT data at one station. As expected, the 0.1 Ωm sill causes the largest change in the apparent resistivity and phase data. The more resistive 10 and 30 Ωm sills do not cause much of a change from the calculated inversion data and are not plotted in Figure 3.16 because they overlap the inversion response.

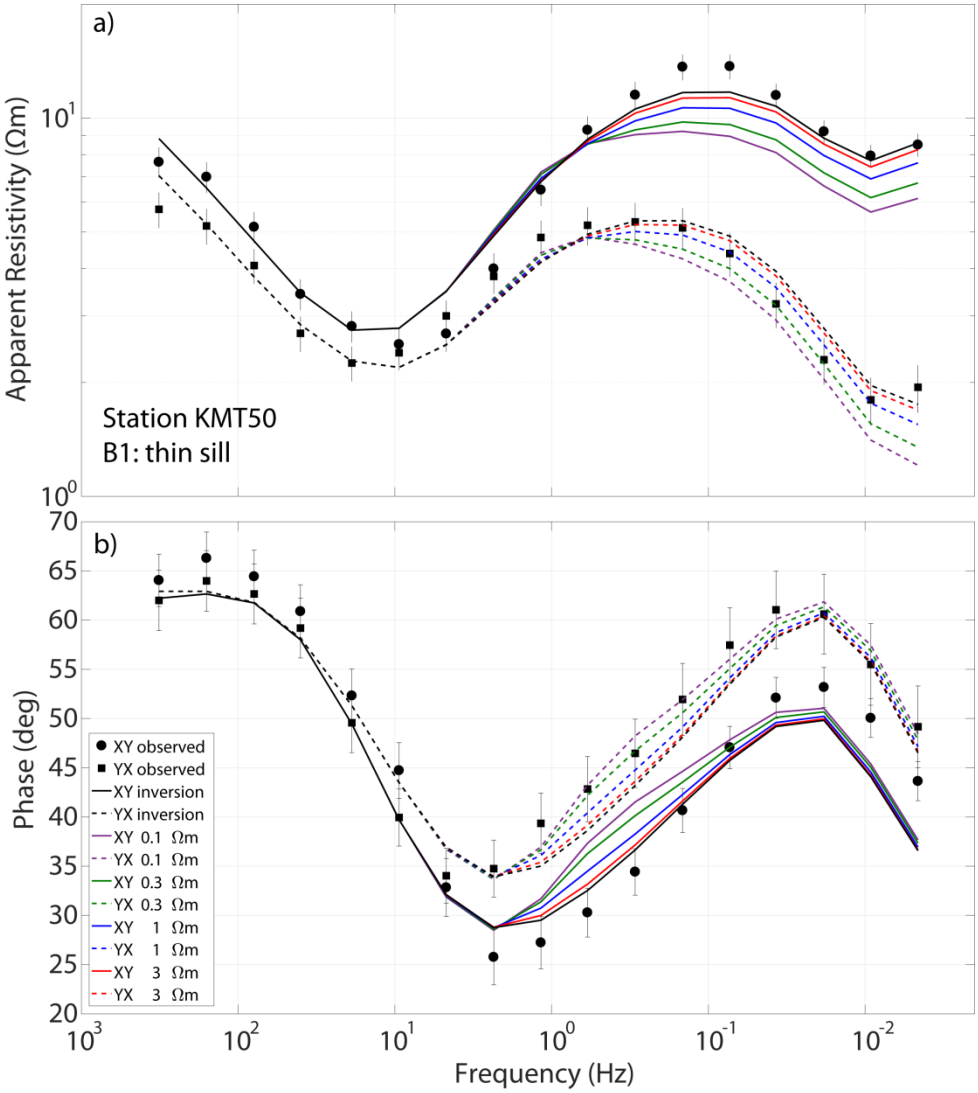


Figure 3.16: Comparison of a) apparent resistivity and b) phase data from the station KMT50. The measured data, predicted data from the 3-D inversion, and predicted data from the inversion resistivity model with synthetic sills added are shown. Circles and squares are the observed MT data, and the black lines are the calculated inversion response. Colored lines are the calculated data for synthetic sills added to the inversion resistivity model. See figure legend for symbol definitions. Note that the 10 Ωm and 30 Ωm sill responses are omitted because they are nearly coincident with the inversion response.

We can examine trends in the entire MT dataset in order to assess if the data are sensitive to the synthetic sills. Figure 3.17 shows a cross-plot of the normalized impedance data residuals for the 3, 1, 0.3, and 0.1 Ωm (83, 250, 833, 2500 S) sills. The cross-plot is a qualitative way to examine the difference between the two sets of data residuals. In each

panel, the residuals for every station and all eight components of the complex impedance are shown. If the residuals from the inversion and the edited model response are exactly the same, they will plot on the dashed 1-to-1 line. In this case, the addition of the 3 Ωm sill does not move the plotted impedance residuals appreciably from the 1-to-1 line. In fact, the K-S test returns a p-value of 1 and the change in misfit between the two models is less than 0.01. We can conclude that the MT data fit is not appreciably changed when the 3 Ωm sill is added to the model. When the resistivity of the sill is decreased to 1 Ωm, 0.3 Ωm, and 0.1 Ωm, the K-S test returns p-values less than 1, and the changes in r.m.s. misfit are greater than 0.01. In these cases it is apparent that the MT data for the inversion and edited models are different. These sills have conductances of 250, 833, and 2500 S. In particular, the 0.3 Ωm and 0.1 Ωm sills are detected by the MT data because the corresponding p-values are lower than the significance level of 0.05.

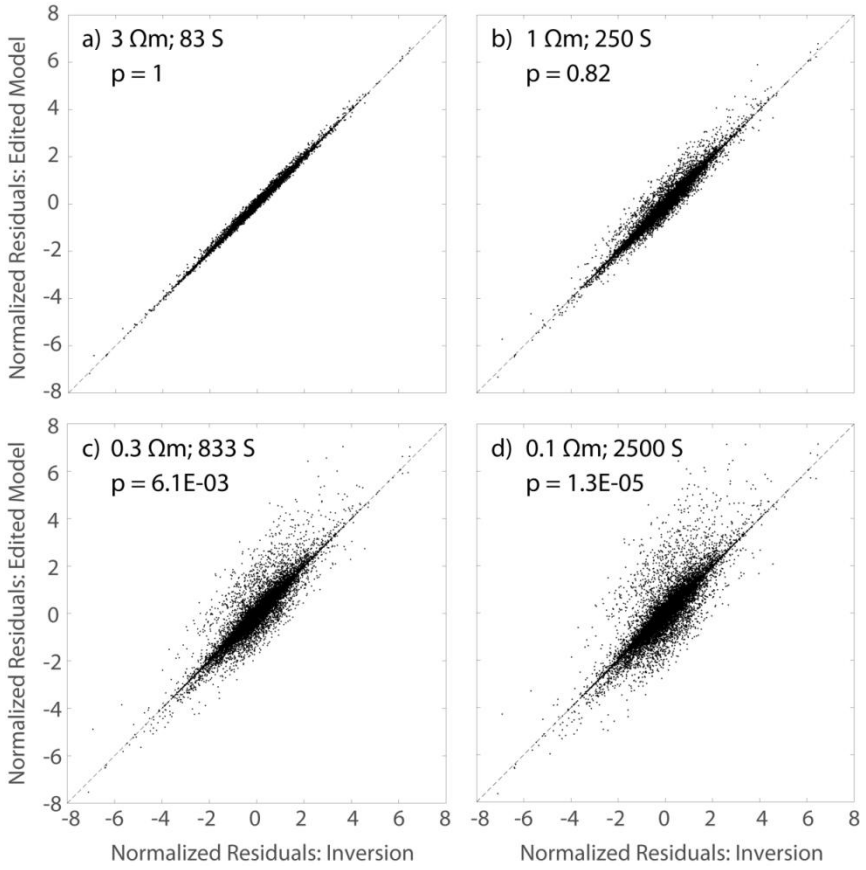


Figure 3.17: Cross-plot of impedance residuals from the unconstrained 3-D inversion resistivity model and the edited resistivity model with a) 3 Ωm (83 S) sill, b) 1 Ωm (250 S) sill, c) 0.3 Ωm (833 S) sill, and d) 0.1 Ωm (2500 S) sill. In a and b the impedance residuals for both models plot close to

the 1-to-1 line (dashed line) and the K-S test returns a statistically insignificant p-value with alpha = 0.05. When the impedance residuals of both models show a large difference as in c and d, the p-value is statistically significant.

The r.m.s. misfit increases the most (0.15) with the 0.1 Ωm sill. However, in this case the r.m.s. misfit is still rather low (1.19), which could subjectively be considered as an acceptable fit to the observed MT data. The p-value returned by the K-S test is 1.3E-05, which is far below the significance level of 0.05. This suggests that the data residuals from the inversion model and edited model can be considered to be drawn from two different distributions, and thus the two models are different enough for a change in data to be detected. This also highlights why a small change in r.m.s. misfit alone is not sufficient to determine whether two datasets are different in a significant way. The change in impedance residuals, shown in Figure 3.18, also supports this conclusion. Figure 3.18 shows the normalized change in each impedance component for every station and period between the inversion model and the model with the 0.1 Ωm sill. Values between 0 and 1 correspond to changes smaller than the imposed error floor and are plotted in white to emphasize changes larger than the error floor. Many stations show a normalized difference greater than 1 for intermediate and long periods, which suggests that these data are sensitive to the addition of the 0.1 Ωm sill despite a relatively small change in overall r.m.s. misfit. Note that the normalized differences are greater for the off-diagonal components ($Z_{xy}$ and $Z_{yx}$) than the diagonal components ($Z_{xx}$ and $Z_{yy}$) due to the fact that the same error floor was applied to all components, and the diagonal components are one to two orders of magnitude smaller than the off-diagonal components. Figure 3.19 shows the p-values for each station when comparing the inversion model and the model with the 0.1 Ωm sill. Most of the stations with a statistically significant difference in residuals are located directly above the sill. Note that several stations did not contain data > 50 s and are shown as a grey circle in Figure 3.19. Stations located above the southeastern corner of the sill show a high p-value, suggesting that they would not be sensitive to the presence of the sill. Conversely, some stations that are not located directly above the sill have statistically significant p-values. We believe this is because the p-value depends on several factors such as the resistivity model recovered by the inversion, the fit of the predicted data, and the distance to the sill.

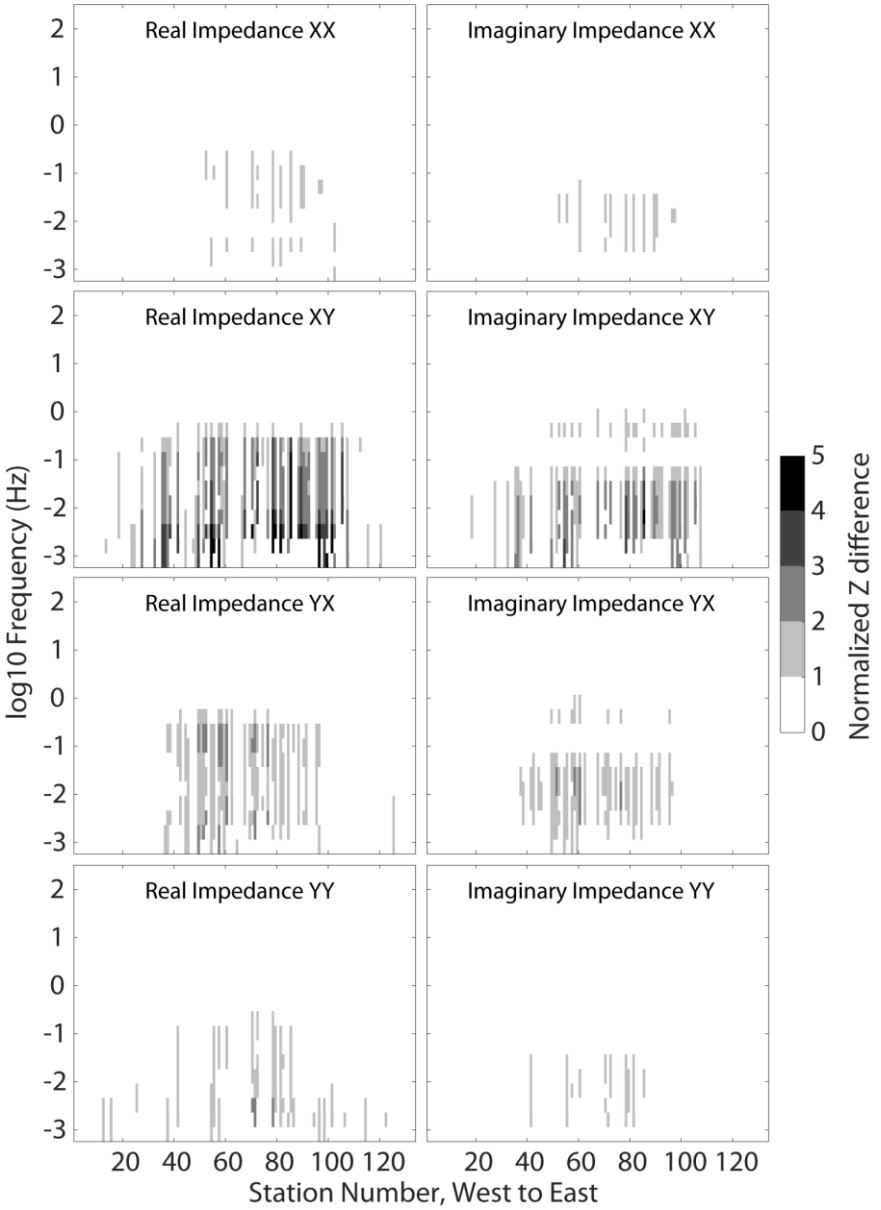


Figure 3.18: Difference in impedance normalized by error floor for the resolution test with a 0.1 Ωm (2500 S) sill added to the 3-D inversion resistivity model.

We would expect stations located above the highly conductive clay layer to have a diminished resolution toward any deeper conductors. This is likely due to the fact that the 1-D conductance is a simple approximation that does not accurately represent the current flow in all parts of a 3-D model. The true conductance will be different from the 1-D conductance when conductivity varies in the horizontal x- and y-directions. However, the test sills underlie a significant area below Krafla and are relatively 1-D compared to the cubic test

magma bodies. As predicted in Section 3.5.1, a conductor below C1 would need a conductance greater than 300 S to be detected by the MT data. The results from the test sills support this idea, as only the sills with conductances greater than that of C1 (833 and 2500 S) produced statistically significant p-values and appreciable changes in r.m.s. misfit.

#### 3.6.2.3. Resolution test: cubic magma bodies (B2 and B3)

We also tested if the MT data were sensitive to hypothetical cubic magma bodies at the same location as the sill. The small test cube (B2) had dimensions of 0.5 km x 0.5 km x 0.5 km while the large cube had dimensions of 1 km x 1 km x 1 km (see Figure 3.15 for locations). As seen in Table 3.1 and Table 3.2, the small and large cubes were not detected for the tested resistivities. The r.m.s. misfit remained at 1.04 when the small and large cubes were edited into the model with resistivities of 30, 10, 3, 1, 0.3, and 0.1 Ωm. In addition, the K-S test returned a statistically insignificant p-value of 1 for each test with the small and large cubes. Thus, editing the model to include even a 1 $km^3$ conductive magma body does not produce an appreciable change in the MT data, implying that the MT data are insensitive to a small intrusion at the bottom of the IDDP-1 well.

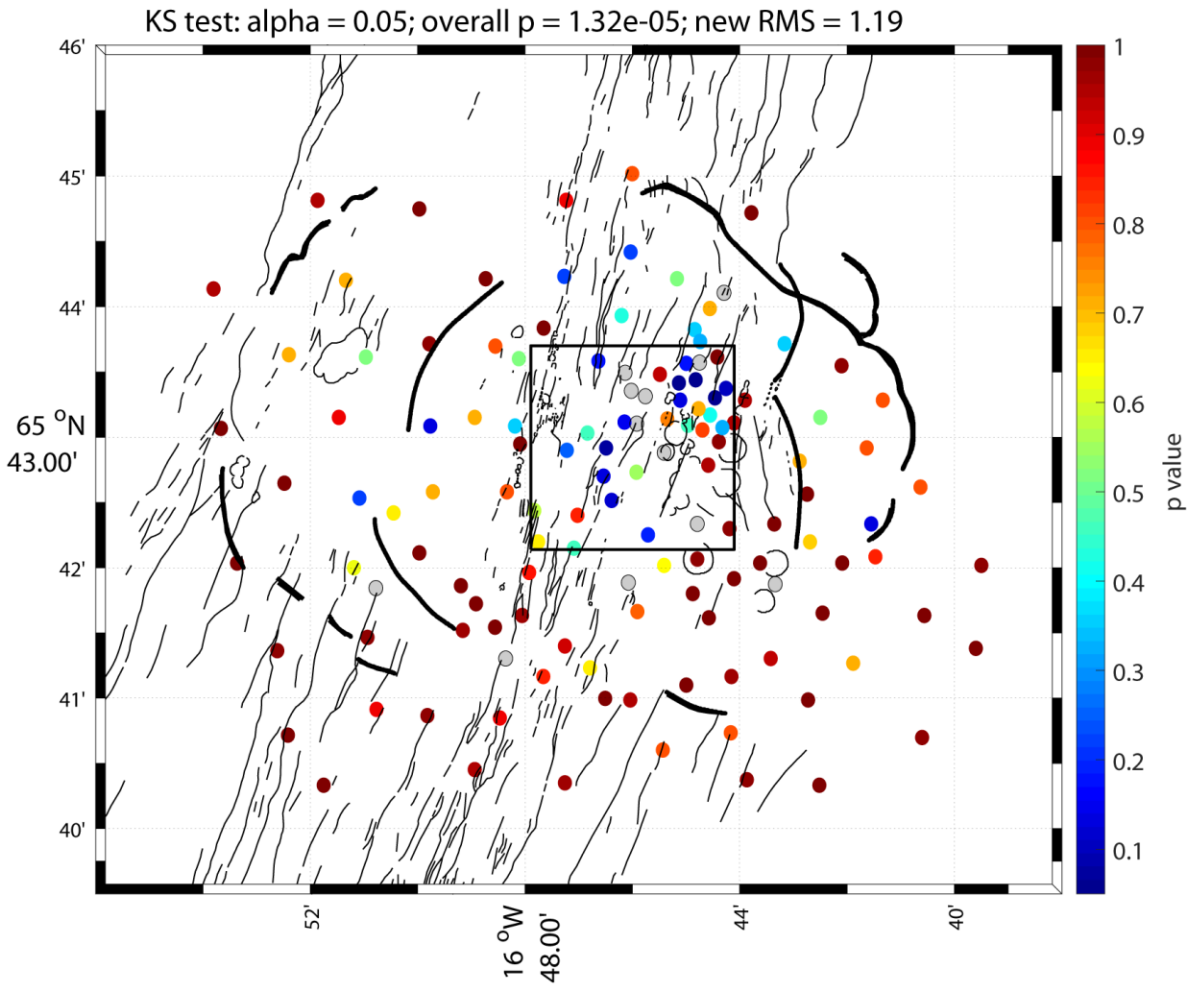


Figure 3.19: Asymptotic p-values returned by the K-S test at each MT station when comparing impedance residuals of the inversion model and model with a 0.1 Ωm (2500 S) sill. Grey circles = MT stations with no data above 50 s. The black box shows the outline of the sill.

Out of our 18 resolution tests we found that the MT data are only sensitive to the presence of the 0.3 Ωm and 0.1 Ωm sills. Even though the sill was only 0.25 km thick compared to the 0.5 and 1 km thick cubes, the resolution tests showed that the 0.3 and 0.1 Ωm (833 and 2500 S) sills would be easily detected by the MT data, while the 0.3 and 0.1 Ωm (3,333 and 10,000 S) cubes would be undetected. This seems to contradict the idea that anomalies of higher conductance would be more easily detected by MT data. Though the large cube has a conductance 4 times greater than the sill, it is not at all detected by the MT data. This suggests that the volume distribution of conductivity is also important in determining whether or not MT data are sensitive to the presence of a 3-D anomaly.

It is important to note that the test sill is larger than the expected size of rhyolite intrusions below Krafla. For example, silicic glass was recovered from the cuttings of well K-39, which suggests that the well intersected a thin sill on the order of 1 - 10 m thick (Mortensen et al., 2010). We did not add a 10 m thick sill to a depth of 1.6 km b.s.l. in the model because this is well below the expected spatial resolution of the MT method at such a depth. In addition, because the inversion is more stable when neighboring cells are a similar size (no more than ~1.5 times larger) it would not be computationally feasible to include such thin cells at such a depth in the model.

## 3.7. Conclusions

We have re-examined the MT data at the Krafla geothermal field in order to understand why the IDDP-1 well unexpectedly drilled into unanticipated rhyolite magma at 1.6 km b.s.l. With a new 3-D MT inversion and resolution tests, we have addressed three possible reasons why the magma body was initially undetected:

(1) the location of the rhyolitic magma directly beneath a highly conductive clay layer makes it difficult to be resolved with the MT method;
(2) the rhyolitic magma body intersected by IDDP-1 has a relatively high resistivity that does not present itself as an obvious anomaly in the resistivity model.
(3) the magma body was not detected due to limitations of the 1-D inversion.

(1) The Krafla geothermal field contains a clay layer about 0.5 km thick. We have shown that the 1-D conductance of the clay layer exceeds 300 S locally which limits the resolution of deeper low resistivity features. We edited test magma bodies into our inversion resistivity model in order to assess the MT data resolution. Our resolution tests with a sill and two magma cubes tested the maximum resistivity that would produce a statistically significant difference in the MT data. The MT data only showed a statistically significant difference when the 0.3 Ωm (833 S) and 0.1 Ωm (2500 S) sills (3 km x 3 km x 0.25 km) were added to the model. Out of the 6 test sills, only the sills with conductance greater than C1 (300 S) were detected by the MT data. These sills are much less resistive than our predicted range of 0.7 to 30 Ωm. This implies that the MT data would have detected these sills if one existed at this

depth, and that the observed MT data do not support the existence of a thin sill at a depth of 1.6 km below sea level. The 3 Ωm and 1 Ωm sills did not produce a large change in r.m.s. misfit or statistically significant p-values; thus we cannot preclude the existence of one of these sills based on these resolution tests alone. However, wells within one kilometre of IDDP-1 and of similar depth such as K10 (1.515 km b.s.l.), K11 (1.720 km), and K25 (1.555 km) did not intersect magma. Clearly the sill model is too simplistic and the actual distribution of intrusions varies on a spatial scale that is not resolvable by the MT data at this depth. The small magma cubes (0.125 $km^3$ and 1 $km^3$) were also undetected by the MT data when considering overall r.m.s. misfit and the two-sample KS-test. Although these cubes have conductances as high as 10,000 S, it is clear that they are too small to affect the overall bulk resistivity at a depth of 1.6 km b.s.l.

(2) Using available petrological and laboratory melt data, we estimate that for a large range of melt fractions (0.1 to 0.9) the Krafla rhyolite could have a bulk resistivity of 0.7 to 30 Ωm. This is relatively high compared to the resistivity of silicic magma reservoirs in the Taupo Volcanic Zone, New Zealand, and the Laguna del Maule volcanic field, Chile. Although the IDDP-1 rhyolite is located in a low resistivity region of our resistivity model (~ 7 Ωm), the low resistivity can be due to several factors. From the resolution tests we can conclude that the magma body would only be detected if it was a large 0.1 or 0.3 Ωm sill. However, it is clear that resistivity is not the only factor in detection because the MT data were insensitive to smaller magma bodies of 0.1 and 0.3 Ωm resistivity. Thus we cannot conclusively determine if the rhyolite was undetected due to a relatively high resistivity. Future tests could involve more realistically shaped magma bodies to reflect the complex distribution of melt below Krafla.

(3) The location and geometry of the deep conductor C3 was different in our 3-D resistivity model compared to the 1-D resistivity model of Árnason et al. (2007). A 1-D inversion is an approximation that may not be accurate in complex geological settings. The MT phase tensor data show evidence for 3-D structures at intermediate frequencies, which indicates that 3-D inversion is more appropriate. However, with respect to points (1) and (2), even the 3-D inversion has limited sensitivity to the IDDP-1 rhyolite. The 3-D inversion provides a more

accurate resistivity model than the 1-D inversion, but limited resolution to deep conductors is a general limitation of the MT method.

Our new 3-D resistivity model includes features that agree well with observed alteration and mineralogy from drill cuttings. The shallow clay layer contains high-CEC smectite and zeolite, and appears as a low resistivity feature in the upper 0.3 km of the model. The chlorite-epidote core beneath the Vitismor and Leirbotnar fields is a resistive feature in contrast to a conductive zone immediately to the east, associated with aqueous fluids within the Hveragil fault system and a major feed zone beneath Sudurhlidar. A large, low resistivity feature (C3) is present beneath the northern inner caldera at a depth of about 2 km b.s.l. We believe there are two possible interpretations for this feature: (1) a zone of partial melt, or (2) a zone of dehydrated chlorite and epidote alteration minerals. The possibility of partial melt is not clearly supported by seismic velocity and observed shear wave attenuation. With respect to dehydrated chlorite and epidote, recent laboratory melt studies show that when heated above 500°C, chlorite and epidote release aqueous fluids that significantly decrease electrical resistivity. Chlorite decomposition also leads to the formation of interconnected magnetite, further decreasing electrical resistivity (Manthilake et al., 2016). Low resistivity zones observed beneath the Hengill and Námafjall geothermal fields in Iceland have also been linked to dehydration of alteration minerals (Nono et al., 2020). However, our resolution tests suggest that the MT data do not have the ability to differentiate between small magma bodies that are periodically intruded into shallow depths beneath Krafla.

A conceptual model of the Krafla geothermal field and the underlying magmatic system is illustrated in Figure 3.20. The IDDP-1 and K-39 wells intersected rhyolite magma at 1.6 km and 2.1 km b.s.l., respectively. These are shallower than the ~3 km depth to a deep magma chamber first predicted by Einarsson (1978). Analysis of Krafla rhyolites suggests a component of re-melted, hydrothermally altered basalt (Elders et al., 2011; Jónasson, 1994, 2007; Zierenberg et al., 2013). These may exist as local pockets of rhyolite melt below Krafla. Above 500 to 600°C chlorite and epidote alteration minerals are dehydrated and lead to a decrease in resistivity as water is released and magnetite is formed (red dashed line in Figure 3.20).

This study has implications for interpretation of features, particularly conductors, in volcanic geothermal settings. A shallow clay layer is a common feature of volcanic systems that experienced low-temperature (100 to 220°C) hydrothermal alteration. We have shown limited resolution to magma intrusions that are located beneath the clay layer. The Krafla MT data were only sensitive to the synthetic sill at 1.6 km b.s.l. when the sill was unrealistically large and the resistivity was at the lower end of the range predicted from petrological and laboratory melt data. Thus, resolution tests should be performed before interpretation of conductors beneath a shallow clay layer.

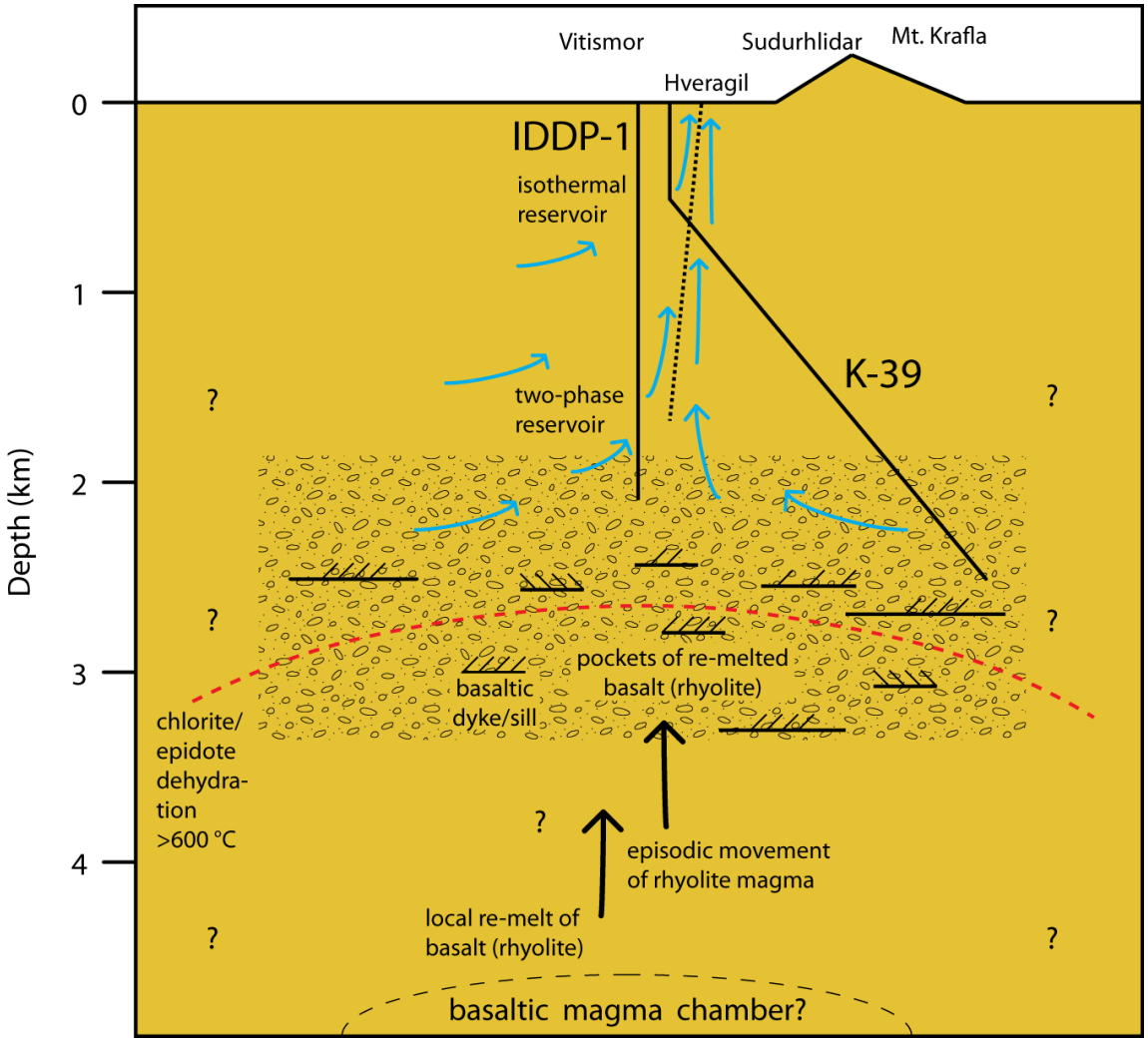


Figure 3.20: Conceptual west-to-east cross section model of the Krafla geothermal system and underlying magmatic system. Blue arrows: fluid flow based on hydrogeological model of Pope et al. (2016).

# 4. Magnetotelluric investigations at the Canoe Reach geothermal prospect

## 4.1. Introduction

It has long been recognized that Southeastern British Columbia, Canada has significant potential for geothermal energy development due to an elevated heat flow (Davis & Lewis, 1984; Hyndman, 2010), relatively high geothermal gradients (Majorowicz & Grasby, 2010), and the presence of more than 20 thermal springs distributed along major fault zones (Grasby & Hutcheon, 2001) (see Figure 4.1). One such fault is the Southern Rocky Mountain Trench Fault (SRMTF), an extensional structure named after the major valley (Southern Rocky Mountain Trench; SRMT) that divides the Columbia Mountains from the Canadian Rocky Mountains (Clague, 1974; Leech, 1966). There are 8 thermal springs spatially associated with the SRMTF, and their outlet temperatures have been recorded as high as 67°C (Ghomshei, 2007). Some areas along the SRMTF, such as the Canoe River spring near Valemount, British Columbia, have attracted interest from commercial geothermal developers over the past few decades. However, finding an economically viable geothermal resource is challenging in an area without an obvious upper crustal heat source such as a magma body. Potential geothermal resources along the SRMTF are non-magmatic and likely fault-controlled convection-dominated plays as defined in the categorization scheme of Moeck (2014). Thermal springs can guide geothermal exploration by indicating areas where permeability and temperature gradients are favorable to hot fluid circulation in the crust. However, the presence of thermal springs does not necessarily indicate that a favorable geothermal resource exists at depth (Ferguson & Grasby, 2011) and conversely, a favorable geothermal resource may not exhibit a clear surface expression such as a thermal spring (e.g. Dobson, 2016; Faulds & Hinz, 2015). In these cases geophysical methods such as magnetotellurics (MT) can be used in conjunction with geological mapping and geochemistry to map potential geothermal resources in the subsurface (e.g. Cumming, 2009). MT measures the electrical resistivity of the Earth, which is a useful property because it varies by several orders of magnitude for Earth materials. MT is sensitive to resistivity structure at greater depths than other electromagnetic exploration methods, and is widely used for geothermal exploration due to its sensitivity to fluids in the crust.

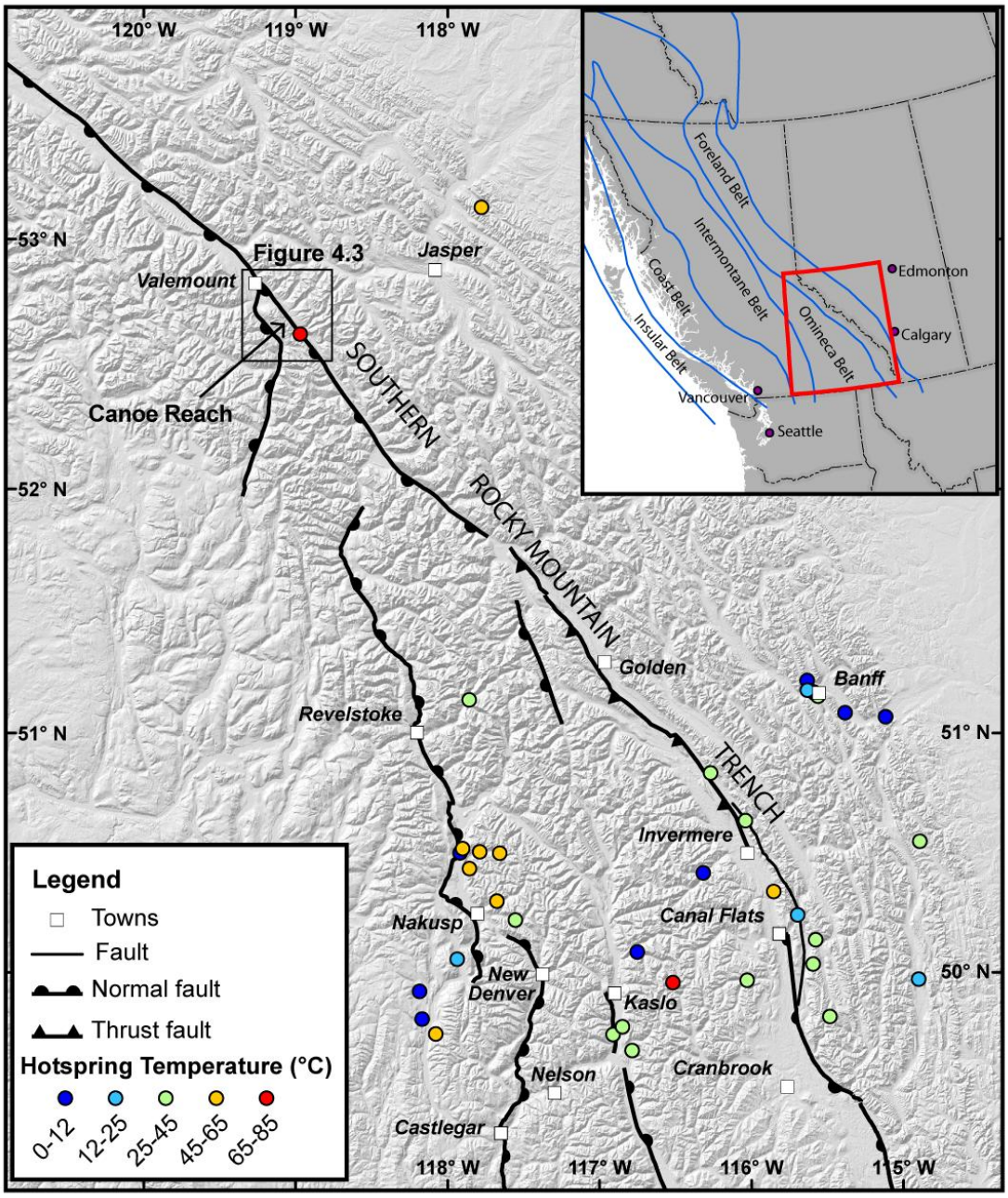


Figure 4.1: Map of thermal springs in southeast British Columbia, Canada. The Canoe Reach area, which is the location of the Canoe River thermal spring, is situated at the boundary between the southern Foreland and Omineca morphogeological belts along the Southern Rocky Mountain Trench fault. Other major faults in the southeastern Cordillera are shown, as well as associated thermal springs. The black box shows the location of detailed geological map in Figure 4.3. Digital elevation model from NASA/METI/AIST/Japan Spacesystems & U.S./Japan ASTER Science Team (2018).

A number of regional scale MT surveys have been conducted over the past four decades to image the crust and upper mantle beneath the Canadian Cordillera (Gough, 1986; Kurtz et al., 1986; Ledo & Jones, 2001; Rippe et al., 2013; Soyer & Unsworth, 2006). Rippe et al. (2013) presented a 2-D resistivity model extending from Vancouver Island to the Western Canadian Sedimentary Basin in Alberta (Figure 4.2). The model exhibits a low resistivity upper mantle beneath the Omineca Belt (at distances of 400 to 600 km) in contrast to the high resistivity beneath the Foreland Belt. The model interpretation supports the hypothesis that mantle upwelling and possible backarc convection could explain the elevated heat flow beneath the southeastern Canadian Cordillera (Currie et al., 2004; Ledo & Jones, 2001). The model also contains a low resistivity feature that could correspond to fluids in the uppermost crust beneath the SRMT at about 52°N, near the town of Valemount. A more detailed MT survey within the SRMT, examining shallower depths at greater resolution, is needed to investigate the cause of this conductor, and explore the implications for a potential geothermal resource.

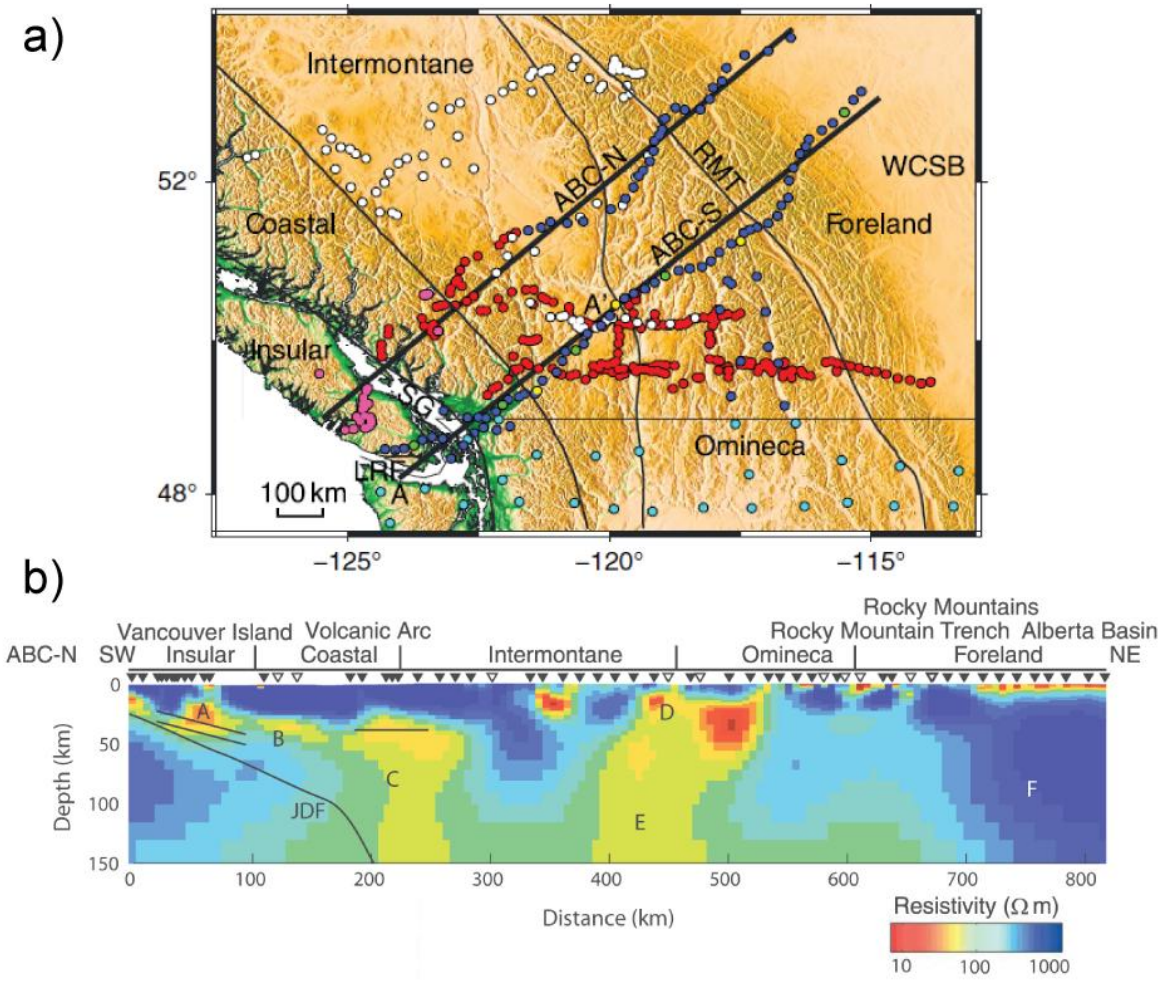


Figure 4.2: Map of selected magnetotelluric stations collected in the Canadian Cordillera and resistivity model from the ABC-N transect. a) colored circles show locations of magnetotelluric stations collected in different years. The ABC-N transect extends from the Western Canada Sedimentary Basin (WCSB) to Vancouver Island, and crosses the Canoe Reach area in the Rocky Mountain Trench (RMT). b) 2-D resistivity model obtained from inversion of the ABC-N magnetotelluric data. The resistivity model contains a conductor in the upper 10 km beneath the RMT. Adapted with permission from Rippe et al. (2013), Figure 1 and Figure 11.

Past geophysical and geological studies have provided some insights into the geometry and displacement of the SRMTF, and how the crustal structure might control fluid circulation beneath the SRMT. A series of seismic reflection profiles across the SRMT between the United States border and the town of Canal Flats (49°N to 50.25°N) revealed that the SRMTF in this location is composed of high-offset (up to 12 km), southwest-dipping

normal faults (Van Der Velden & Cook, 1996). Further north near the town of Golden (51.25°N), bedrock mapping suggested that fault offset was small (< 6 km), and distributed across multiple structures (Kubli & Simony, 1994). Finally, between Golden and Valemount (51.25°N to 52.8°N), geological cross sections indicate a dip separation of less than 4 km across a single strand of the SRMTF (Gal & Ghent, 1990; McDonough & Morrison, 1990; McDonough & Murphy, 1994; Murphy, 2007). Grasby & Hutcheon (2001) suggested that the presence or absence of thermal springs along the SRMT is largely controlled by fault geometry, pointing out that the gap in thermal springs between Radium and Canoe River is roughly associated with the segment of distributed displacement near Golden identified by Kubli & Simony (1994). Unfortunately, the majority of geological and geophysical cross-sections in the vicinity of the SRMT either start or terminate in the valley, rather than crossing it. Consequently, it is difficult to reach any certain conclusions about the along-strike heterogeneity of the SRMTF.

Several studies have identified parts of the SRMT as regions of high geothermal potential (Fairbank et al., 1992; Grasby et al., 2012). In particular, the Canoe Reach area (the northern arm of Kinbasket Lake) near Valemount has received attention because of the Canoe River thermal spring with its high outflow temperature of up to 67°C. This chapter focuses on MT surveys that took place in two regions of Canoe Reach herein referred to as: (1) Canoe Reach North, an area ~15 km southeast of Valemount near the intersection of the Purcell Thrust and SRMT faults; and (2) Canoe Reach South, an area ~30 km southeast of Valemount in the vicinity of the Canoe River thermal spring (see Figure 4.3). This region has an extensive history of deformation that has juxtaposed blocks of Paleoproterozoic basement gneisses and thin, discontinuous layers of metasediments. Some samples of foliated metamorphic rocks such as schist and gneiss have demonstrated electrical anisotropy, where electrical resistivity is highly dependent on the measurement direction (e.g. Mareschal et al., 1992; Mathez et al., 1995; Rauen & Lastovickova, 1995) which may be due to graphite or other conductive phases. To consider the possibility of anisotropic lithology at Canoe Reach, the inversions of MT data described below all utilized both isotropic and anisotropic inversion algorithms. The resulting resistivity models have considerable differences that suggest that anisotropic modeling is necessary in a structurally complicated setting such as Canoe Reach. Additionally, interpretation of low resistivity features in these resistivity

models requires care due to limited geological information. While low resistivity may reasonably correspond to fluids in the vicinity of the Canoe River thermal spring, other conductive phases such as connected graphite or sulfides may also cause a low resistivity.

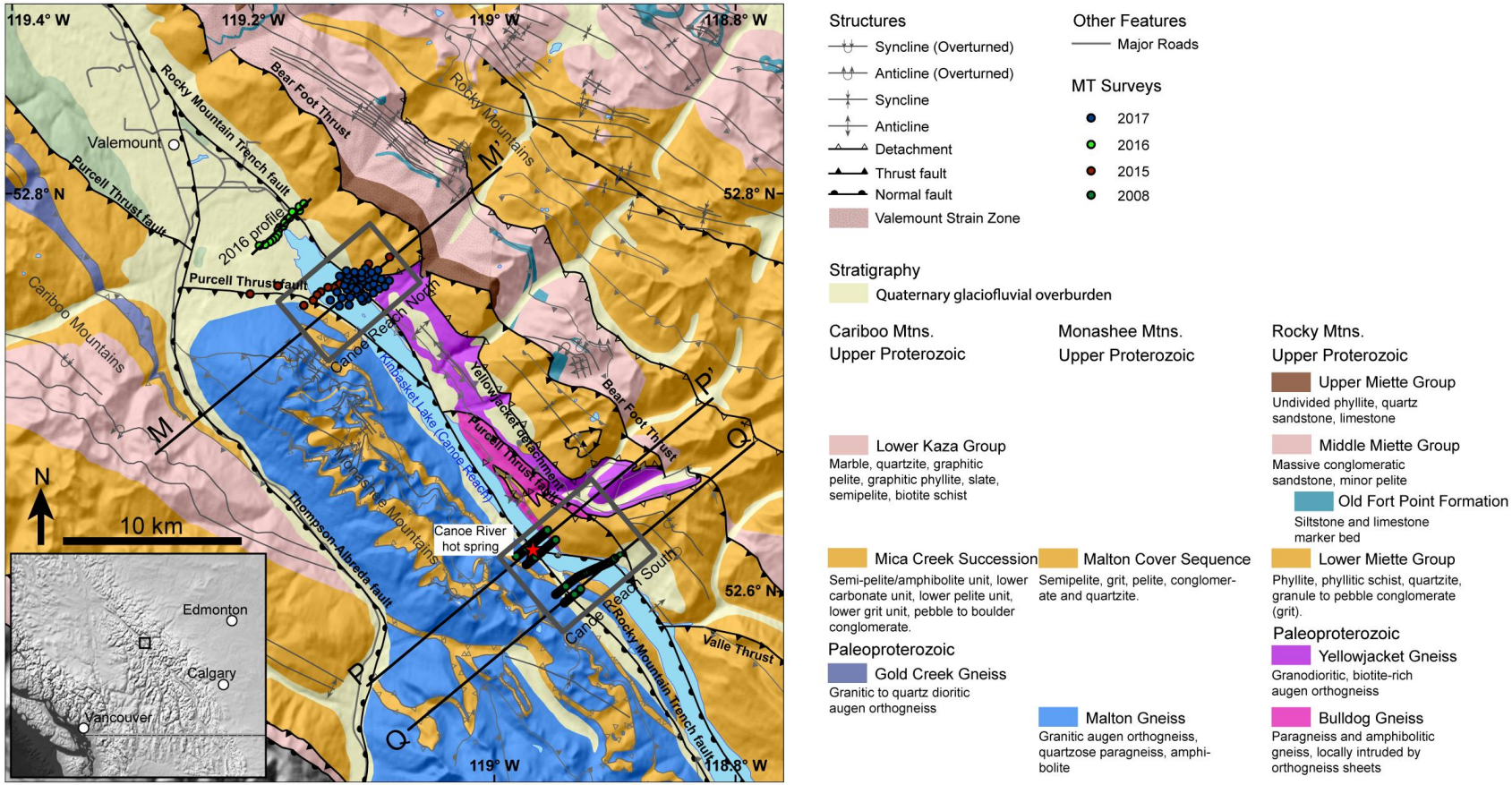


Figure 4.3: Geological map of the Rocky Mountain Trench area southeast of Valemount. Grey boxes show the locations of the Canoe Reach North and South study areas. Map compiled from McDonough et al. (1991), McDonough & Morrison (1990), McDonough & Mountjoy (1990), and McDonough & Murphy (1994).

## 4.2. Geological setting

### 4.2.1. Regional tectonics

The Canadian Cordillera has traditionally been considered an accretionary orogen, that developed with the addition of allochthonous terranes to the western margin of North America from the Jurassic to the Paleogene (e.g. Monger et al., 1982). A competing interpretation has argued in favor of a collisional orogen of a composite continent to the west coast of North America in the Late Cretaceous (Hildebrand, 2015; Johnston, 2008).

The Canadian Cordillera is often divided into five distinct physiographic belts (Monger et al., 1982). From east to west, these are the: Foreland, Omineca, Intermontane, Coast, and Insular belts. The Foreland and Omineca Belts are separated for much of the length of the Cordillera by the Rocky Mountain Trench (RMT), a major NNW-SSE trending valley that extends about 1600 km from Montana to the northern border of British Columbia. Beyond this point the RMT is concurrent with the Tintina Trench that extends another ~1000 km from Yukon to eastern Alaska. To the east of the RMT are folded and faulted Proterozoic to Mesozoic sedimentary strata of the Foreland Belt, and to the west are predominantly greenschist to amphibolite grade metamorphic rocks of the Omineca Belt that are generally thought to be stratigraphically equivalent to those in the Foreland Belt (Read et al., 1991). The Omineca Belt is also intruded by a significant volume of Jurassic, Cretaceous, and Paleogene plutonic suites, and several high-grade metamorphic core complexes believed to be exhumed crystalline basement are exposed along its western margin. Additionally, metasedimentary and metavolcanics rocks in the westernmost Omineca Belt are believed to belong to the allochtonous Quesnellia Terrane (Klepacki, 1985). The RMT is further divided into two sections: the northern RMT (north of ~54°N) and the southern RMT. The northern RMT coincides with the Northern Rocky Mountain Trench Fault (NRMTF), which continues northward into the Yukon and Alaska, linking with the Tintina Trench/Fault. The NRMTF and Tintina Fault are dominated by dextral strike-slip motion (Gabrielse, 1985; M. C. Pope & Sears, 1997; Roddick, 1967; Struik, 1993) while the SRMTF is characterized by Cenozoic extension that resulted in high-angle, southwest-dipping normal faults (Clague, 1974; Van Der Velden & Cook, 1996). The causes of the contrast in structure between the northern

RMT and the southern RMT are still not conclusively determined. Cenozoic extension may have resulted from NRMTF dextral motion being transformed to southeast-northwest transtension south of about 54°N (Price & Carmichael, 1986; Van Der Velden & Cook, 1996). The remainder of dextral strike-slip displacement south of 54°N is instead thought to have been accommodated on the en-echelon Yalakom, Ross Lake, and Fraser fault system to the west (Price & Carmichael, 1986; Van Der Velden & Cook, 1996).

### 4.2.2. Canoe Reach geology

#### 4.2.2.1. Stratigraphy

This study focuses on the Canoe Reach area, located on the northern arm of the Kinbasket Lake reservoir (see Figure 4.3). The Canoe Reach area is underlain by the Paleoproterozoic Yellowjacket, Bulldog, and Malton gneisses, which all belong to the Malton Gneiss Complex (McDonough & Parrish, 1991). The Malton Gneiss is described as a layered succession of quartzofeldspathic paragneiss, mafic amphibolitic gneiss, and granitoid orthogneiss dated at 1987.3 Ma by the U-Pb zircon method (McDonough & Parrish, 1991). The Bulldog Gneiss is a layered succession of quartzofeldspathic paragneiss and amphibolitic gneiss intruded by sheets of orthogneiss dated at 1870 Ma by Mcdonough & Parrish (1991). The Yellowjacket Gneiss is a granodioritic orthogneiss also dated to 1870 Ma by Mcdonough & Parrish (1991). The NNW-SSE trending SRMTF runs along the floor of the SRMT and separates the Yellowjacket and Bulldog gneiss on the east from the Malton gneiss on the west. The Lower Miette Group is a Neoproterozoic (1000 - 540 Ma) parautochthonous unit consisting of a thin and discontinuous lower granule sandstone unit overlain by a thick quartzite and calc-silicate bearing pelite (McDonough & Simony, 1988). The Lower Miette Group is correlated across the SRMTF as a quartzite-pelite cover sequence unconformably overlying the Yellowjacket and Bulldog Gneisses and thin infolds of a lithologically equivalent quartzite-pelite unit within the Malton Gneiss. Mylonitic fabric observed at the basement-cover contact between the Yellowjacket/Bulldog/Malton Gneiss and overlying Miette Group is interpreted to represent a basal detachment with unknown (but probably minor) displacement (McDonough & Simony, 1988).

#### 4.2.2.2. Structure and metamorphism

The structural evolution of the Valemount area is described in detail by McDonough & Simony (1988) and is briefly summarized here. The first episode of deformation is expressed by the Yellowjacket detachment, the mylonitic contact between parauthochtonous Lower Miette metasediments and the underlying Yellowjacket, Bulldog, and Malton Gneisses. The Yellowjacket detachment was active prior to peak staurolite-kyanite-grade metamorphism. It is generally horizontal to shallowly-dipping over much of the study area.

The Bear Foot Thrust is a pre- to syn-metamorphic dextral-reverse structure that brought the Yellowjacket Gneiss and overlying Lower Miette cover northeastward overtop of the Middle Miette Group. The timing of amphibolite-facies metamorphism and oblique thrusting on the Bear Foot Thrust is constrained between 165 and 100 Ma, and offset is estimated to be at least 50 km (McDonough & Simony, 1988). A zone of highly NW-SE lineated Middle Miette pebble conglomerate in the footwall of the Bear Foot thrust is known as the Valemount Strain Zone (McDonough & Simony, 1989).

The Purcell Thrust is a post-metamorphic, regional thrust fault that truncates earlier structures (e.g., the Bear Foot Thrust) in its footwall. The Purcell Thrust carried the Bulldog and Malton Gneiss over the Yellowjacket Gneiss and its cover. Overprinting of mylonite by brittle fractures suggests uplift of 5 - 8 km from a ductile regime at 15 - 18 km depth. Total offset is estimated to be around 15 km (McDonough & Simony, 1988).

The North Thompson – Albreda Fault (NTAF) is a post-metamorphic, Eocene, west-side-down brittle normal fault separating the Monashee Mountains in the east from the Cariboo Mountains to the west. A vertical offset of about 4 km is needed to explain the contrast in metamorphic isograds across the fault (Pell & Simony, 1981). The Purcell Thrust is offset by about 3 km along the NTAF near the town of Valemount, where the NTAF terminates at the SRMT (Murphy, 1990b).

Similar to the NTAF, the SRMTF in the SRMT postdates metamorphism and is believed to be a west-side-down normal fault with a dip separation of up to 2 km (McDonough & Simony, 1988). Estimates of dextral strike separation along the SRMTF range from less than 10 km (McDonough & Simony, 1988), to 55 km (Murphy, 1990a). A larger estimate of up to 60 km of dextral strike separation was proposed north of Canoe Reach, in the Walker Creek fault zone (54°N), near the transition between the NRMT and the

SRMT (McMechan, 2000). Farther north, dextral strike separation of faults within the NRMT and Tintina Trench was estimated to be 450 to 750 km (Gabrielse, 1985; Tempelman-Kluit, 1979). Other workers estimated up to 1500 km of dextral strike separation along the combined NRMT and SRMT (Chamberlain & Lambert, 1985; Lambert & Chamberlain, 1988).

### 4.2.3. Canoe River thermal spring

Several studies have conducted geochemical analyses of the Canoe River thermal spring discharge to understand the underlying reservoir. Recent estimates of the Canoe River spring reservoir temperature from various geochemical geothermometers are 135°C ($SiO_2$), 230°C (Na/Li), and 260°C inferred from Na/K (Ghomshei, 2007). Fairbank & Faulkner (1992) obtained temperatures of 187°C from Na-K-Ca and 129°C from $SiO_2$ geothermometers. Ghomshei (2007) suggested that the $SiO_2$ geothermometer (135°C) may underestimate the reservoir temperature due to mixing of the thermal spring water with surface water. On the other hand, the Na/K geothermometer may be inaccurate for high concentrations of Ca, and some Ca/Na concentrations reported by Ghomshei (2007) may not be suitable for the Na/K geothermometer following the guideline of Karingithi (2007). Though they did not consider the Canoe River spring, Grasby et al. (2000) took the average of the $SiO_2$ and Na-K-Ca geothermometers for other silicate-hosted springs in the Cordillera. Given the position of the Canoe River spring in the center of the predominately silicic Malton Gneiss Complex, the combination of these two geothermometers may be similarly appropriate, and would suggest a reservoir temperature of 158°C. While there is some discrepancy between the various geothermometers, even the lowest of these temperatures suggest viability for direct use or even electricity generation via binary cycle power plant (Franco & Villani, 2009).

In order to fully understand the nature of the Canoe River spring, parameters such as the host rock and fault permeability, infiltration rate, topography, and heat source need to be studied (e.g. C. B. Forster & Smith, 1988). The spring is located on the eastern edge of the Omineca Belt, a region of high heat flow (~80 $mW/m^2$) likely due to high radiogenic heat production in the crust and/or a shallow asthenosphere (Davis & Lewis, 1984; Hyndman & Currie, 2011). Despite these possible heat sources, the locations of thermal springs in the

Canadian Cordillera are not necessarily correlated with regions of high heat flow (Ferguson & Grasby, 2011; Grasby & Hutcheon, 2001). The origin of the enhanced rock or fault permeability at the Canoe River spring is also not fully understood, although the 50 l/s discharge rate computed by Ghomshei (2007) suggests that bulk permeability is high enough for convective heating of groundwater. Infiltration rate also has a large effect on thermal spring discharge. The stable isotope composition of thermal spring waters in the Canadian Cordillera is consistent with a local meteoric source (D. M. Allen et al., 2006; Phillips, 1994); thus mean annual precipitation can be used as an estimate for infiltration rate (C. B. Forster & Smith, 1988). Grasby & Hutcheon (2001) did not find a strong correlation between thermal spring locations and mean annual precipitation in the Canadian Cordillera, suggesting that infiltration rate is not a strong control on thermal spring location in the Canadian Cordillera. The topography profile was another parameter studied in numerical simulations of mountain groundwater flow by C. B. Forster & Smith (1988). The typical topographic profile in the Canadian Cordillera is generally concave as expected for a glaciated mountain belt (Grasby & Hutcheon, 2001), and therefore does not contain as large a recharge area as the opposite extreme, a convex profile (C. B. Forster & Smith, 1988). This fact, along with broad consistency of topographic profiles throughout the Canadian Cordillera, does not help explain the location of the Canoe River spring. As Grasby & Hutcheon (2001) concluded, the primary control on distribution of thermal springs in the southern Canadian Cordillera is the existence of brittle fractures in the crust that provide sufficient permeability for the flow of heated groundwater.

For well-constrained examples in the eastern Foreland belt (e.g., Banff hot springs), Grasby & Hutcheon (2001) propose that precipitation on topographic highs percolates vertically through the mountain massif until it encounters a shallow-angle fault at depth. Due to the fact that faults are often impermeable to cross-fault flow, but highly permeable to fault-parallel flow (Caine et al., 1996), groundwater is forced to the surface where faults outcrop in fault-controlled valley bottoms. This model does not offer an explanation for the specific location of discharge along strike, and is also less easily applied to thermal springs in more structurally complex regions in the Cordilleran hinterland. Other work in hydrothermally-active regions in the southwest US and New Zealand has identified specific features of fault zones that are conducive to thermal upwellings (Curewitz & Karson, 1997; Faulds & Hinz,

2015; Sibson, 1996). These include: fault intersections, local zones of extension (e.g., pull-aparts), and fault segments with increased complexity (e.g. multiple splays). Near the Canoe River thermal spring, a footwall splay of the SRMTF mapped by McDonough & Morrison (1990) that intersects with the main fault zone may be an example of one of these features. The MT method, which is sensitive to electrically conductive fluids in the crust, may allow the imaging of hydrothermal fluid pathways, and provides an indication of the structural controls on the localization of the Canoe Reach spring.

## 4.3. MT data at Canoe Reach

### 4.3.1. Summary

In 2008 Quantec Geoscience Ltd. collected a total of 109 MT soundings in the Canoe Reach South area (see Figure 4.3). The MT soundings were collected over four SE-NW profiles with a station spacing of 100 m. Stations located on Kinbasket Lake were collected with specialized lake-bottom sensors. Lines A and B intersect the location of the Canoe River thermal spring. The processed MT data yielded impedance data in the frequency range 10,000 - 0.001 Hz. No tipper data were collected during the Canoe Reach South MT surveys.

A total of 73 broadband MT stations were collected at Canoe Reach North in the summers of 2015, 2016, and 2017 with the goal of resolving the location and structure of the SRMTF and other faults inferred to be below and adjacent to Kinbasket Lake. The deployments were completed by a joint project between the University of Alberta and Borealis GeoPower Inc. as part of their exploration in this region. A Phoenix Geophysics Ltd. broadband MT system was deployed for approximately 6 – 18 hours at each station, resulting in data in the frequency band 300 – 0.001 Hz. The inter-station spacing was approximately 250 – 500 m.

During 2015 and 2017 the MT stations were collected across the floor of the SRMT when the Kinbasket Lake level was low. Station placement at the edges of the profile on the SRMT slopes was limited by steep topography and dense vegetation. These stations were collected in a 3-D array to be used for a high resolution, 3-D analysis of the Canoe Reach geothermal prospect. In 2016, MT stations were collected along a ~ 5 km profile located 10

km SE of Valemount (green circles in Figure 4.3). The single profile only allowed for 2-D inversion of these data. These results are included in Appendix B.1.

### 4.3.2. Canoe Reach North: MT data from the 2015-2017 grid

Figure 4.4 shows maps of apparent resistivity and phase data for stations in the Canoe Reach North grid. The data are displayed using a nearest-neighbor interpolation. Each map shows data at a single frequency, where a lower frequency corresponds to a greater depth in the Earth. The *xy* and *yx* components of the data are shown, where $\rho_{xy}$ corresponds to the apparent resistivity calculated from the electric field polarized in the *x* direction and the magnetic field in the *y* direction. The outline of Kinbasket Lake at a high water level is shown for reference, but the MT stations were collected when the water level was low and the lake bed was exposed. The data at each of the four frequencies will be described below.

Map views of phase tensor ellipses also reveal spatial variations in subsurface resistivity structure. The phase tensor is unaffected by galvanic distortion and gives an estimate of the subsurface structure dimensionality (i.e. 1-D, 2-D, or 3-D). Additionally, the phase tensor principal axes are aligned with the direction of maximum inductive current flow, which is a 3-D generalization of the 2-D geoelectric strike. Induction arrows calculated from tipper data are also used to examine variations in subsurface resistivity. Induction arrows are sensitive to lateral resistivity variations and point toward conductors when plotted in the Parkinson convention (Parkinson, 1959). Together, the phase tensor and induction arrows give complementary information about the subsurface resistivity. Figure 4.5 shows the Canoe Reach North phase tensor ellipses and induction arrows at four frequencies. The apparent resistivity, phase, induction arrows, and phase tensor ellipses at each frequency are described below.

- Frequency = 100 Hz

  The first row of Figure 4.4 shows a frequency of 100 Hz where the *xy* and *yx* apparent resistivity data are very similar. Some stations on Kinbasket Lake have anomalously low apparent resistivity due to small near-surface conductors such as pools of water and mud patches. These amplitude shifts can be attributed to local electric field distortions (static shifts) because these anomalies do not appear in the

phase data. The phase data show that stations on Kinbasket Lake have phase values less than 45° indicating increasing apparent resistivity with depth. Stations on the northeastern and western edges of the survey area have phases greater than 45° that indicate decreasing resistivity with depth.

At a frequency of 100 Hz, phase tensor ellipses on Kinbasket Lake have low skew angles (< 3°) while stations on the northeast shore show local variations in phase tensor azimuth and skew (Figure 4.5a). The low skew angles and circular ellipses suggest 1-D or 2-D structure below the lake at this frequency, but the large variation in ellipse azimuths on the northeast shore of Kinbasket Lake suggests an underlying 3-D resistivity structure.

Most stations have small induction arrow magnitudes at this frequency. Some induction arrows on the northeast shore point NNE, and may be sensitive to a conductor outside of the survey area.

- Frequency = 10 Hz

Stations on Kinbasket Lake are sensitive to a conductor as both the *xy* and *yx* phase data are greater than 45°. Stations on the northeastern and western edges of the survey area also have high phase values approaching 90° which indicate the presence of a conductive body.

Figure 4.5b shows a clear distinction between phase tensor ellipses on the lake bed and on the northeast shore, similar to the apparent resistivity and phase data. Phase tensor ellipses on the lake bed have smaller skew (< 5°) and are aligned to approximately N45°E. The phase tensor ellipses on the northeast shore show more variation in azimuth and larger skew angles, with some skew angles greater than 10°.

Induction arrow magnitudes are small at this frequency. Some induction arrows on the northeast shore point toward the NE, while some on the lake point NNW.

- Frequency = 1 Hz

The phase data on Kinbasket Lake return to values below 45° as the data are sensitive to a resistor below the lake. Stations on the northeastern edge of the survey

have anomalously high phases, and some stations even have an out of quadrant *yx* phase. This effect can be caused by deflections of the electric field from particular 3-D geometries or anisotropic resistivity structure.

At this frequency the majority of phase tensor ellipses align to about N45°E (Figure 4.5c). It is possible that these stations are sensitive to the same regional resistivity structure at this frequency. Induction arrows on the lake point to the NW and may be sensitive to a regional conductor outside of the survey area.

- Frequency = 0.1 Hz

At this frequency there is a large contrast between the high (>100 Ωm) apparent resistivity on the lake and the low (~ 1 to 10 Ωm) apparent resistivity on the northeast shore. The majority of stations have *xy* and *yx* phases above 45° indicating the presence of a deep, regional conductor below Canoe Reach.

At this frequency the phase tensor major axes are aligned WNW, which is approximately perpendicular to those at a frequency of 1 Hz (Figure 4.5d). Most ellipses have relatively low skew angles (< 5°) in contrast to higher values at frequencies of 10 and 1 Hz.

The induction arrows at most stations point northeast. This observation, along with the consistent spatial alignment of phase tensor ellipses, suggests that the data are sensitive to a deep regional structure at this frequency.

In summary, the MT data at Canoe Reach North exhibit indications of 3-D resistivity structure including (1) out-of-quadrant phases and (2) phase tensor skew angles greater than 5°. These unusual observations could also be indicators of electrical anisotropy. However, it is difficult to identify whether MT data are affected by 3-D structure, anisotropy, or both. Out-of-quadrant phases in MT data have been demonstrated for 2-D anisotropic resistivity models (e.g. Heise & Pous, 2003). Therefore, the possibility of electrically anisotropic structure should be investigated at Canoe Reach North.

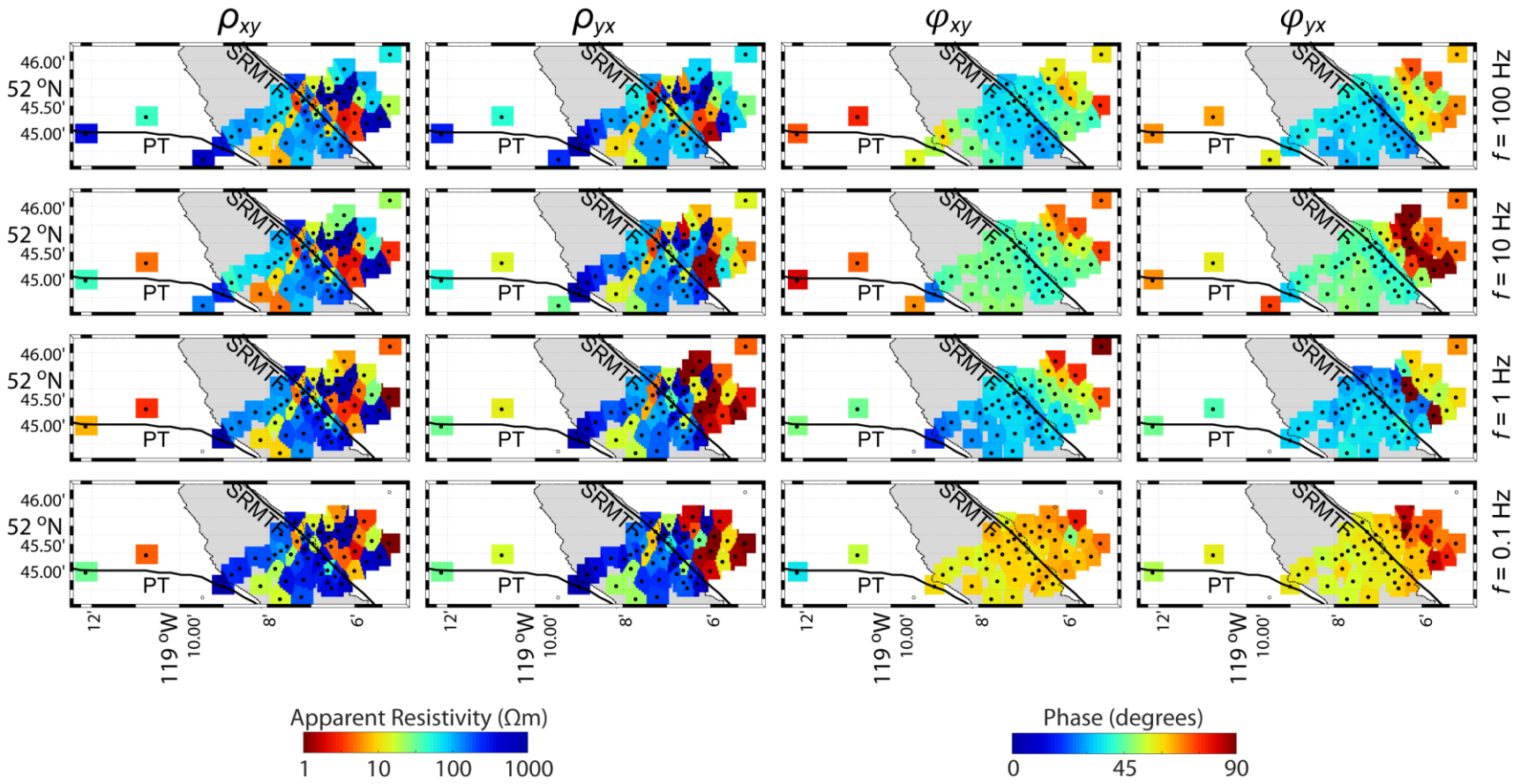


Figure 4.4: Maps of Canoe Reach North apparent resistivity ($\rho$) and phase ($\varphi$) data at four frequencies. *xy* (*yx*) = data from electric field polarized to geographic north (east). Black points show locations of MT stations. Grey shading = Kinbasket Lake. SRMTF = Southern Rocky Mountain Trench Fault; PT = Purcell Thrust.

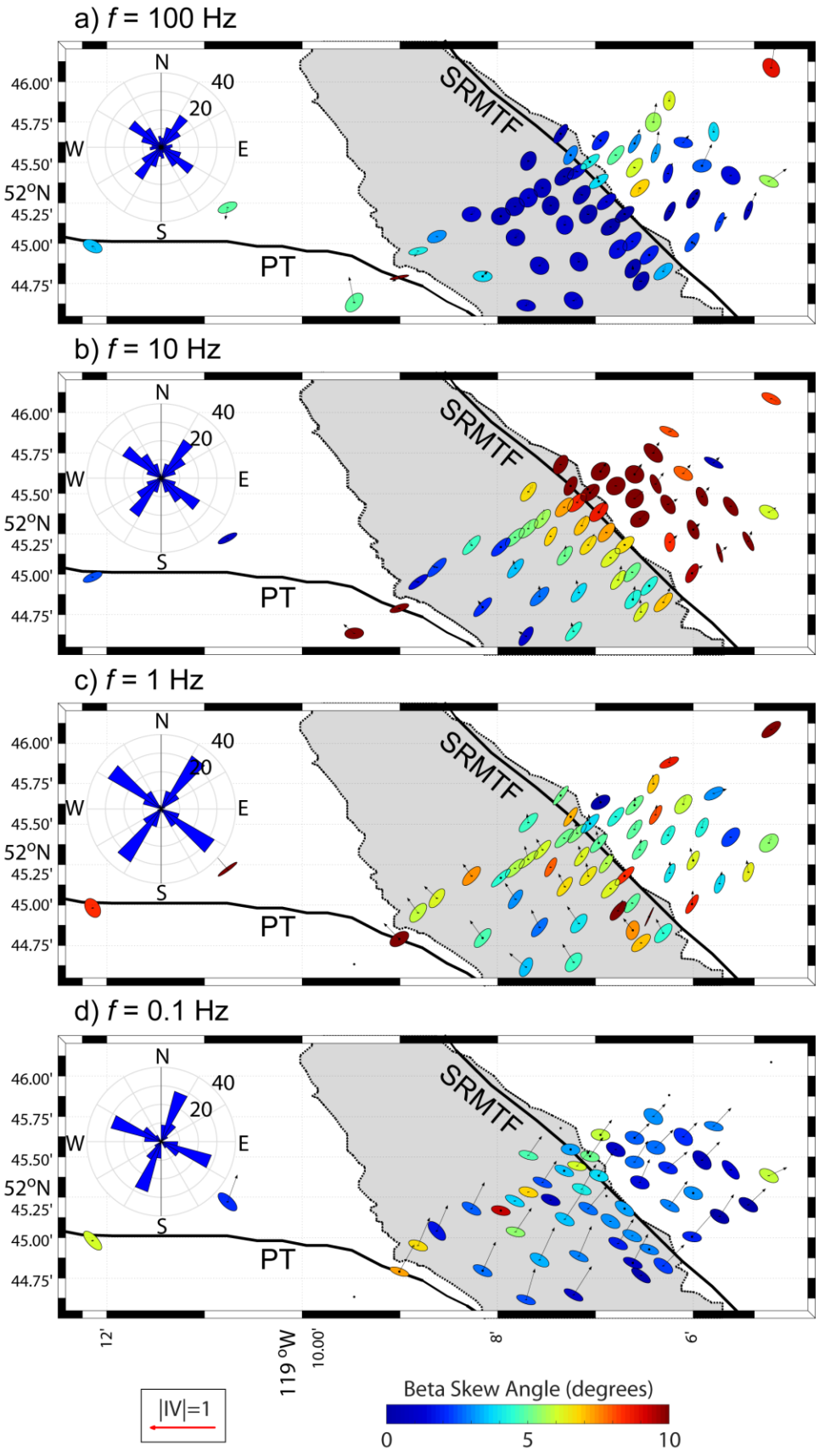
a) f = 100 Hz
b) f = 10 Hz
c) f = 1 Hz
d) f = 0.1 Hz
N
E
S
W
40
20
SRMTF
PT
46.00'
45.75'
45.50'
52°N
45.25'
45.00'
44.75'
12'
119 °W
10.00'
8'
6'
|IV|=1
Beta Skew Angle (degrees)
0
5
10

Figure 4.5: Phase tensor ellipse and induction arrow maps of Canoe Reach North MT data at four frequencies. The lengths of the phase tensor ellipse axes are normalized to the maximum phase tensor value. Inset rose diagram shows histogram of phase tensor azimuth at each frequency. Grey shading = Kinbasket Lake. SRMTF = Southern Rocky Mountain Trench Fault; PT = Purcell Thrust. Induction arrow (IV) magnitude = 1 shown as red arrow.

### 4.3.3. Canoe Reach North: MT data from the 2016 profile

This section describes the MT data collected in a SW-NE profile located about 10 km SE of the town of Valemount (see Figure 4.3). Maps of the apparent resistivity and phase data are shown in Figure 4.6 and maps of phase tensor ellipses and induction arrows are shown in Figure 4.7. The data are shown at four representative frequencies described below.

- Frequency = 100 Hz

  At this frequency both the *xy* and *yx* apparent resistivities are greater than 100 Ωm in the middle of the profile. The SW and NE ends of the profile generally have a lower resistivity. The *xy* phase is less than 45° in the middle of the profile, indicating an increasing resistivity with depth. Stations at the SW and NE ends have *xy* phases greater than 45°, indicating a decreasing resistivity with depth. The *yx* phases are generally greater than or equal to 45°, suggesting a decrease in resistivity with depth. Similar to the *xy* phases, the *yx* phases are higher for stations at the SW and NE ends of the profile.

  Phase tensor ellipses above the middle of the profile are not clearly aligned and have low skew angles ($\beta < 3°$). Stations at the NE and SW ends of the profile have higher skew angles ($\beta > 3°$) and might be sensitive to off-profile features. Induction arrow magnitudes are generally small except in the NE, where arrows point away from the profile toward the NE.

- Frequency = 10 Hz

  At this frequency, stations in the middle of the profile have higher apparent resistivity values than those on the SW and NE ends. The phase angles have a similar trend to those at 100 Hz. However, the three stations at the NE end clearly have

higher phases than the rest of the stations. At this frequency and lower frequencies, it is clear that the data at these three stations differ from stations in the middle of the profile. The station on the SW end of the profile is also distinct with a lower *yx* apparent resistivity (< 10 Ωm) than the stations in the middle of the profile.

The phase tensor ellipses also show a clear difference between stations at the ends of the profile and those in the middle of the profile. At this frequency, ellipses in the middle of the profile show a SW-NE alignment with $\beta < 4°$, which is indicative of a 2-D resistivity structure. Ellipses at the NE and SW end of the profile have higher skew angles ($\beta > 4°$) and are not aligned with ellipses in the middle of the profile. Induction arrows in the NE side of the profile tend to point toward the NE, and those on the SW end point toward the SW. These data might be sensitive to conductors located outside of the survey area. Interestingly, the station at the SW end of the profile has an induction arrow that points toward the NE, which is the opposite direction of the neighboring station. In a 2-D Earth this would indicate a conductor located between the two stations, but more stations to the SW are needed to confirm this idea.

- Frequency = 1 Hz

At this frequency, some stations on the NE end of the profile have very low apparent resistivities (< 3 Ωm). Both the *xy* and *yx* phases are less than 45° at all other stations, which might be a response to a large resistor. Most phase tensor ellipses are still aligned to the SW-NE. Induction arrows are still small in magnitude and do not show a regular alignment for all stations.

- Frequency = 0.1 Hz

The apparent resistivity maps appear similar to those at a frequency of 0.1 Hz. However, there is a noticeable difference in the phase maps. All stations have phases greater than 45°, which might be a response to a regional-scale conductor similar. The stations in the 2015-2017 grid also have phases greater than 45° at a frequency of 0.1 Hz, and therefore may be sensitive to the same structure. Out-of-quadrant phases (>

90°) at the SW and NE ends of the profile might be indicative of 3-D and/or anisotropic structure.

The phase tensor ellipses in the middle of the profile are aligned roughly in the E-W direction, and may be sensitive to a different structure than at a frequency of 1 Hz. The phase tensor ellipses at the NE end of the profile are highly eccentric with high skew angles ($\beta$ > 10°), that may indicate a 3-D and/or anisotropic structure. Induction arrows point to the north and northeast, which is a similar direction to stations in the 2015-2017 grid. This is further evidence that all stations at Canoe Reach North are sensitive to the same regional structure at this frequency.

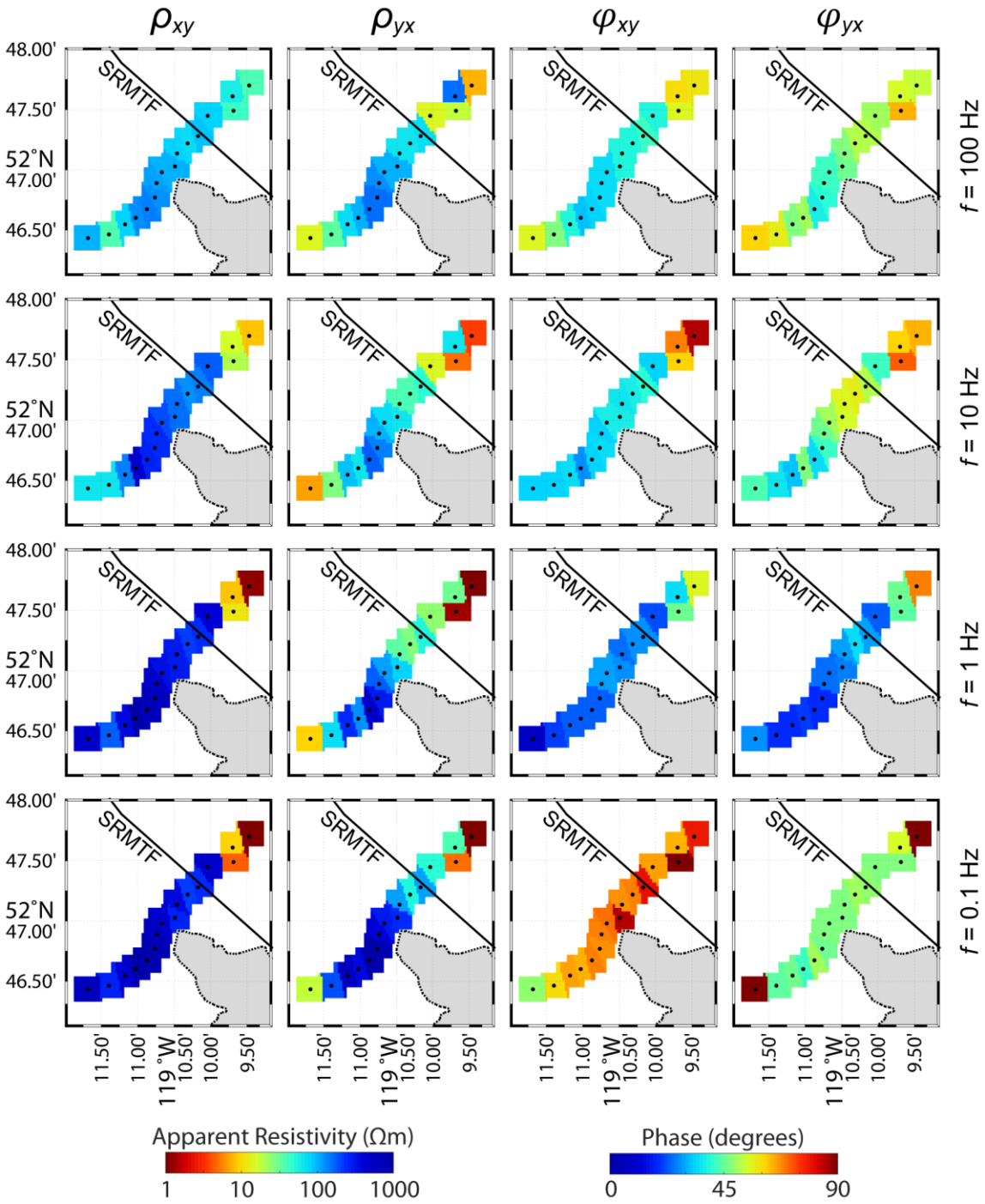


Figure 4.6: Maps of apparent resistivity ($\rho$) and phase ($\varphi$) data from the 2016 profile at Canoe Reach North. Data are shown at four selected frequencies. *xy* (*yx*) = data from electric field polarized to geographic north (east). Black points show locations of MT stations. Grey shading = Kinbasket Lake. SRMTF = Southern Rocky Mountain Trench Fault.

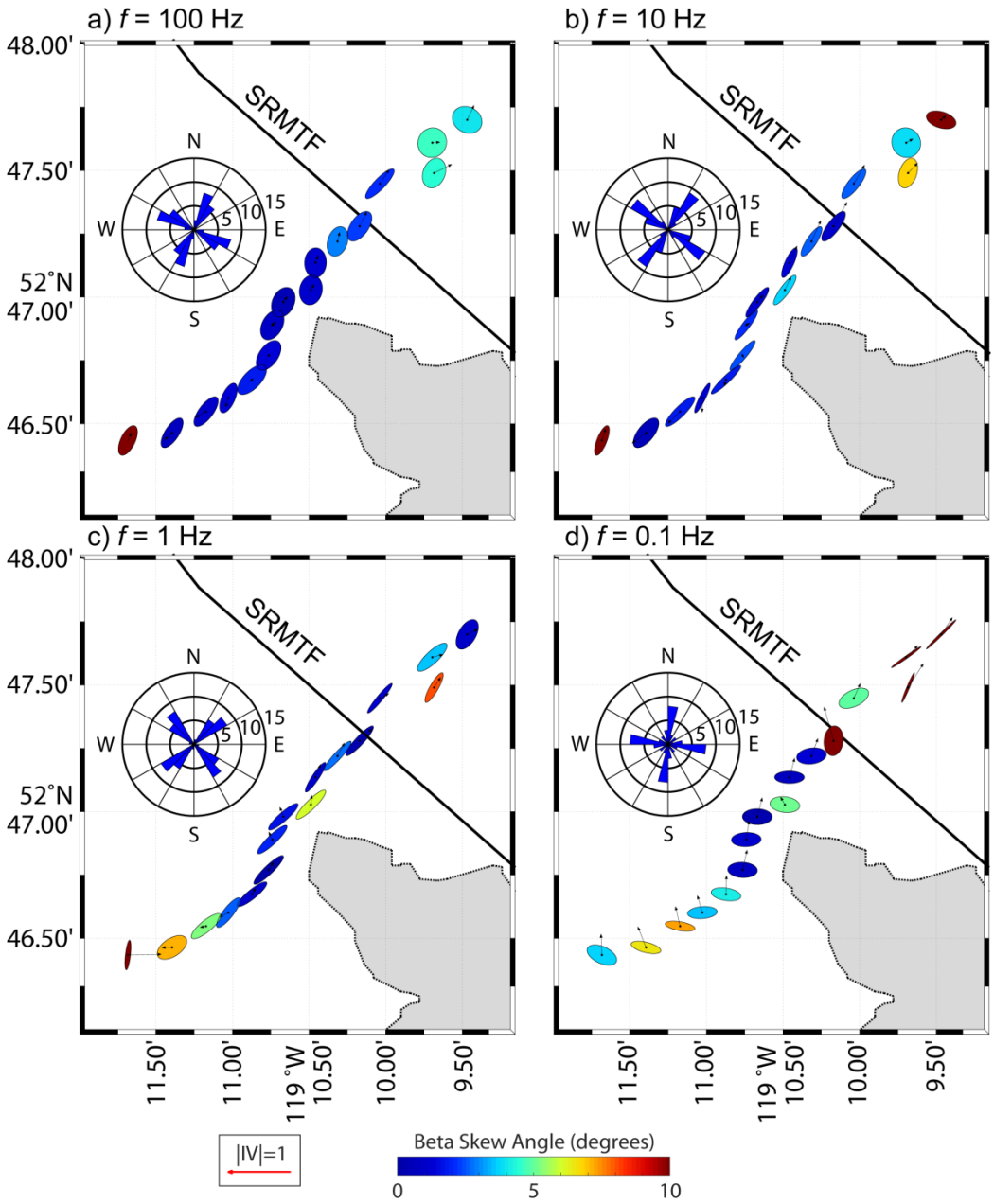


Figure 4.7: Maps of phase tensor ellipses and induction arrows from the 2016 profile in Canoe Reach North. Data are shown at four selected frequencies. The lengths of the phase tensor ellipse axes are normalized to the maximum phase tensor value. Inset rose diagram shows histogram of phase tensor azimuth at each frequency. Grey shading = Kinbasket Lake. SRMTF = Southern Rocky Mountain Trench Fault. Induction arrow (IV) magnitude = 1 shown as red arrow.

### 4.3.4. Canoe Reach South: Lines A and B MT Data

Figure 4.8 shows maps of the Lines A and B apparent resistivity and phase data, and Figure 4.9 shows maps of phase tensor ellipses. Some stations on the Kinbasket Lake shores had noisy data at the highest and lowest frequencies that had to be removed. The data maps show some broad trends in location and frequency described below.

- Frequency = 650 Hz

  Both modes show a high apparent resistivity (> 1000 Ωm) on the lake shores and a lower apparent resistivity (< 100 Ωm) on the lake. Some stations on the northeast side of the profiles have a very high resistivity (> 5000 Ωm) while a few stations have very low resistivity (< 10 Ωm). This may indicate some distortion from small structures causing local static shifts in the data. The *xy* and *yx* phase angles are greater than 45° on the west shore, indicating a decreasing resistivity with depth. Stations on the lake have phase angles less than 45° which means resistivity increases with depth. Two stations exhibit an anomalously high *yx* phase ($\varphi_{yx}$) that smoothly varies with frequency, and therefore may correspond to local 3-D structure.

  Stations on the southwest shore have phase tensor ellipses aligned to the NE with low values of $|\beta|$, suggesting a 2-D structure at this frequency. The ellipse axes are not as uniformly aligned on the lake and some ellipses have $|\beta| > 5°$ which might indicate 3-D structure below the lake.

- Frequency = 100 Hz

  The apparent resistivity maps show similar values and trends as the 650 Hz data. $\varphi_{xy}$ is $\leq 45°$ for all stations while $\varphi_{yx}$ is still greater than 45° for stations on the southwest shore.

  Phase tensor ellipses on the southwest shore are still aligned to the NE with $|\beta| < 5°$. The ellipses on the lake show more uniform alignment to the NNE than at 650 Hz, but there are still anomalously high values of $|\beta|$ close to the northeast shore.

- Frequency = 20 Hz

At this frequency the *xy* apparent resistivity $\rho_{xy}$ is greater than 100 Ωm at all stations, while $\rho_{yx}$ at most stations has increased slightly from a frequency of 100 Hz. $\varphi_{xy}$ is less than 45° at all stations, indicating an increasing resistivity with depth. $\varphi_{yx}$ is also decreasing with frequency at most stations but has higher values than $\varphi_{xy}$.

Phase tensor ellipses on the southwest shore are aligned to the NNE but the alignment shifts to the NE on the lake. Unlike at higher frequencies, stations on the southwest shore have values of $|\beta| > 5°$.

- Frequency = 5 Hz

At this frequency $\rho_{xy}$ is high ( > 1000 Ωm) which follows the increasing trend from higher frequencies. $\rho_{yx}$ is also high on both shores but lower (~ 100 Ωm) on the lake. Similar to the data at 20 Hz, values of $\varphi_{xy}$ are less than 45° at all stations, but stations on the lake have a higher $\varphi_{yx}$ than at 20 Hz, which might be due to a deep conductor.

The phase tensor ellipses are mostly aligned to N30°E. Stations on the southwest shore have $|\beta| < 3°$ and uniformly aligned ellipses, suggesting an underlying 2-D structure at this frequency. Stations on the lake also show a uniform alignment toward the NE, but a few stations still have an anomalously high $|\beta| > 5°$.

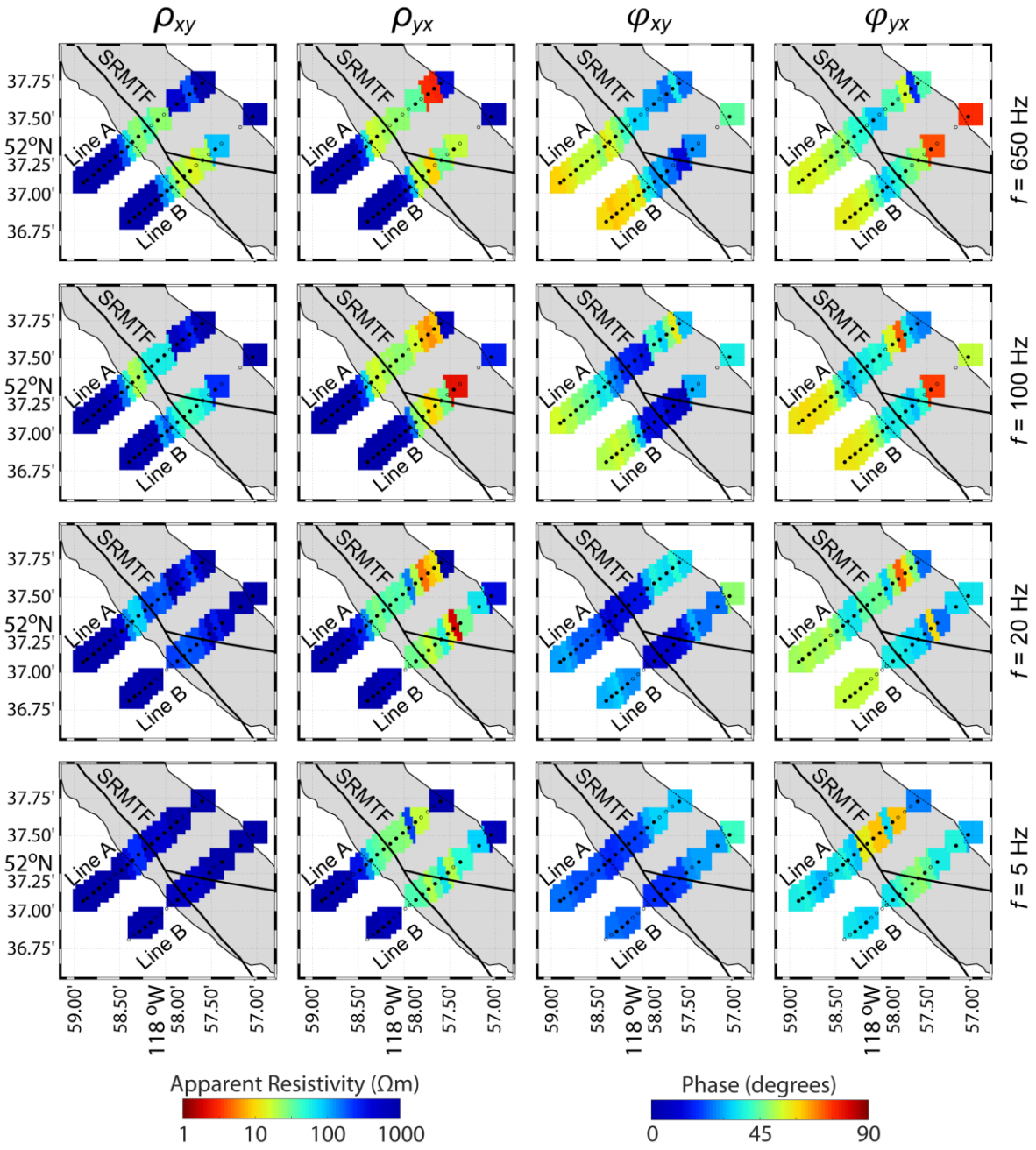


Figure 4.8: Maps of Lines A and B apparent resistivity ($\rho$) and phase ($\varphi$) data shown at four frequencies. *xy* (*yx*) = data from electric field polarized to geographic north (east). Black points show locations of MT stations. Grey shading = Kinbasket Lake. SRMTF = Southern Rocky Mountain Trench Fault.

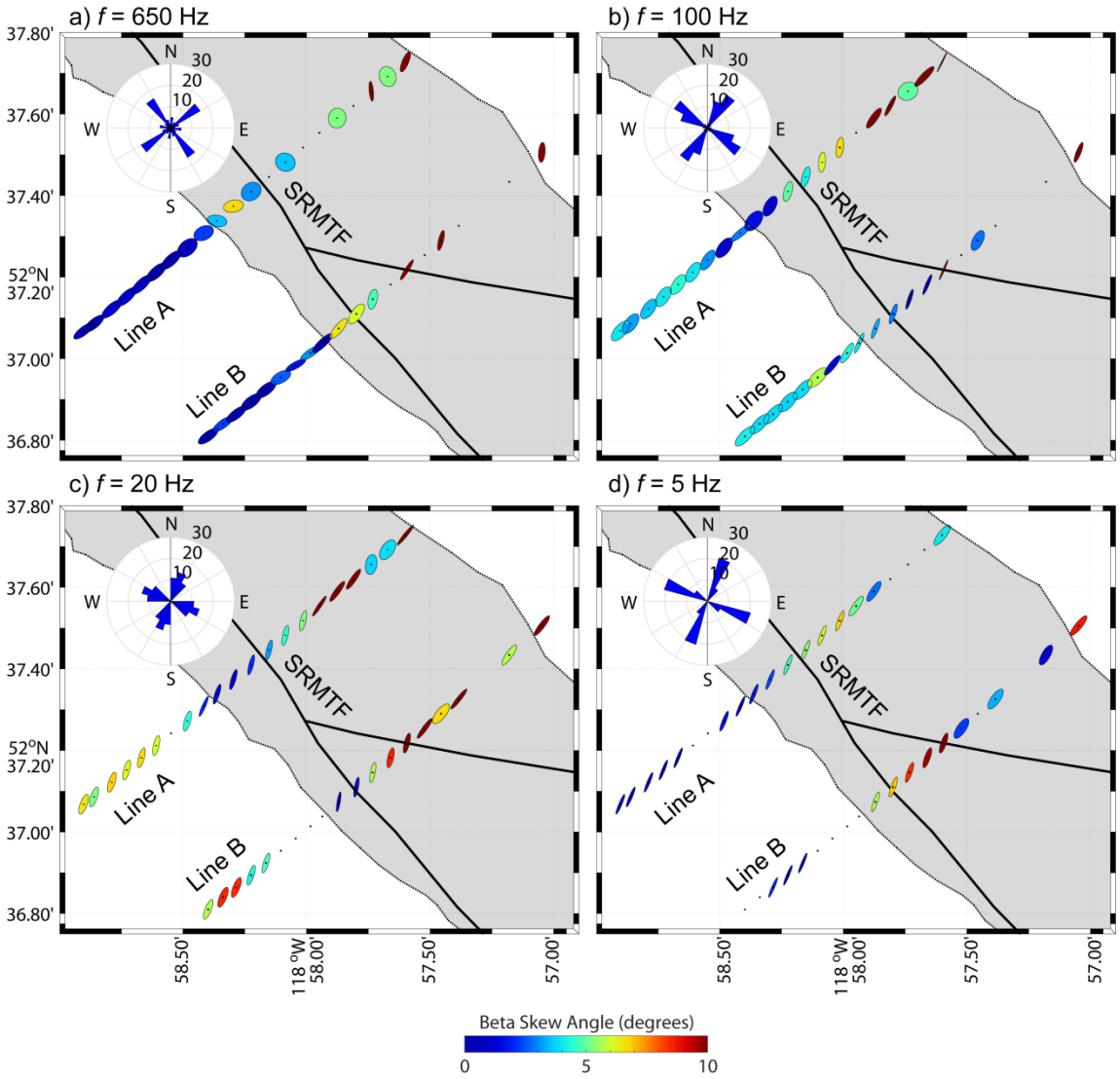


Figure 4.9: Maps of Lines A and B phase tensor ellipses at four frequencies. The lengths of the phase tensor ellipse axes are normalized to the maximum phase tensor value. Inset rose diagram shows histogram of phase tensor azimuth at each frequency. Grey shading = Kinbasket Lake. SRMTF = Southern Rocky Mountain Trench Fault.

### 4.3.5. Canoe Reach South: Lines C and D MT Data

The Lines C and D apparent resistivity and phase data are shown as maps in Figure 4.10, and the phase tensor ellipses are shown as maps in Figure 4.11. Due to the close station spacing, only every second phase tensor ellipse is plotted for clarity. The data are shown at four frequencies which will be described below.

- Frequency = 800 Hz

At this frequency, both $\rho_{xy}$ and $\rho_{yx}$ are high (> 1000 Ωm) on the shores and generally lower on Kinbasket Lake. An exception occurs in the middle of Line D, where $\rho_{yx}$ is low with anomalously high $\varphi_{yx}$. In general, $\varphi_{xy}$ and $\varphi_{yx}$ are greater than 45° on the shores and less than 45° on the lake.

The phase tensor major axes are not oriented in the same direction from station to station, which is likely due to 3-D local variations in resistivity.

- Frequency = 100 Hz

The apparent resistivity maps are similar to those at 800 Hz. However, at this frequency there is a noticeable difference between $\varphi_{xy}$ and $\varphi_{yx}$. While most stations on the lake and the northeast shore have $\varphi_{xy}$ and $\varphi_{yx}$ greater than 45°, stations on the southwest shore have $\varphi_{xy}$ less than 45°.

At this frequency the phase tensor ellipses on the southwest shore are aligned to the NE with the exception of the anomalous stations in the middle of Line D. However, the ellipses on the northeast side of Line C are oriented toward the NW.

- Frequency = 20 Hz

Stations on the southwest and northeast shore still have higher apparent resistivities than those on the lake, and have phase angles ≤ 45°. Stations in the middle of Line D still have anomalously high $\varphi_{yx}$. Most stations on the lake have high phase angles greater than 60°, indicating a rapidly decreasing apparent resistivity with depth.

The phase tensor major axes are aligned toward the NE on the southwest shore but an aligned toward the NW on the northeast side of Line C. Many stations on the lake have $|\beta| > 5°$, which indicates an underlying 3-D resistivity structure.

- Frequency = 5 Hz

The apparent resistivity maps are similar to those at 20 Hz. The apparent resistivities on the southwest shore are still high (> 1000 Ωm) and the apparent

resistivities on the lake have decreased to less than 10 Ωm. The phase maps are also similar to those at 20 Hz except that $\varphi_{xy}$ is less than $\varphi_{yx}$ on the lake.

The phase tensor ellipse orientations are similar to those at 20 Hz. However, at this frequency all ellipses on the lake have their major axes aligned to the NW and the alignment clearly transitions to the NE at the southwest shore.

The Lines C and D phase tensor ellipses at frequencies of 20 and 5 Hz have similarities to those at Lines A and B at the same frequencies. The stations on the southwest shore on all 4 lines have ellipses oriented to the NE, which suggests that these stations might be sensitive to the same regional structure. The stations on Kinbasket Lake generally have higher values of $|\beta|$ than those on the southwest shore, which might indicate 3-D structure beneath the lake.

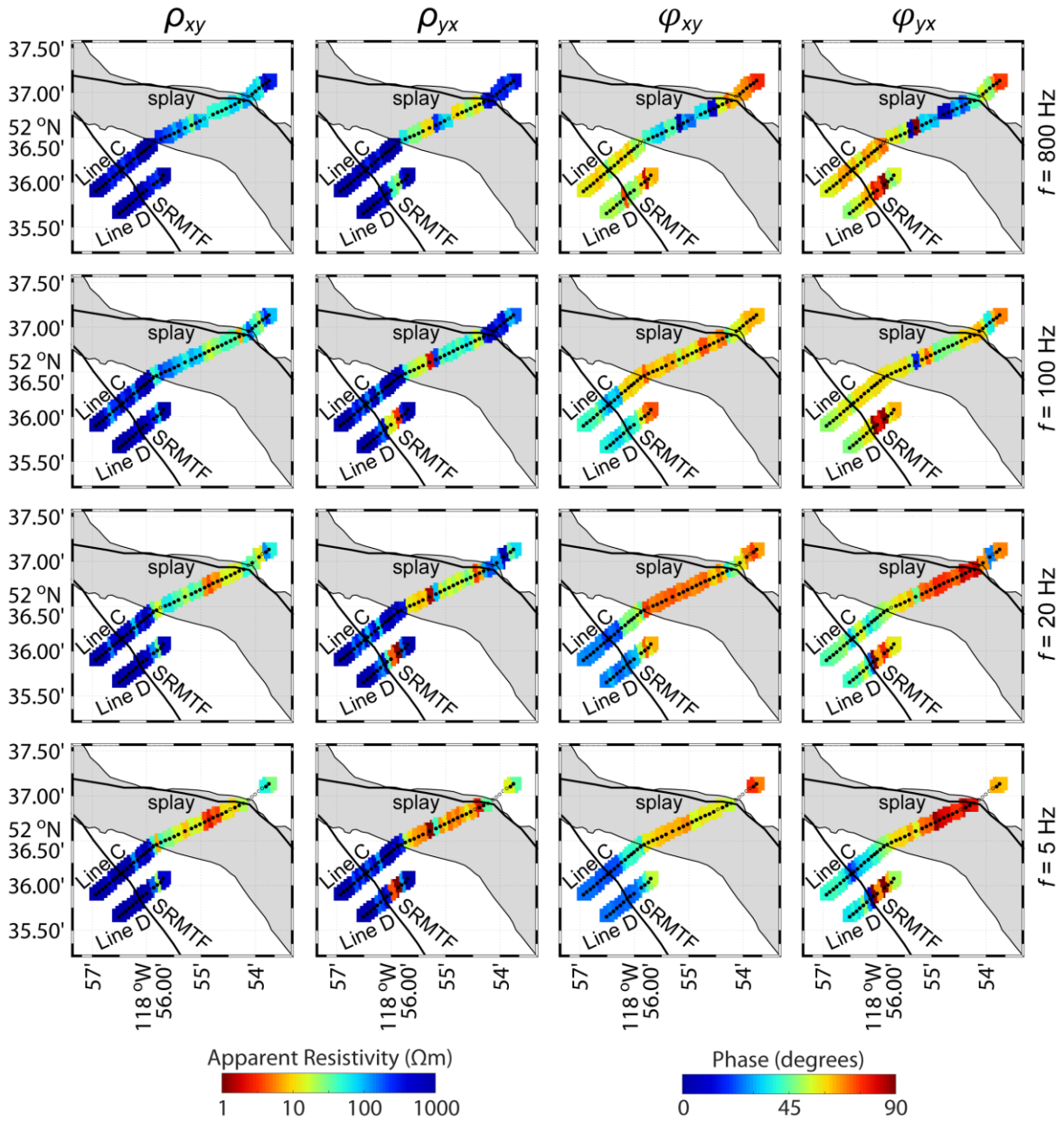


Figure 4.10: Maps of Lines C and D apparent resistivity ($\rho$) and phase ($\varphi$) data shown at four frequencies. *xy* (*yx*) = data from electric field polarized to geographic north (east). Black points show locations of MT stations. Grey shading = Kinbasket Lake. SRMTF = Southern Rocky Mountain Trench Fault; splay = mapped splay of the SRMTF.

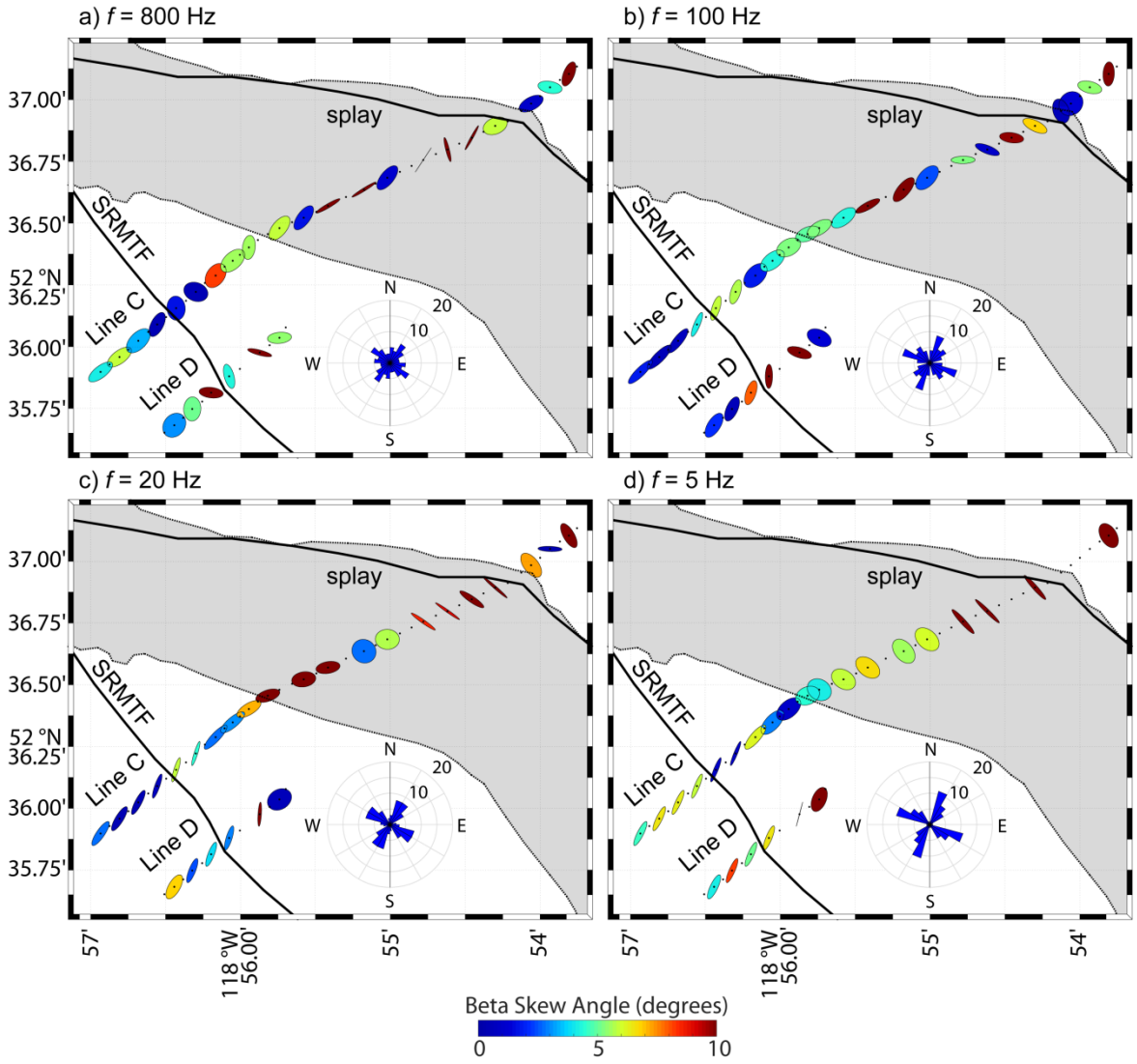


Figure 4.11: Maps of Lines C and D phase tensor ellipses at four frequencies. The lengths of the phase tensor ellipse axes are normalized to the maximum phase tensor value. Inset rose diagram shows histogram of phase tensor azimuth at each frequency. Grey shading = Kinbasket Lake. SRMTF = Southern Rocky Mountain Trench Fault; splay = mapped splay of the SRMTF.

## 4.4. 3-D inversions of the Canoe Reach MT data

### 4.4.1. Summary

The MT data described in the previous section were separated into three groups for 3-D inversion: (1) the Canoe Reach North area, (2) Lines A and B in the Canoe Reach South area, and (3) Lines C and D in the Canoe Reach South area. The profile collected in 2016 was not included in the Canoe Reach North 3-D inversion because it is located about 5 km

away from the grid of MT stations. If all stations at Canoe Reach North were included, the large distance between the grid and profile would require a mesh with many cells that would require an impractical amount of computational resources. Therefore, 2-D inversions of the 2016 profile were conducted separately. Figures of the modeled data and the preferred resistivity model are included in the Appendix (Figure B.1 and Figure B.2). Due to the evident 3-D nature of the MT data shown in the previous section, the remainder of this chapter focuses on results from 3-D inversions of the MT data.

This study used isotropic and anisotropic inversions to obtain resistivity models of the Canoe Reach area. The isotropic inversions used the 3-D ModEM code of Kelbert et al. (2014). The anisotropic inversions used a modified version of the ModEM code that solves for axial anisotropy, i.e. the three principal resistivities $\rho_x$, $\rho_y$, and $\rho_z$ (Kong et al., 2020). The off-diagonal terms of the resistivity tensor are assumed to be zero. As a result, the anisotropy strike, dip, and slant angles are zero because this code assumes the anisotropy axes are aligned with the inversion coordinate system.

In this study, the anisotropic inversion axes are aligned to geographic coordinates. This is a limitation of the anisotropic inversion because the true anisotropic axes of any electrically anisotropic lithology may not be aligned to geographic coordinates. Therefore, resistivity contrasts in the true anisotropic axes are projected to the assumed geographic coordinate system. Even if the true anisotropic axes are not aligned to geographic coordinates, the anisotropic inversion can provide qualitative information on anisotropic resistivity contrasts. Future work will explore how the choice of different anisotropic axes in the inversion affects the inversion result.

Table 4.1 contains parameters related to the MT data used in each 3-D inversion. Note that the Canoe Reach North inversions used the full impedance tensor at all stations and tipper data available at 44 stations. The Canoe Reach South inversions only used the full impedance tensor because no tipper data were collected at these stations. Impedance data were assigned an error floor of 5% of $\sqrt{|Z_{xy}\, Z_{yx}|}$ while tipper data were assigned a constant error of 0.02.

Table 4.2 contains a summary of the inversion model parameters. The core cell sizes are the horizontal ($x$, $y$) dimensions of model cells in the area that includes MT stations.

Outside the core area, the models contain padding cells for numerical stability that increase in width by a factor of 1.5. For additional accuracy in modeling, all inversions included topography due to the steep slopes on both sides of the SRMT. In Table 4.2, the layer thickness is the *z* dimension of cells in layers that include topography (i.e. all layers above Kinbasket Lake, which is the lowest topographic point in all models). At the lowest topographic point in the model, layer thickness increases geometrically by the given increase factor. The number of model cells, which represents a trade-off between computation speed and spatial resolution, is also given in Table 4.2. All inversions used a uniform resistivity value for the starting model that was determined from several test inversions. The final root mean square (r.m.s.) misfit of the isotropic and anisotropic inversions is given in Table 4.1.

Mesh design for the Lines C and D inversion was complicated by the fact that the original mesh contained a large number of cells that required an unreasonable amount of computational resources. Therefore, the MT data were down-sampled by only including every second station. This effectively increased the station spacing from 100 m to 200 m. This down-sampling is reasonable when considering the mesh cell size and the approximate depth of investigation of the highest frequency. A common guideline is to include several model cells between neighboring stations in order to allow smooth resistivity variations (Miensopust, 2017). In the down-sampled model the smallest lateral cell size was 50 m, one quarter of the station spacing. Additionally, considering the highest frequency is 3940 Hz, the depth of investigation is 80 m in a 100 Ωm halfspace. Thus it would not be practical to make the cells smaller in order to fit more cells between stations. In order to test the effect of down-sampling, the data were split into two sets: (1) every second odd-numbered station and (2) every second even-numbered station in Lines C and D. Only the data and the resistivity model from the even-numbered inversion are shown here because the two inversions resulted in reasonable data misfit and similar models. See Figure B.19 in the Appendix for a comparison of the odd and even-numbered resistivity models.

Table 4.1: Canoe Reach inversion: data parameters

| Name | Stations | Number of Frequencies | Frequency Range (Hz)<br><br>Maximum<br>Minimum | Responses | Error Floor | Final r.m.s. misfit: iso. / aniso. |
|---|---|---|---|---|---|---|
| Canoe Reach North | 57 | 23 | 320<br>0.0125 | Impedance Tipper | 5%,<br>0.02 | 2.06 /<br>1.59 |
| Lines AB | 40 | 17 | 11440<br>1.4 | Impedance | 5% | 1.37 /<br>1.28 |
| Lines CD (even) | 28 | 27 | 3940<br>1.2 | Impedance | 5% | 1.59 /<br>1.24 |

Table 4.2: Canoe Reach inversion: model parameters

| Name | Core cell size ($x$, $y$) (m) | Layer thickness (m) and increase factor | Cell Number ($x$, $y$, $z$) | Starting model (Ωm) | Covariance smoothing factor |
|---|---|---|---|---|---|
| Canoe Reach North | 50 x 50 | 50 (1.1) | 74, 134, 83 | 50 | 0.5 |
| Lines AB | 30 x 30 | 30 (1.15) | 98, 108, 83 | 100 | 0.3 |
| Lines CD (even) | 50 x 50 | 50 (1.1) | 90, 104, 88 | 100 | 0.3 |

### 4.4.2. Canoe Reach North resistivity models

The Canoe Reach North MT data were inverted to obtain 3-D isotropic and anisotropic resistivity models. Note that the inversion parameters shown in Table 4.1 and Table 4.2 are only those from the final preferred inversions. Different values of the starting model resistivity and the covariance smoothing factor were tested to understand their influence on the resulting resistivity model.

The preferred isotropic and anisotropic inversions converged to overall root mean square (r.m.s.) misfits of 2.06 and 1.59, respectively. See the Appendix, Figure B.3 to Figure B.6 for maps of the observed and modeled apparent resistivity and phase data at four frequencies. Maps of the observed and modeled tipper data are also shown at four frequencies in Figure B.7 to Figure B.10. Overall, the modeled data from the isotropic and anisotropic inversions match the observed data acceptably well. The overall r.m.s. misfits and r.m.s. misfit by frequency are plotted in Figure 4.12. Note that for all frequencies the

anisotropic inversion achieved a lower r.m.s. misfit. This outcome is not surprising since the anisotropic inversion has more degrees of freedom to fit the observed data. Figure 4.13 further demonstrates the improved r.m.s. misfit obtained by the anisotropic inversion. Each colored circle represents the location of an MT station and the filled color corresponds to the difference in r.m.s. misfit between the isotropic and anisotropic inversions at the indicated frequency. A negative difference in r.m.s. misfit indicates a lower r.m.s. misfit for the anisotropic inversion. It is clear that the majority of stations have a lower r.m.s. misfit in the anisotropic inversion.

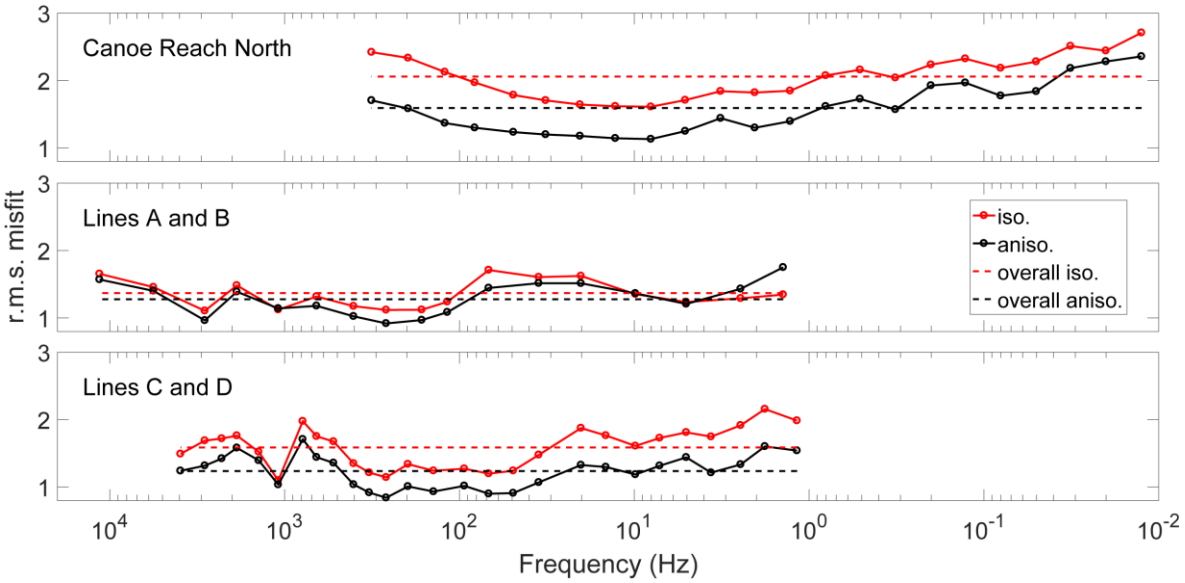


Figure 4.12: Root mean square (r.m.s.) misfit by frequency for the three groups of Canoe Reach 3-D MT inversions. Circles connected by solid lines are the r.m.s. misfit calculated for each frequency; the dashed lines show the overall misfit for an inversion. Red circles and lines correspond to the isotropic inversions; black circles and lines correspond to the anisotropic inversions.

The misfit is generally higher for the shortest and longest frequencies for both the isotropic and anisotropic inversions. The misfit at high frequencies may be affected by the choice of regularization between the data fit and model smoothness. If the model was allowed to be rougher (i.e. larger resistivity variations between neighboring cells) the r.m.s. misfit may decrease for high frequencies; however, if the model is too rough it may not accurately represent the geology.

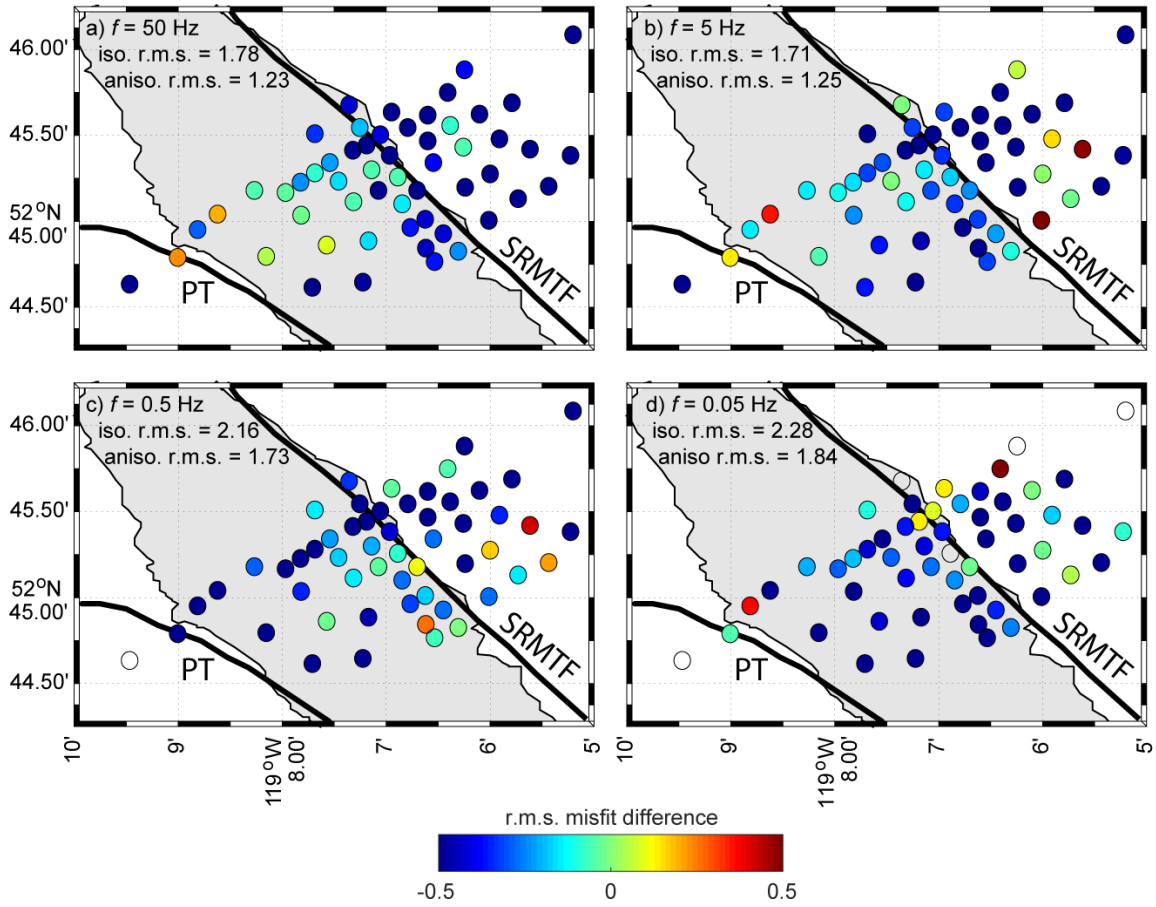


Figure 4.13: Change in root mean square (r.m.s.) misfit of combined impedance and tipper data at Canoe Reach North at four frequencies a) to d). Each colored circle represents the difference in r.m.s. misfit between the isotropic and anisotropic inversions at the given frequency for an MT station. The misfits from the isotropic (iso.) and anisotropic (aniso.) inversions are also shown for each of the four frequencies. A difference in r.m.s. misfit that is negative indicates a lower misfit for the anisotropic inversion. White circle = no data at this station at given frequency. Grey shading = Kinbasket Lake. SRMTF = Southern Rocky Mountain Trench Fault; PT = Purcell Thrust.

Figure 4.14 shows horizontal map slices through the isotropic and anisotropic models for comparison. The first column contains slices through the isotropic model while the other three columns contain slices through the anisotropic model. Note that conductors (C) and resistors (R) prefixed with "I" refer to those features in the isotropic inversion while features (F) prefixed with "A" refer to significant parts of the anisotropic inversions, which are not necessarily conductors or resistors in all components of the resistivity. This nomenclature is consistently used throughout the text in this chapter. These three columns contain the

principal anisotropic resistivities $\rho_x$, $\rho_y$, and $\rho_z$. Parts of the resistivity models not beneath the MT stations have been masked because these parts of the model are not well-constrained by the available MT data. The isotropic model contains several distinct features listed below:

- IC1: a shallow conductor beneath the western shore of Kinbasket Lake with a low resistivity (< 10 Ωm) on the west end of profile CR1 (Figure 4.14). The western extent of this feature is not accurately resolved because it extends outside of the station array.

- IC2: shallow conductor in the upper 0.2 km beneath Kinbasket Lake with a resistivity between 10 and 30 Ωm.

- IC3: a linear, NW-SE aligned conductor on the northeast side of Kinbasket Lake with a very low resistivity (< 3 Ωm).

- IC4: a narrow, NE dipping conductor below the northeast shore of Kinbasket Lake with a very low resistivity (< 3 Ωm). This feature extends vertically from about 0.3 to -1 km b.s.l. (Figure 4.14).

- IC5: a NNW dipping conductor with a very low resistivity (< 3 Ωm) that extends outside the northern extent of the MT survey.

- IR1: highly resistive (> 300 Ωm) feature underlying Kinbasket Lake and the western shore.

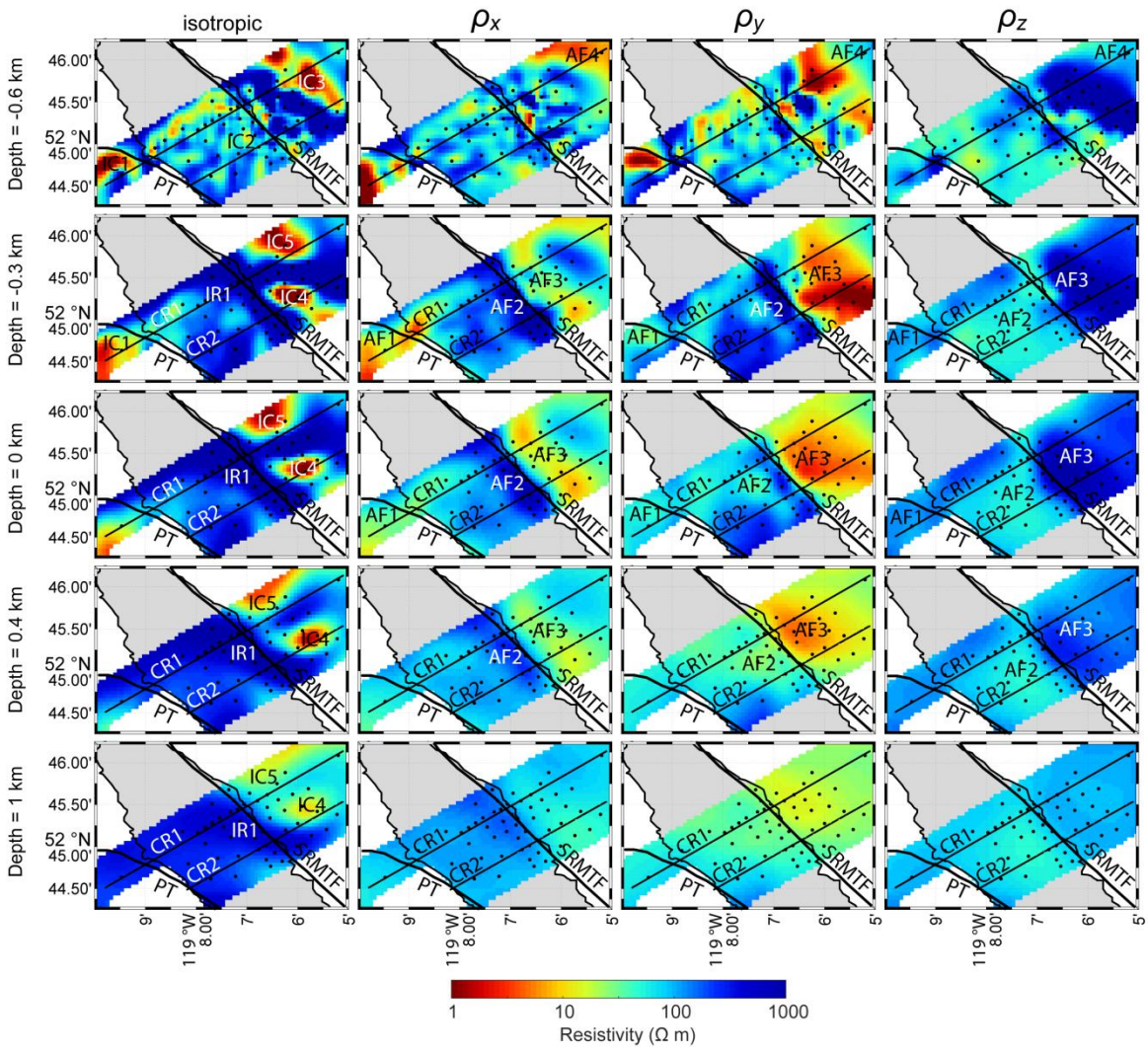


Figure 4.14: Horizontal slices through the Canoe Reach North isotropic and anisotropic 3-D resistivity models. Each row contains slices at a particular depth. The first column shows the model from the isotropic inversion. The next three columns show the model from the anisotropic inversion containing the principal anisotropic resistivities $\rho_x$, $\rho_y$, and $\rho_z$, which are measured in the N-S, E-W, and vertical directions, respectively. Model areas poorly constrained by the MT data are shown as white. CR1 and CR2 are the profiles shown in Figure 4.15. Black filled circles show locations of MT stations. PT = Purcell Thrust. SRMTF = Southern Rocky Mountain Trench Fault. Grey shading = Kinbasket Lake. IR1, IC1, IC2, IC3, IC4, IC5, AF1, AF2, AF3, and AF4 are features described in the text. Positive *x* direction = north, positive *y* direction = east, positive *z* direction = downward.

The same features are seen in vertical slices through the isotropic resistivity model in Figure 4.15. The surface traces of the profiles plotted in Figure 4.15, CR1 and CR2, are

shown in Figure 4.14. A geological cross section through the same area is also shown in Figure 4.15 (see Figure 4.3 for the profile location). The geological cross section was constructed independently of the resistivity model, based upon the bedrock contacts and structural measurements on 1:50k scale maps and associated cross-sections produced by McDonough et al. (1991), McDonough & Morrison (1990), McDonough & Mountjoy (1990), and McDonough & Murphy (1994). The outlines of the CR1 and CR2 slices are projected onto the geological cross section. Each resistivity model slice is less than 1 km from the geological cross section. The vertical slices clearly show that the conductors IC3, IC4, and IC5 are separate features.

There are four major features in the anisotropic resistivity model:

- AF1: a feature below the west shore of Kinbasket Lake that is spatially coincident with IC1. This feature is the most resistive in $\rho_z$, moderately resistive in $\rho_y$, and highly conductive (< 10 Ωm) in $\rho_x$.

- AF2: a feature below Kinbasket Lake. This feature is moderately resistive (~50 Ωm) and spatially continuous in $\rho_z$. This feature has more spatial variations in the $\rho_x$ and $\rho_y$ models. The horizontal slices of $\rho_x$ and $\rho_y$ in Figure 4.14 show that AF2 contains some moderately resistivity bands (~50 Ωm) combined with areas of higher resistivity (> 300 Ωm).

- AF3: Figure 4.14 and Figure 4.15 show that the more resistive AF2 is separated from AF3 by a NW-SE striking boundary. This boundary is clearly seen at depths of -0.3, 0, and 0.4 km in the $\rho_x$ and $\rho_y$ horizontal slices (Figure 4.14), where the resistivity contrast across the boundary is as much as two orders of magnitude. A resistivity contrast of about one order of magnitude is also apparent in the horizontal slices of $\rho_z$. In map view AF3 has a spatially homogenous $\rho_y$ and $\rho_z$, but contains significant variation in $\rho_x$. This variation is clearly seen in Figure 4.14 at depths of -0.3 and 0 km, where $\rho_x$ of AF3 is split into neighboring conductive and resistive bands with a NW-SE strike.

- AF4: a feature on the easternmost part of the model that extends from the surface to a depth of about -0.5 km. As seen in Figure 4.14 and Figure 4.15, this feature is highly conductive in the $\rho_x$ model (< 10 Ωm) and moderately resistive in $\rho_y$ and $\rho_z$ (~50 Ωm).

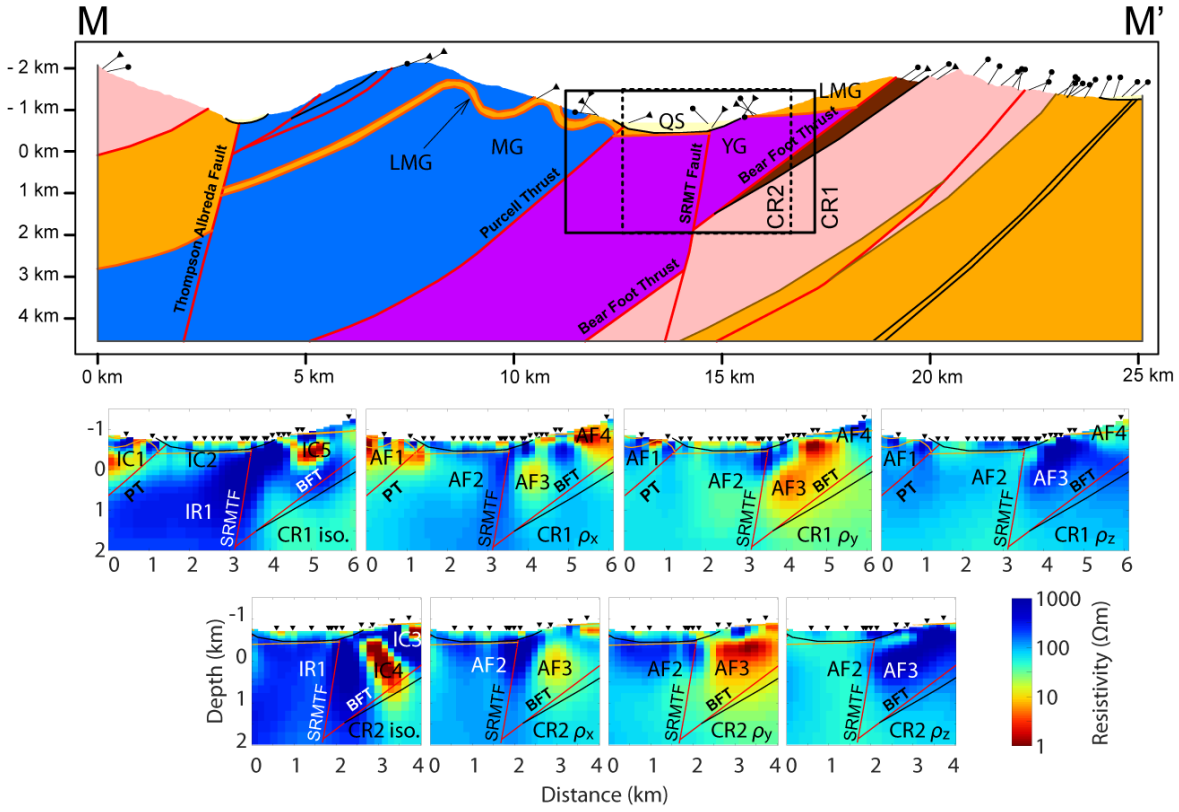


Figure 4.15: Geological cross section M-M' through Canoe Reach North and vertical slices through the Canoe Reach North resistivity models. iso. = isotropic model; $\rho_x$, $\rho_y$, and $\rho_z$ are the principal resistivity values in the anisotropic model, with $\rho_x$ measured in the N-S direction, $\rho_y$ measured in the E-W direction, and $\rho_z$ measured in the vertical direction. See Figure 4.3 for M-M' location and lithology legend; see Figure 4.14 for CR1 and CR2 locations in map view. Projected locations of CR1 and CR2 slices are shown on the geological cross section. See Section 4.5.1 for interpretation of the features IC1, IC2, IC3, IC4, IC5, AF1, AF2, AF3, and AF4. PT = Purcell Thrust; SRMTF = Southern Rocky Mountain Trench Fault; BFT = Bear Foot Thrust; LMG = Lower Miette Group; MG = Malton Gneiss; QS = Quaternary sediments; YG = Yellowjacket Gneiss. Pins at surface of geological cross section indicate dip angles from bedding (circles) and metamorphic cleavage (triangles).

### 4.4.3. Lines A and B resistivity models

The Lines A and B MT data were inverted to obtain isotropic and anisotropic resistivity models. Several permutations of inversion parameters were tested in order to choose a final, preferred resistivity model. The preferred isotropic inversion converged to a r.m.s. misfit of 1.37, and the anisotropic inversion converged to a misfit of 1.28 (see Figure 4.12). Compared to the r.m.s. misfit values from the Canoe Reach North inversions, the r.m.s. misfit values from the Lines A and B inversions are lower and more similar to each other. This suggests that the anisotropic inversion was required to fit the Canoe Reach North MT data, while a satisfactory data fit was achieved with both the isotropic and anisotropic inversions of the Line A and B MT data.

The Lines A and B anisotropic inversion resulted in a lower overall r.m.s. misfit, but unlike the Canoe Reach North inversions, the Lines A and B anisotropic inversion did not reduce the r.m.s. misfit for each frequency (Figure 4.12). The isotropic inversion already resulted in an acceptable misfit of 1.37 and the anisotropic inversion appears to have only provided a marginal improvement.

Maps of the observed and modeled data are shown in the Appendix, Figure B.11 to Figure B.14. In general, the isotropic and anisotropic inversions were able to reasonably reproduce the observed MT data. The r.m.s. misfit by frequency in Figure 4.12 demonstrates that a low misfit was achieved for all frequencies. The pseudo-section in Figure 4.16 is a concise way to view the r.m.s. misfit for each station and frequency because these data were collected in profiles. While the overall misfit is acceptably low, it is clear that stations on the west side of Lines A and B tend to have a lower misfit. This could be due to possible difficulty of fitting the MT data with an extreme 3-D nature (i.e. large values of $|\beta|$).

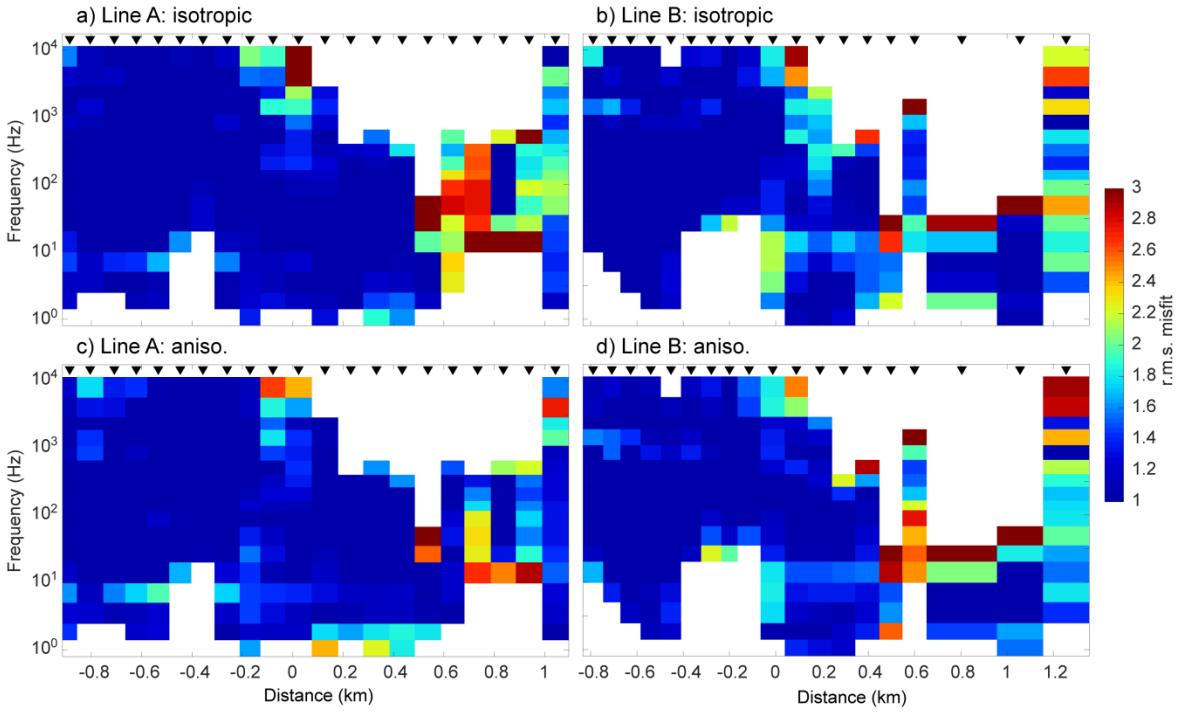


Figure 4.16: Pseudo-sections of r.m.s. misfit as a function of frequency for the Lines A and B 3-D isotropic and anisotropic inversions. Misfit from the isotropic inversion shown for a) Line A stations and b) Line B stations. Misfit from the anisotropic inversion shown for c) Line A stations and d) Line B stations. Each column corresponds to a MT station and each row is a frequency. White = masked data prior to inversion.

Figure 4.17 and Figure 4.18 show horizontal and vertical slices through the Lines A and B resistivity model. Several resistivity features that can be correlated with the geology are listed below:

- IC6: a thin (~0.1 km) conductor underlying the bottom of the lake. In map view (Figure 4.17) this feature appears to be concentrated beneath the MT stations and contains a narrow band between Line A and Line B. However, it should be noted that the resistivity model between the two profiles is not well-constrained by the data, and this connecting band may not be required by the data.

- IC7: a moderately conductive (10-30 Ωm), southwest-dipping feature beneath Line A. This feature is seen in map view in Figure 4.17. Similar to IC6, the spatial extent of IC7 is not well-constrained between the two profiles.

- IC8: a conductor beneath the eastern edge of Line A. This feature is located on the edge of the profile and thus its location and extent is not well constrained.

- IC9: similar to IC7, this is a moderately conductive, southwest-dipping feature beneath Line B. IC7 and IC9 have a similar resistivity and geometry and may correspond to the same feature beneath Lines A and B. However, due to the lack of MT stations between Lines A and B, it is not possible to confirm if the features are connected.

- IR2: a highly resistive (> 1000 Ωm) feature underlying IC6. As seen in Figure 4.18, IR2 extends below 0 km b.s.l.

The anisotropic resistivity model for Lines A and B contains most of the same features as the isotropic resistivity model. These anisotropic features are summarized below:

- AF5: a highly conductive (< 10 Ωm) feature in the uppermost 0.1 km beneath Kinbasket Lake. This feature is conductive in the $\rho_x$, $\rho_y$, and $\rho_z$ models, and its location is similar to that of IC6 in the isotropic model.

- AF6: a sub-vertical feature beneath Line A in the same location as IC7 in the isotropic model. This feature is highly conductive in $\rho_z$ (< 10 Ωm), moderately conductive in $\rho_y$ (~50 Ωm), but does not appear as a distinct feature in the $\rho_x$ model.

- AF7: This feature appears in the same location as IC8 in the isotropic model. AF7 is moderately conductive in $\rho_x$ (10 - 30 Ωm) but is not an obvious anomaly in $\rho_y$ and $\rho_z$.

- AF8: a feature beneath Line B in the same location as IC9 in the isotropic model. This feature is moderately conductive in $\rho_x$ and $\rho_z$ (10 - 30 Ωm) but resistive in $\rho_y$ (300 Ωm). It may be related to AF6 along-strike.

- AF9: This feature underlies AF5 beneath both Lines A and B. AF9 is highly resistive in $\rho_x$ ( > 300 Ωm) and moderately resistive in $\rho_y$ and $\rho_z$ (~100 Ωm).

- AF10: a feature beneath the southwest shore of Kinbasket Lake. This feature is seen on Lines A and B and is relatively conductive in $\rho_x$ (~30 Ωm) but resistive in $\rho_y$ and $\rho_z$ (> 100 Ωm).

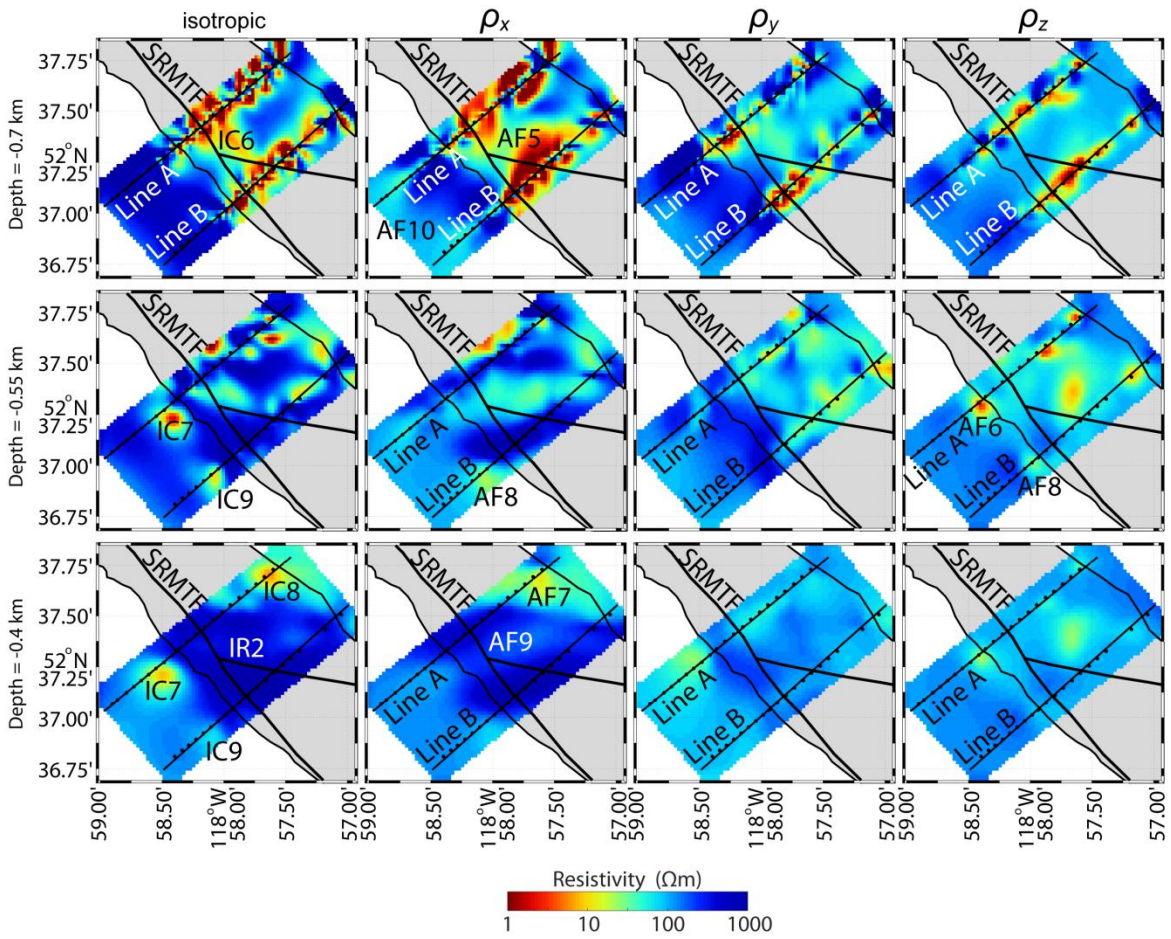


Figure 4.17: Horizontal slices through the Canoe Reach South Lines A and B isotropic and anisotropic resistivity models. Each row contains slices at a particular depth. The first column shows the model from the isotropic inversion. The next three columns show the model from the anisotropic inversion containing the principal anisotropic resistivities $\rho_x$, $\rho_y$, and $\rho_z$, which are measured in the N-S, E-W, and vertical directions, respectively. Model areas poorly constrained by the MT data are shown as white. Grey shading = Kinbasket Lake. Lines A and B are the profiles shown in Figure 4.18. Black filled circles show locations of MT stations. SRMTF = Southern Rocky Mountain Trench Fault. IR2, IC6, IC7, IC8, IC9, AF5, AF6, AF7, AF8, and AF9 are features described in the text. Positive *x* direction = north, positive *y* direction = east, positive *z* direction = downward.

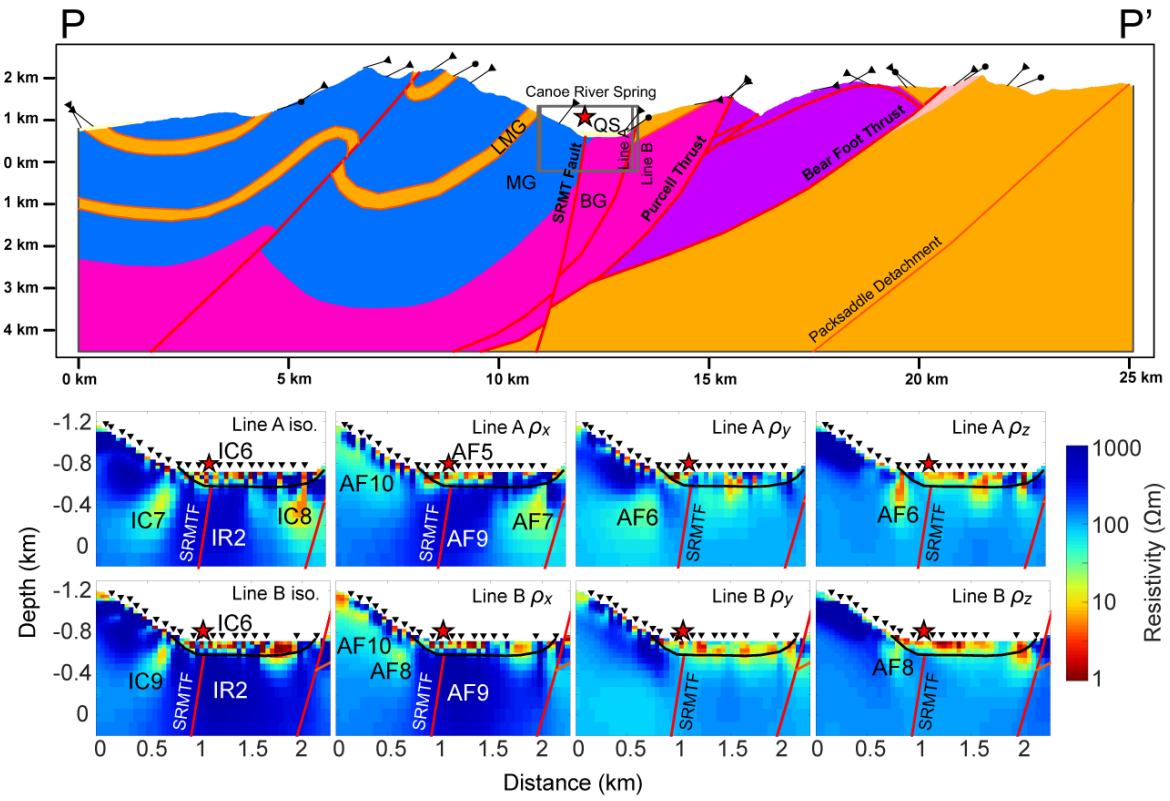


Figure 4.18: Geological cross section P-P' through Canoe Reach South and vertical slices through the Lines A and B resistivity model. iso. = isotropic model; $\rho_x$, $\rho_y$, and $\rho_z$ are the principal resistivity values in the anisotropic model, with $\rho_x$ measured in the N-S direction, $\rho_y$ measured in the E-W direction, and $\rho_z$ measured in the vertical direction. See Figure 4.3 for P-P' location and lithology legend; see Figure 4.17 for Lines A and B in map view. Projected locations of Line A and Line B slices are shown on the geological cross section. See Section 4.5.2 for interpretation of features IR2, IC6, IC7, IC8, IC9, AF5, AF6, AF7, AF8, AF9, and AF10. Red star is the location of the Canoe River thermal spring. SRMTF = Southern Rocky Mountain Trench Fault; BG = Bulldog Gneiss; LMG = Lower Miette Group; MG = Malton Gneiss; QS = Quaternary sediments. Pins at surface of geological cross section indicate dip angles from bedding (circles) and metamorphic cleavage (triangles).

### 4.4.4. Lines C and D resistivity models

This section describes the isotropic and anisotropic resistivity models obtained from inversions of the Lines C and D MT data. As previously described, multiple combinations of parameters in Table 4.2 were tested in order to choose a final, preferred resistivity model.

The isotropic inversion of the Lines C and D MT data resulted in a r.m.s. misfit of 1.59 and the anisotropic inversion resulted in a r.m.s. misfit of 1.24 (see Figure 4.12). Maps

of the observed and modeled data are presented in the Appendix, Figure B.15 to Figure B.18. These maps show that the inversions produced a good match to the spatial trends in the observed data. The pseudo-sections in Figure 4.19 show little systematic bias in r.m.s. misfit by MT station and frequency. The anisotropic inversion generally improved the r.m.s. misfit, especially at the west side of Line C, but some stations in the middle of Line C and the west side of Line D have r.m.s. misfits greater than 2 from the isotropic and anisotropic inversions. Similar to the Canoe Reach North and the Lines A and B inversions, the Lines C and D anisotropic inversion achieved a lower overall misfit than the isotropic inversion. This is likely due to the anisotropic inversion containing more adjustable model parameters to fit the MT data.

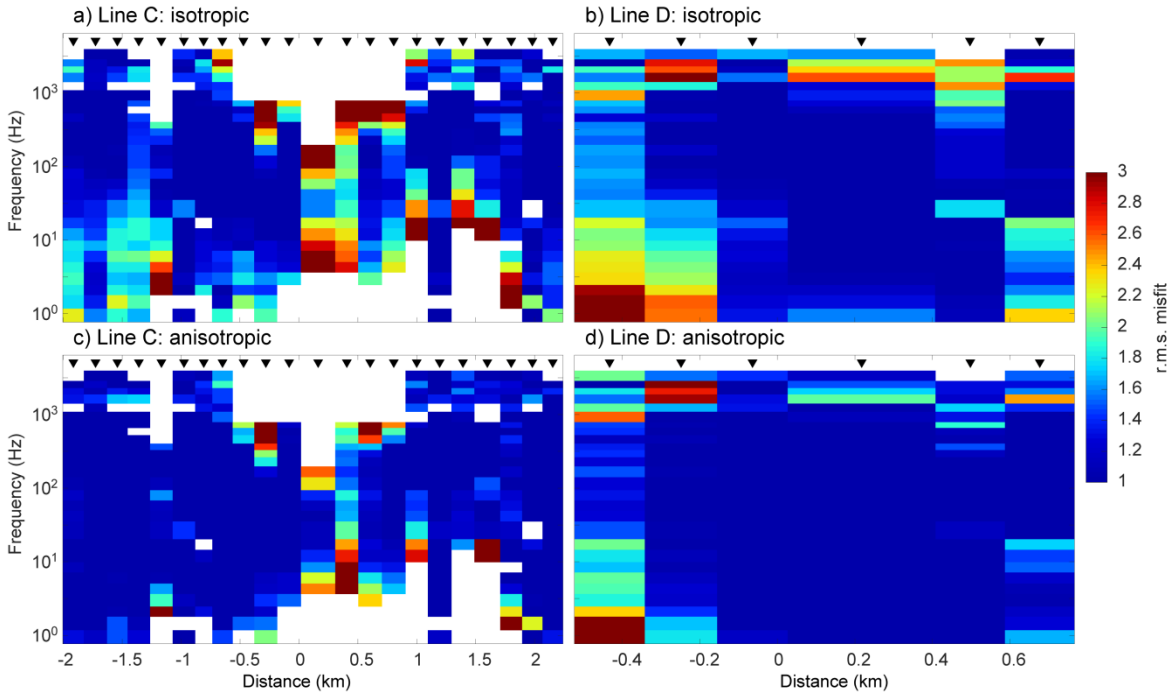


Figure 4.19: Pseudo-sections of r.m.s. misfit as a function of frequency for the Lines C and D 3-D isotropic and anisotropic inversions. Misfit from the isotropic inversion shown for a) Line C stations and b) Line D stations. Misfit from the anisotropic inversion shown for c) Line C stations and d) Line D stations. Each column corresponds to a MT station and each row is a frequency. White = masked data prior to inversion.

Horizontal and vertical slices (Figure 4.20 and Figure 4.21) through the Lines C and D isotropic resistivity model contain two major features summarized below:

- IR3: a resistive ( > 300 Ωm) feature beneath the western shore of Kinbasket Lake. This feature is seen beneath Lines C and D.

- IC10: a large, low-resistivity feature below Line C and Kinbasket Lake. While the location of IC10 appears limited to beneath Line C, its lateral extent is not well-constrained due to a lack of MT station coverage.

The anisotropic inversion contains three major features discussed below.

- AF11: this feature coincides with IC10 from the isotropic inversion, and is relatively conductive in $\rho_x$ and $\rho_y$ (~10 Ωm) and resistive in $\rho_z$ (100 - 300 Ωm). Horizontal slices show that AF11 is located directly beneath the Line C stations at depths of 0.3 to 0 km.

- AF12: this feature is located beneath the west shore of Kinbasket Lake. Beneath Line C, AF12 is more conductive in $\rho_z$ (10 - 30 Ωm) than in $\rho_x$ and $\rho_y$ (~ 100 - 300 Ωm). A conductive feature in $\rho_z$ also appears beneath the west shore along Line D.

- AF13: This feature is adjacent to feature AF11 and is similarly more conductive in $\rho_x$ and $\rho_y$ than in $\rho_z$. It has a particularly low resistivity (< 10 Ωm) in the $\rho_y$ model. AF13 is not located directly beneath Lines C and D and therefore is not as well constrained as other features.

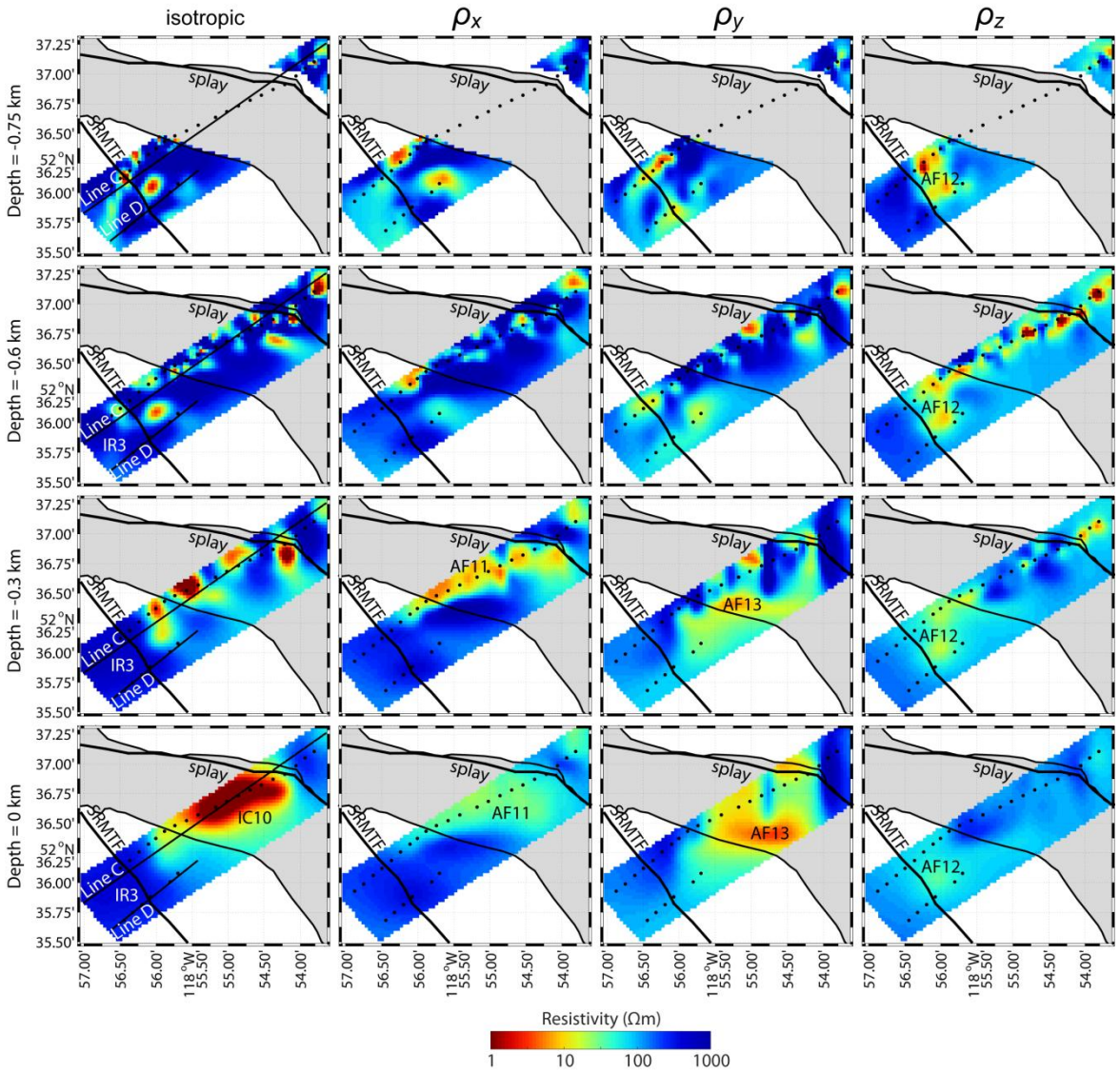


Figure 4.20: Horizontal slices through the Canoe Reach South Lines C and D isotropic and anisotropic 3-D resistivity models. Each row contains slices at a particular depth. The first column shows the model from the isotropic inversion. The next three columns show the model from the anisotropic inversion containing the principal anisotropic resistivities $\rho_x$, $\rho_y$, and $\rho_z$, which are measured in the N-S, E-W, and vertical directions, respectively. Model areas poorly constrained by the MT data are shown as white. The lake surface is at -0.73 km depth, and is therefore plotted as white in the first row. Grey shading = Kinbasket Lake. Lines C and D are the profiles shown in Figure 4.21. Black filled circles show locations of MT stations. SRMTF = Southern Rocky Mountain Trench Fault; splay = mapped splay of the SRMTF. IR3, IC10 AF11, AF12, and AF13 are features described in the text. Positive $x$ direction = north, positive $y$ direction = east, positive $z$ direction = downward.

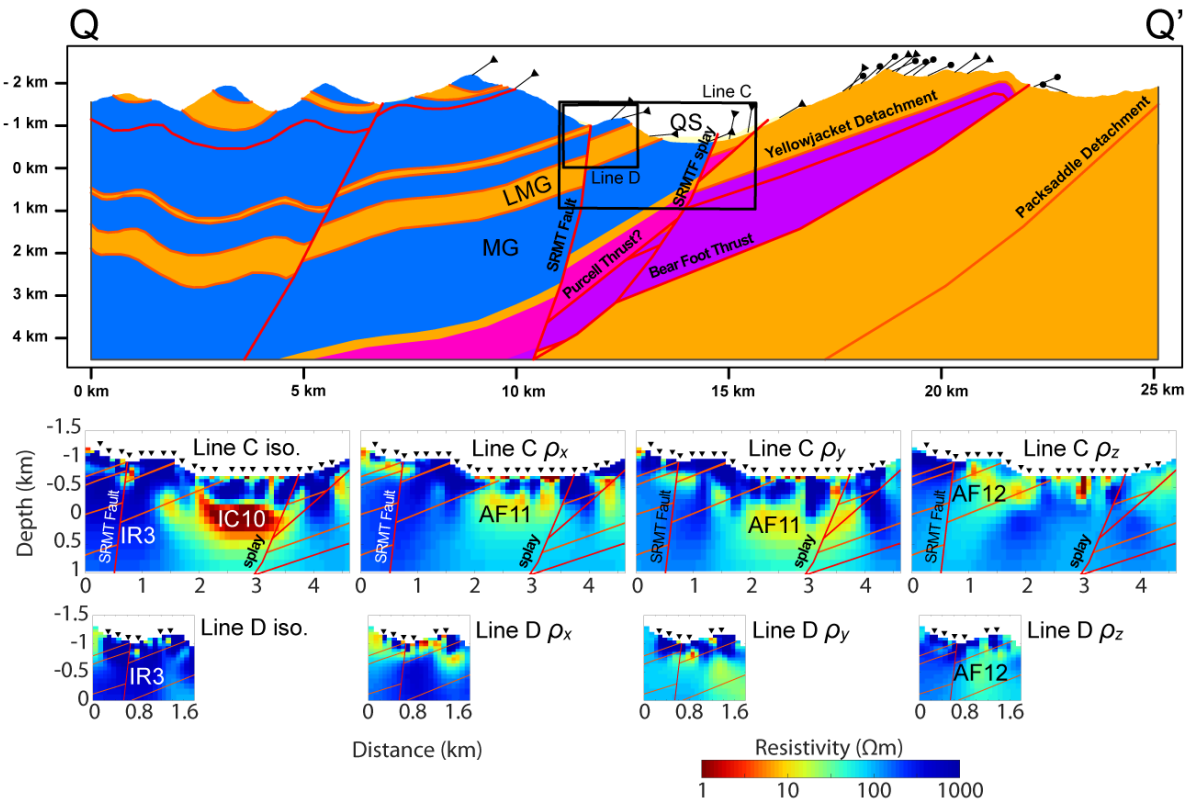


Figure 4.21: Geological cross section Q-Q' through Canoe Reach South and vertical slices through the Lines C and D resistivity models. iso. = isotropic model; $\rho_x$, $\rho_y$, and $\rho_z$ are the principal resistivity values in the anisotropic model, with $\rho_x$ measured in the N-S direction, $\rho_y$ measured in the E-W direction, and $\rho_z$ measured in the vertical direction. See Figure 4.3 for Q-Q' location and lithology legend; see Figure 4.20 for Line C and D locations in map view. Projected locations of Line C and Line D slices are shown on the geological cross section. See Section 4.5.3 for interpretation of features IR3, IC10, AF11, and AF12. SRMTF = Southern Rocky Mountain Trench Fault; splay = SRFMT splay; LMG = Lower Miette Group; MG = Malton Gneiss; QS = Quaternary sediments. Pins at surface of geological cross section indicate dip angles from bedding (circles) and metamorphic cleavage (triangles).

## 4.5. Discussion

### 4.5.1. Canoe Reach North: resistivity model interpretation

Figure 4.14 and Figure 4.15 reveal substantial differences between the isotropic and anisotropic resistivity models. The most drastic differences are seen in the eastern part of the models, beneath the northeast shore of Kinbasket Lake. The isotropic model contains three

highly conductive features (IC3, IC4, and IC5) within the highly resistive IR1 feature. Features IC4 and IC5 are narrow, sub-vertical features that extend from depths of -0.3 km to about 1 km. In contrast, the same model area has a simpler structure in the anisotropic model. The anisotropic model contains the feature AF3 that has a spatially homogenous $\rho_y$ and $\rho_z$. Considering $\rho_x$, AF3 can be divided into a conductive and resistive band, both striking approximately NW-SE. Compared to the locations of IC4 and IC5, AF3 in the anisotropic model has a better spatial correlation with faults in the geological cross section in Figure 4.15. The location of AF3 agrees with the Yellowjacket Gneiss block bounded by the SRMTF and the Bear Foot Thrust. IC4 and IC5 are also located in the footwall of the SRMTF. However, it is difficult to reconcile the orientation of IC4 and IC5 with the inferred locations of the SRMTF and Bear Foot Thrust.

The Canoe Reach North area appears to be an example where the isotropic inversion is inadequate to model the MT data. Although this area is expected to be geologically complicated with several overprinting deformation events, the alternating high-to-low resistivities of IR1, IC4, and IC5 are not easily explained by the geology. Previous authors have suggested that macro-anisotropic features in an isotropic resistivity model may be indicative of anisotropy on a smaller scale (e.g. Kellett et al., 1992; Patro & Egbert, 2011). The anisotropic inversion simplifies the resistivity model by allowing AF3 to have an axial anisotropy, instead of requiring the multiple features present in the isotropic model. Furthermore, the geological units in the study area are known to be highly structurally anisotropic due to the protracted history of contractional deformation; several folds and imbricated thrust sheets impart a strong NW-SE-striking structural grain to the region, and at a microscopic scale, gneisses and schists of the Malton Complex and Miette Group are highly foliated (McDonough & Simony, 1988).

The following interpretation focuses on the anisotropic model rather than the isotropic model for the following reasons:

(1) The anisotropic model contains features that are more easily explained geologically than features in the isotropic model. In particular, feature IC4 in the isotropic model is a narrow, cylindrical, sub-vertical conductor that is difficult to reconcile with the known geological structure. Instead of the alternating macro-anisotropic features in the isotropic model (IC4,

IR1, and IC5) the anisotropic model contains a single feature AF3 that is more spatially continuous, particularly in the along-strike direction.

(2) Features in the anisotropic model are in better agreement with the mapped geology. The geometry (strike and dip) of the Bear Foot Thrust is particularly well constrained by geological mapping because it juxtaposes distinct lithologies, and unlike the SRMTF, outcrops are not obscured beneath glacial cover. Thus, it is appropriate to use the Bear Foot Thrust as a constraint on the selection of the best MT model. The geometry of the SRMTF is less well constrained and cannot be relied upon as a guide for MT model interpretation. Feature IC4 in the isotropic model dips almost perpendicular to the inferred plane of the SRMTF and the well-constrained plane of the Bear Foot Thrust, while the AF3 feature in the anisotropic model is bounded by the SRMTF and Bear Foot Thrust fault. In map view, the strike of AF3 is parallel to the strike of the primary foliation in the Yellowjacket Gneiss.

(3) The anisotropic model provides a better fit to the observed MT data than the isotropic model. The improved r.m.s. misfit is observed across all frequencies, and no spatial bias in r.m.s. misfit is observed. An improved r.m.s. misfit does not always result in a more realistic resistivity model, but this fact does provide some confidence in the anisotropic model features.

(4) Given the high degree of structural anisotropy in the region, it may be a reasonable assumption that electrical resistivity is also anisotropic.

#### 4.5.1.1. AF1 and AF4: Lower Miette Group tectonic slices

Feature AF1 is a shallow conductor located beneath the southwest shore of Kinbasket Lake. This feature is best seen in the vertical slice CR1 between the depths -0.7 to 0 km (Figure 4.15). AF4 is located on the east shore of Kinbasket Lake, extending from the surface to a depth of -0.5 km. AF1 and AF4 coincide with mapped locations of the Lower Miette Group overlying or interleaved with the Yellowjacket Gneiss. Both AF1 and AF4 are conductive in $\rho_x$ (<10 Ωm) but more resistive (50 - 300 Ωm) in $\rho_y$ and $\rho_z$. The fact that both features have similar resistivities in the $\rho_x$, $\rho_y$, and $\rho_z$ models and a similar degree of anisotropy support the interpretation that these features correlate with the same lithology. The locations of AF1 and AF4 in the resistivity model agree with the stratigraphic correlation

of the parautochthonous Lower Miette cover sequence across the Purcell Thrust by McDonough & Simony (1988).

AF1 also spatially coincides with the Malton Gneiss in the hanging wall of the Purcell Thrust fault. If AF1 corresponds to the Malton Gneiss, the resistivity model suggests that it has a distinct resistivity from the Yellowjacket Gneiss (AF2). Due to lithological similarities between the Malton and Yellowjacket gneisses (both are largely orthogneisses with granodioritic protoliths; McDonough & Parrish, (1991), AF1 more likely corresponds to the Lower Miette cover than to the Malton Gneiss.

Note that the location of feature AF1 also corresponds to the hanging wall of the Purcell Thrust fault, which has been interpreted as a post-metamorphic brittle fault. If fluid is pooling against the Purcell Thrust, it would likely be a low resistivity feature. However, AF1 is only appreciably conductive in $\rho_x$ (< 10 Ωm) which would imply an anisotropic resistivity for the Purcell Thrust at this locality. While this remains a possibility, it is unclear why fluids in the fault would not cause a low resistivity in $\rho_y$ and $\rho_z$ as well. This possibility is discussed in detail in Section 4.5.5.

The Lower Miette Group itself is a more likely candidate for anisotropy because it is known to be internally structurally anisotropic; planar muscovite crystals define the primary cleavage planes and separate parallel layers of quartz, both of which are oriented perpendicular to shortening of the pelitic protolith. Resistivity measurements of similar pelitic schists in Alaska revealed anomalous resistivity behavior that was ultimately linked to the presence of a microscopic graphite strand occurring parallel to the schistocity (Mathez et al., 1995),

#### 4.5.1.2. AF2 and AF3: Yellowjacket Gneiss offset by the SRMTF

As seen in Figure 4.15, these two features underlie the upper 2 km beneath Kinbasket Lake. A sharp resistivity contrast can be seen in $\rho_x$, $\rho_y$, and $\rho_z$ across the inferred plane of the SRMTF. Existing maps and balanced geological cross sections suggest that the Yellowjacket Gneiss should occur on both sides of the SRMTF with minor dip separation (~2 km). McDonough & Simony (1988) additionally allow for dextral strike separation of no more than 10 km across the SRMTF (although Murphy, 1990a, argues in favor of up to 55 km of strike separation). However, no outcrop of the Yellowjacket Gneiss is found on the

west side of the SRMTF and thus its presence there is only inferred. The strong resistivity contrast across the SRMTF observed in the resistivity model could be explained by either (1) different permeabilities and fluid content on either side of the fault or (2) different lithologies on either side of the fault due to greater offset than previously recognized. The latter case is preferred, as it is difficult to explain the anisotropic nature of the resistivity anomaly with fluids. Furthermore, the Yellowjacket Gneiss is not a particularly permeable rock. Fault juxtaposition more readily explains the contrast and provides some constraint on the magnitude of fault offset: dip separation would have to be greater than 2 km (the maximum resolution depth of the model), as no correlative zones of low resistivity are observed in the hanging wall of the fault. Similarly, because the resistivity contrast spans the horizontal extent of the MT survey, strike separation larger than the horizontal extent of the MT survey (> 2 km) may have occurred. Given that resistivity anisotropy is unlikely to change rapidly along geological strike, the previous strike separation estimates of up to 10 km (McDonough & Simony, 1988) and up to 55 km (Murphy, 1990a) cannot be ruled out.

### 4.5.2. Lines A and B: resistivity model interpretation

Unlike the Canoe Reach North isotropic and anisotropic inversions, which produced features with starkly different geometries, the Lines A and B isotropic and anisotropic resistivity models contain features with largely similar geometries (see Figure 4.17 and Figure 4.18). The Canoe Reach North anisotropic model is geometrically/structurally simpler than the isotropic model whereas there is no such disparity between the Line A and B isotropic and anisotropic models. Therefore, it is possible that the Canoe Reach South area is less anisotropic than the Canoe Reach North area. However, some features exhibit a moderate degree of anisotropy that aids our model interpretation below. The following interpretation focuses on the anisotropic features because the isotropic and anisotropic models contained features in similar locations.

#### 4.5.2.1. AF6, AF7, and AF8: Fluids hosted within the SRMT fault/splay zone

The features AF6 and AF8 are located beneath Lines A and B, respectively. These features are located close to the Canoe River spring (red star in Figure 4.18) which must have a nearby fluid source. The SRMTF is a reasonable candidate for a permeable fluid pathway

due to its proximity to the thermal spring. The SRMTF is mapped to intersect the Canoe River spring in this area although this may have been a deliberate choice of the mappers (McDonough & Morrison, 1990) who reasonably assumed that the spring was fault-controlled; the exact trace of the fault is obscured by valley sediment infill and the Kinbasket reservoir, and the location of the spring may have been used as a lone constraint on the location of the fault. Regardless of the exact location of the surface trace of the main fault strand, a regional-scale fault could reasonably contain a fracture zone several hundred meters in width, potentially occupying the entire valley floor.

Interestingly, AF6 is more conductive in $\rho_z$ than in $\rho_x$ and $\rho_y$ (Figure 4.18). In fact, AF6 is not a discernible feature in the $\rho_x$ model and is a moderately conductive feature in the $\rho_y$ model that does not connect to the surface. AF8 is similarly conductive in $\rho_z$; however, it is moderately conductive in $\rho_x$, and indiscernible in the $\rho_y$ model. The anisotropic resistivity may be related to a possible intersection of the SRMTF and its splay below the Canoe River spring, which might be conducive to vertical fluid flow. Sibson (1996) showed that fault intersections often act as "tubes" for fluid flow, and the linear geometry of the AF6 and AF8 conductors is consistent with this view. The possibility of electrically anisotropic fault zones is further discussed in Section 4.5.5.

Due to the distribution of the MT stations in two parallel profiles offset by ~1 km, the MT data have limited sensitivity to the volume between Lines A and B. Therefore, it is not possible with the existing MT data to confirm the location of conductors between Lines A and B. However, because the SRMTF runs along the floor of the SRMT, it is likely that the same fracture system is connected beneath Lines A and B.

AF7 is an east-west trending feature that is conductive in the $\rho_x$ model. This feature is close to the intersection of the main SRMTF and its splay and therefore may be a permeable zone containing fluids. Alternatively, the decreased resistivity in $\rho_x$ may also be due to an anisotropic lithology such as the Lower Miette Group. However, due to its location on the edge of the MT survey profile, AF7 is not well resolved and therefore its interpretation is uncertain.

#### 4.5.2.2. AF9: Bulldog Gneiss

This feature occurs in the hanging wall of the Purcell Thrust which contains the Bulldog and Malton Gneisses (see Figure 4.18). The southwest boundary of AF9 (the resistive body in the $\rho_x$ model) correlates with the SRMTF; therefore, AF9 may be the Bulldog Gneiss in the footwall of the SRMTF opposite to the Malton Gneiss in the hanging wall of the SRMTF. AF9 is weakly anisotropic (less than one order of magnitude resistivity difference) compared to AF3 in the Canoe Reach North model that was interpreted as the Yellowjacket Gneiss.

#### 4.5.2.3. AF10: Malton Gneiss or Lower Miette Group tectonic slices

AF10 appears in the anisotropic resistivity model to the southwest of Kinbasket Lake, extending from the surface (maximum elevation of 1.2 km) to a depth of about 0.6 km a.s.l. This feature does not display strong anisotropy, with $\rho_x$ about 1 order of magnitude less than $\rho_y$ and $\rho_z$. The location of AF10 in the anisotropic model corresponds to the Malton Gneiss and a thin tectonic slice of Lower Miette Group metasediments (see geological cross section in Figure 4.18). AF10 has about the same degree of anisotropy as AF9, which is interpreted as the Bulldog Gneiss. However, $\rho_x$ is the most resistive direction for AF9 while it is the most conductive direction for AF10. Thus, some mechanism is needed to describe this difference in anisotropy.

AF10 is also located close to a mapped outcrop of the Lower Miette Group. At Canoe Reach North, the anisotropic features AF1 and AF4 are spatially correlated to the Lower Miette Group on the east and west shores of Kinbasket Lake. These features are most conductive in $\rho_x$, which is also the case for AF10. However, AF1 and AF4 have principal resistivities that differ by up to two orders of magnitude, while those of AF10 only differ by approximately one order of magnitude. If AF10 also corresponds to the Lower Miette Group, one explanation for this discrepancy is a possible difference in the alignment of the principal resistivity axes, i.e. the anisotropic strike, dip, and/or plunge angles are different at Canoe Reach North and Canoe Reach South. When the anisotropy axes are not aligned with the model coordinate system, some mixing of the principal resistivities will occur when modeled

in the model coordinate system. Therefore, similarities in principal resistivity values between features should only be interpreted qualitatively.

### 4.5.3. Lines C and D: resistivity model interpretation

#### 4.5.3.1. AF11 and AF13: Possible fluids in SRMTF fracture zone

The most striking feature in both the isotropic and anisotropic models is AF11, an anisotropic feature beneath Line C and Kinbasket Lake (see Figure 4.21). The most likely causes of high conductivity are fluids or a conductive phase within an anisotropic rock. Fluids would need permeable fractures or faults to reside in the Malton Gneiss, the rock unit mapped beneath Kinbasket Lake in the footwall of the SRMTF. The location of faults beneath Line C can be deduced from surface mapping. From Figure 4.3, this model coincides with a bend in Kinbasket Lake where the lake is oriented roughly east-west in a ~5 km segment. At this segment of the lake, a splay of the SRMTF is mapped to follow the north shore until it intersects with the main SRMTF at the Canoe River spring. South of the Canoe River spring, the main SRMTF continues southeast on the west side of Kinbasket Lake. Line C spans the SRMT where the surface distance between the SRMTF and its splay is about 3 km. The dip angles of the SRMTF and its splay, which would be invaluable to the interpretation of AF11, are poorly constrained at this location. If AF11 does correspond to fluids in a fracture zone of the SRMTF and its splay, some mechanism is needed to explain the low resistivity in $\rho_x$ and $\rho_y$, but the high resistivity in $\rho_z$. It is also possible that AF11 corresponds to the Malton Gneiss, as a high degree of anisotropy was also observed at Canoe Reach North in the Yellowjacket Gneiss. The decreased resistivity may be explained by a small amount of conductive phases such as graphite or sulfide that are connected in the foliation direction.

AF13 is a feature visible in the horizontal slices of the Lines C and D anisotropic model (Figure 4.20). This feature has low values of $\rho_y$ (< 10 Ωm) but is moderately resistive in $\rho_x$ (>100 Ωm) and $\rho_z$ (30 - 100 Ωm). AF13 occurs at the same depth and is adjacent to feature AF11; however, they appear as distinct anisotropic features in the model. Due to its proximity to AF11, AF13 may be the same feature, which is likely a permeable zone at the intersection of the SRMTF and its splay. However, it is unclear if a fracture zone would be

horizontally anisotropic in adjacent regions. It should be noted that the deepest parts of AF13 (beneath 0 km b.s.l.) are not beneath the Lines C and D MT stations and thus not as well constrained by the MT data.

#### 4.5.3.2. AF12: Fluids within the SRMTF

This feature is a near-surface conductor in the $\rho_z$ model beneath Lines C and D (see Figure 4.20). There are some small, near-surface conductors in the $\rho_x$ and $\rho_y$ models in nearly the same location, but the spatial correlation is not exact. The vertical slice below Line C in Figure 4.21 reveals that AF12 is about one order of magnitude less resistive in $\rho_z$ than in $\rho_x$ and $\rho_y$. Interestingly, it is evident from Figure 4.18 that the feature AF6 beneath Line A is also significantly more conductive in $\rho_z$, and both features AF6 and AF12 are located < 1 km from the mapped location of the SRMTF. Below Line B, AF8 is also conductive in $\rho_z$ and close to the SRMTF, thus AF6, AF8, and AF12 may correspond to the same fracture zone spanning ~ 5 km from Line D to the Canoe River spring.

Similar to other anisotropic features, AF12 coincides with the mapped location of the Lower Miette Group, a semipelitic unit that demonstrates structural anisotropy on the grain scale. In the absence of conductive fluids, an interconnected conductive phase such as graphite needs to be present in order to explain the decreased resistivity of this rock. This possibility cannot be ruled out based on the resistivity models alone.

### 4.5.4. Do these resistivity models help constrain geometry of the SRMTF?

The geometry of the SRMTF is poorly resolved in the transition from the SRMT to the NRMT between the latitudes of 53°N and 54°N. In this area, thick glacial overburden obscures the location of the SRMTF and it is therefore assumed to run parallel to the SRMT valley floor. A second question is the amount of dextral strike-slip that occurred in this transition area. Estimates in the Canoe Reach area range from < 10 km (McDonough & Simony, 1988), to 55 km (Murphy, 1990a).

The Canoe Reach North resistivity model provides some constraint on the SRMTF offset. The anisotropic model contains a resistivity contrast between features AF2 and AF3 that agrees with the mapped location and approximate dip of the SRMTF (Figure 4.15). The nature of the resistivity contrast, as discussed above, remains uncertain. The significant

resistivity contrast is suggestive of a difference in lithology across the SRMTF, possibly juxtaposed by fault displacement. Unfortunately, the resistivity model lacks the spatial extent to constrain the sense and magnitude of displacement, as no piercing points or marker horizons are apparent. The SRMTF dip separation was estimated to be less than 2 km by McDonough & Simony (1988), and the fact that the strong resistivity contrast persists to 2 km depth implies that either dip separation was greater than 2 km, and/or significant dextral strike separation occurred. Dextral separations of less than 10 km (McDonough & Simony, 1988) and up to 55 km (Murphy, 1990a) cannot be ruled out because the horizontal resistivity contrast between AF2 and AF3 spans the resistivity model.

### 4.5.5. Anisotropic resistivity of faults

Prior to interpreting the anisotropy of features in the resistivity models, it is important to reiterate an important limitation of the axial anisotropic inversion. The axial anisotropy inversion assumes a coordinate system aligned to geographic north, and therefore the inversion coordinate system is not necessarily aligned to the SRMTF strike and dip. Notably, the SRMTF strikes roughly N40°W, which likely means that the principal resistivity aligned with the SRMTF strike is projected onto the $x$ and $y$ directions in the inversion coordinate system. This likely has the largest effect on resistivity in the $x$ and $y$ directions, as the SRMTF is steeply dipping and more closely aligned to the $z$ direction of the inversion coordinate system. Thus, interpretation is not heavily based on the principal resistivity magnitudes, and instead focuses on qualitative assessment of the electrical anisotropy.

The permeability of brittle faults has been shown to be anisotropic, displaying higher permeability parallel to the fault plane (e.g. Caine et al., 1996; S. Zhang et al., 1999). Recent studies relate permeability anisotropy to electrical anisotropy. For example, Kirkby et al. (2016) and Kirkby & Heinson (2017) used simulated resistor networks to test changes in permeability and resistivity as fracture networks opened. These studies showed a non-linear increase in permeability and a corresponding decrease in resistivity as fractures were opened. In their 3-D models with a moderate fracture density, Kirkby & Heinson (2017) reported an electrical resistivity anisotropy factor up to 160 and permeability anisotropy factor up to $10^9$. While anisotropy in resistivity and permeability were demonstrated by Kirkby & Heinson (2017), only a few studies connect anisotropy of fracture zones to MT measurements.

For example, MT data have been shown to be sensitive to electrical anisotropy from hydraulic fracturing of sedimentary basins, which may be required to create a viable enhanced geothermal system (EGS). Peacock et al. (2012) and Peacock et al. (2013) reported on the use of MT to monitor the distribution of injected fluids at the Paralana EGS site in South Australia. These two studies used changes in the observed phase tensor data to infer the preferred flow direction of injected fluids, but noted that the induced fracture network produced phase tensor data that could not be fully reproduced by a 3-D isotropic resistivity model. MacFarlane et al. (2014) modeled the same MT data set with a 2-D anisotropic model and suggested that electrical anisotropy was consistent with the permeability changes from hydraulic fracturing. Conversely, a similar MT survey conducted at the Habanero EGS in South Australia did not find evidence of electrical anisotropy (Didana et al., 2017), despite a 2:1 permeability anisotropy inferred by micro-seismic studies (Holl & Barton, 2015; Llanos et al., 2015). It is unclear if this discrepancy is due to the difficulty of detecting anisotropy in MT data, the non-uniqueness of inverting MT data, or a difference in lithology at the two EGS sites. In addition to EGS monitoring, geothermal exploration of the Otway Basin in South Australia with MT found electrical anisotropy attributed to N-NW oriented fluid-filled fractures (Kirkby et al., 2015). These studies show that MT data are sensitive to electrical anisotropy related to permeability anisotropy of fracture networks.

In the current study at Canoe Reach, it is unclear if brittle faulting in the SRMTF presents a similar degree of permeability/electrical anisotropy as in the South Australian sedimentary basins of the aforementioned studies. The Canoe Reach South resistivity models contain the anisotropic features AF6, AF8, and AF12 that correspond to mapped locations of the SRMTF and demonstrate decreased resistivity in $\rho_z$, which is sub-parallel to the fault dip. Following the conceptual model of Caine et al. (1996), fluids may be confined to a local conduit or a more distributed fracture system, depending on the spatial extent of the fault damage zone. If the SRMTF has a fracture zone on the order of tens or hundreds of meters, the volume of fluid-filled fractures should be large enough to be detected by MT.

An alternative hypothesis is that anisotropy is caused by structural features local to the fault slip surface, rather than a distributed fracture network. For example, structural anisotropy in faults has been observed as corrugations on a centimeter to kilometer scale (e.g. Edwards et al., 2018; Ferrill et al., 1999; Hancock & Barka, 1987). Corrugations are

commonly observed parallel to slip direction and may enhance permeability and therefore decrease resistivity parallel to the slip direction. If the most recent slip direction of faults in the SRMT is down-to-the-west, the SRMTF could be corrugated along the down-to-the-west slip direction. Such corrugations would restrict fluid flow perpendicular to the slip direction (i.e. roughly the *xy* plane) and enhance flow in the slip direction.

The SRMTF permeability and resistivity may be controlled by a combination of a conduit along the fault plane and a surrounding damage zone. These features could also vary along the strike of the SRMTF. For example, at Canoe Reach North, where the SRMTF is mapped as a single strand, fluid flow may be restricted to a local conduit along the fault plane. At Canoe Reach South the SRMTF and its splay may intersect and contain an extensive damage zone below Kinbasket Lake. Differences in local fracture distribution and lithology may explain why $\rho_z > \rho_y > \rho_x$ for AF6 and $\rho_z > \rho_y \approx \rho_x$ for AF12. Note that because the inversion coordinate system is aligned with geographic coordinates and not with the SRMTF strike and dip, there is some uncertainty in interpreting differences in $\rho_x$ and $\rho_y$. Therefore, these results alone cannot conclusively show that fluids in the SRMTF fracture zone are anisotropic; however, previous studies of hydraulic fracture zones and synthetic resistor networks suggest that fracture zones can have significant anisotropy in both permeability and resistivity.

### 4.5.6. Implications for geothermal exploration at Canoe Reach

The resistivity models contain features that help characterize the subsurface beneath the Canoe River thermal spring. Features AF6 and AF8 beneath Lines A and B coincide with the locations of the SRMTF and the thermal spring (Figure 4.18). These two features have a sub-vertical geometry and low $\rho_z$, which may imply a permeable fluid pathway parallel to the SRMTF dip direction. On Lines C and D, feature AF12 has a low $\rho_z$ and matches the location of the SRMTF, and thus may also correspond to a fluid permeable zone (Figure 4.21). However, its location also agrees with rocks of the Lower Miette Group, which displays anisotropy at a microscopic scale and may contain conductive minerals aligned in the foliation direction. Interpretation of IC10/AF11/AF13, a large feature beneath Kinbasket Lake at Canoe Reach South, is also uncertain. This feature has low $\rho_x$ and $\rho_y$, but is resistive in $\rho_z$. If AF11 corresponds to a fluid permeable fracture zone, it is unclear why the feature

would have higher values of $\rho_z$. Thus, given their proximity to the mapped SRMTF, features AF6, AF8, and AF12 more likely correspond to fluid permeable zones, yet the possibility that they correspond to an anisotropic unit such as the Lower Miette Group cannot be ruled out.

It is unclear if there is an underlying geothermal reservoir at Canoe Reach North because there are no surface thermal manifestations. The MT survey was performed to investigate a region near the Purcell and SRMT Faults that might host a permeable zone with elevated fluid content. The anisotropic resistivity model contains low resistivity features, but the evidence presented above suggests that these features more likely correspond to changes in lithology rather than to elevated concentrations of fluids. For example, the anisotropic feature AF3 corresponds to Yellowjacket Gneiss in the footwall of the SRMTF (Figure 4.15). This feature may contain conductive minerals such as graphite or sulfides connected along grain boundaries oriented in the ~SW-NE direction of observed deformation. If these minerals exist in the sub-planar foliation of the Yellowjacket Gneiss, it may explain why AF3 has low values of $\rho_x$ and $\rho_y$, which may be sub-parallel to the foliation direction, and resistive in $\rho_z$ which is nearly perpendicular to the foliation direction. The low resistivity of AF3 is more difficult to explain with fluids. If AF3 corresponds to fluids, some mechanism is needed to explain the high $\rho_z$values. The fluid would need to be predominantly connected in the *x* and *y* directions which might be possible in thin aquifer lenses of inter-bedded shale and sandstone, but unlikely for gneiss. Furthermore, if AF3 corresponds to a permeable fracture system of the SRMTF, higher permeability is expected along the fault plane. Due to the steep dip (~70°) of the SRMTF, $\rho_z$ should be relatively low if fluids exist along the fault plane. Therefore, it is unlikely that fluids are the cause of the low resistivity observed at Canoe Reach North.

### 4.5.7. The value of anisotropic resistivity modeling in structurally controlled geothermal systems

Structurally controlled systems such as fold and thrust belts are inherently anisotropic. This anisotropy can be observed on a macroscopic scale such as in individual thrust sheets of kilometer scale, or on a microscopic scale such as mylonitic fabric in a deformed rock. In the case of microscopic anisotropy, a preferred orientation can be visually

distinguished or detected by contrasts in physical properties, such as seismic anisotropy from gneiss foliation (Brosch et al., 2000; Kern et al., 2008). Electrical anisotropy on a microscopic scale has also been reported in strongly foliated gneiss (Laštovičková et al., 1993; Rauen & Laštovičková, 1995). Therefore, electrical anisotropy might be a common phenomenon in highly deformed rocks.

Modeling MT data is challenging when the spatial dimensions of electrical anisotropy are much smaller than the MT signal induction scale. For example, anisotropy arising from a preferred arrangement of mineral grains may exist on a millimeter length scale, while the maximum resolution of MT data, determined from the highest measured signal frequency, is typically tens to hundreds of meters. Clearly, resistivity variations on a millimeter length scale cannot be produced in an isotropic model. An isotropic inversion algorithm can instead fit an anisotropic MT dataset with macro-scale anisotropic features (i.e. Heise & Pous, 2001). This can lead to uncertainty in model interpretation. Other workers have observed this effect in 2-D isotropic inversions of field MT data, and have interpreted their data with 1-D or 2-D anisotropic models (e.g. (Heinson & White, 2005; Patro et al., 2005; Wannamaker et al., 2008; Ye et al., 2019). In these examples, the authors used additional geological knowledge in order to choose the isotropic or anisotropic model for interpretation.

The current study contains an example of macro-anisotropic features in the 3-D isotropic inversion of the Canoe Reach North MT data. The macro-anisotropy was exhibited by the sub-vertical, highly conductive features IC4 and IC5 embedded in the highly resistive IR1. At first glance, the inversion was able to fit the measured MT data to a reasonable overall r.m.s. misfit of 2.06. However, features IC4 and IC5 were difficult to reconcile with the mapped geology which does not exhibit such a high degree of heterogeneity. The anisotropic inversion simplified the resistivity model by replacing features IC4 and IC5 with the feature AF3 that is more spatially continuous than the isotropic model. In addition, AF3 is an anisotropic block with spatial boundaries that agree with the mapped SRMTF and Bear Foot Thrust. Therefore, the model containing AF3 as an anisotropic unit in the footwall of the SRMTF is preferred over the isotropic model with multiple sub-vertical conductors IC4 and IC5.

MT exploration for geothermal resources has been successfully applied worldwide at hydrothermal volcanic settings, where the structure can be approximated as electrically

isotropic. This assumption may be invalid for structurally complicated regions such as Canoe Reach. As many highly deformed geological settings are typically targets for geothermal exploration, electrical anisotropy in the upper crust may be a common problem when modeling MT data. With the increasing availability of 2-D and 3-D anisotropic modeling algorithms, it is becoming more feasible to model MT data with models that include axial or general anisotropy. Thus it is prudent to investigate the possibility of anisotropic resistivity in structurally complicated settings especially if the MT data exhibit indicators of anisotropy. As in the Canoe Reach North resistivity models, a more geologically simple anisotropic model might be more realistic than an isotropic model with extraneous features.

## 4.6. Conclusion

### 4.6.1. Summary

This chapter has presented an analysis of MT data collected at the Canoe Reach geothermal prospect near Valemount, British Columbia. Canoe Reach is a structurally complicated region that has undergone several generations of deformation since the Mesozoic. The structurally complex geology provided challenges to the 3-D inversion of MT data and the interpretation of electrical resistivity models. Major findings from the resistivity models obtained from inversion of the MT data are summarized below.

### 4.6.2. Canoe Reach North

The grid of 73 MT stations in this area was collected by the University of Alberta and Borealis GeoPower Inc. The MT survey was conducted near the intersection of the Purcell Thrust and the SRMTF, two major regional faults exhibiting brittle fractures. The MT phase tensor data indicate that the structure below the northeast shore of Kinbasket Lake is 3-D. Some MT stations on the northeast shore even had out of quadrant phases, which is an indication of 3-D structure or 2-D/3-D electrical anisotropy.

Therefore, 3-D isotropic and 3-D anisotropic inversions of the Canoe Reach North data were conducted, and these resulted in significantly different resistivity models. The resistivity model obtained from the anisotropic inversion is preferred because it contains a simpler resistivity structure that is in better agreement with the mapped geology. The

anisotropic model contains a sharp resistivity contrast between features AF2 and AF3 that corresponds to the mapped location of the Southern Rocky Mountain Trench Fault (SRMTF). This contrast is visible in Figure 4.22. In this figure, vertical slices from the $\rho_y$ resistivity model are shown (i.e. resistivity measured in the east-west direction). While AF2 and AF3 are interpreted as the Yellowjacket Gneiss, the lithology of AF3 in the footwall of the SRMTF may be associated with fluids or a solid conductive phase such as graphite or sulfides. Fluids would need to be connected in thin, horizontal lenses to explain the high values of $\rho_z$ observed for AF3, which is unlikely for a Proterozoic Gneiss. Therefore, graphite or sulfides connected along the foliation of the gneiss are more consistent with the anisotropic resistivity than fluids. The anisotropic resistivity model also provides information on the SRMTF offset. The dip separation is probably greater than 2 km, and/or significant dextral strike separation occurred because the resistivity contrast between AF2 and AF3 spans the horizontal and vertical areas of MT data sensitivity.

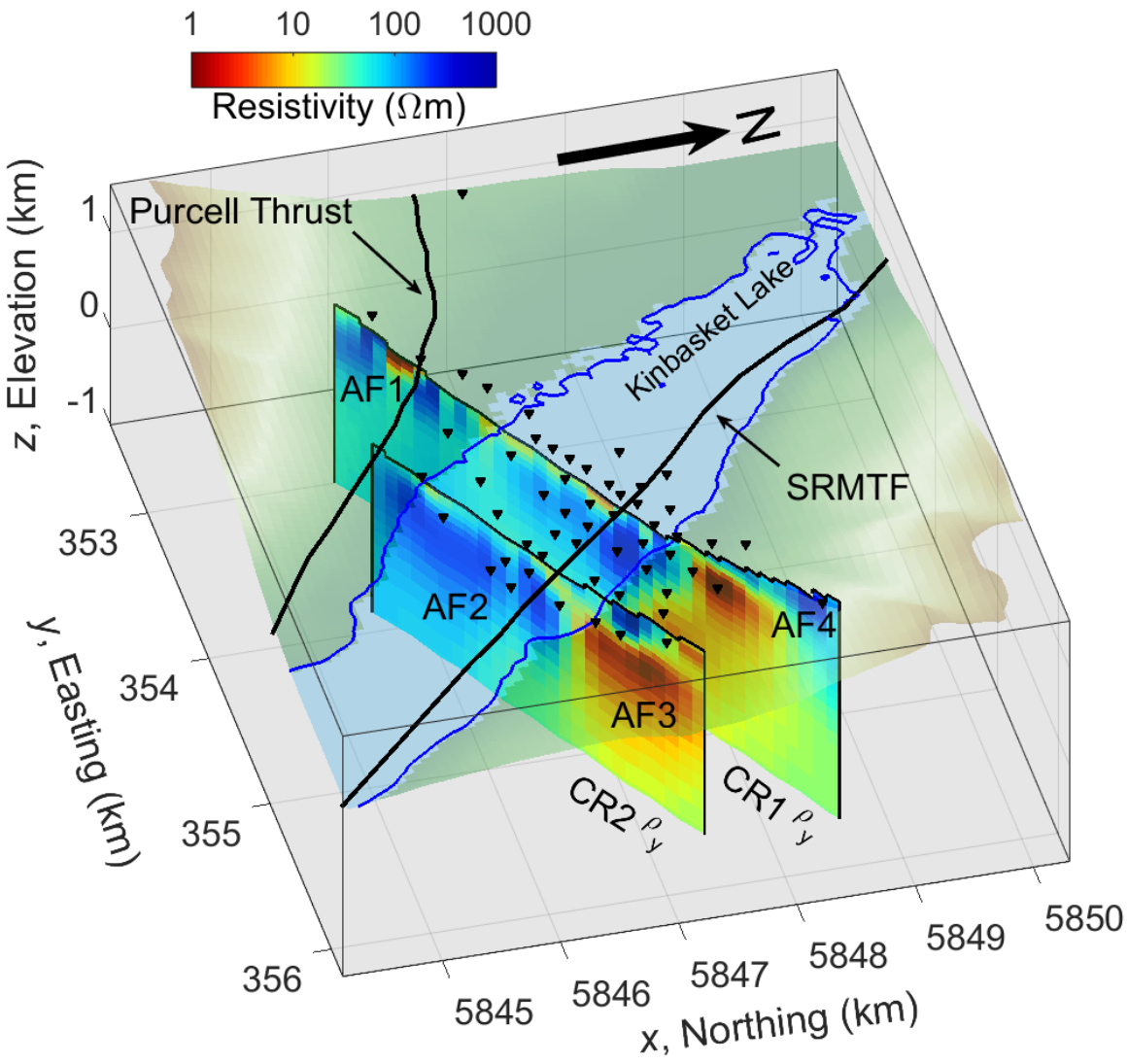


Figure 4.22: 3-D perspective of the Canoe Reach North area with vertical slices from the 3-D anisotropic resistivity model. Vertical slices through the $\rho_y$ model are shown, which is the resistivity measured in the *y* direction. The CR1 and CR2 model slices from the $\rho_x$ and $\rho_z$ models are also shown in Figure 4.15. The *xyz* coordinate system is aligned to geographic coordinates. Black inverted triangles are locations of MT stations. SRMTF = Southern Rocky Mountain Trench Fault. AF1, AF2, AF3, and AF4 are anisotropic features described in the text. AF1 and AF4 are interpreted as the Lower Miette Group metasedimentary sequence. AF2 and AF3 are two lithologic units of the Yellowjacket Gneiss separated by the SRMTF. The low $\rho_y$ values of AF3 may be explained by graphite or sulfides in the foliation of the gneiss. Digital elevation model from NASA JPL (2013).

### 4.6.3. Canoe Reach South

The Canoe Reach South data set consists of 109 MT stations collected by Quantec Geoscience Ltd. The stations were collected on four SW-NE profiles in the vicinity of the Canoe River thermal spring. Phase tensor data on Lines A and B indicate a relatively 2-D resistivity structure beneath Kinbasket Lake at the location of the Canoe River thermal spring. MT data from Lines C and D, located 5 km southeast of the spring, suggest a more complicated 3-D resistivity structure.

As with the Canoe Reach North data set, 3-D isotropic and 3-D anisotropic inversions were conducted for the Canoe Reach South data set. Due to the distribution of MT stations, the data were organized into two groups for inversion: (1) Lines A and B, and (2) Lines C and D. The isotropic and anisotropic inversions of the Lines A and B data produced similar resistivity models. On Lines A and B, AF6 and AF8 are sub-vertical, low resistivity features beneath the Canoe River spring. These features have low values of $\rho_z$, which is the principal resistivity most closely oriented to the ~70° dip of the SRMTF. Therefore, features AF6 and AF8 might correspond to fluids within a fracture zone of the SRMTF.

Isotropic and anisotropic inversions of the Lines C and D also obtained similar resistivity models. The Lines C and D models contain AF12, a feature with a low $\rho_z$ that might be fluids within the SRMTF. See Figure 4.23 for a 3-D perspective of Canoe Reach South, including vertical slices from the $\rho_z$ models (i.e. resistivity measured in the vertical direction). AF6, AF8 (not shown), and AF12 might all correspond to the same SRMTF fracture zone beneath the southwest shore of Kinbasket Lake.

AF11 and AF13 are features with low $\rho_x$ and $\rho_y$ beneath Kinbasket Lake. See Figure 4.24 for a 3-D perspective with vertical slices from the $\rho_x$ models (note that only AF11 is shown). These features may correspond to fluids at the intersection of the SRMTF and its splay in the upper few km beneath Kinbasket Lake. This interpretation is uncertain because these features do not have a similar anomaly in the $\rho_z$ model (see Figure 4.23), and the dip angles of the SRMTF and its splay are not well-constrained in this location.

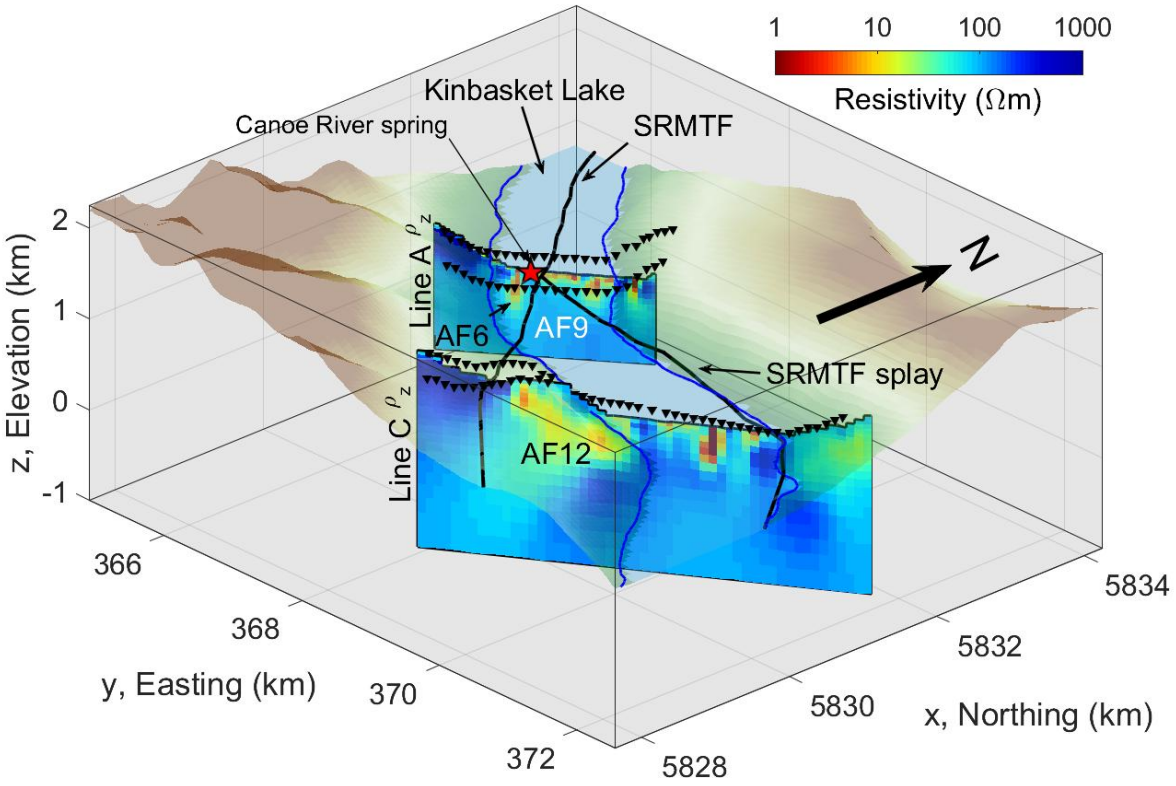


Figure 4.23: 3-D perspective of the Canoe Reach South area with vertical slices from the 3-D anisotropic resistivity models. Vertical slices through the $\rho_z$ models are shown, which is the resistivity measured in the *z* direction. See Figure 4.18 and Figure 4.21 for slices through the $\rho_x$ and $\rho_y$ models. The *xyz* coordinate system is aligned to geographic coordinates. SRMTF = Southern Rocky Mountain Trench Fault. Black inverted triangles are the locations of MT stations. AF6, AF9, and AF12 are features in the anisotropic resistivity models described in the text. AF9 corresponds to the Bulldog Gneiss in the footwall of the SRMTF beneath Kinbasket Lake. AF6 and AF12 may correspond to fluids within the SRMTF. Digital elevation model from NASA JPL (2013).

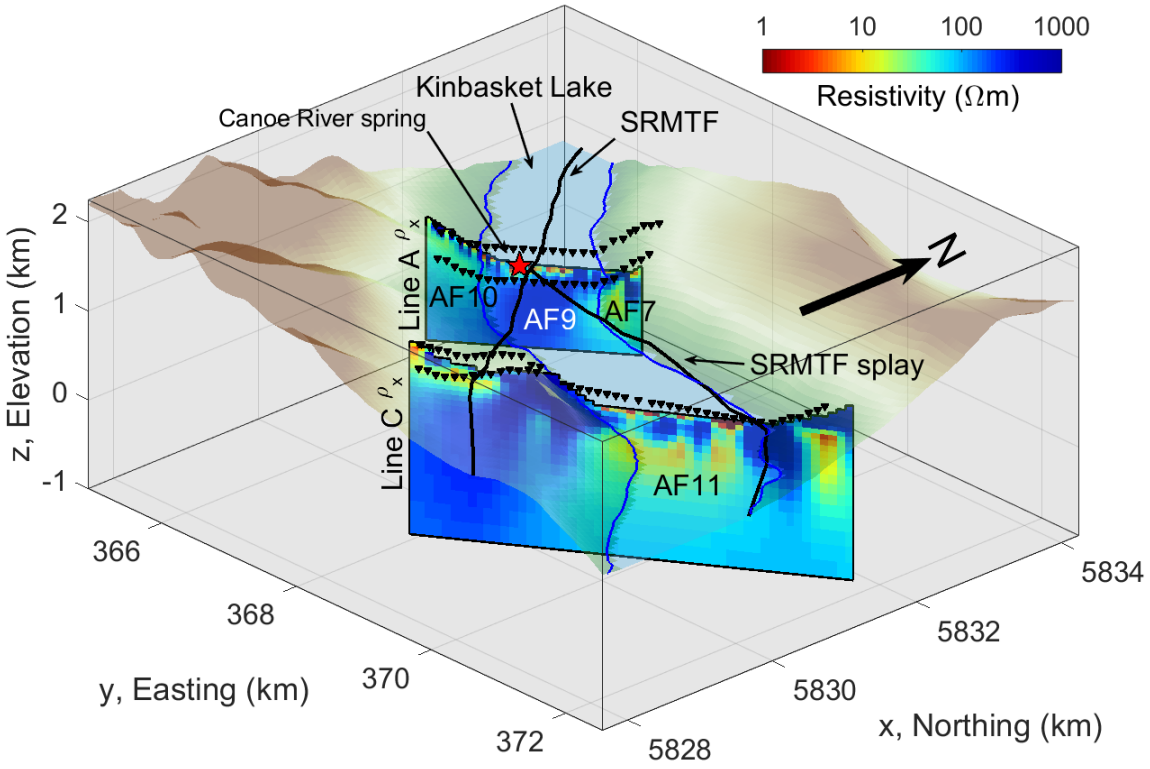


Figure 4.24: 3-D perspective of the Canoe Reach South area with vertical slices from the 3-D anisotropic resistivity models. Vertical slices through the $\rho_x$ models are shown, which is the resistivity measured in the *x* direction. See Figure 4.18 and Figure 4.21 for slices through the $\rho_y$ and $\rho_z$ models. The *xyz* coordinate system is aligned to geographic coordinates. SRMTF = Southern Rocky Mountain Trench Fault. Black inverted triangles are the locations of MT stations. AF7, AF9, AF10, and AF11 are features in the anisotropic resistivity models described in the text. The interpretation of AF7 is uncertain due to its location at the edge of Line A; it may correspond to fluids or the Lower Miette Group metasedimentary sequence. AF9 corresponds to the Bulldog Gneiss in the footwall of the SRMTF beneath Kinbasket Lake. AF10 is in the hanging wall of the SRMTF and may correspond to the Malton Gneiss or Lower Miette Group. AF11 and AF13 (not shown) may correspond to fluids in a fracture zone beneath Kinbasket Lake. Digital elevation model from NASA JPL (2013).

### 4.6.4. Implications for geothermal exploration

This study has implications for geothermal exploration at Canoe Reach and other structurally complex settings. Features AF6, AF8, and AF12 in the Canoe Reach South resistivity models are anisotropic resistivity features in the SRMTF which may be fluids in a fracture zone. These features have a low $\rho_z$, which may be the principal resistivity most closely aligned to the the ~70° dip direction of the SRMTF. Two possible explanations for anisotropic resistivity of fluids in a fault zone are (1) an anisotropic permeability associated with fractures in the fault damage zone, and (2) structural anisotropy such as fault corrugations parallel to fault slip direction. Although there is a lack of case studies demonstrating that MT can detect electrical anisotropy of fluids in faults, there is evidence to suggest that these settings are indeed electrically anisotropic. Studies with simulated resistor networks have demonstrated that permeability anisotropy and resistivity anisotropy are correlated and that both are significant in moderately fractured media (Kirkby et al., 2016; Kirkby & Heinson, 2017). In addition, studies that modeled MT data at a hydraulically fractured EGS site (MacFarlane et al., 2014) and at a sedimentary basin (Kirkby et al., 2015) suggest that electrical anisotropy is necessary to model the distribution of fluids in these fracture zones. Structural anisotropy along fault planes may also contribute to anisotropic permeability and anisotropic resistivity. Corrugations are commonly observed on fault planes at centimeter to kilometer scales (e.g. Edwards et al., 2018; Ferrill et al., 1999; Hancock & Barka, 1987) and may enhance permeability and lower the resistivity parallel to the slip direction. If the most recent slip direction of faults in the SRMT is down-to-the-west, the SRMTF could be corrugated along the down-to-the-west slip direction. These corrugations would restrict fluid flow perpendicular to the slip direction and enhance flow in the slip direction. The cause of electrical anisotropy is likely attributed to a combination of these two factors: the orientation of fractures and structural features of fault planes. The orientation of fractures is likely the dominant feature if the SRMTF has an extensive damage zone, which may be the case at Canoe Reach South. If fluid flow is more restricted to a conduit along the fault plane, which may be the case at Canoe Reach North, then structural features such as fault corrugations might be the dominant feature to cause anisotropy.

This study demonstrates the value of modeling electrical anisotropy in a highly metamorphosed and structurally complex setting. Electrical anisotropy has been reported in

highly foliated metamorphic rocks and may be common; however, 3-D inversion of MT data with electrical anisotropy is still not widely utilized. The example from Canoe Reach North, where the 3-D anisotropic resistivity model was simpler and more consistent with the geology than the 3-D isotropic model, suggests that electrical anisotropy should be considered in structurally complex settings.

The resistivity models show some potential targets for further exploration at Canoe Reach. Conductive features that may correspond to fluids within fractures of the SRMTF include AF6, AF8, and AF12, which are located at Canoe Reach South. The interpretation of features AF11 and AF13 is less certain because these features are located between the SRMTF and its splay, which have poorly constrained dip angles. In contrast, the conductive feature AF3 at Canoe Reach North coincides with the SRMTF but is more likely associated with graphite or sulfides than fluids in the Yellowjacket Gneiss.

# 5. Conclusions

## 5.1. Summary

This thesis has investigated how geothermal exploration with the magnetotelluric (MT) method can be developed to make the method more useful and reduce uncertainty. Chapter 1 stated two areas where research is needed: (1) obtaining more reliable resistivity models from MT data, and (2) interpretation of resistivity models to correctly identify low resistivity features and infer rock properties such as permeability and porosity. Improvements in these two areas of research were demonstrated through case studies from the Krafla geothermal field in Iceland and the Canoe Reach area in British Columbia, Canada.

## 5.2. Results from the Krafla volcanic field, Iceland

Krafla is an active volcanic field in northeast Iceland that hosts a geothermal power station with an installed capacity of 60 MWe. Recent studies have modeled the distribution of supercritical fluids below the existing geothermal fields (e.g. Scott et al., 2015) and others have proposed that replacing steam with supercritical fluids could generate an order of magnitude more electrical power from a geothermal well (Fridleifsson & Elders, 2005). The IDDP-1 well was drilled in 2009 to reach supercritical fluids at an estimated depth of 4 to 5 km below the Krafla geothermal field. However, drilling ended prematurely at a depth of 2.1 km when the drill head encountered a pocket of rhyolite magma. The presence of rhyolite magma at this depth was not predicted by multiple geophysical surveys, including MT. This motivated the work presented in Chapter 4, which focused on (1) obtaining a reliable 3-D resistivity model below Krafla, and (2) understanding the sensitivity of the MT data to rhyolite magma at shallow depth. The major results are summarized below.

### 5.2.1. Results from a new 3-D inversion of the Krafla MT data

#### 5.2.1.1. Improvements to the inversion procedure

The goal of inverting MT data is to obtain a resistivity model that fits the observed data to an acceptable statistical level. Due to this statistical approach and the limitations of the physics of the MT method, inversions are non-unique and result in a range of acceptable

models. Additional data can be included in the inversion to reduce the range of acceptable resistivity models. This motivated the current work on the Krafla MT data, where Rosenkjaer et al. (2015) noted inconsistencies between 3-D resistivity models obtained by different authors using different inversion algorithms.

Previous authors published 3-D resistivity models obtained from inverting the Krafla MT data (Gasperikova et al. 2015; Lindsey & Newman 2015; Rosenkjaer et al. 2015). However, there were inconsistencies between the 3-D resistivity models obtained with different inversion algorithms. Chapter 4 presented a different approach to modeling the Krafla MT data in an attempt to recover a reliable resistivity model. The attempted improvements to the inversion procedure included:

- Using an interpolated 1-D resistivity model derived from inversion MT and time domain electromagnetic (TEM) data as a model constraint. This constraint was implemented as a "prior model" in the ModEM inversion algorithm. The prior model is a constraint on the final resistivity model because the inversion penalizes deviations from the prior model. The default prior model was a uniform halfspace, which effectively constrains the final model to be spatially smooth. However, the inversion using the 1-D resistivity model as a prior model obtained a very similar model as the inversion using a uniform halfspace as a prior model. The two resistivity models contain similar structure and both inversions obtained similarly acceptable r.m.s. misfits. Therefore, using the 1-D resistivity model as a prior model did not significantly impact the final resistivity model.

- Using the full impedance tensor data, instead of only the off-diagonal components used by previous authors. This improvement was implemented to recover resistivity structure that might be constrained by the diagonal elements of the impedance tensor. The diagonal terms are non-zero for 3-D resistivity structure; therefore including them in the inversion might better constrain 3-D features in the resistivity model. Previous workers justified neglecting the diagonal impedance terms because they are often much smaller than the off-diagonal terms. However, some Krafla MT stations contain diagonal terms that are of the same order of magnitude as the off-diagonal terms at frequencies below 0.1 Hz. Therefore, using the full impedance tensor was

expected to improve resolution of 3-D structures in the resistivity model. However, the resistivity model obtained from inverting the full impedance tensor contained similar structures to those reported by previous authors. In this case the addition of the diagonal impedance elements did not significantly impact the final interpretation of the resistivity model. This may be due to the diagonal elements only being significant at a small fraction of the MT data frequencies. However, there is no obvious threshold value above which the diagonal elements are significant, and thus the full impedance tensor should be inverted to ensure that no information is neglected.

- Using a fine mesh with the smallest cells being 100 m x 100 m x 30 m, as opposed to the 250 m x 250 m x 50 m cells used by previous authors. A finer mesh was expected to improve the inversion result for the following reasons. Smaller cells with horizontal dimensions of 100 m by 100 m allow the inversion to include small-scale resistivity structure that may be required at high frequencies. In addition, the smaller cells allow the inversion to implicitly model 3-D bodies that cause galvanic distortion of MT data. However, similar to using the full impedance tensor, the inversions implementing the fine mesh recovered a resistivity model similar to those obtained by previous authors.

The three improvements listed above were implemented to obtain a more reliable resistivity model. Due to the fact that different inversion algorithms were used, it is impossible to quantify improvements over the models presented by previous authors. However, following the inversion approach outlined above, the preferred resistivity model contained a large conductor (C3) at a depth of approximately 2 km near the bottom of the IDDP-1 well. The location of C3 at the bottom of IDDP-1, where rhyolite magma was encountered, was a significant finding that required careful interpretation summarized in the following section.

#### 5.2.1.2. Interpretation of the C3 conductor beneath Krafla

The final preferred 3-D resistivity model contained features similar to those interpreted by previous authors. An extensive low resistivity feature (C1) in the top 0.3 to 0.5

km of the resistivity model corresponds to the clay layer containing smectite-zeolite alteration products. A resistive feature (R1) below the producing geothermal field corresponds to chlorite-epidote alteration at temperatures of 200 to 300°C. A sub-vertical conductor (C2) is associated with aqueous fluids in the Hveragil fault system, which is a major feed zone in the Sudurhlidar subfield. C3 is a large, low resistivity (<10 Ωm) feature at about 2 km b.s.l. seen in Figure 5.1.

Unlike previously published resistivity models, the model from Chapter 4 shows that IDDP-1 terminates on the edge of a low resistivity feature (C3). This is illustrated in Figure 5.1, where the bottom of IDDP-1 intersects the 7 Ωm isosurface. Chapter 4 presented two possible interpretations for C3: (1) a zone of partial melt, or (2) a zone of dehydrated chlorite and/or epidote minerals. The MT data alone cannot resolve whether C3 is caused by either or a combination of these factors. Seismic evidence, including S-wave shadows in the Krafla caldera (green dashed lines in Figure 5.1) does not support the existence of partial melt at 2 km depth. Other studies have proposed more complicated melt geometries beneath Krafla, where evolved rhyolite melt is episodically transported through a dyke and sill complex (e.g. Jónasson, 2007). Small magma bodies in a dyke and sill complex may be too small to be imaged with geophysical methods, including MT.

C3 may also correspond to dehydrated chlorite and epidote minerals. Recent work has shown that rocks containing chlorite and epidote minerals decrease in electrical resistivity when heated to temperatures above 500 to 600°C (Manthilake et al. 2016; Hu et al. 2017). Nono et al. (2018) measured a resistivity of approximately 3 to 30 Ωm for Icelandic rocks containing chlorite/epidote at above 500 to 600°C, which agrees with the resistivity of C3. Dehydration of chlorite and epidote might also explain low resistivity zones below the Hengill and Namafjall geothermal fields in Iceland (Nono et al., 2020). Thus, dehydration of chlorite and epidote may contribute to the low resistivity of C3 below Krafla.

The final interpretation of C3 presented in Chapter 4 incorporates both partial melt and dehydration of chlorite and epidote. The IDDP-1 and K-39 wells intersected rhyolite magma that may exist within a dyke and sill complex instead of a large, continuous magma chamber. At depths below IDDP-1, where the temperature is estimated to be about 500°C, dehydration of chlorite and epidote minerals may explain the low resistivity of feature C3.

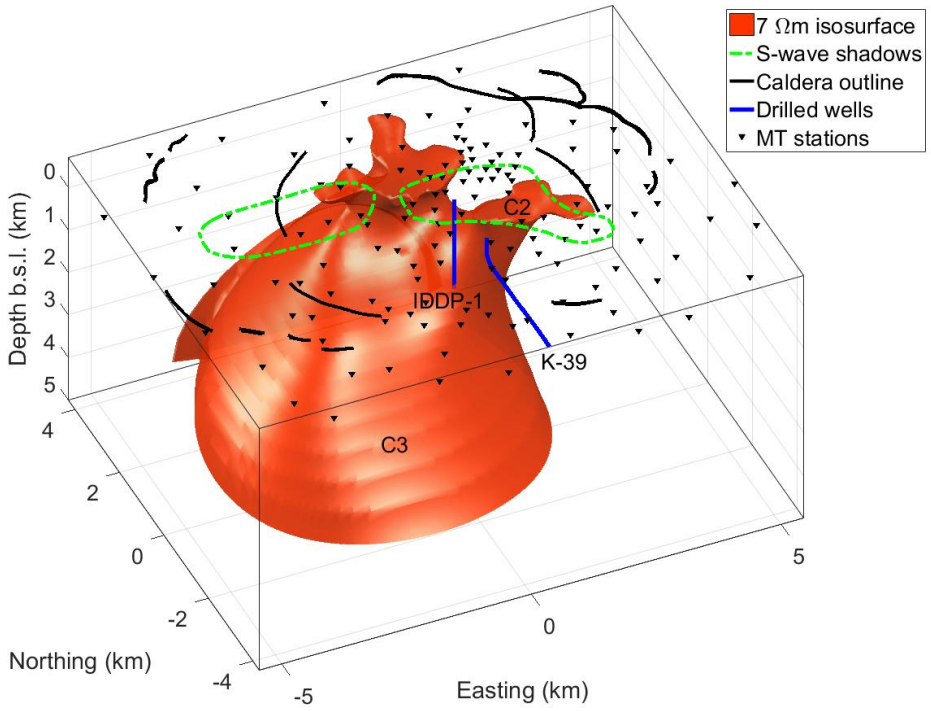


Figure 5.1: 3-D view of the low resistivity features below the Krafla volcanic field plotted as a 7 Ωm isosurface. The low resistivity clay layer (C1) in the top 0.5 km of the model is excluded. S-wave shadow areas from Einarsson (1978).

### 5.2.2. MT data sensitivity to small rhyolite magma bodies

The rhyolite magma body encountered by IDDP-1 was not detected by pre-drilling MT exploration. Chapter 4 describes a set of resolution tests that were performed to understand the sensitivity of MT data to the resistivity structure at the bottom of IDDP-1. These resolution tests were performed to determine the size and resistivity needed for a rhyolite magma body to be detected by the MT data. First, using petrological data from Elders et al. (2011) and Zierenberg et al. (2013) and the empirical relation of Guo et al. (2016), the resistivity of pure rhyolite melt recovered from IDDP-1 was calculated to be in the range 0.6 to 0.9 Ωm. The melt fraction of the IDDP-1 rhyolite magma is difficult to estimate; however, the fact that an aphyric glass was recovered suggests a relatively high melt fraction. In the absence of quantitative data, a wide range of melt fractions from 0.1 to 0.9 was considered, and from these values the bulk resistivity of the IDDP-1 rhyolite magma was estimated to be 0.7 to 30 Ωm. These are relatively high values compared to the

resistivity of other silicic magma reservoirs studied with MT. Heise et al. (2010) estimated a resistivity of ~ 0.3 Ωm and a melt fraction of ~50% for a silicic plume beneath the Taupo Volcanic Zone, and Cordell et al. (2018) estimated a resistivity of ~1 Ωm and a melt fraction of <35% for a silicic magma chamber below Laguna del Maule. The relatively low 1.77 %wt $H_2O$ of the IDDP-1 rhyolite magma contributes significantly to the relatively high calculated resistivity (Elders et al., 2011).

Based on this analysis, 18 hypothetical magma bodies were considered and added to the final resistivity model at the bottom of IDDP-1. Six different resistivity values were tested: 30, 10, 3, 1, 0.3, and 0.1 Ωm, and three geometries were tested: a thin sill (3 km x 3 km x 0.25 km), a 0.125 $km^3$ cube, and a 1 $km^3$ cube. The vertical conductance of each magma body was also calculated because the conductance would likely need to be higher than that of the overlying clay layer (300 S) in order to be detected. In order to assess the MT data sensitivity, the data computed from the edited resistivity model were compared to the data computed from the unedited model. Two methods were used to determine if the MT data were sensitive to the hypothetical magma bodies: (1) comparison of r.m.s. misfit values, and (2) the Kolmogorov-Smirnov (K-S) statistical test. Comparing the r.m.s. misfit of the data from two models is subjective because it is unclear how much of a difference is significant. The K-S test may be a more reliable indicator because it computes an asymptotic p-value that can be compared to a significance level. Using both methods, it was shown that the MT data were only sensitive to thin sills with resistivities of 0.3 and 0.1 Ωm. Note that these resistivities are below those expected of the IDDP-1 rhyolite, and the sill may be unrealistically large. Therefore, smaller and/or more resistive features at the bottom of IDDP-1 may be undetectable by the MT data collected at Krafla. Some undetected magma bodies had high conductances (1000 to 10000 S) which suggests that the vertical conductance of a 3-D body may not determine if it can be detected.

The fact that the MT data were insensitive to any of the hypothetical cubes and the sills with resistivity greater than 0.3 Ωm illustrates the difficulty in detecting small features at large depth with MT. This has implications for exploration of supercritical resources at the base of existing geothermal fields. The heat sources for high temperature geothermal resources such as those in Iceland are magma bodies in the upper crust. MT has limitations that are associated with these high-temperature settings: (1) limited resolution to conductors

beneath conductive clay alteration, and (2) limited resolution to small and/or resistive magma bodies. These limitations should be considered when using MT to image the deep parts of high-temperature geothermal systems.

## 5.3. Results from Canoe Reach area, British Columbia

Canoe Reach is the northern arm of the Kinbasket Lake reservoir, located in the Rocky Mountain Trench (RMT). The RMT is a NNW-SSE trending valley that extends about 1600 km from Montana to the northern border of British Columbia. The southern RMT hosts 8 thermal springs coincident with the Southern Rocky Mountain Trench Fault (SRMTF), which may indicate the presence of potential geothermal resources. One example is the Canoe River thermal spring located about 30 km southeast from the town of Valemount. Recorded outlet temperatures as high as 67°C suggest that the Canoe River thermal spring may be the surface manifestation of a possible high potential geothermal reservoir (Ghomshei, 2007). The Canoe River thermal spring cannot be attributed to a known source of heat in the area. One possibility is that the groundwater is heated by deep circulation within the underlying Southern Rocky Mountain Trench Fault (SRMTF). The magnetotelluric (MT) work at Canoe Reach was performed to image fluid zones in the SRMTF that may be related to a potential geothermal reservoir. The major results are summarized below.

### 5.3.1. Canoe Reach North

This area contained 73 MT stations collected by the University of Alberta and Borealis GeoPower Inc. The grid of MT stations is near the location of the intersection of the Purcell Thrust and the SRMTF, two major regional faults exhibiting brittle fractures. The apparent resistivity, phase, and phase tensor data showed a clear contrast between stations on Kinbasket Lake and those on the northeast shore. Some stations on the northeast shore even had anomalous out-of-quadrant phase, which can be an indication of 3-D resistivity structure or electrical anisotropy. At a frequency of 10 Hz, the phase tensor ellipses on the lake and on the northeast shore have approximately perpendicular orientations, which is a large contrast over a small distance (< 2 km) and indicative of 3-D resistivity structure. In summary, the data indicate that the electrical resistivity structure beneath Canoe Reach North has a 3-D geometry and cannot be approximated as 2-D.

The first inversion of the Canoe Reach North MT data was performed with an algorithm assuming isotropic resistivity. The 3-D resistivity model obtained from this inversion contains a resistive (> 300 Ωm) feature underlying Kinbasket Lake and its northeast shore. The model also contains three narrow, sub-vertical features which are low resistivity (< 3 Ωm) features below the northeast shore. As a result of these features, the resistivity model contains alternating conductive and resistive features that are difficult to reconcile with the mapped geology.

The anisotropic inversion of the Canoe Reach North MT data produced a significantly different resistivity model compared to the isotropic inversion. The difference is greatest beneath the northeast shore, where the anisotropic model contains a single anisotropic feature (AF3) instead of the alternating macro-anisotropic features observed in the isotropic model (IC4, IR1, and IC5). AF3 is spatially continuous and is bounded by the inferred planes of the Bear Foot Thrust and SRMTF, while IC4 in the isotropic model dips almost perpendicular to the inferred planes of the Bear Foot Thrust and the SRMTF. Therefore, the anisotropic model is preferred over the isotropic model because it contains a simpler structure that is in better agreement with the mapped geology. While the anisotropic inversion also produced a better fit to the observed MT data, this is somewhat expected since the anisotropic model has more degrees of freedom than the isotropic model to fit the observed MT data.

A 3-D perspective of the Canoe Reach North area and the anisotropic resistivity model is shown in Figure 5.2. Vertical slices through the $\rho_y$ model are shown. AF1 is a feature below the southwest shore of Kinbasket Lake that has low values of $\rho_x$ (see Figure 4.15) but is more resistive in $\rho_y$ and $\rho_z$. This feature is located in the hanging wall of the Purcell Thrust and likely corresponds to metasediments of the Lower Miette Group. While it is possible to correlate the low $\rho_x$ to fluids in the brittle Purcell Thrust, it is unclear why fluids would produce high values of $\rho_y$ and $\rho_z$. AF4 has similar resistivity values to AF1 and likely corresponds to the Lower Miette Group cover sequence that overlies the Yellowjacket Gneiss. AF2 is a resistive feature in the $\rho_x$, $\rho_y$, and $\rho_z$ models below the lake and the southwest shore. This feature is adjacent to AF3, an anisotropic feature below the northeast shore and in the inferred footwall of the SRMTF. AF3 has low values of $\rho_y$, intermediate $\rho_x$, and high $\rho_z$. Similar to AF1, the low resistivity of AF3 might be due to fluids in a brittle fault (the SRMTF) or due to an electrically anisotropic lithology. The lithologic interpretation is

preferred because it is unclear why fluids in the fault would have such a large degree of anisotropy (around two orders of magnitude for AF3). Therefore, AF2 and AF3 might be two lithologically distinct units of the Yellowjacket Gneiss, offset by an uncertain amount of dip-slip and dextral offset. The amount of offset is not well constrained by the current MT data set, but given that the resistivity contrasts span the vertical and horizontal extent of the MT survey, dip-slip and dextral offset may be greater than 2 km. The low resistivity of AF3 might be due to interconnected graphite or sulfides, and electrical anisotropy is possible if these are connected along the foliation direction.

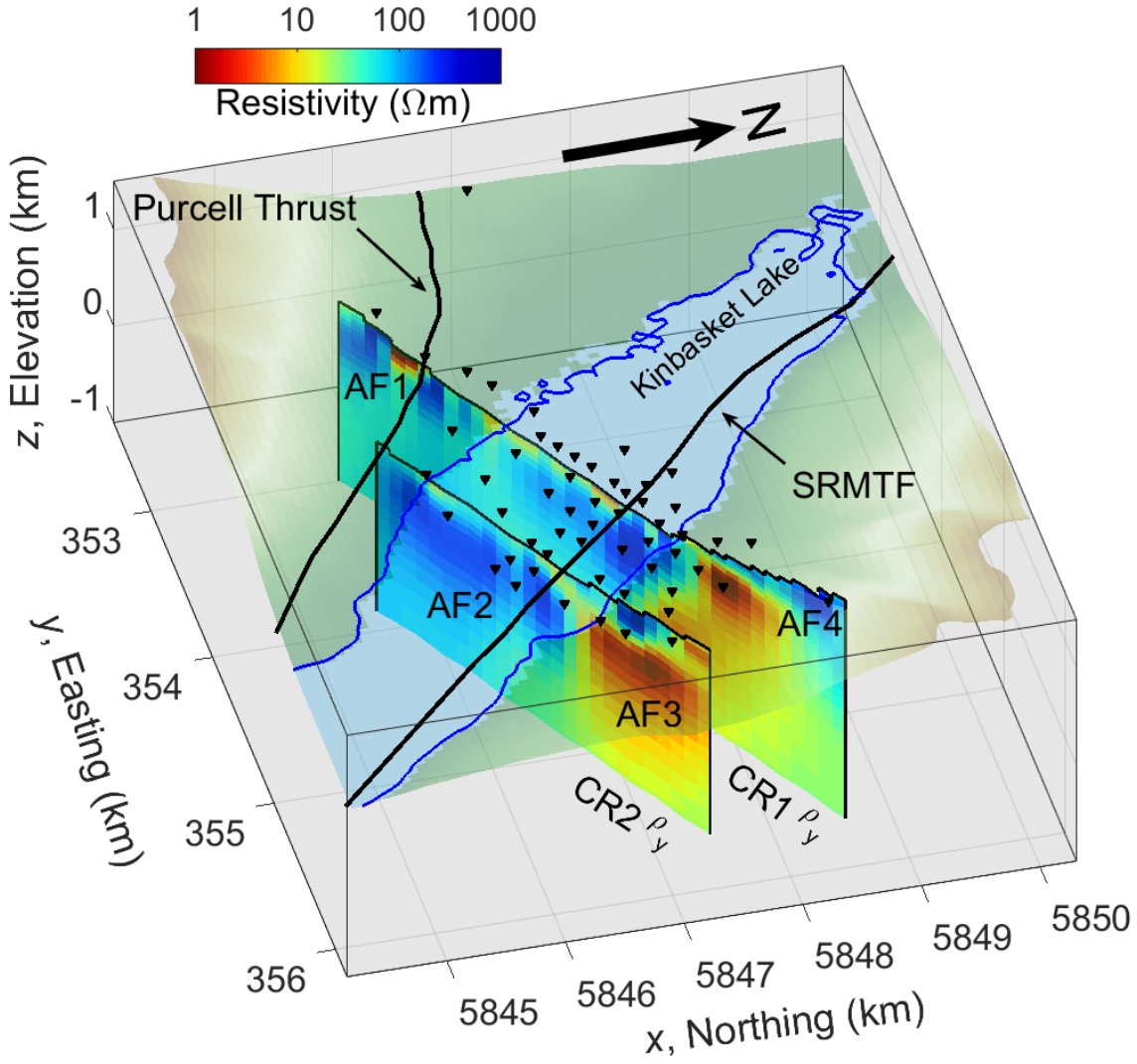


Figure 5.2: 3-D perspective of the Canoe Reach North area with vertical slices from the 3-D anisotropic resistivity model. Vertical slices through the $\rho_y$ model are shown, which is the resistivity measured in the $y$ direction. The CR1 and CR2 model slices from the $\rho_x$ and $\rho_z$ models are also

shown in Figure 4.15. The *xyz* coordinate system is aligned to geographic coordinates. Black inverted triangles are locations of MT stations. SRMTF = Southern Rocky Mountain Trench Fault. AF1, AF2, AF3, and AF4 are anisotropic features described in the text. AF1 and AF4 are interpreted as the Lower Miette Group metasedimentary sequence. AF2 and AF3 are two lithologic units of the Yellowjacket Gneiss separated by the SRMTF. The low $\rho_y$ values of AF3 may be explained by graphite or sulfides in the foliation of the gneiss. Digital elevation model from NASA JPL (2013).

### 5.3.2. Canoe Reach South

This area was investigated using 109 MT stations collected by Quantec Geoscience Ltd. The stations were collected in four SW-NE profiles in the vicinity of the Canoe River thermal spring. The phase tensor data suggest a relatively 2-D structure beneath Lines A and B, which cross the location of the Canoe River spring. Lines C and D phase tensor data show greater spatial variability, indicating a 3-D resistivity structure.

The Canoe Reach South data were inverted in two groups: the Lines A and B data, and the Lines C and D data. For each group, the isotropic and anisotropic inversions obtained similar resistivity models. Features identified as conductors in the isotropic models also appeared as conductors in the anisotropic models, albeit with variable principal resistivity values. Figure 5.3 shows a 3-D perspective of the Canoe Reach South area, with vertical slices from the $\rho_z$ models to demonstrate some of the main features. Features AF6 and AF8, which may correspond to fluids in the SRMTF, have a low $\rho_z$ with higher values of $\rho_x$ and/or $\rho_y$. These features are located beneath the Canoe River spring and may indicate sub-vertical pathways for fluid within the SRMTF. AF12 is a feature beneath the southwest shore that, similar to AF6 and AF8, has a low $\rho_{zz}$ and is located at the mapped SRMTF (see Figure 5.3) Therefore, AF6, AF8, and AF12 may all correspond to fluids in the SRMTF. AF9 is a feature with a moderate to high resistivity in each of its principal resistivities, and likely corresponds to the Bulldog Gneiss in the footwall of the SRMTF.

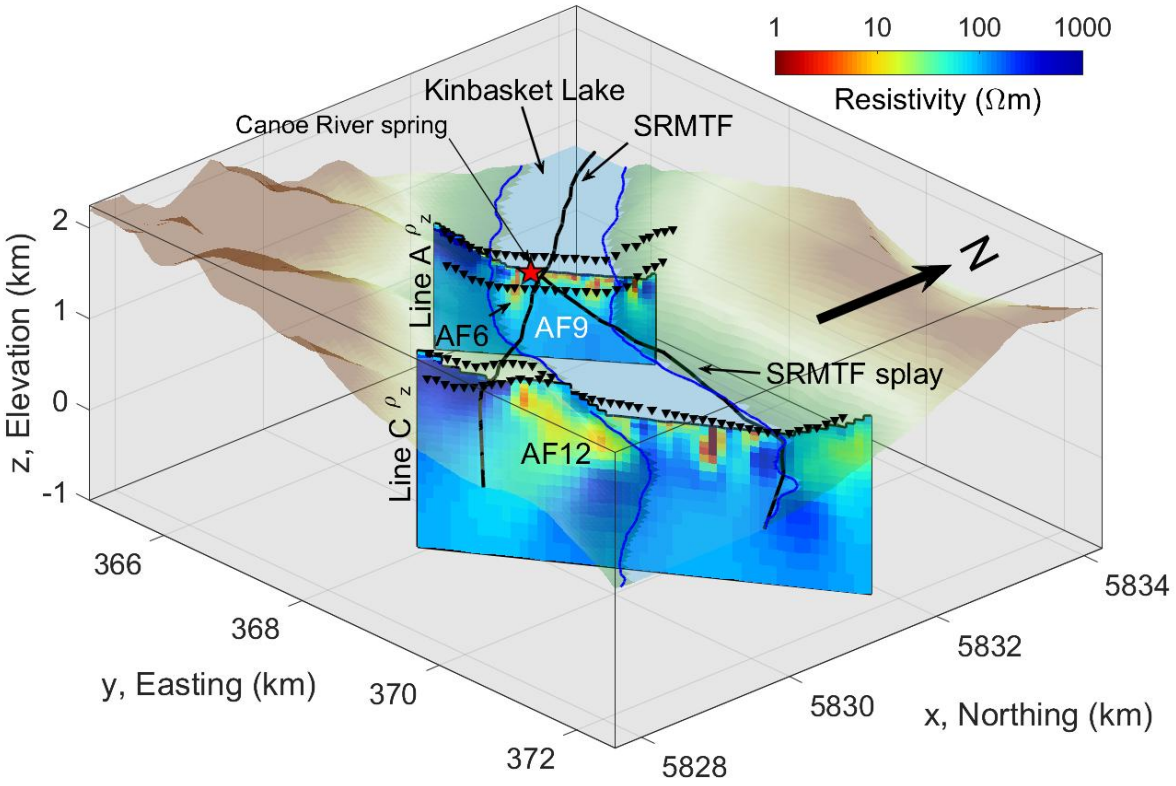


Figure 5.3: 3-D perspective of the Canoe Reach South area with vertical slices from the 3-D anisotropic resistivity models. Vertical slices through the $\rho_z$ model are shown, which is the resistivity measured in the *z* direction. See Figure 4.18 and Figure 4.21 for slices through the $\rho_x$ and $\rho_y$ models. The *xyz* coordinate system is aligned to geographic coordinates. SRMTF = Southern Rocky Mountain Trench Fault. Black inverted triangles are the locations of MT stations. AF6, AF9, and AF12 are features in the anisotropic resistivity models described in the text. AF9 corresponds to the Bulldog Gneiss in the footwall of the SRMTF beneath Kinbasket Lake. AF6 and AF12 may correspond to fluids within the SRMTF. Digital elevation model from NASA JPL (2013).

Figure 5.4 shows the same 3-D perspective as in Figure 5.3, but with slices from the $\rho_x$ models to show different anisotropic features. The interpretation of AF7 is uncertain because it is on the edge of the MT survey. AF7 is only appreciably conductive in $\rho_x$, and may correspond to either (1) an anisotropic unit such as the Lower Miette Group, or (2) a permeable zone in the intersection of the SRMTF and its splay. AF10 is a feature that is most conductive in $\rho_x$ and could represent the Lower Miette Group or the Malton Gneiss. The

most notable features below Lines C and D are IC10 in the isotropic model and AF11 and AF13 in the anisotropic model (AF11 is shown in Figure 5.4). IC10 is a highly conductive (< 3 Ωm) feature while AF11 and AF13 have low values of $\rho_x$ and $\rho_y$ (~ 10 Ωm). These features may correspond to fluid in the intersection between the SRMTF and its splay. However, interpretation of AF11 and AF13 is uncertain because these features do not have low values of $\rho_z$, and the dip angles of the SRMTF and its splay are not well-constrained at this location.

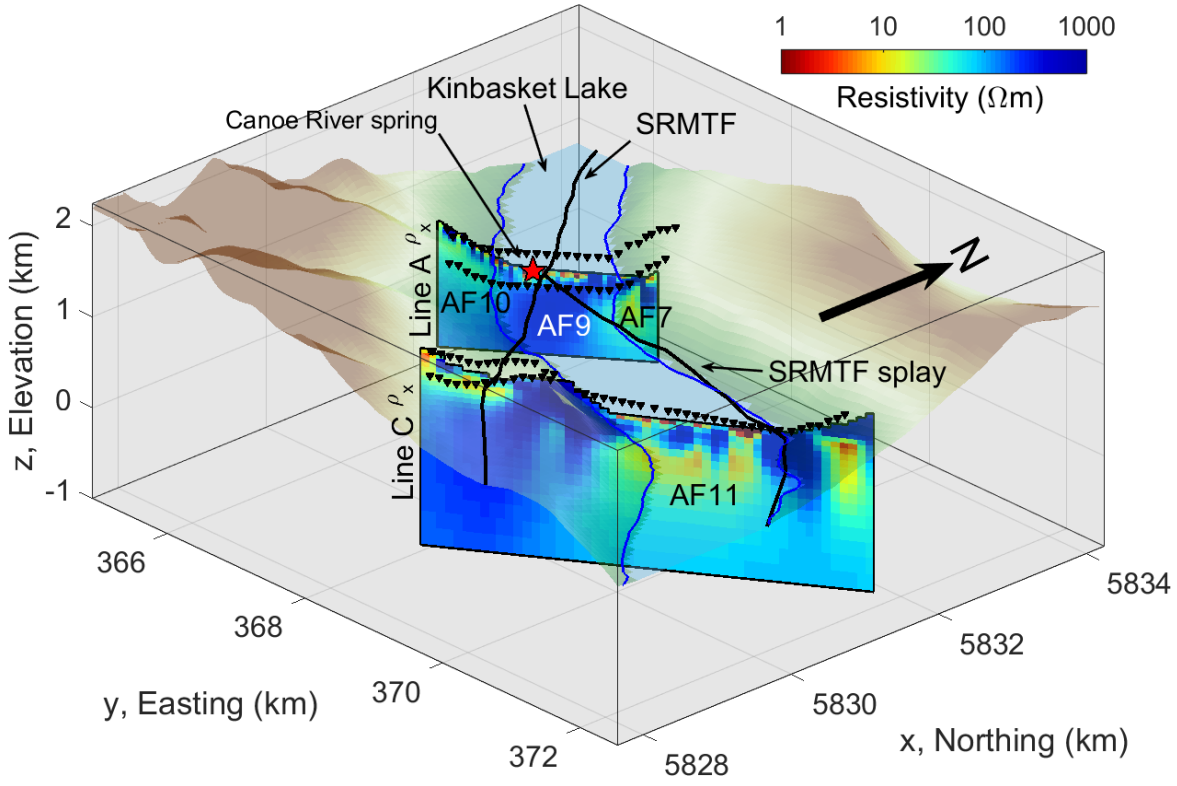


Figure 5.4: 3-D perspective of the Canoe Reach South area with vertical slices from the 3-D anisotropic resistivity models. Vertical slices through the $\rho_x$ model are shown, which is the resistivity measured in the *x* direction. See Figure 4.18 and Figure 4.21 for slices through the $\rho_y$ and $\rho_z$ models. The *xyz* coordinate system is aligned to geographic coordinates. SRMTF = Southern Rocky Mountain Trench Fault. Black inverted triangles are the locations of MT stations. AF7, AF9, AF10, and AF11 are features in the anisotropic resistivity models described in the text. The interpretation of AF7 is uncertain due to its location at the edge of Line A; it may correspond to fluids or the Lower Miette Group metasedimentary sequence. AF9 corresponds to the Bulldog Gneiss in the footwall of the

SRMTF beneath Kinbasket Lake. AF10 is in the hanging wall of the SRMTF and may correspond to the Malton Gneiss or Lower Miette Group. AF11 and AF13 (not shown) may correspond to fluids in a fracture zone beneath Kinbasket Lake. Digital elevation model from NASA JPL (2013).

### 5.3.3. Implications for geothermal exploration

This study has implications for MT exploration in fault-hosted geothermal systems. The Canoe Reach South resistivity models contained features AF6, AF8, and AF12 that agree with the mapped location of the SRMTF. These features had an anisotropic resistivity, with $\rho_z$ as the lowest principal resistivity. Anisotropy of fault zones may be attributed to anisotropic permeability due to fracture orientation, or structural anisotropy along the fault plane. Fracture systems have been shown to be anisotropic in both permeability and resistivity in simulated resistor network studies (Kirkby et al., 2016; Kirkby & Heinson, 2017). MT data have also been used to model the electrical anisotropy of fluid-filled fracture zones at a hydraulically fractured EGS site (MacFarlane et al., 2014) and at a sedimentary basin (Kirkby et al., 2015). In addition to fracture zones, structural anisotropy along fault planes may also contribute to anisotropic permeability and anisotropic resistivity. For example, fault corrugations are commonly observed on fault planes at centimeter to kilometer scales (e.g. Edwards et al., 2018; Ferrill et al., 1999; Hancock & Barka, 1987) and may enhance permeability and lower the resistivity parallel to the slip direction. In fault-hosted geothermal settings, a combination of fracture and structural permeability might contribute to anisotropic permeability and anisotropic resistivity.

Fault corrugations are a possible explanation for the observed electrical anisotropy at Canoe Reach South. Fault corrugations occur in the direction of slip and may enhance permeability in the slip direction. In the case of the SRMTF, the most recent motion is thought to be west-side-down normal faulting with a dip of approximately 70°. Therefore, enhanced fluid flow along the slip direction may correspond to a decreased resistivity in $\rho_z$ observed for features AF6, AF8, and AF12.

Anisotropic permeability of a fracture zone might also explain the anisotropic features AF11 and AF13 observed at Canoe Reach South. These features are located beneath Kinbasket Lake, where the SRMTF and its splay may intersect and host an extensive fracture zone. However, features AF11 and AF13 do not have extensive low resistivity features in the

$\rho_z$ model, which might be expected for the steeply dipping SRMTF. Note that because the inversion coordinate system is not aligned to the SRMTF dip and strike, some mixing of the principal resistivities is to be expected. Performing an inversion with the coordinate system aligned to the anisotropic axes will lead to improved interpretation of the contrasts between principal resistivity values. To this end, additional inversions are required to test the effect of changing the coordinate system.

This study has shown the importance of determining electrical anisotropy during geophysical studies of structurally complex settings. In highly deformed settings, anisotropy can be on a microscopic scale such as foliation in metamorphic rocks. The Canoe Reach North inversion shows how an isotropic inversion can be inadequate to reliably model structures that contain electrically anisotropic rocks. With the increased availability of 3-D inversion algorithms that can include electrical anisotropy, it is worth using one of these algorithms to validate an interpretation that infers an isotropic resistivity structure, especially if the MT data show possible indications of anisotropy.

The resistivity models at Canoe Reach South contain features that are relevant to geothermal exploration. Features AF6, AF8, and AF12 exhibit low $\rho_z$ values that may indicate the presence of fluids within the SRMTF. These features are located on the same ~ 5 km segment of the SRMTF that may contain a permeable fracture zone below the Canoe River thermal spring. About 5 km southeast of the spring, the SRMTF and its splay have an unknown geometry beneath Kinbasket Lake. At this location, features AF11 and AF13 have low $\rho_x$ and $\rho_y$ values that may represent fluids at the intersection of the SRMTF and its splay at depth. However, whether these features are associated with low resistivity features at the thermal spring is uncertain. Additional geophysical work is required to map the extent of these low resistivity zones and to determine if these zones constitute a suitable reservoir for geothermal development.

Finally, inversions of the Canoe Reach North data emphasize that caution is required in interpreting resistivity models. At Canoe Reach North, the footwall of the SRMTF contains the feature AF3 that has low values of $\rho_y$. Although this feature could be explained by the presence of fluids within the SRMTF, it is more likely that the low resistivity is explained by minerals such as graphite or sulfides. If the properties of AF3 are due to the presence fluids, the fluids would need to be predominantly connected in the *x* and *y*

directions to explain the observed combination of low values of $\rho_x$ and $\rho_y$, but high values of $\rho_z$. This might be explained by thin aquifer lenses in horizontally layered beds, but this is unlikely for the highly deformed Yellowjacket Gneiss. In addition, AF3 has high values of $\rho_z$, while decreased values would be expected if fluids were present in the steeply dipping (~ 70°) SRMTF. The low resistivity of AF3 is more simply explained by a solid phase with a low resistivity such as graphite or sulfides. If connected along the foliation direction of the gneiss, these minerals could drastically lower the principal resistivities parallel to the foliation direction. Therefore, the anisotropic low resistivity observed at Canoe Reach is more likely due to graphite or sulfides than fluids.

## 5.4. Opportunities for future work

### 5.4.1. Krafla

(1) Joint seismic and MT inversion

A joint inversion allows subsurface models to be constrained by more than one data set by including more than one type of data in the inversion objective function. Of the many geophysical studies conducted at Krafla, the MT and seismic methods are most sensitive to the deep (> 2 km) structure beneath the volcanic field. A joint inversion of seismic and MT data could improve the imaging of structures near the bottom of IDDP-1 at 2.1 km depth.

Joint inversions can reduce the range of acceptable models by combining datasets sensitive to different physical properties. A key issue to develop joint inversions is to determine how to mathematically link more than one data type in the inversion algorithm. A mathematical link is required for the joint inversion to find a common solution that fits each of the datasets included in the inversion. A link can be established by assuming a mathematical relationship between physical properties, i.e. seismic velocity and electrical resistivity (e.g. Heincke et al., 2017). Alternatively, physical properties can be indirectly linked through empirical relationships to rock properties (i.e. Gao et al., 2012; Hoversten et al., 2006). However, limitations of these approaches are (1) the accuracy of the assumed mathematical relationships between physical properties and/or rock properties, and (2) the fact that relationships between physical properties may not hold for all conditions.

Another approach to mathematically link the different types of data is by constraining the model structure. One of these approaches is the cross-gradient method (Gallardo and Meju, 2004; Gallardo 2007), which minimizes the cross product of the spatial gradients of the physical properties. In essence, this approach enforces structural consistency between the physical property models. The cross gradient method has been successful in obtaining physical property models that are consistent with each other and currently is the most popular method to couple data sets in a joint inversion (Moorkamp, 2017). Further work on a normalized cross gradient has also improved the method such that shallow and deep cross gradients are equally weighted (Bennington et al., 2015).

A cooperative joint inversion is another possibility. Note that a cooperative joint inversion is different from a joint inversion because it inverts individual datasets separately. For example, a model of physical properties obtained from an initial Inversion A can be used to constrain Inversion B, a subsequent inversion of a different physical property. The constraints from Inversion A can be applied at the start of Inversion B or regularly between iterations of Inversion B (Le et al., 2016). With the availability of MT, gravity, and active seismic data at Krafla, a cooperative/joint inversion could be attempted in the near future.

(2) Re-processing and inversion of tipper data

Tipper data are computed from vertical magnetic field data and are sensitive to lateral changes in resistivity. These data are a complementary data set to the MT impedance data and may provide improved spatial resolution in the resistivity model. Tipper data are available at about 40 MT stations at Krafla. However, the data were noisy at many of these stations. The vertical magnetic field component may have been affected by noise from the nearby geothermal wells and power plants. Removal of noisy time series segments may improve the tipper data set and allow it to be inverted with the MT impedance data.

(3) Alteration mineralogy as a constraint in the MT inversion

Digital stratigraphy/alteration data are available from 25 wells in the Krafla geothermal field. The data can be used to define a simple resistivity model to be used as a

constraint in the inversion, because resistivity of hydrothermal systems in Iceland is correlated to alteration (Árnason et al., 2000). For example, a conductive layer (~ 1 to 10 Ωm) can be placed in the model corresponding to shallow depths where smectite is present. A more resistive (> 100 Ωm) layer can be placed where the logs recorded more resistive chlorite-epidote minerals.

This simple resistivity model can be implemented as a prior model in the ModEM inversion algorithm. The inversion minimizes deviations from the prior model, and thus the prior model is a constraint on the final resistivity model. This would be particularly useful in defining the transition from conductive smectite to resistive chlorite-epidote alteration because MT has limited resolution to the bottom of conductive features.

(4) Exploring the possibility of electrical anisotropy below the Krafla volcanic field

The Krafla MT study did not address whether anisotropic resistivity structure exists beneath Krafla. Previous studies have observed evidence of seismic anisotropy in the shallow crust (< 2 km depth) due to the N-S alignment of fissures in the volcanic field (Brandsdóttir et al., 1997; Tang et al., 2008). MT has been shown to be sensitive to the direction of fluid flow in electrically anisotropic fracture networks created by EGS (MacFarlane et al., 2014). Therefore, if the fissure swarm at Krafla is electrically anisotropic, the anisotropy might produce an observable effect in the MT data. Future work could include analyzing the Krafla MT data for indications of anisotropy and performing a 3-D anisotropic inversion.

### 5.4.2. Canoe Reach

(1) Additional geophysics surveys to validate the MT resistivity models

Data from additional geophysical surveys can improve the interpretation of resistivity features at Canoe Reach. For example, a magnetic survey could map the distribution of magnetic minerals such as magnetite and ilmenite. However, the concentration of these minerals depends on the lithology and metamorphic history, and may be highly variable for metamorphic rocks such as those present at Canoe Reach. At Canoe Reach, a magnetic survey might be sensitive to a lithologic boundary between an orthogneiss such as the

Yellowjacket Gneiss and a rock with a pelitic protolith such as the Lower Miette Group. If magnetic data could define lithologic boundaries, these additional constraints could help interpret the Canoe Reach resistivity models.

An induced polarization (IP) survey would be useful for detecting sulfides and graphite, which are highly chargeable (Telford et al., 1990). The chargeability data could help determine the cause of the low resistivity of AF3 in Canoe Reach North.

(2) Additional MT stations at Canoe Reach South

The current study used MT data collected on four profiles that crossed Kinbasket Lake. As a result, the 3-D resistivity models are well-constrained beneath the stations but have poorer resolution away from the stations. Additional stations could be collected between the profiles in order to better constrain the resistivity model. A coarse grid of stations with approximately 250 to 500 m spacing could provide a more detailed view of the possible SRMTF fracture zone beneath the Canoe River thermal spring. For example, more data between Lines A and B could determine if the features AF6 and AF8 are connected along strike.

## 5.5. The future of MT in geothermal exploration

This thesis has shown that although MT is a proven technique for geothermal exploration, improvements in the inversion methodology and methods for assessing resistivity models are needed. Inversion algorithms assuming 1-D and 2-D resistivity structure, which have been used in the past due to computational limits, are not suitable for more general 3-D resistivity structure. With the availability of 3-D inversion algorithms and high performance computational resources, 3-D inversion should be universally applied to MT data collected during geothermal exploration. Similarly, simplifications to the inversion process, such as inverting only the off-diagonal impedance elements, are no longer needed. Although the Krafla 3-D resistivity model did not change significantly when using either (1) off-diagonal elements of the impedance tensor or (2) the full impedance tensor, the same result cannot be expected for all MT data sets. It is impossible to conclusively justify neglecting the diagonal impedance elements by examining the ratio of diagonal to off-

diagonal elements. When the diagonal elements are within one to two orders of magnitude of the off-diagonal elements, it should not be assumed that the diagonal elements can be neglected.

As the Canoe Reach study showed, the assumption that subsurface structure is electrically isotropic should always be critically examined in structurally complex geological settings. While the isotropic inversion of the Canoe Reach North data produced a resistivity model with a satisfactory fit to the observed MT data, the anisotropic inversion produced a spatially simpler model that was in better agreement with the known geology. With the increasing availability of 2-D and 3-D anisotropic inversion algorithms, isotropic models should be carefully verified.

The Kolmogorov-Smirnov (K-S) statistical test, along with other statistical approaches, should be used to assess the sensitivity of MT data to the deeper parts of a resistivity model. The asymptotic *p*-value obtained from the K-S test is an example of a statistical measure that is more robust than simply examining relative changes in r.m.s. data misfit. This approach can be extended to other geophysical methods such as seismic tomography, where hypothesis tests such as the checkerboard test are commonly used to determine the sensitivity of the data to different parts of the model.

Great improvements have been made in the methods available for the inversion of MT data and interpretation of resistivity models. Continued improvements in this area will require that inversion and interpretation includes data from more than one geophysical method. The logical next step is to include MT data in a joint inversion with data sensitive to other physical properties, such as seismic or gravity data. As previously mentioned, the cross gradient approach is a promising joint inversion method that has been implemented in multiple 2-D studies of MT and seismic data (e.g. Bennington et al., 2015; Gallardo & Meju, 2007; Wu et al., 2020); MT, seismic, and gravity data (R. Zhang et al., 2020); and MT, gravity, and magnetic data (Oliver-Ocaño et al., 2019). Cooperative joint inversion is another possibility, with 3-D cooperative joint inversion of MT and seismic data demonstrated by Takam Takougang et al. (2015) and Le et al. (2016).

Recent studies have also investigated the use of MT as a monitoring tool for enhanced geothermal systems (EGS). EGS require methods that detect the location of fracture networks created by fluid injection. Micro-seismic arrays are usually used because they are

sensitive to the location of newly-created fractures. However, MT can provide additional information by directly detecting where the injected fluids are located in the subsurface. In case studies by Didana et al. (2017), Peacock et al. (2012), and Peacock et al. (2013), the authors measured MT data before, during, and after fluid injection at EGS sites. These studies detected changes in the MT data that were above the level of measurement error. The MT data also allowed the authors to infer the approximate direction of fluid flow in the fracture networks, and the results agreed well with concurrent micro-seismic data. These case studies show that MT and micro-seismic can be used as complementary methods to monitoring fluid injection at EGS sites.

# Bibliography


Allen, D. M., Grasby, S. E., & Voormeij, D. A. (2006). Determining the circulation depth of thermal springs in the southern Rocky Mountain Trench, south-eastern British Columbia, Canada using geothermometry and borehole temperature logs. *Hydrogeology Journal*, *14*(1–2), 159–172. https://doi.org/10.1007/s10040-004-0428-z

Allen, R. M., Nolet, G., Morgan, W. J., Vogfjörd, K., Bergsson, B. H., Erlendsson, P., Foulger, G. R., Jakobsdóttir, S., Julian, B. R., Pritchard, M., Ragnarsson, S., & Stefánsson, R. (1999). The thin hot plume beneath Iceland. *Geophysical Journal International*, *137*(1), 51–63. https://doi.org/10.1046/j.1365-246x.1999.00753.x

Arango, C., Marcuello, A., Ledo, J., & Queralt, P. (2009). 3D magnetotelluric characterization of the geothermal anomaly in the Llucmajor aquifer system (Majorca, Spain). *Journal of Applied Geophysics*, *68*(4), 479–488. https://doi.org/https://doi.org/10.1016/j.jappgeo.2008.05.006

Araya Vargas, J., Meqbel, N. M., Ritter, O., Brasse, H., Weckmann, U., Yáñez, G., & Godoy, B. (2019). Fluid Distribution in the Central Andes Subduction Zone Imaged With Magnetotellurics. *Journal of Geophysical Research: Solid Earth*, *124*(4), 4017–4034. https://doi.org/10.1029/2018JB016933

Ármannsson, H., & Fridriksson, T. (2009). Application of Geochemical Methods. *Short Course VII on Exploration for Geothermal Resources*, 1–8.

Árnason, K., Eysteinsson, H., & Hersir, G. P. (2010). Joint 1D inversion of TEM and MT data and 3D inversion of MT data in the Hengill area, SW Iceland. *Geothermics*, *39*(1), 13–34. https://doi.org/10.1016/j.geothermics.2010.01.002

Árnason, K., Karlsdóttir, R., Eysteinsson, H., Flóvenz, Ó. G., & Thor, S. (2000). the Resistivity Structure of High-Temperature Geothermal Systems in Iceland. *Proceedings World Geothermal Congress*, 923–928.

Árnason, K., Vilhjalmsson, A. M., & Bjorndsdottir, T. (2007). A study of the Krafla volcano using gravity, micro-earthquake and MT data. In *Unpublished Report to Landsvirkjun*.

Arnórsson, S. (1995). Geothermal systems in Iceland: Structure and conceptual models—I. High-temperature areas. *Geothermics*, *24*(5), 561–602. https://doi.org/https://doi.org/10.1016/0375-6505(95)00025-9

Arnott, S. K., & Foulger, G. R. (1994). The Krafla spreading segment, Iceland, 1. Three-dimensional crustal structure and the spatial and temporal distribution of local earthquakes. *Journal of Geophysical Research*, *99*(B12). https://doi.org/10.1029/94jb01465

Avdeev, D. B. (2005). Three-dimensional electromagnetic modelling and inversion from theory to application. *Surveys in Geophysics*, *26*(6), 767–799.

Avdeeva, A., Moorkamp, M., Avdeev, D., Jegen, M., & Miensopust, M. P. (2015). Three-dimensional inversion of magnetotelluric impedance tensor data and full distortion matrix. *Geophysical Journal International*, *202*(1), 464–481. https://doi.org/10.1093/gji/ggv144

Axelsson, G., Egilson, T., & Gylfadóttir, S. S. (2014). Modelling of temperature conditions near the bottom of well IDDP-1 in Krafla, Northeast Iceland. *Geothermics*, *49*(March 2009), 49–57. https://doi.org/10.1016/j.geothermics.2013.05.003

Bahr, K. (1988). Interpretation of the magnetotelluric impedance tensor: regional induction and local telluric distortion. *J. Geophys.*, *62*(1), 119–127. https://doi.org/10.1016/S0016-7878(87)80002-0

Bai, D., Unsworth, M. J., Meju, M. A., Ma, X., Teng, J., Kong, X., Sun, Y., Sun, J., Wang, L., Jiang, C., Zhao, C., Xiao, P., & Liu, M. (2010). Crustal deformation of the eastern Tibetan plateau revealed by magnetotelluric imaging. *Nature Geoscience*, *3*(5), 358–362. https://doi.org/10.1038/ngeo830

Banks, J., & Harris, N. B. (2018). Geothermal potential of Foreland Basins: A case study from the Western Canadian Sedimentary Basin. *Geothermics*, *76*, 74–92. https://doi.org/10.1016/J.GEOTHERMICS.2018.06.004

Baños, R., Manzano-Agugliaro, F., Montoya, F. G., Gil, C., Alcayde, A., & Gómez, J. (2011).

Optimization methods applied to renewable and sustainable energy: A review. *Renewable and Sustainable Energy Reviews*, *15*(4), 1753–1766. https://doi.org/10.1016/j.rser.2010.12.008

Barros, N., Cole, J. J., Tranvik, L. J., Prairie, Y. T., Bastviken, D., Huszar, V. L. M., Del Giorgio, P., & Roland, F. (2011). Carbon emission from hydroelectric reservoirs linked to reservoir age and latitude. *Nature Geoscience*, *4*(9), 593–596. https://doi.org/10.1038/ngeo1211

Batini, F., & Nicolich, R. (1985). P and S reflection seismic profiling and well logging in the travale geothermal field. *Geothermics*, *14*(5), 731–747. https://doi.org/https://doi.org/10.1016/0375-6505(85)90049-5

Beardsmore, G. (2004). The Influence of Basement on Surface Heat Flow in the Cooper Basin. *Exploration Geophysics*, *35*(4), 223–235. https://doi.org/10.1071/EG04223

Becken, M., Ritter, O., Park, S. K., Bedrosian, P. A., Weckmann, U., & Weber, M. (2008). A deep crustal fluid channel into the San Andreas Fault system near Parkfield, California. *Geophysical Journal International*, *173*(2), 718–732. https://doi.org/10.1111/j.1365-246X.2008.03754.x

Bellani, S., Brogi, A., Lazzarotto, A., Liotta, D., & Ranalli, G. (2004). Heat flow, deep temperatures and extensional structures in the Larderello Geothermal Field (Italy): Constraints on geothermal fluid flow. *Journal of Volcanology and Geothermal Research*, *132*(1), 15–29. https://doi.org/10.1016/S0377-0273(03)00418-9

Bennington, N. L., Zhang, H., Thurber, C. H., & Bedrosian, P. A. (2015). Joint inversion of seismic and magnetotelluric data in the Parkfield Region of California using the normalized cross-gradient constraint. *Pure and Applied Geophysics*, *172*(5), 1033–1052.

Bertrand, E. A., Caldwell, T. G., Hill, G. J., Wallin, E. L., Bennie, S. L., Cozens, N., Onacha, S. A., Ryan, G. A., Walter, C., Zaino, A., & Wameyo, P. (2012). Magnetotelluric imaging of upper-crustal convection plumes beneath the Taupo Volcanic Zone, New Zealand. *Geophysical Research Letters*, *39*(2). https://doi.org/10.1029/2011GL050177

Bibby, H. M., Caldwell, T. G., Davey, F. J., & Webb, T. H. (1995). Geophysical evidence on the structure of the Taupo Volcanic Zone and its hydrothermal circulation. *Journal of Volcanology and Geothermal Research*, *68*(1), 29–58. https://doi.org/https://doi.org/10.1016/0377-0273(95)00007-H

Bibby, H. M., Dawson, G. B., Rayner, H. H., Bennie, S. L., & Bromley, C. J. (1992). Electrical resistivity and magnetic investigations of the geothermal systems in the Rotorua area, New Zealand. *Geothermics*, *21*(1–2), 43–64. https://doi.org/10.1016/0375-6505(92)90067-J

Bibby, H. M., Risk, G. F., Grant Caldwell, T., & Heise, W. (2009). Investigations of deep resistivity structures at the Wairakei geothermal field. *Geothermics*, *38*(1), 98–107. https://doi.org/https://doi.org/10.1016/j.geothermics.2008.07.002

Björnsson, A., Eysteinsson, H., & Beblo, M. (2005). Crustal formation and magma genesis beneath Iceland: Magnetotelluric constraints. *Special Paper 388: Plates, Plumes and Paradigms*, *2388*(38), 665–686. https://doi.org/10.1130/0-8137-2388-4.665

Blackwell, D. D., Wisian, K. W., Benoit, D., & Gollan, B. (1999). Structure of The Dixie Valley Geothermal System, a "Typical" Basin and Range Geothermal System, From Thermal and Gravity Data. *Geothermal Resources Council Transactions*, *23*, 525–531.

Blewitt, G., Coolbaugh, M., Holt, W., Kreemer, C., Davis, J. L., & Bennett, R. A. (2002). Targeting of potential geothermal resources in the Great Basin from regional relationships between geodetic strain and geological structures. *Geothermal Resources Council Transactions*, *26*, 523–525.

Boden, T. A., Andres, R. J., & Marland, G. (2017). *Global, Regional, and National Fossil-Fuel CO2 Emissions (1751 - 2014)*. https://doi.org/10.3334/CDIAC/00001_V2017

Booker, J. R. (2014). The Magnetotelluric Phase Tensor: A Critical Review. *Surveys in Geophysics*, *35*(1), 7–40. https://doi.org/10.1007/s10712-013-9234-2

Börner, R. U. (2010). Numerical modelling in geo-electromagnetics: Advances and challenges. *Surveys in Geophysics*, *31*(2), 225–245. https://doi.org/10.1007/s10712-009-9087-x

BP. (2019). *BP Statistical Review of World Energy*.

Brandsdóttir, B., Menke, W., Einarsson, P., White, R. S., & Staples, R. K. (1997). Färoe-Iceland Ridge Experiment 2. Crustal structure of the Krafla central volcano. *Journal of Geophysical Research: Solid Earth*, *102*(B4), 7867–7886. https://doi.org/10.1029/96JB03799

Brosch, F. J., Schachner, K., Blümel, M., Fasching, A., & Fritz, H. (2000). Preliminary investigation results on fabrics and related physical properties of an anisotropic gneiss. *Journal of Structural Geology*, *22*(11), 1773–1787. https://doi.org/https://doi.org/10.1016/S0191-8141(00)00106-1

Buland, A., & Kolbjørnsen, O. (2012). Bayesian inversion of CSEM and magnetotelluric data. *Geophysics*, *77*(1), E33–E42.

Caine, J. S., Evans, J. P., & Forster, C. B. (1996). Fault zone architecture and permeability structure. *Geology*, *24*(11), 1025. https://doi.org/10.1130/0091-7613(1996)024<1025:FZAAPS>2.3.CO;2

Caldwell, T. G., Bibby, H. M., & Brown, C. (2004). The magnetotelluric phase tensor. *Geophysical Journal International*, *158*(2), 457–469. https://doi.org/10.1111/j.1365-246X.2004.02281.x

Campanyà, J., Ledo, J., Queralt, P., Marcuello, A., Muñoz, J. A., Liesa, M., & Jones, A. G. (2018). New geoelectrical characterization of a continental collision zone in the Central – Eastern Pyrenees: Constraints from 3-D joint inversion of electromagnetic data. *Tectonophysics*, *742–743*, 168–179. https://doi.org/https://doi.org/10.1016/j.tecto.2018.05.024

Chamberlain, V. E., & Lambert, R. S. J. (1985). Cordilleria, a newly defined Canadian microcontinent. *Nature*, *314*(6013), 707–713.

Chave, A. D., & Smith, J. T. (1994). On electric and magnetic galvanic distortion tensor decompositions. *Journal of Geophysical Research: Solid Earth*, *99*(B3), 4669–4682.

Chave, A. D., Thomson, D. J., & Ander, M. E. (1987). On the robust estimation of power spectra, coherences, and transfer functions. *Journal of Geophysical Research*, *92*(B1), 633. https://doi.org/10.1029/JB092iB01p00633

Chen, J., Hoversten, G. M., Key, K., Nordquist, G., & Cumming, W. (2012). Stochastic inversion of magnetotelluric data using a sharp boundary parameterization and application to a geothermal site. *Geophysics*, *77*(4), E265–E279. https://doi.org/10.1190/geo2011-0430.1

Chouteau, M., & Tournerie, B. (2000). Analysis of magnetotelluric data showing phase rolling out of quadrant (PROQ). *SEG Technical Program Expanded Abstracts*, 344–346.

Clague, J. J. (1974). The St. Eugene Formation and the Development of the Southern Rocky Mountain Trench. *Canadian Journal of Earth Sciences*, *11*(7), 916–938. https://doi.org/10.1139/e74-091

Cordell, D., Unsworth, M. J., & Díaz, D. (2018). Imaging the Laguna del Maule Volcanic Field, central Chile using magnetotellurics: Evidence for crustal melt regions laterally-offset from surface vents and lava flows. *Earth and Planetary Science Letters*, *488*, 168–180. https://doi.org/10.1016/j.epsl.2018.01.007

Cumming, W. (2009). Geothermal Resource Conceptual Models Using Surface Exploration Data. *Thirty-Fourth Workshop on Geothermal Reservoir Engineering*, SGP-TR-187.

Cumming, W., & Mackie, R. L. (2010). Resistivity imaging of geothermal resources using 1D, 2D and 3D MT inversion and TDEM static shift correction illustrated by a Glass Mountain case history. *Proceedings World Geothermal Congress*, 25–29.

Curewitz, D., & Karson, J. A. (1997). Structural settings of hydrothermal outflow: Fracture permeability maintained by fault propagation and interaction. *Journal of Volcanology and Geothermal Research*. https://doi.org/10.1016/S0377-0273(97)00027-9

Currie, C. A., Wang, K., Hyndman, R. D., & He, J. (2004). The thermal effects of steady-state slab-driven mantle flow above a subducting plate: The Cascadia subduction zone and backarc. *Earth and Planetary Science Letters*, *223*(1–2), 35–48. https://doi.org/10.1016/j.epsl.2004.04.020

Davies, J. H., & Davies, D. R. (2010). Earth's surface heat flux. *Solid Earth*, *1*(1), 5–24. https://doi.org/10.5194/se-1-5-2010

Davis, E. E., & Lewis, T. J. (1984). Heat flow in a back-arc environment: intermontane and Omineca crystalline belts, southern Canadian Cordillera. *Canadian Journal of Earth Sciences*, *21*(6), 715–726. https://doi.org/10.1139/e84-077

Deemer, B. R., Harrison, J. A., Li, S., Beaulieu, J. J., Delsontro, T., Barros, N., Bezerra-Neto, J. F., Powers, S. M., Dos Santos, M. A., & Vonk, J. A. (2016). Greenhouse gas emissions from reservoir water surfaces: A new global synthesis. *BioScience*, *66*(11), 949–964. https://doi.org/10.1093/biosci/biw117

DeMets, C., Gordon, R. G., Argus, D. F., & Stein, S. (1990). Current plate motions. *Geophysical Journal International*, *101*(2), 425–478. https://doi.org/10.1111/j.1365-246X.1990.tb06579.x

Didana, Y. L., Heinson, G., Thiel, S., & Krieger, L. (2017). Magnetotelluric monitoring of permeability enhancement at enhanced geothermal system project. *Geothermics*, *66*, 23–38. https://doi.org/https://doi.org/10.1016/j.geothermics.2016.11.005

Dini, A., Gianelli, G., Puxeddu, M., & Ruggieri, G. (2005). Origin and evolution of Pliocene-Pleistocene granites from the Larderello geothermal field (Tuscan Magmatic Province, Italy). *Lithos*, *81*(1–4), 1–31. https://doi.org/10.1016/j.lithos.2004.09.002

Dobson, P. F. (2016). A review of exploration methods for discovering hidden geothermal systems. *Geothermal Resources Council Transactions*, *40*, 695–706.

Edwards, J. H., Kluesner, J. W., Silver, E. A., Brodsky, E. E., Brothers, D. S., Bangs, N. L., Kirkpatrick, J. D., Wood, R., & Okamoto, K. (2018). Corrugated megathrust revealed offshore from Costa Rica. *Nature Geoscience*, *11*(3), 197–202. https://doi.org/10.1038/s41561-018-0061-4

Egbert, G. D. (1990). Comments On 'Concerning dispersion relations for the magnetotelluric impedance tensor' By E. Yee and K. V. Paulson. *Geophysical Journal International*, *102*(1), 1–8. https://doi.org/10.1111/j.1365-246X.1990.tb00525.x

Egbert, G. D., & Booker, J. R. (1986). Robust estimation of geomagnetic transfer functions. *Geophysical Journal of the Royal Astronomical Society*, *87*(1), 173–194. https://doi.org/10.1111/j.1365-246X.1986.tb04552.x

Egbert, G. D., Eisel, M., Boyd, O. S., & Morrison, H. F. (2000). DC trains and Pc3s: Source effects in mid-latitude geomagnetic transfer functions. *Geophysical Research Letters*, *27*(1), 25–28. https://doi.org/10.1029/1999GL008369

Eggertsson, G. H., Lavallée, Y., Kendrick, J. E., & Markússon, S. H. (2020). Improving fluid flow in geothermal reservoirs by thermal and mechanical stimulation: The case of Krafla volcano, Iceland. *Journal of Volcanology and Geothermal Research*, *391*, 106351. https://doi.org/10.1016/j.jvolgeores.2018.04.008

Einarsson, P. (1978). S-wave shadows in the Krafla Caldera in NE-Iceland, evidence for a magma chamber in the crust. *Bulletin Volcanologique*, *41*(3), 187–195. https://doi.org/10.1007/BF02597222

Eisel, M., & Haak, V. (1999). Macro-anisotropy of the electrical conductivity of the crust: A magnetotelluric study of the German Continental Deep Drilling site (KTB). *Geophysical Journal International*, *136*(1), 109–122. https://doi.org/10.1046/j.1365-246X.1999.00707.x

Elders, W. A., Fridleifsson, G. Ó., & Albertsson, A. (2014). Drilling into magma and the implications of the Iceland Deep Drilling Project (IDDP) for high-temperature geothermal systems worldwide. *Geothermics*, *49*, 111–118. https://doi.org/10.1016/j.geothermics.2013.05.001

Elders, W. A., Fridleifsson, G. Ó., Zierenberg, R. A., Pope, E. C., Mortensen, A. K., Gudmundsson, Á., Lowenstern, J. B., Marks, N. E., Owens, L., Bird, D. K., Reed, M., Olsen, N. J., & Schiffman, P. (2011). Origin of a rhyolite that intruded a geothermal well while drilling at the Krafla volcano, Iceland. *Geology*, *39*(3), 231–234. https://doi.org/10.1130/G31393.1

Evans, K. F., Genter, A., & Sausse, J. (2005). Permeability creation and damage due to massive fluid injections into granite at 3.5 km at Soultz: 1. Borehole observations. *Journal of Geophysical Research: Solid Earth*, *110*(4), 1–19. https://doi.org/10.1029/2004JB003168

Evans, K. F., Moriya, H., Niitsuma, H., Jones, R. H., Phillips, W. S., Genter, A., Sausse, J., Jung, R., & Baria, R. (2005). Microseismicity and permeability enhancement of hydrogeologic structures during massive fluid injections into granite at 3 km depth at the Soultz HDR site. *Geophysical Journal International*, *160*(1), 388–412. https://doi.org/10.1111/j.1365-246X.2004.02474.x

Fairbank, B. P., Faulkner, R. L., Hickson, C. J., Roots, C., Souther, J., G, Woodsworth, G. J., Jessop, A., M, Bentkowski, W. H., Lewis, T., J, Macrae, J. M., Rowling, J., Church, B. N., & Finvers, M. (1992). *Geothermal resources of British Columbia*. https://doi.org/10.4095/133397

Fargione, J., Hill, J., Tilman, D., Polasky, S., & Hawthorne, P. (2008). Land Clearing and the Biofuel Carbon Debt. *Science*, *319*(5867), 1235 LP – 1238. https://doi.org/10.1126/science.1152747

Farquharson, C. G., Oldenburg, D., Haber, E., & Shekhtman, R. (2002). An algorithm for the three-dimensional inversion of magnetotelluric data. *72nd SEG Annual Meeting*, 649–652. https://doi.org/10.1111/j.1365-2478.2007.00614.x

Faulds, J. E., & Hinz, N. H. (2015). Favorable Tectonic and Structural Settings of Geothermal Systems in the Great Basin Region , Western USA: Proxies for Discovering Blind Geothermal Systems. *Proceedings World Geothermal Congress*, *April*, 1–6.

Faulds, J. E., Hinz, N. H., Coolbaugh, M. F., Shevenell, L. A., Siler, D. L., DePolo, C. M., Hammond, W. C., Kreemer, C., Oppliger, G., Wannamaker, P. E., Queen, J. H., & Visser, C. F. (2015). Integrated geologic and geophysical approach for establishing geothermal play fairways and discovering blind geothermal systems in the great basin region, western USA: A progress report. *Geothermal Resources Council Transactions*, *39*, 691–700.

Ferguson, G., & Grasby, S. E. (2011). Thermal springs and heat flow in North America. *Geofluids*, *11*(3), 294–301. https://doi.org/10.1111/j.1468-8123.2011.00339.x

Ferrill, D. A., Stamatakos, J. A., & Sims, D. (1999). Normal fault corrugation: Implications for growth and seismicity of active normal faults. *Journal of Structural Geology*. https://doi.org/10.1016/S0191-8141(99)00017-6

Flóvenz, Ó. G., & Gunnarsson, K. (1991). Seismic crustal structure in Iceland and surrounding area. *Tectonophysics*, *189*(1), 1–17. https://doi.org/https://doi.org/10.1016/0040-1951(91)90483-9

Flóvenz, Ó. G., & Saemundsson, K. (1993). Heat flow and geothermal processes in Iceland. *Tectonophysics*, *225*(1), 123–138. https://doi.org/https://doi.org/10.1016/0040-1951(93)90253-G

Forster, C. B., & Smith, L. (1988). Groundwater flow systems in mountainous terrain: 2. Controlling factors. *Water Resources Research*, *24*(7), 1011–1023. https://doi.org/10.1029/WR024i007p01011

Forster, P., Ramaswamy, V., Artaxo, P., Berntsen, T., Betts, R., Fahey, D. W., Haywood, J., Lean, J., Lowe, D. C., Myhre, G., Nganga, J., Prinn, R., Raga, G., Schulz, M., & Van Dorland, R. (2007). *Changes in Atmospheric Constituents and in Radiative Forcing Chapter 2*. Cambridge University Press. http://www.ipcc.ch/pdf/assessment-report/ar4/wg1/ar4-wg1-chapter2.pdf

Foulger, G. R., & Anderson, D. L. (2005). A cool model for the Iceland hotspot. *Journal of Volcanology and Geothermal Research*, *141*(1), 1–22. https://doi.org/https://doi.org/10.1016/j.jvolgeores.2004.10.007

Franco, A., & Villani, M. (2009). Optimal design of binary cycle power plants for water-dominated, medium-temperature geothermal fields. *Geothermics*, *38*(4), 379–391. https://doi.org/10.1016/j.geothermics.2009.08.001

Fridleifsson, G. Ó., Ármannsson, H., Árnason, K., Bjarnason, I. Þ., & Gíslason, G. (2003). Iceland Deep Drilling Project PART I Geosciences – Site selection. In *IDDP Feasibility Report* (Issue May).

Fridleifsson, G. Ó., Ármannsson, H., Guomundsson, Á., Árnason, K., Mortensen, A. K., Pálsson, B., & Einarsson, G. M. (2014). Site selection for the well IDDP-1 at Krafla. *Geothermics*, *49*, 9–15. https://doi.org/10.1016/j.geothermics.2013.06.001

Fridleifsson, G. Ó., & Elders, W. A. (2005). The Iceland Deep Drilling Project: A search for deep unconventional geothermal resources. *Geothermics*, *34*(3), 269–285. https://doi.org/10.1016/j.geothermics.2004.11.004

Fridleifsson, G. Ó., Elders, W. A., Zierenberg, R. A., Stefánsson, A., Fowler, A. P. G., Weisenberger, T. B., Harðarson, B. S., & Mesfin, K. G. (2017). The Iceland Deep Drilling Project 4 . 5 km deep well , IDDP-2 , in the seawater-recharged Reykjanes geothermal field in SW Iceland has

successfully reached its supercritical target. *Scientific Drilling*, 1–12. https://doi.org/10.5194/sd-23-1-2017

Gabrielse, H. (1985). Major dextral transcurrent displacements along the Northern Rocky Mountain Trench and related lineaments in north-central British Columbia. *Bulletin of the Geological Society of America*, *96*(1), 1–14. https://doi.org/10.1130/0016-7606(1985)96<1:MDTDAT>2.0.CO;2

Gal, L. P., & Ghent, E. D. (1990). Metamorphism in the Solitude Range, southwestern Rocky Mountains, British Columbia: comparison with adjacent Omineca Belt rocks and tectonometamorphic implications for the Purcell Thrust. *Canadian Journal of Earth Sciences*, *27*(11), 1511–1520. https://doi.org/10.1139/e90-161

Gallardo, L. A., & Meju, M. A. (2007). Joint two-dimensional cross-gradient imaging of magnetotelluric and seismic traveltime data for structural and lithological classification. *Geophysical Journal International*, *169*(3), 1261–1272. https://doi.org/10.1111/j.1365-246X.2007.03366.x

Gamble, T. D., Goubau, W. M., & Clarke, J. (1979). Magnetotellurics with a remote magnetic reference. *Geophysics*, *44*(1), 53–68. https://doi.org/10.1190/1.1440923

Gao, G., Abubakar, A., & Habashy, T. M. (2012). Joint petrophysical inversion of electromagnetic and full-waveform seismic data. *Geophysics*, *77*(3), WA3–WA18. https://doi.org/10.1190/geo2011-0157.1

Garcia, X., & Jones, A. G. (2002). Atmospheric sources for audio-magnetotelluric (AMT) sounding. *Geophysics*, *67*(2), 448–458. https://doi.org/10.1190/1.1468604

Gasperikova, E., Rosenkjaer, G. K., Árnason, K., Newman, G. A., & Lindsey, N. J. (2015). Resistivity characterization of the Krafla and Hengill geothermal fields through 3D MT inverse modeling. *Geothermics*, *57*, 246–257. https://doi.org/10.1016/j.geothermics.2015.06.015

Georgilakis, P. S. (2008). Technical challenges associated with the integration of wind power into power systems. *Renewable and Sustainable Energy Reviews*, *12*(3), 852–863. https://doi.org/https://doi.org/10.1016/j.rser.2006.10.007

Ghomshei, M. M. (2007). *Qualifying Report On: A High-Grade Geothermal Resource In The Canadian Rockies; Canoe Hot Springs, Valemount, British Columbia*.

Gibert, B., Levy, L., Sigmundsson, F., Hersir, G. P., & Flovenz, Ó. G. (2017). Electrical conductivity of basaltic and rhyolitic melts from Krafla central volcano, Iceland. *Proceedings of the IMAGE Final Conference, Akureyri, Iceland*, 4–6.

Glover, P. W. J., Hole, M. J., & Pous, J. (2000). A modified Archie's law for two conducting phases. *Earth and Planetary Science Letters*, *180*(3), 369–383. https://doi.org/https://doi.org/10.1016/S0012-821X(00)00168-0

Goldenfum, J. A. (2012). Challenges and solutions for assessing the impact of freshwater reservoirs on natural GHG emissions. *Ecohydrology & Hydrobiology*, *12*(2), 115–122.

Goubau, W. M., Gamble, T. D., & Clarke, J. (1978). Magnetotelluric data analysis: removal of bias. *Geophysics*, *43*(6), 1157–1166. https://doi.org/10.1190/1.1440885

Gough, D. I. (1986). Mantle upflow tectonics in the Canadian Cordillera. *Journal of Geophysical Research: Solid Earth*, *91*(B2), 1909–1919. https://doi.org/10.1029/JB091iB02p01909

Grasby, S. E., Allen, D. M., Bell, S., Chen, Z., Ferguson, G., Jessop, A., Kelman, M., Ko, M., Majorowicz, J., Moore, M., Raymond, J., & Therrien, R. (2012). *Geothermal energy resource potential of Canada*. https://doi.org/10.4095/291488

Grasby, S. E., & Hutcheon, I. (2001). Controls on the distribution of thermal springs in the southern Canadian Cordillera. *Canadian Journal of Earth Sciences*, *38*(3), 427–440. https://doi.org/10.1139/e00-091

Grasby, S. E., Hutcheon, I., & Krouse, H. R. (2000). The influence of water–rock interaction on the chemistry of thermal springs in western Canada. *Applied Geochemistry*, *15*(4), 439–454. https://doi.org/10.1016/S0883-2927(99)00066-9

Groom, R. W., & Bailey, R. C. (1989). Decomposition of magnetotelluric impedance tensors in the

presence of local three-dimensional galvanic distortion. *Journal of Geophysical Research*, *94*(B2), 1913–1925. https://doi.org/10.1029/JB094iB02p01913

Gudmundsson, A. (1998). Magma chambers modeled as cavities explain the formation of rift zone central volcanoes and their eruption and intrusion statistics. *Journal of Geophysical Research: Solid Earth*, *103*(B4), 7401–7412. https://doi.org/10.1029/97JB03747

Gul, M., Kotak, Y., & Muneer, T. (2016). Review on recent trend of solar photovoltaic technology. *Energy Exploration & Exploitation*, *34*(4), 485–526. https://doi.org/10.1177/0144598716650552

Guo, X., Zhang, L., Behrens, H., & Ni, H. (2016). Probing the status of felsic magma reservoirs: Constraints from the P-T-H2O dependences of electrical conductivity of rhyolitic melt. *Earth and Planetary Science Letters*, *433*, 54–62. https://doi.org/10.1016/j.epsl.2015.10.036

Haber, E., Ascher, U. M., & Oldenburg, D. W. (2004). Inversion of 3D electromagnetic data in frequency and time domain using an inexact all-at-once approach. *Geophysics*, *69*(5), 1216–1228. https://doi.org/10.1190/1.1801938

Haizlip, J. R. (2016). Application of geochemistry to resource assessment and geothermal development projects. In *Geothermal Power Generation* (pp. 77–106). Elsevier. https://doi.org/10.1016/B978-0-08-100337-4.00004-8

Hancock, P. L., & Barka, A. A. (1987). Kinematic indicators on active normal faults in Western Turkey. *Journal of Structural Geology*, *9*(5–6), 573–584. https://doi.org/10.1016/0191-8141(87)90142-8

Heincke, B., Jegen, M., Moorkamp, M., Hobbs, R. W., & Chen, J. (2017). An adaptive coupling strategy for joint inversions that use petrophysical information as constraints. *Journal of Applied Geophysics*, *136*, 279–297. https://doi.org/https://doi.org/10.1016/j.jappgeo.2016.10.028

Heinson, G., & White, A. (2005). Electrical resistivity of the Northern Australian lithosphere: Crustal anisotropy or mantle heterogeneity? *Earth and Planetary Science Letters*, *232*(1), 157–170. https://doi.org/https://doi.org/10.1016/j.epsl.2004.12.029

Heise, W., Caldwell, T. G., Bibby, H. M., & Bannister, S. C. (2008). Three-dimensional modelling of magnetotelluric data from the Rotokawa geothermal field, Taupo Volcanic Zone, New Zealand. *Geophysical Journal International*, *173*(2), 740–750. https://doi.org/10.1111/j.1365-246X.2008.03737.x

Heise, W., Caldwell, T. G., Bibby, H. M., & Bennie, S. L. (2010). Three-dimensional electrical resistivity image of magma beneath an active continental rift, Taupo Volcanic Zone, New Zealand. *Geophysical Research Letters*, *37*(10). https://doi.org/10.1029/2010GL043110

Heise, W., & Pous, J. (2001). Effects of anisotropy on the two-dimensional inversion procedure. *Geophysical Journal International*, *147*(3), 610–621. https://doi.org/10.1046/j.0956-540x.2001.01560.x

Heise, W., & Pous, J. (2003). Anomalous phases exceeding 90° in magnetotellurics: anisotropic model studies and a field example. *Geophysical Journal International*, *155*(1), 308–318. https://doi.org/10.1046/j.1365-246X.2003.02050.x

Hickson, C. J., Huttrer, G., Kunkel, T., Majorowicz, J., Yehia, R., Lund, J., Raffle, K., Moore, M., Woodsworth, G., Boyd, T., & Hjorth, L. (2016). Investigating the Potential for Direct-Use Geothermal Resources in British Columbia : A New Geoscience BC Project. *Geoscience BC Summary of Activities 2015*, *1*, 69–78.

Hildebrand, R. S. (2015). Dismemberment and northward migration of the Cordilleran orogen: Baja-BC resolved. *GSA Today*, *25*(11), 4–11.

Hill, G. J., Caldwell, T. G., Heise, W., Chertkoff, D. G., Bibby, H. M., Burgess, M. K., Cull, J. P., & Cas, R. A. F. (2009). Distribution of melt beneath Mount St Helens and Mount Adams inferred from magnetotelluric data. *Nature Geoscience*, *2*(11), 785–789. https://doi.org/10.1038/ngeo661

Hillis, R., Hand, M., Mildren, S., Reid, P., Reynolds, S., & Nelson, E. (2004). Hot Dry Rock Geothermal Exploration in Australia. *ASEG Extended Abstracts*, *2004*(1), 1–4. https://doi.org/10.1071/aseg2004ab069

Holl, H.-G., & Barton, C. (2015). Habanero field—structure and state of stress. *Proceedings World Geothermal Congress*, 19–25.

House, L. (1987). Locating microearthquakes induced by hydraulic fracturing in crystalline rock. *Geophysical Research Letters*, *14*(9), 919–921. https://doi.org/10.1029/GL014i009p00919

Hoversten, G. M., Cassassuce, F., Gasperikova, E., Newman, G. A., Chen, J., Rubin, Y., Hou, Z., & Vasco, D. (2006). Direct reservoir parameter estimation using joint inversion of marine seismic AVA and CSEM data. *Geophysics*, *71*(3), C1–C13. https://doi.org/10.1190/1.2194510

Hu, H., Dai, L., Li, H., Hui, K., & Sun, W. (2017). Influence of dehydration on the electrical conductivity of epidote and implications for high-conductivity anomalies in subduction zones. *Journal of Geophysical Research: Solid Earth*, *122*(4), 2751–2762. https://doi.org/10.1002/2016JB013767

Hu, W., Abubakar, A., & Habashy, T. M. (2009). Joint electromagnetic and seismic inversion using structural constraints. *Geophysics*, *74*(6). https://doi.org/10.1190/1.3246586

Hyndman, R. D. (2010). The consequences of Canadian Cordillera thermal regime in recent tectonics and elevation: a reviewThis article is one of a series of papers published in this Special Issue on the theme Lithoprobe — parameters, processes, and the evolution of a continent.G. *Canadian Journal of Earth Sciences*, *47*(5), 621–632. https://doi.org/10.1139/E10-016

Hyndman, R. D., & Currie, C. A. (2011). Why is the North America Cordillera high? Hot backarcs, thermal isostasy, and mountain belts. *Geology*, *39*(8), 783–786. https://doi.org/10.1130/G31998.1

Ichihara, H., & Mogi, T. (2009). A realistic 3-D resistivity model explaining anomalous large magnetotelluric phases: The L-shaped conductor model. *Geophysical Journal International*, *179*(1), 14–17. https://doi.org/10.1111/j.1365-246X.2009.04310.x

Ichihara, H., Mogi, T., & Yamaya, Y. (2013). Three-dimensional resistivity modelling of a seismogenic area in an oblique subduction zone in the western Kurile arc: Constraints from anomalous magnetotelluric phases. *Tectonophysics*. https://doi.org/10.1016/j.tecto.2013.05.020

IEA. (2019). *Global Energy & CO2 Status Report 2019*.

IPCC. (2014). Climate Change 2014: Synthesis Report. In *Contribution of Working Groups I, II and III to the Fifth Assessment Report of the Intergovernmental Panel on Climate Change [Core Writing Team, R.K. Pachauri and L.A. Meyer (eds.)]*. https://doi.org/10.1017/CBO9781139177245.003

Jarchow, C. M., Thompson, G. A., Catchings, R. D., & Mooney, W. D. (1993). Seismic evidence for active magmatic underplating beneath the Basin and Range Province, western United States. *Journal of Geophysical Research: Solid Earth*, *98*(B12), 22095–22108. https://doi.org/10.1029/93JB02021

Johnston, S. T. (2008). The Cordilleran Ribbon Continent of North America. *Annual Review of Earth and Planetary Sciences*, *36*(1), 495–530. https://doi.org/10.1146/annurev.earth.36.031207.124331

Jolie, E., Moeck, I., & Faulds, J. E. (2015). Quantitative structural–geological exploration of fault-controlled geothermal systems—A case study from the Basin-and-Range Province, Nevada (USA). *Geothermics*, *54*, 54–67. https://doi.org/10.1016/j.geothermics.2014.10.003

Jónasson, K. (1994). Rhyolite volcanism in the Krafla central volcano, north-east Iceland. *Bulletin of Volcanology*, *56*(6–7), 516–528. https://doi.org/10.1007/BF00302832

Jónasson, K. (2007). Silicic volcanism in Iceland: Composition and distribution within the active volcanic zones. *Journal of Geodynamics*, *43*(1), 101–117. https://doi.org/10.1016/j.jog.2006.09.004

Jones, A. G. (1988). Static shift of magnetotelluric data and its removal in a sedimentary basin environment. *Geophysics*, *53*(7), 967–978. https://doi.org/10.1190/1.1442533

Jones, A. G. (2012). Distortion decomposition of the magnetotelluric impedance tensors from a one-dimensional anisotropic Earth. *Geophysical Journal International*, *189*(1), 268–284. https://doi.org/10.1111/j.1365-246X.2012.05362.x

Jones, A. G., Chave, A. D., Egbert, G. D., Auld, D., & Bahr, K. (1989). A comparison of techniques for magnetotelluric response function estimation. *Journal of Geophysical Research: Solid Earth*, *94*(B10), 14201–14213. https://doi.org/10.1029/JB094iB10p14201

Jousset, P., Haberland, C., Bauer, K., & Arnason, K. (2011). Hengill geothermal volcanic complex (Iceland) characterized by integrated geophysical observations. *Geothermics*, *40*(1), 1–24. https://doi.org/10.1016/j.geothermics.2010.12.008

Kao, D. W., & Rankin, D. (1977). Enhancement Of Signal-To-Noise Ratio In Magnetotelluric Data. *Geophysics*, *42*(1), 103–110. https://doi.org/10.1190/1.1440703

Karingithi, C. W. (2007). Chemical Geothermometers for Geothermal Exploration. *Short Course II on Surface Exploration for Geothermal Resources, Lake Naivasha, Kenya, 2-17 November, 2007*. https://doi.org/10.5382/rev.01.03

Karlsdóttir, R., Vilhjálmsson, A. M., & Teklesenbet, A. (2015). Námafjall High Temperature Field in N Iceland . A 3D Resistivity Model Derived from MT Data. *Proceedings World Geothermal Congress*, *April*, 19–25.

Kelbert, A., Meqbel, N., Egbert, G. D., & Tandon, K. (2014). Computers & Geosciences ModEM : A modular system for inversion of electromagnetic geophysical data. *Computers and Geosciences*, *66*, 40–53. https://doi.org/10.1016/j.cageo.2014.01.010

Kellett, R. L., Mareschal, M., & Kurtz, R. D. (1992). A model of lower crustal electrical anisotropy for the Pontiac Subprovince of the Canadian Shield. *Geophysical Journal International*, *111*(1), 141–150. https://doi.org/10.1111/j.1365-246X.1992.tb00560.x

Kern, H., Ivankina, T. I., Nikitin, A. N., Lokajíček, T., & Pros, Z. (2008). The effect of oriented microcracks and crystallographic and shape preferred orientation on bulk elastic anisotropy of a foliated biotite gneiss from Outokumpu. *Tectonophysics*, *457*(3), 143–149. https://doi.org/https://doi.org/10.1016/j.tecto.2008.06.015

Kim, D., Brown, L. D., Árnason, K., Águstsson, K., & Blanck, H. (2017). Magma reflection imaging in Krafla, Iceland, using microearthquake sources. *Journal of Geophysical Research: Solid Earth*, *122*(7), 5228–5242. https://doi.org/10.1002/2016JB013809

Kirkby, A., & Heinson, G. (2017). Three-dimensional resistor network modeling of the resistivity and permeability of fractured rocks. *Journal of Geophysical Research: Solid Earth*, *122*(4), 2653–2669. https://doi.org/10.1002/2016JB013854

Kirkby, A., Heinson, G., Holford, S., & Thiel, S. (2015). Mapping fractures using 1D anisotropic modelling of magnetotelluric data: a case study from the Otway Basin, Victoria, Australia. *Geophysical Journal International*, *201*(3), 1961–1976. https://doi.org/10.1093/gji/ggv116

Kirkby, A., Heinson, G., & Krieger, L. (2016). Relating permeability and electrical resistivity in fractures using random resistor network models. *Journal of Geophysical Research: Solid Earth*, *121*(3), 1546–1564. https://doi.org/10.1002/2015JB012541

Kiyan, D., Jones, A. G., & Vozar, J. (2013). The inability of magnetotelluric off-diagonal impedance tensor elements to sense oblique conductors in three-dimensional inversion. *Geophysical Journal International*, *196*(3), 1351–1364. https://doi.org/10.1093/gji/ggt470

Klepacki, D. W. (1985). *Stratigraphy and structural geology of the Goat Range area, Southeastern British Columbia*. Massachusetts Institute of Technology.

Kong, W., Lin, C., Tan, H., Peng, M., Tong, T., & Wang, M. (2018). The Effects of 3D Electrical Anisotropy on Magnetotelluric Responses: Synthetic Case Studies. *Journal of Environmental and Engineering Geophysics*, *23*(1), 61–75. https://doi.org/10.2113/JEEG23.1.61

Kong, W., Lin, C., Unsworth, M. J., Tan, H., Lee, B., Peng, M., Wang, M., & Tong, T. (2020). *Three-dimensional inversion of magnetotelluric data for a resistivity model with arbitrary anisotropy [manuscript submitted for publication]*.

Kubli, T. E., & Simony, P. S. (1994). The Dogtooth duplex, a model for the structural development of the northern Purcell Mountains. *Canadian Journal of Earth Sciences*, *31*(11), 1672–1686. https://doi.org/10.1139/e94-150

Kurtz, R. D., DeLaurier, J. M., & Gupta, J. C. (1986). A magnetotelluric sounding across Vancouver

Island detects the subducting Juan de Fuca plate. *Nature*, *321*(6070), 596–599.
Lachenbruch, A. H., Sass, J. H., & Morgan, P. (1994). Thermal regime of the southern Basin and Range Province: 2. Implications of heat flow for regional extension and metamorphic core complexes. *Journal of Geophysical Research*, *99*(B11). https://doi.org/10.1029/94jb01890
Lambert, R. S. J., & Chamberlain, V. E. (1988). Cordilleria Revisited, with a Three-Dimensional Model for Cretaceous Tectonics in British Columbia. *The Journal of Geology*, *96*(1), 47–60. https://doi.org/10.1086/629192
Laštovičková, M., Losito, G., & Trova, A. (1993). Anisotropy of electrical conductivity of dry and saturated KTB samples. *Physics of the Earth and Planetary Interiors*, *81*(1), 315–324. https://doi.org/https://doi.org/10.1016/0031-9201(93)90138-Y
Le, C. V. A., Harris, B. D., Pethick, A. M., Takam Takougang, E. M., & Howe, B. (2016). Semiautomatic and Automatic Cooperative Inversion of Seismic and Magnetotelluric Data. *Surveys in Geophysics*, *37*(5), 845–896. https://doi.org/10.1007/s10712-016-9377-z
Ledo, J., & Jones, A. G. (2001). Regional electrical resistivity structure of the southern Canadian Cordillera and its physical interpretation. *Journal of Geophysical Research: Solid Earth*, *106*(B12), 30755–30769. https://doi.org/10.1029/2001JB000358
Leech, G. B. (1966). The Rocky Mountain Trench. *The World Rift System: Geological Survey of Canada Paper*, 14–66.
Legarth, B., Huenges, E., & Zimmermann, G. (2005). Hydraulic fracturing in a sedimentary geothermal reservoir: Results and implications. *International Journal of Rock Mechanics and Mining Sciences*, *42*(7), 1028–1041. https://doi.org/https://doi.org/10.1016/j.ijrmms.2005.05.014
Levy, L. (2019). *Electrical properties of hydrothermally altered rocks: observations and interpretations based on laboratory, field and borehole studies at Krafla volcano, Iceland*. École Normale Supérieure and University of Iceland.
Lezaeta, P., Chave, A., Jones, A. G., & Evans, R. (2007). Source field effects in the auroral zone: Evidence from the Slave craton (NW Canada). *Physics of the Earth and Planetary Interiors*, *164*(1), 21–35. https://doi.org/https://doi.org/10.1016/j.pepi.2007.05.002
Lezaeta, P., & Haak, V. (2003). Beyond magnetotelluric decomposition: Induction, current channeling, and magnetotelluric phases over 90°. *Journal of Geophysical Research: Solid Earth*, *108*(B6), 1–20. https://doi.org/10.3969/j.issn.1672-5921.2013.10.009
Lindsey, N. J., & Newman, G. A. (2015). Improved workflow for 3D inverse modeling of magnetotelluric data: Examples from five geothermal systems. *Geothermics*, *53*(February), 527–532. https://doi.org/10.1016/j.geothermics.2014.09.004
Llanos, E. M., Zarrouk, S. J., & Hogarth, R. A. (2015). Numerical model of the Habanero geothermal reservoir, Australia. *Geothermics*, *53*, 308–319. https://doi.org/https://doi.org/10.1016/j.geothermics.2014.07.008
Lukawski, M. Z., Anderson, B. J., Augustine, C., Capuano, L. E., Beckers, K. F., Livesay, B., & Tester, J. W. (2014). Cost analysis of oil, gas, and geothermal well drilling. *Journal of Petroleum Science and Engineering*, *118*, 1–14. https://doi.org/10.1016/j.petrol.2014.03.012
MacFarlane, J., Thiel, S., Pek, J., Peacock, J. R., & Heinson, G. (2014). Characterisation of induced fracture networks within an enhanced geothermal system using anisotropic electromagnetic modelling. *Journal of Volcanology and Geothermal Research*, *288*, 1–7. https://doi.org/https://doi.org/10.1016/j.jvolgeores.2014.10.002
Mackie, R. L., Smith, J. T., & Madden, T. R. (1994). Three-dimensional electromagnetic modeling using finite difference equations: The magnetotelluric example. *Radio Science*, *29*(4), 923–935.
Mackie, R. L., Watts, M. D., & Rodi, W. (2007). Joint 3D inversion of marine CSEM and MT data. *SEG Technical Program Expanded Abstracts 2007*, 574–578. https://doi.org/10.1190/1.2792486
Madden, T. R., & Mackie, R. L. (1989). Three-dimensional Magnetotelluric Modeling and Inversion. *Proceedings of the IEEE*, *77*(2), 318–333. https://doi.org/10.1109/5.18628
Majorowicz, J., & Grasby, S. E. (2010). Heat flow, depth–temperature variations and stored thermal energy for enhanced geothermal systems in Canada. *Journal of Geophysics and Engineering*,

*7*(3), 232–241. https://doi.org/10.1088/1742-2132/7/3/002
Majorowicz, J., & Moore, M. (2014). The feasibility and potential of geothermal heat in the deep Alberta foreland basin-Canada for CO2 savings. *Renewable Energy*, *66*, 541–549. https://doi.org/https://doi.org/10.1016/j.renene.2013.12.044
Manthilake, G., Bolfan-Casanova, N., Novella, D., Mookherjee, M., & Andrault, D. (2016). Dehydration of chlorite explains anomalously high electrical conductivity in the mantle wedges. *Science Advances*, *2*(5). https://doi.org/10.1126/sciadv.1501631
Mareschal, M., Fyfe, W. S., Percival, J., & Chan, T. (1992). Grain-boundary graphite in Kapuskasing gneisses and implications for lower-crustal conductivity. *Nature*, *357*(6380), 674–676. https://doi.org/10.1038/357674a0
Martí, A. (2014). The Role of Electrical Anisotropy in Magnetotelluric Responses: From Modelling and Dimensionality Analysis to Inversion and Interpretation. *Surveys in Geophysics*, *35*(1), 179–218. https://doi.org/10.1007/s10712-013-9233-3
Martí, A., Queralt, P., Ledo, J., & Farquharson, C. G. (2010). Dimensionality imprint of electrical anisotropy in magnetotelluric responses. *Physics of the Earth and Planetary Interiors*. https://doi.org/10.1016/j.pepi.2010.07.007
Massey Jr, F. J. (1951). The Kolmogorov-Smirnov test for goodness of fit. *Journal of the American Statistical Association*, *46*(253), 68–78.
Mathez, E. A., Duba, A. G., Peach, C. L., Leger, A., Shankland, T. J., & Plafker, G. (1995). Electrical conductivity and carbon in metamorphic rocks of the Yukon- Tanana Terrane, Alaska. *Journal of Geophysical Research*, *100*(B6). https://doi.org/10.1029/95jb00615
Maxwell, J. C. (1861). On physical lines of force. *The London, Edinburgh, and Dublin Philosophical Magazine and Journal of Science*, *21*(141), 338–348.
McDonough, M. R., & Morrison, M. L. (1990). *Ptarmigan Creek West Half, British Columbia [83d/10]*. https://doi.org/10.4095/128194
McDonough, M. R., Morrison, M. L., Currie, L. D., Walker, R. T., Pell, J., & Murphy, D. C. (1991). *Canoe Mountain, British Columbia*. https://doi.org/10.4095/133385
McDonough, M. R., & Mountjoy, E. W. (1990). *Geology, Lucerne [83d/15 West - Half] map area, British Columbia*. https://doi.org/10.4095/128147
McDonough, M. R., & Murphy, D. C. (1994). *Geology, Valemount, West of the Sixth Meridian, British Columbia*. https://doi.org/10.4095/203490
McDonough, M. R., & Parrish, R. R. (1991). Proterozoic gneisses of the Malton Complex, near Valemount, British Columbia: U–Pb ages and Nd isotopic signatures. *Canadian Journal of Earth Sciences*, *28*(8), 1202–1216. https://doi.org/10.1139/e91-108
McDonough, M. R., & Simony, P. S. (1988). Structural evolution of basement gneisses and Hadrynian cover, Bulldog Creek area, Rocky Mountains, British Columbia. *Canadian Journal of Earth Sciences*, *25*(10), 1687–1702. https://doi.org/10.1139/e88-159
McDonough, M. R., & Simony, P. S. (1989). Valemount strain zone: a dextral oblique-slip thrust system linking the Rocky Mountain and Omineca belts of the southeastern Canadian Cordillera. *Geology*, *17*(3), 237–240. https://doi.org/10.1130/0091-7613(1989)017<0237:VSZADO>2.3.CO;2
McMechan, M. E. (2000). Walker Creek fault zone, central Rocky Mountains, British Columbia—southern continuation of the Northern Rocky Mountain Trench fault zone. *Canadian Journal of Earth Sciences*, *37*(9), 1259–1273. https://doi.org/10.1139/e00-038
McNamara, D. D., Sewell, S., Buscarlet, E., & Wallis, I. C. (2016). A review of the Rotokawa Geothermal Field, New Zealand. *Geothermics*, *59*, 281–293. https://doi.org/10.1016/j.geothermics.2015.07.007
McNeice, G. W., & Jones, A. G. (2001). Multisite, multifrequency tensor decomposition of magnetotelluric data. *Geophysics*, *66*(1), 158–173. https://doi.org/10.1190/1.1444891
Miensopust, M. P. (2017). Application of 3-D Electromagnetic Inversion in Practice: Challenges, Pitfalls and Solution Approaches. *Surveys in Geophysics*, *38*(5), 869–933.

https://doi.org/10.1007/s10712-017-9435-1
Miensopust, M. P., Queralt, P., Jones, A. G., Avdeev, D., Avdeeva, A., Börner, R. U., Bosch, D., Egbert, G. D., Farquharson, C. G., Franke-Börner, A., Garcia, X., Han, N., Hautot, S., Holtham, E., Hübert, J., Khoza, D., Kiyan, D., Le Pape, F., Ledo, J., … Vozar, J. (2013). Magnetotelluric 3-D inversion-a review of two successful workshops on forward and inversion code testing and comparison. *Geophysical Journal International*, *193*(3), 1216–1238. https://doi.org/10.1093/gji/ggt066
Miller, R. L., & Kahn, J. S. (1962). *Statistical Analysis in the Geological Sciences*. Wiley.
Moeck, I. S. (2014). Catalog of geothermal play types based on geologic controls. *Renewable and Sustainable Energy Reviews*, *37*, 867–882. https://doi.org/https://doi.org/10.1016/j.rser.2014.05.032
Monger, J. W. H., Price, R. A., & Tempelman-Kluit, D. J. (1982). Tectonic accretion and the origin of the two major metamorphic and plutonic welts in the Canadian Cordillera. *Geology*, *10*(2), 70–75. https://doi.org/10.1130/0091-7613(1982)10<70:TAATOO>2.0.CO;2
Moorkamp, M. (2017). Integrating Electromagnetic Data with Other Geophysical Observations for Enhanced Imaging of the Earth: A Tutorial and Review. *Surveys in Geophysics*, *38*(5), 935–962. https://doi.org/10.1007/s10712-017-9413-7
Moorkamp, M., Heincke, B., Jegen, M., Roberts, A. W., & Hobbs, R. W. (2011). A framework for 3-D joint inversion of MT, gravity and seismic refraction data. *Geophysical Journal International*, *184*(1), 477–493. https://doi.org/10.1111/j.1365-246X.2010.04856.x
Mortensen, A. K., Egilson, T., Gautason, B., Árnadóttir, S., & Guomundsson, A. (2014). Stratigraphy, alteration mineralogy, permeability and temperature conditions of well IDDP-1, Krafla, NE-Iceland. *Geothermics*, *49*, 31–41. https://doi.org/10.1016/j.geothermics.2013.09.013
Mortensen, A. K., Grönvold, K., Gudmundsson, Á., Steingrímsson, B., & Egilson, T. (2010). Quenched silicic glass from well KJ-39 in Krafla, north-eastern Iceland. *Proceedings World Geothermal Congress*, 1–6.
Muñoz, G. (2014). Exploring for Geothermal Resources with Electromagnetic Methods. *Surveys in Geophysics*, *35*(1), 101–122. https://doi.org/10.1007/s10712-013-9236-0
Muñoz, G., Bauer, K., Moeck, I., Schulze, A., & Ritter, O. (2010). Exploring the Groß Schönebeck (Germany) geothermal site using a statistical joint interpretation of magnetotelluric and seismic tomography models. *Geothermics*, *39*(1), 35–45. https://doi.org/https://doi.org/10.1016/j.geothermics.2009.12.004
Murphy, D. C. (1990a). Direct evidence for dextral strike-slip displacement from mylonites in the southern Rocky Mountain Trench near Valemont, British Columbia. *Current Research, Part E, Geological Survey of Canada, Paper*, *90*, 91–95.
Murphy, D. C. (1990b). *Geology of Canoe River map area [83D]*. https://doi.org/10.4095/131316
Murphy, D. C. (2007). *Geology, Canoe River, British Columbia-Alberta*. https://doi.org/10.4095/223752
NASA/METI/AIST/Japan Spacesystems, & U.S./Japan ASTER Science Team. (2018). *ASTER Global Digital Elevation Model V003*. distributed by NASA EOSDIS Land Processes DAAC. https://doi.org/https://doi.org/10.5067/ASTER/ASTGTM.003
NASA JPL. (2013). *NASA Shuttle Radar Topography Mission Global 1 arc second [Data set]*. NASA EOSDIS Land Processes DAAC. https://doi.org/https://doi.org/10.5067/MEaSUREs/SRTM/SRTMGL1.003
Newman, G. A., & Alumbaugh, D. L. (2000). Three-dimensional magnetotelluric inversion using non-linear conjugate gradients. *Geophysical Journal International*, *140*(2), 410–424. https://doi.org/10.1046/j.1365-246x.2000.00007.x
Newman, G. A., Gasperikova, E., Hoversten, G. M., & Wannamaker, P. E. (2008). Three-dimensional magnetotelluric characterization of the Coso geothermal field. *Geothermics*, *37*(4), 369–399. https://doi.org/https://doi.org/10.1016/j.geothermics.2008.02.006
Nono, F., Gibert, B., Parat, F., Loggia, D., Cichy, S. B., & Violay, M. (2020). Electrical conductivity

of Icelandic deep geothermal reservoirs up to supercritical conditions: Insight from laboratory experiments. *Journal of Volcanology and Geothermal Research*, *391*. https://doi.org/10.1016/j.jvolgeores.2018.04.021

Ogawa, Y. (2002). On two-dimensional modeling of magnetotelluric field data. *Surveys in Geophysics*, *23*(2–3), 251–273. https://doi.org/10.1023/A:1015021006018

Oliva-Urcia, B., Kontny, A., Vahle, C., & Schleicher, A. M. (2011). Modification of the magnetic mineralogy in basalts due to fluid–rock interactions in a high-temperature geothermal system (Krafla, Iceland). *Geophysical Journal International*, *186*(1), 155–174. https://doi.org/10.1111/j.1365-246X.2011.05029.x

Oliver-Ocaño, F. M., Gallardo, L. A., Romo-Jones, J. M., & Pérez-Flores, M. A. (2019). Structure of the Cerro Prieto Pull-apart basin from joint inversion of gravity, magnetic and magnetotelluric data. *Journal of Applied Geophysics*, *170*, 103835. https://doi.org/10.1016/j.jappgeo.2019.103835

Onacha, S. A. (2006). *Hydrothermal fault zone mapping using seismic and electrical measurements*. Duke University.

Pádua, M. B., Padilha, A. L., & Vitorello, Í. (2002). Disturbances on magnetotelluric data due to DC electrified railway: A case study from southeastern Brazil. *Earth, Planets and Space*, *54*(5), 591–596. https://doi.org/10.1186/BF03353047

Pandarinath, K., Shankar, R., Torres-Alvarado, I. S., & Warrier, A. K. (2014). Magnetic susceptibility of volcanic rocks in geothermal areas: application potential in geothermal exploration studies for identification of rocks and zones of hydrothermal alteration. *Arabian Journal of Geosciences*, *7*(7), 2851–2860. https://doi.org/10.1007/s12517-013-1013-3

Parkinson, W. D. (1959). Directions of Rapid Geomagnetic Fluctuations. *Geophysical Journal International*, *2*(1), 1–14. https://doi.org/10.1111/j.1365-246X.1959.tb05776.x

Patro, P. K., Brasse, H., Sarma, S. V. S., & Harinarayana, T. (2005). Electrical structure of the crust below the Deccan Flood Basalts (India), inferred from magnetotelluric soundings. *Geophysical Journal International*, *163*(3), 931–943. https://doi.org/10.1111/j.1365-246X.2005.02789.x

Patro, P. K., & Egbert, G. D. (2011). Application of 3D inversion to magnetotelluric profile data from the Deccan Volcanic Province of Western India. *Physics of the Earth and Planetary Interiors*, *187*(1), 33–46. https://doi.org/https://doi.org/10.1016/j.pepi.2011.04.005

Peacock, J. R., Thiel, S., Heinson, G. S., & Reid, P. (2013). Time-lapse magnetotelluric monitoring of an enhanced geothermal system. *Geophysics*, *78*(3), B121–B130. https://doi.org/10.1190/geo2012-0275.1

Peacock, J. R., Thiel, S., Reid, P., & Heinson, G. (2012). Magnetotelluric monitoring of a fluid injection: Example from an enhanced geothermal system. *Geophysical Research Letters*, *39*(17), 3–7. https://doi.org/10.1029/2012GL053080

Pek, J., & Santos, F. A. M. (2002). Magnetotelluric impedances and parametric sensitivities for 1-D anisotropic layered media. *Computers and Geosciences*, *28*(8), 939–950. https://doi.org/10.1016/S0098-3004(02)00014-6

Pek, J., & Verner, T. (1997). Finite-difference modelling of magnetotelluric fields in two-dimensional anisotropic media. *Geophysical Journal International*, *128*(3), 505–521. https://doi.org/10.1111/j.1365-246X.1997.tb05314.x

Pell, J., & Simony, P. S. (1981). Stratigraphy, structure, and metamorphism in the southern Cariboo Mountains, British Columbia. *Current Research, Part A. Geological Survey of Canada*, *81-1A*, 227–230.

Pellerin, L., Johnston, J. M., & Hohmann, G. W. (1996). A numerical evaluation of electromagnetic methods in geothermal exploration. *Geophysics*, *61*(1), 121–130. https://doi.org/10.1190/1.1443931

Phillips, R. J. (1994). *Isotope hydrogeology and aqueous geochemistry of selected British Columbia hotsprings*. University of Ottawa (Canada).

Piña-Varas, P., & Dentith, M. (2018). Magnetotelluric data from the Southeastern Capricorn Orogen,

Western Australia: An example of widespread out-of-quadrant phase responses associated with strong 3-D resistivity contrasts. *Geophysical Journal International*, *212*(2), 1022–1032. https://doi.org/10.1093/gji/ggx459

Piña-Varas, P., Ledo, J., Queralt, P., Marcuello, A., & Perez, N. (2018). On the detectability of Teide volcano magma chambers (Tenerife, Canary Islands) with magnetotelluric data. *Earth, Planets and Space*, *70*(1). https://doi.org/10.1186/s40623-018-0783-y

Pope, E. C., Bird, D. K., Arnórsson, S., & Giroud, N. (2016). Hydrogeology of the Krafla geothermal system, northeast Iceland. *Geofluids*, *16*(1), 175–197. https://doi.org/10.1111/gfl.12142

Pope, M. C., & Sears, J. W. (1997). Cassiar platform, north-central British Columbia: A miogeoclinal fragment from Idaho. *Geology*, *25*(6), 515–518. https://doi.org/10.1130/0091-7613(1997)025<0515:CPNCBC>2.3.CO;2

Pous, J., Heise, W., Schnegg, P. A., Muoz, G., Martí, J., & Soriano, C. (2002). Magnetotelluric study of the Las Canadas caldera (Tenerife, Canary Islands): Structural and hydrogeological implications. *Earth and Planetary Science Letters*, *204*(1–2), 249–263. https://doi.org/10.1016/S0012-821X(02)00956-1

Pribnow, D., & Schellschmidt, R. (2000). Thermal tracking of upper crustal fluid flow in the Rhine graben. *Geophysical Research Letters*, *27*(13), 1957–1960. https://doi.org/10.1029/2000GL008494

Price, R. A., & Carmichael, D. M. (1986). Geometric test for Late Cretaceous- Paleogene intracontinental transform faulting in the Canadian Cordillera. *Geology*, *14*(6), 468–471. https://doi.org/10.1130/0091-7613(1986)14<468:GTFLCI>2.0.CO;2

Rauen, A., & Laštovičková, M. (1995). Investigation of electrical anisotropy in the deep borehole KTB. *Surveys in Geophysics*, *16*(1), 37–46. https://doi.org/10.1007/BF00682711

Read, P. B., Woodsworth, G. J., Greenwood, H. J., Ghent, E. D., Evenchick, C., & A. (1991). *Metamorphic map of the Canadian Cordillera*. https://doi.org/10.4095/134142

Rippe, D., Unsworth, M. J., & Currie, C. A. (2013). Magnetotelluric constraints on the fluid content in the upper mantle beneath the southern Canadian Cordillera: Implications for rheology. *Journal of Geophysical Research: Solid Earth*, *118*(10), 5601–5624. https://doi.org/10.1002/jgrb.50255

Roberts, B. P., & Sandberg, C. (2011). The Role of Energy Storage in Development of Smart Grids. *Proceedings of the IEEE*, *99*(6), 1139–1144. https://doi.org/10.1109/JPROC.2011.2116752

Robertson, K., Thiel, S., & Meqbel, N. (2020). Quality over quantity: on workflow and model space exploration of 3D inversion of MT data. *Earth, Planets and Space*, *72*(1), 2. https://doi.org/10.1186/s40623-019-1125-4

Roddick, J. A. (1967). Tintina Trench. *The Journal of Geology*, *75*(1), 23–33.

Rodi, W., & Mackie, R. L. (2001). Nonlinear conjugate gradients algorithm for 2-D magnetotelluric inversion. *Geophysics*, *66*(1), 174–187. https://doi.org/10.1190/1.1444893

Rogelj, J., Hare, W., Lowe, J., Vuuren, D. P. Van, Riahi, K., & Matthews, B. (2011). Emission pathways consistent with a 2 ◦ C global temperature limit. *Nature Climate Change*, *1*(11), 413–418. https://doi.org/10.1038/nclimate1258

Rogelj, J., Luderer, G., Pietzcker, R. C., Kriegler, E., Schaeffer, M., Krey, V., & Riahi, K. (2015). Energy system transformations for limiting end-of-century warming to below 1.5 °C. *Nature Climate Change*, *5*(6), 519–527. https://doi.org/10.1038/nclimate2572

Rosenberg, C. L., & Handy, M. R. (2005). Experimental deformation of partially melted granite revisited: Implications for the continental crust. *Journal of Metamorphic Geology*, *23*(1), 19–28. https://doi.org/10.1111/j.1525-1314.2005.00555.x

Rosenkjaer, G. K., Gasperikova, E., Newman, G. A., Árnason, K., & Lindsey, N. J. (2015). Comparison of 3D MT inversions for geothermal exploration: Case studies for Krafla and Hengill geothermal systems in Iceland. *Geothermics*, *57*, 258–274. https://doi.org/10.1016/j.geothermics.2015.06.001

Sæmundsson, K. (1991). Geology of the Krafla system (in Icelandic). In *Náttúra Mývatns (The*

*Natural History of Lake Mývatn*. The Icelandic Natural History Society Reykjavík.
Salem, A., Furuya, S., Aboud, E., Elawadi, E., Jotaki, H., & Ushijima, K. (2005). Subsurface structural mapping using gravity data of Hohi geothermal area, Central Kyushu, Japan. *Proceedings World Geothermal Congress*.
Sasaki, S. (1998). Characteristics of microseismic events induced during hydraulic fracturing experiments at the Hijiori hot dry rock geothermal energy site, Yamagata, Japan. *Tectonophysics*, *289*(1–3), 171–188. https://doi.org/10.1016/S0040-1951(97)00314-4
Sasaki, Y. (2004). Three-dimensional inversion of static-shifted magnetotelluric data. *Earth, Planets and Space*, *56*(2), 239–248. https://doi.org/10.1186/BF03353406
Sasaki, Y., & Meju, M. A. (2006). Three-dimensional joint inversion for magnetotelluric resistivity and static shift distributions in complex media. *Journal of Geophysical Research: Solid Earth*, *111*(B5). https://doi.org/10.1029/2005JB004009
Schuler, J., Greenfield, T., White, R. S., Roecker, S. W., Brandsdóttir, B., Stock, J. M., Tarasewicz, J., Martens, H. R., & Pugh, D. (2015). Seismic imaging of the shallow crust beneath the Krafla central volcano, NE Iceland. *Journal of Geophysical Research: Solid Earth*, *120*(10), 7156–7173. https://doi.org/10.1002/2015JB012350
Scott, S., Driesner, T., & Weis, P. (2015). Geologic controls on supercritical geothermal resources above magmatic intrusions. *Nature Communications*, *6*, 1–6. https://doi.org/10.1038/ncomms8837
Scott, S., Driesner, T., & Weis, P. (2016). The thermal structure and temporal evolution of high-enthalpy geothermal systems. *Geothermics*, *62*, 33–47. https://doi.org/10.1016/j.geothermics.2016.02.004
Sibson, R. H. (1996). Structural permeability of fluid-driven fault-fracture meshes. *Journal of Structural Geology*, *18*(8), 1031–1042. https://doi.org/10.1016/0191-8141(96)00032-6
Sigmarsson, O., H m ond, C., Condomines, M., Fourcade, S., & Oskarsson, N. (1991). Origin of silicic magma in Iceland revealed by Th isotopes. *Geology*, *19*(6), 621–624. https://doi.org/10.1130/0091-7613(1991)019<0621:OOSMII>2.3.CO;2
Siler, D. L., & Faulds, J. E. (2013). Three-dimensional geothermal fairway mapping: examples from the western Great Basin, USA. *Geothermal Resources Council Transactions*, *37*, 327–332.
Simpson, F., & Bahr, K. (2005). *Practical Magnetotellurics*. Cambridge University Press. https://doi.org/10.1017/CBO9780511614095
Sims, W. E., Bostick, F. X., & Smith, H. W. (1971). The estimation of magnetotelluric impedance tensor elements from measured data. *Geophysics*, *36*(5), 938–942. https://doi.org/10.1190/1.1440225
Siripunvaraporn, W. (2012). Three-Dimensional Magnetotelluric Inversion: An Introductory Guide for Developers and Users. *Surveys in Geophysics*, *33*(1), 5–27. https://doi.org/10.1007/s10712-011-9122-6
Siripunvaraporn, W., & Egbert, G. D. (2000). An efficient data-subspace inversion method for 2-D magnetotelluric data. *Geophysics*, *65*(3), 791–803. https://doi.org/10.1190/1.1444778
Siripunvaraporn, W., Egbert, G. D., & Lenbury, Y. (2002). Numerical accuracy of magnetotelluric modeling: A comparison of finite difference approximations. *Earth, Planets and Space*, *54*(6), 721–725. https://doi.org/10.1186/BF03351724
Siripunvaraporn, W., Egbert, G. D., Lenbury, Y., & Uyeshima, M. (2005). Three-dimensional magnetotelluric inversion: data-space method. *Physics of the Earth and Planetary Interiors*, *150*(1), 3–14. https://doi.org/https://doi.org/10.1016/j.pepi.2004.08.023
Slezak, K., Jozwiak, W., Nowozynski, K., Orynski, S., & Brasse, H. (2019). 3-D studies of MT data in the Central Polish Basin: Influence of inversion parameters, model space and transfer function selection. *Journal of Applied Geophysics*, *161*(December), 26–36. https://doi.org/10.1016/j.jappgeo.2018.11.008
Smith, C. J., Forster, P. M., Rogelj, J., Zickfeld, K., Allen, M., Fuglestvedt, J., & Millar, R. J. (2018). Current fossil fuel infrastructure does not yet commit us to 1.5â€‰°C warming. *Nature*

*Communications*, *2019*, 1–10. https://doi.org/10.1038/s41467-018-07999-w
Smith, J. T. (1996). Conservative modeling of 3-D electromagnetic fields, Part I: Properties and error analysis. *Geophysics*, *61*(5), 1319–1324. https://doi.org/10.1190/1.1444055
Soyer, W., & Unsworth, M. J. (2006). Deep electrical structure of the northern Cascadia (British Columbia, Canada) subduction zone: Implications for the distribution of fluids. *Geology*, *34*(1), 53–56. https://doi.org/10.1130/G21951.1
St. Louis, V. L., Kelly, C. A., Duchemin, E., Rudd, J. W. M., & Rosenberg, D. M. (2000). Reservoir Surfaces as Sources of Greenhouse Gases to the Atmosphere: A Global Estimate. *BioScience*, *50*(9), 766. https://doi.org/10.1641/0006-3568(2000)050[0766:rsasog]2.0.co;2
Struik, L. C. (1993). Intersecting intracontinental Tertiary transform fault systems in the North American Cordillera. *Canadian Journal of Earth Sciences*, *30*(6), 1262–1274. https://doi.org/10.1139/e93-108
Swift, C. M. (1967). *A magnetotelluric investigation of an electrical conductivity anomaly in the southwestern United States*. Massachusetts Institute of Technology.
Takam Takougang, E. M., Harris, B., Kepic, A., & Le, C. V. A. (2015). Cooperative joint inversion of 3D seismic and magnetotelluric data: With application in a mineral province. *Geophysics*, *80*(4), R175–R187. https://doi.org/10.1190/geo2014-0252.1
Tang, C., Rial, J. A., & Lees, J. M. (2008). Seismic imaging of the geothermal field at Krafla, Iceland using shear-wave splitting. *Journal of Volcanology and Geothermal Research*, *176*(2), 315–324.
Telford, W. M., Geldart, L. P., & Sheriff, R. E. (1990). *Applied geophysics*. Cambridge University Press.
Tempelman-Kluit, D. J. (1979). *Transported cataclasite, ophiolite and granodiorite in the Yukon: evidence of arc-continent collision*. https://doi.org/10.4095/105928
ten Grotenhuis, S. M., Drury, M. R., Spiers, C. J., & Peach, C. J. (2005). Melt distribution in olivine rocks based on electrical conductivity measurements. *Journal of Geophysical Research: Solid Earth*, *110*(B12). https://doi.org/10.1029/2004JB003462
Tester, J. W., Anderson, B. J., Batchelor, A. S., Blackwell, D. D., DiPippo, R., Drake, E. M., Garnish, J., Livesay, B., Moore, M. C., Nichols, K., Petty, S., Nafi Toksoz, M., Veatch, R. W., Baria, R., Augustine, C., Murphy, E., Negraru, P., & Richards, M. (2007). Impact of enhanced geothermal systems on US energy supply in the twenty-first century. *Philosophical Transactions of the Royal Society A: Mathematical, Physical and Engineering Sciences*, *365*(1853), 1057–1094. https://doi.org/10.1098/rsta.2006.1964
Trainor-Guitton, W., & Hoversten, G. M. (2011). Stochastic inversion for electromagnetic geophysics: practical challenges and improving convergence efficiency. *Geophysics*, *76*(6), F373–F386.
Tryggvason, A., Rögnvaldsson, S. T., & Flóvenz, Ó. G. (2002). Three-dimensional imaging of the P- and S-wave velocity structure and earthquake locations beneath Southwest Iceland. *Geophysical Journal International*, *151*(3), 848–866. https://doi.org/10.1046/j.1365-246X.2002.01812.x
Tryggvason, E. (1994). Surface deformation at the Krafla volcano, North Iceland, 1982–1992. *Bulletin of Volcanology*, *56*(2), 98–107. https://doi.org/10.1007/BF00304105
Ucok, H., Ershagi, I., & Olhoeft, G. R. (1980). Electrical Resistivity of Geothermal Brines. *Journal of Petroleum Technology*, *32*(April), 717–727. https://doi.org/10.2118/7878-PA
UN. (2018). *Application of the United Nations Framework Classification for Resources (UNFC) to Geothermal Energy Resources: Selected Case Studies* (ECE Energy). UN. https://doi.org/https://doi.org/https://doi.org/10.18356/1fc73241-en
UN. (2020). *United Nations Framework Classification for Resources: Update 2019* (ECE Energy). UN. https://doi.org/https://doi.org/https://doi.org/10.18356/44105e2b-en
UNECE. (2016). *Specifications for the application of the United Nations Framework Classification for Fossil Energy and Mineral Reserves and Resources 2009 to Renewable Energy Resources*. https://www.unece.org/fileadmin/DAM/energy/se/pdfs/UNFC/UNFC_specs/UNFC.RE_e.pdf
Unsworth, M. J. (2018). *Geophysics 424 Course Notes*.

Ussher, G., Harvey, C., Johnstone, R., & Anderson, E. (2000). Understanding the resistivities observed in geothermal systems. *Proceedings World Geothermal Congress*, 1915–1920. https://doi.org/10.3168/jds.S0022-0302(04)73373-1

Usui, Y., Ogawa, Y., Aizawa, K., Kanda, W., Hashimoto, T., Koyama, T., Yamaya, Y., & Kagiyama, T. (2016). Three-dimensional resistivity structure of Asama Volcano revealed by data-space magnetotelluric inversion using unstructured tetrahedral elements. *Geophysical Journal International*, *208*(3), 1359–1372. https://doi.org/10.1093/gji/ggw459

Van Der Velden, A. J., & Cook, F. A. (1996). Structure and tectonic development of the southern Rocky Mountain trench. *Tectonics*, *15*(3), 517–544. https://doi.org/10.1029/95TC03288

Wannamaker, P. E. (2005). Anisotropy Versus Heterogeneity in Continental Solid Earth Electromagnetic Studies: Fundamental Response Characteristics and Implications for Physicochemical State. *Surveys in Geophysics*, *26*(6), 733–765. https://doi.org/10.1007/s10712-005-1832-1

Wannamaker, P. E., Doerner, W. M., & Hasterok, D. P. (2007). Integrated dense array and transect MT surveying at dixie valley geothermal area, Nevada; structural controls, hydrothermal alteration and deep fluid sources. *Proceedings, 32th Workshop on Geothermal Reservoir Engineering, Stanford University*.

Wannamaker, P. E., Hasterok, D. P., Johnston, J. M., Stodt, J. A., Hall, D. B., Sodergren, T. L., Pellerin, L., Maris, V., Doerner, W. M., Groenewold, K. A., & Unsworth, M. J. (2008). Lithospheric dismemberment and magmatic processes of the Great Basin-Colorado Plateau transition, Utah, implied from magnetotellurics. *Geochemistry, Geophysics, Geosystems*, *9*(5), n/a-n/a. https://doi.org/10.1029/2007GC001886

Watanabe, N., Numakura, T., Sakaguchi, K., Saishu, H., Okamoto, A., Ingebritsen, S. E., & Tsuchiya, N. (2017). Potentially exploitable supercritical geothermal resources in the ductile crust. *Nature Geoscience*, *10*(2), 140–144. https://doi.org/10.1038/ngeo2879

Weckmann, U., Ritter, O., & Haak, V. (2003). A magnetotelluric study of the Damara Belt in Namibia 2. MT phases over 90° reveal the internal structure of the Waterberg Fault/Omaruru Lineament. *Physics of the Earth and Planetary Interiors*, *138*(2), 91–112. https://doi.org/10.1016/S0031-9201(03)00079-7

Weisenberger, T. B., Axelsson, G., Arnaldsson, A., Blischke, A., Óskarsson, F., Ármannsson, H., Blanck, H., Helgadóttir, H. M., Berthet, J. C. C., & Árnason, K. (2015). Revision of the Conceptual Model of the Krafla Geothermal System. *Iceland GeoSurvey*.

Wiese, H. (1962). Geomagnetische Tiefentellurik Teil II: Die Streichrichtung der untergrundstrukturen des elektrischen Widerstandes, erschlossen aus geomagnetischen Variationen. *Geofisica Pura e Applicata*, *52*(1), 83–103. https://doi.org/10.1007/BF01996002

Williams, C. (2014). Evaluating the volume method in the assessment of identified geothermal resources. *Geothermal Resources Council Transactions*, *38*, 967–974.

Wisian, K. W., & Blackwell, D. D. (2004). Numerical modeling of Basin and Range geothermal systems. *Geothermics*, *33*(6), 713–741. https://doi.org/https://doi.org/10.1016/j.geothermics.2004.01.002

Wolfe, C. J., Th. Bjarnason, I., VanDecar, J. C., & Solomon, S. C. (1997). Seismic structure of the Iceland mantle plume. *Nature*, *385*(6613), 245–247. https://doi.org/10.1038/385245a0

Wu, P., Tan, H., Lin, C., Peng, M., Ma, H., & Yan, Z. (2020). Joint inversion of two-dimensional magnetotelluric and surface wave dispersion data with cross-gradient constraints. *Geophysical Journal International*, *221*(2), 938–950. https://doi.org/10.1093/gji/ggaa045

Yang, B., Egbert, G. D., Kelbert, A., & Meqbel, N. M. (2015). Three-dimensional electrical resistivity of the north-central USA from EarthScope long period magnetotelluric data. *Earth and Planetary Science Letters*, *422*, 87–93. https://doi.org/https://doi.org/10.1016/j.epsl.2015.04.006

Ye, G., Unsworth, M. J., Wei, W., Jin, S., & Liu, Z. (2019). The Lithospheric Structure of the Solonker Suture Zone and Adjacent Areas: Crustal Anisotropy Revealed by a High-Resolution

Magnetotelluric Study. *Journal of Geophysical Research: Solid Earth*, *124*(2), 1142–1163.
Yoshino, T. (2018). *Chapter 11 - Electrical Conductivity Measurement* (Y. Kono & C. B. T.-M. U. P. Sanloup (eds.); pp. 281–319). Elsevier. https://doi.org/https://doi.org/10.1016/B978-0-12-811301-1.00011-3
Yoshino, T., Laumonier, M., McIsaac, E., & Katsura, T. (2010). Electrical conductivity of basaltic and carbonatite melt-bearing peridotites at high pressures: Implications for melt distribution and melt fraction in the upper mantle. *Earth and Planetary Science Letters*, *295*(3), 593–602. https://doi.org/https://doi.org/10.1016/j.epsl.2010.04.050
Zelwer, R., & Morrison, H. F. (1972). Spatial characteristics of midlatitude geomagnetic micropulsations. *Journal of Geophysical Research*, *77*(4), 674–694. https://doi.org/10.1029/JA077i004p00674
Zhang, J. (2011). Pore pressure prediction from well logs: Methods, modifications, and new approaches. *Earth-Science Reviews*, *108*(1–2), 50–63. https://doi.org/10.1016/j.earscirev.2011.06.001
Zhang, R., Li, T., Deng, X., Huang, X., & Pak, Y. (2020). Two-dimensional data-space joint inversion of magnetotelluric, gravity, magnetic and seismic data with cross-gradient constraints. *Geophysical Prospecting*, *68*(2), 721–731. https://doi.org/10.1111/1365-2478.12858
Zhang, S., Tullis, T. E., & Scruggs, V. J. (1999). Permeability anisotropy and pressure dependency of permeability in experimentally sheared gouge materials. *Journal of Structural Geology*, *21*(7), 795–806. https://doi.org/https://doi.org/10.1016/S0191-8141(99)00080-2
Zierenberg, R. A., Schiffman, P., Barfod, G. H., Lesher, C. E., Marks, N. E., Lowenstern, J. B., Mortensen, A. K., Pope, E. C., Bird, D. K., Reed, M. H., Fridleifsson, G. Ó., & Elders, W. A. (2013). Composition and origin of rhyolite melt intersected by drilling in the Krafla geothermal field, Iceland. *Contributions to Mineralogy and Petrology*, *165*(2), 327–347. https://doi.org/10.1007/s00410-012-0811-z
Zimmermann, G., & Reinicke, A. (2010). Hydraulic stimulation of a deep sandstone reservoir to develop an Enhanced Geothermal System: Laboratory and field experiments. *Geothermics*, *39*(1), 70–77. https://doi.org/https://doi.org/10.1016/j.geothermics.2009.12.003

# Appendix A: Krafla

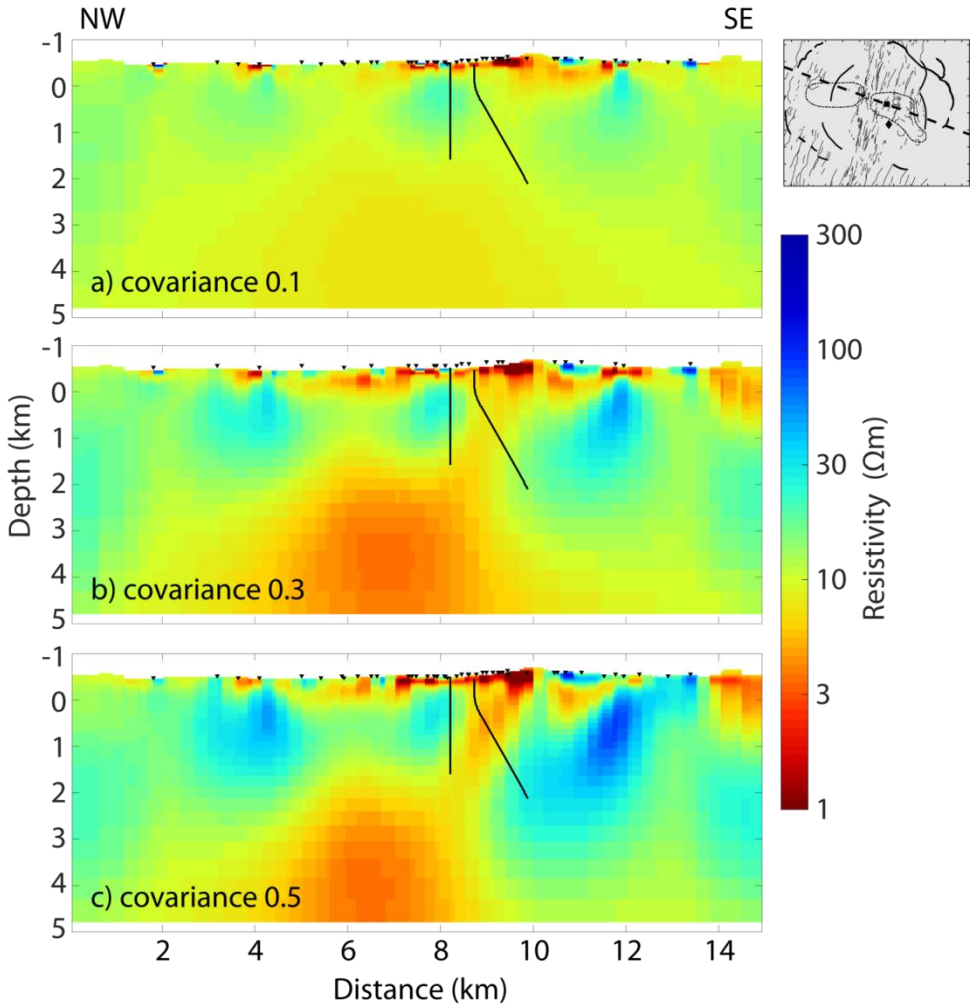


Figure A.1: Vertical slice through 3-D resistivity models obtained from unconstrained inversions with different model covariance values. a) model covariance setting of 0.1 and r.m.s. misfit = 1.44 after 107 inversion iterations; b) model covariance setting of 0.3 and r.m.s. misfit = 1.04 after 98 iterations; c) model covariance setting of 0.5 and r.m.s. misfit = 1.19 after 66 iterations. See inset map for the profile trace.

# Appendix B: Canoe Reach

This appendix contains supplementary information to the Canoe Reach study in Chapter 4.

### Appendix B.1 : 2-D inversion of the Canoe Reach North 2016 profile

This data set contains 16 MT stations along a SW-NE oriented profile. The MT station locations are shown in Figure 4.3. These data were inverted separately due to the large distance from the grid of stations at Canoe Reach North. The 2-D inversion algorithm of Rodi & Mackie (2001) was used to invert these data because of their orientation along a profile. A 3-D inversion could also be used for a profile of MT stations, but careful interpretation is needed for resistivity features that are not located beneath the stations.

The tensor decomposition program of McNeice & Jones (2001) was used to determine a strike direction consistent with the measured MT data. The calculated strike angle showed significant variation by station and frequency. For all stations and the frequency range 300 to 0.05 Hz, the average calculated strike angle was 43° (median of 44°) with a standard deviation of 17°. The data were rotated to a N45°W coordinate system for the 2-D inversion.

Many inversions were run to test the effect of varying different parameters. For example, inversions were run for different combinations of the transverse electric (TE), transverse magnetic (TM), and tipper data. The smoothing parameter was also varied in order to assess the trade-off between data misfit and model smoothness. The final preferred inversion used TE and TM apparent resistivity and phase data in the frequency range 500 to 0.25 Hz. The observed and modeled data are shown in Figure B.1.The inversion resulted in a good fit to the observed data, with an overall r.m.s. misfit of 2.25 with 10% and 5% error floors applied to the apparent resistivity and phase data, respectively.

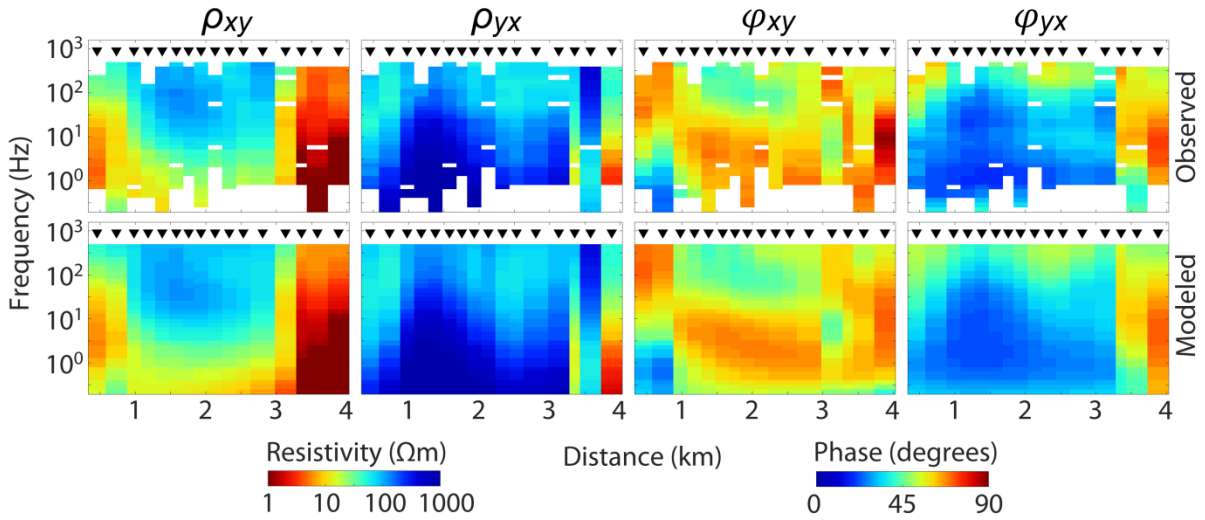


Figure B.1: Pseudo-sections of apparent resistivity ($\rho$) and phase ($\varphi$) data from the preferred 2-D inversion of the Canoe Reach North 2016 profile. The *xy* (*yx*) component corresponds to data calculated with the electric field polarized to N45°W (N45°E). The top row shows the observed data and the second row shows the modeled data. The inversion converged to an r.m.s. misfit of 2.25 with 10% and 5% error floors applied to the apparent resistivity and phase data, respectively. Black inverted triangles show the projected locations of MT stations onto the profile.

The preferred resistivity model obtained from the 2-D inversions is shown in Figure B.2. This inversion used a smoothing parameter (tau) of 20, which was chosen to represent the best trade-off between data misfit and model smoothness of the 12 tau values tested between 1 and 1000. The model contains some prominent resistivity features. The model contains a thin conductor (~ 30 Ωm) near the surface between distances of 0.5 and 2.5 km. The conductor is thin to the SW (~ 100 m thick) but up to 250 m to the NE. This conductor likely corresponds to the Quaternary glaciofluvial overburden (QS) of the SRMT. It is underlain by a resistive feature (> 300 Ωm) that extends to the bottom of the figure. This feature could be the Yellowjacket Gneiss (YG), which is also interpreted below the Canoe Reach North grid about 5 km to the southeast. Two conductive features occur at the SW and NE ends of the model. These features are highly conductive (< 3 Ωm locally). The conductor on the NE end correlates with mapped outcrop of the Lower Miette Group metasedimentary unit (LMG). In this geological setting, possible explanations for the low resistivity are fluids or conductive minerals such as sulfides or graphite. As this unit is described as phyllite-schist-quartzite, there is unlikely an appreciable amount of primary porosity for fluids to exist

in the rock. The decreased resistivity may be caused by a small amount of interconnected graphite or sulfides. The conductive feature at the SW end of the model may also be attributed to conductive minerals. However, interpretation of this feature is less certain because the area is overlain by glaciofluvial overburden. Furthermore, the geometry of this feature might be constrained by data from only one or two MT stations. The station at the SW end of the profile had distinctly different data than nearby stations at frequencies above 1 Hz, which might indicate a different lithology to the SW. Additional MT stations to the SW are needed to better constrain the geometry of this conductor.

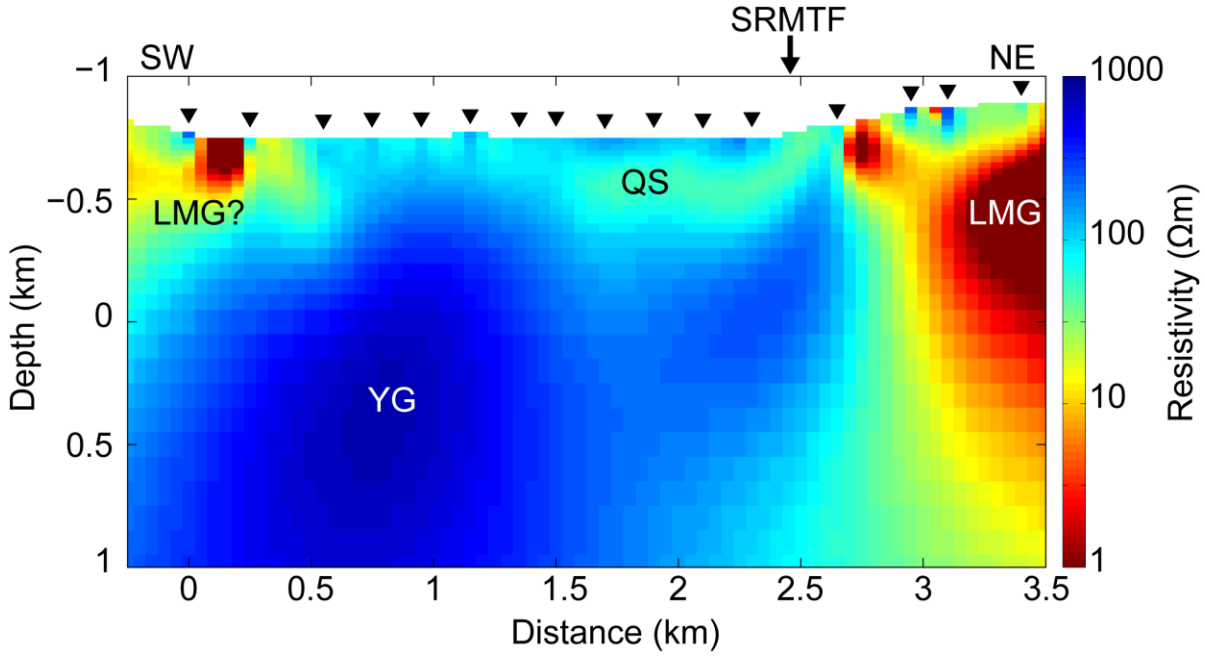


Figure B.2: Preferred 2-D resistivity model obtained from inversion of the Canoe Reach North 2016 MT profile. See Figure 4.3 for the profile location. The inversion used the transverse electric (TE) and transverse magnetic (TM) apparent resistivity and phase data in the frequency range 500 to 0.25 Hz. The inversion converged to a final r.m.s. misfit of 2.25 with 10% and 5% error floors applied to the apparent resistivity and phase data, respectively. This inversion used a smoothing parameter (tau) of 20, which provided a reasonable trade-off between data misfit and model smoothness. Black inverted triangles show the projected locations of MT stations onto the profile. SRMTF indicates the mapped location of the Southern Rocky Mountain Trench Fault. Interpreted resistivity features are labeled. LMG = Lower Miette Group; QS = Quaternary sediments; YG = Yellowjacket Gneiss.

**Appendix B.2 : Observed and modeled data from Canoe Reach North 3-D inversions**

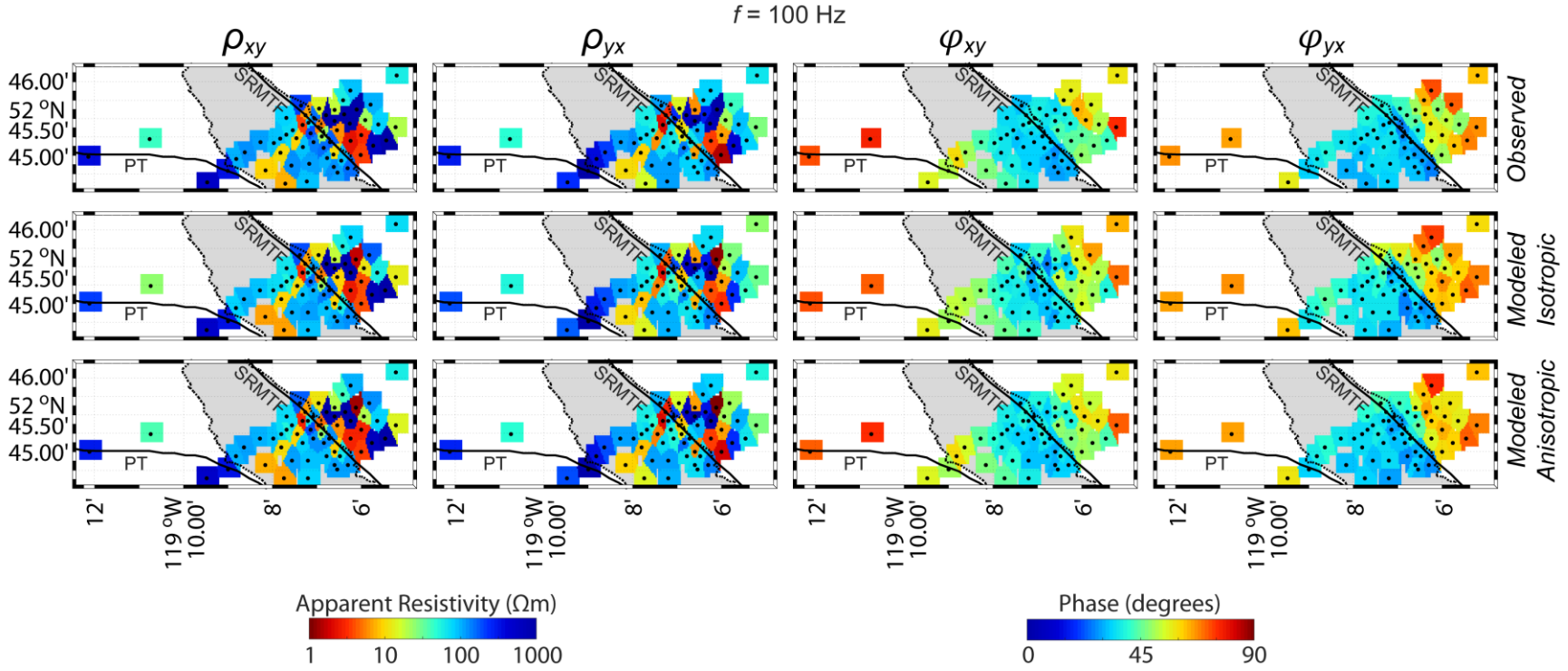


Figure B.3: Maps of Canoe Reach North observed and modeled apparent resistivity ($\rho$) and phase ($\varphi$) data at a frequency of 100 Hz. Modeled data are from isotropic and anisotropic 3-D inversions of the Canoe Reach North data set. *xy* (*yx*) = data from electric field polarized to geographic north (east). Black points show locations of MT stations. Grey shading = Kinbasket Lake. SRMTF = Southern Rocky Mountain Trench Fault; PT = Purcell Thrust.

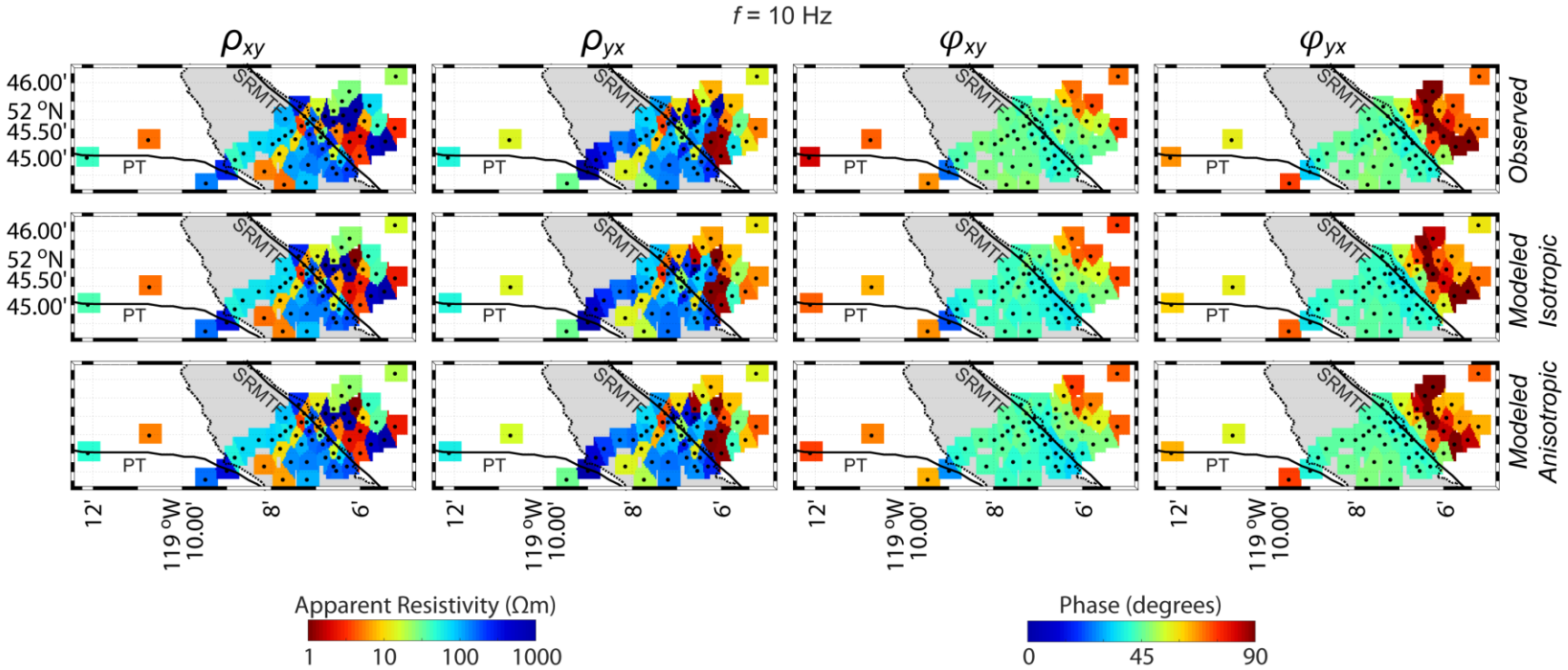


Figure B.4: Maps of Canoe Reach North observed and modeled apparent resistivity ($\rho$) and phase ($\varphi$) data at a frequency of 10 Hz. Modeled data are from isotropic and anisotropic 3-D inversions of the Canoe Reach North data set. *xy* (*yx*) = data from electric field polarized to geographic north (east). Black points show locations of MT stations. Grey shading = Kinbasket Lake. SRMTF = Southern Rocky Mountain Trench Fault; PT = Purcell Thrust.

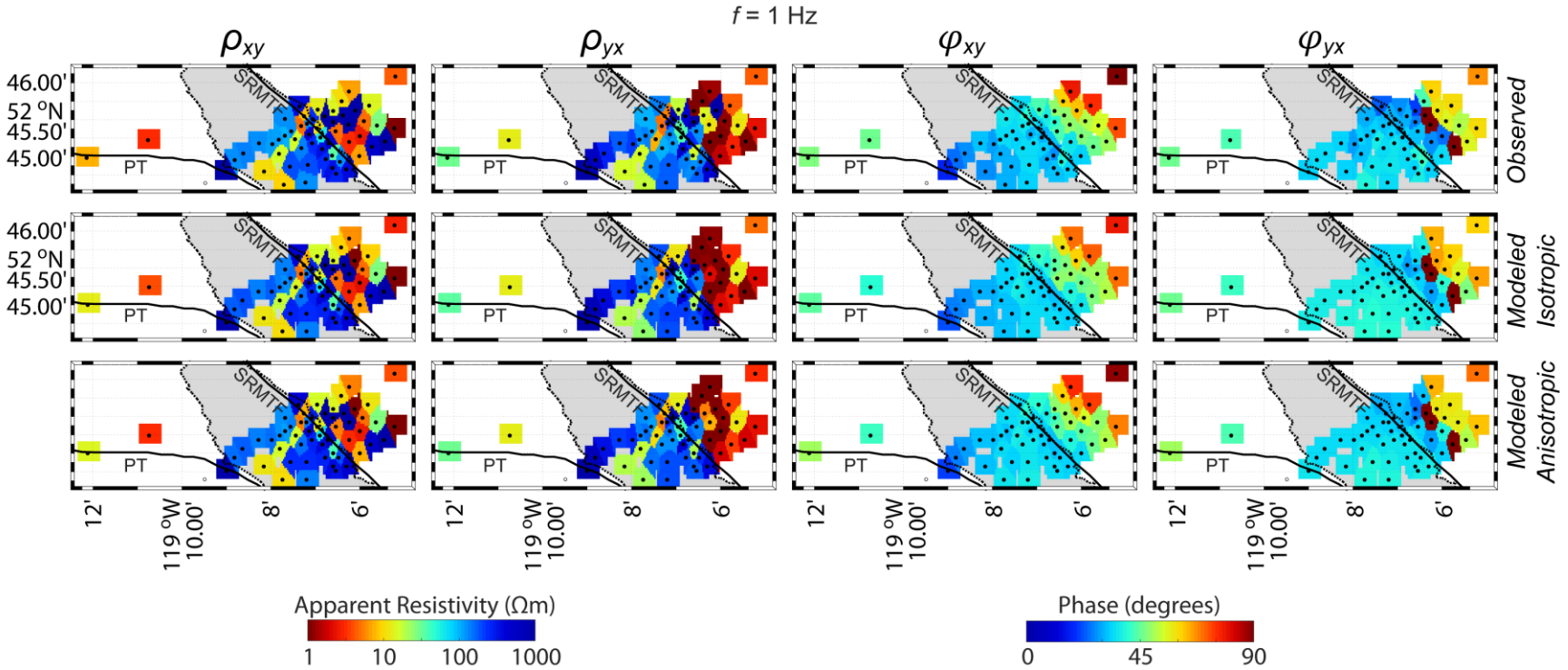


Figure B.5: Maps of Canoe Reach North observed and modeled apparent resistivity ($\rho$) and phase ($\varphi$) data at a frequency of 1 Hz. Modeled data are from isotropic and anisotropic 3-D inversions of the Canoe Reach North data set. *xy* (*yx*) = data from electric field polarized to geographic north (east). Black points show locations of MT stations. Grey shading = Kinbasket Lake. SRMTF = Southern Rocky Mountain Trench Fault; PT = Purcell Thrust.

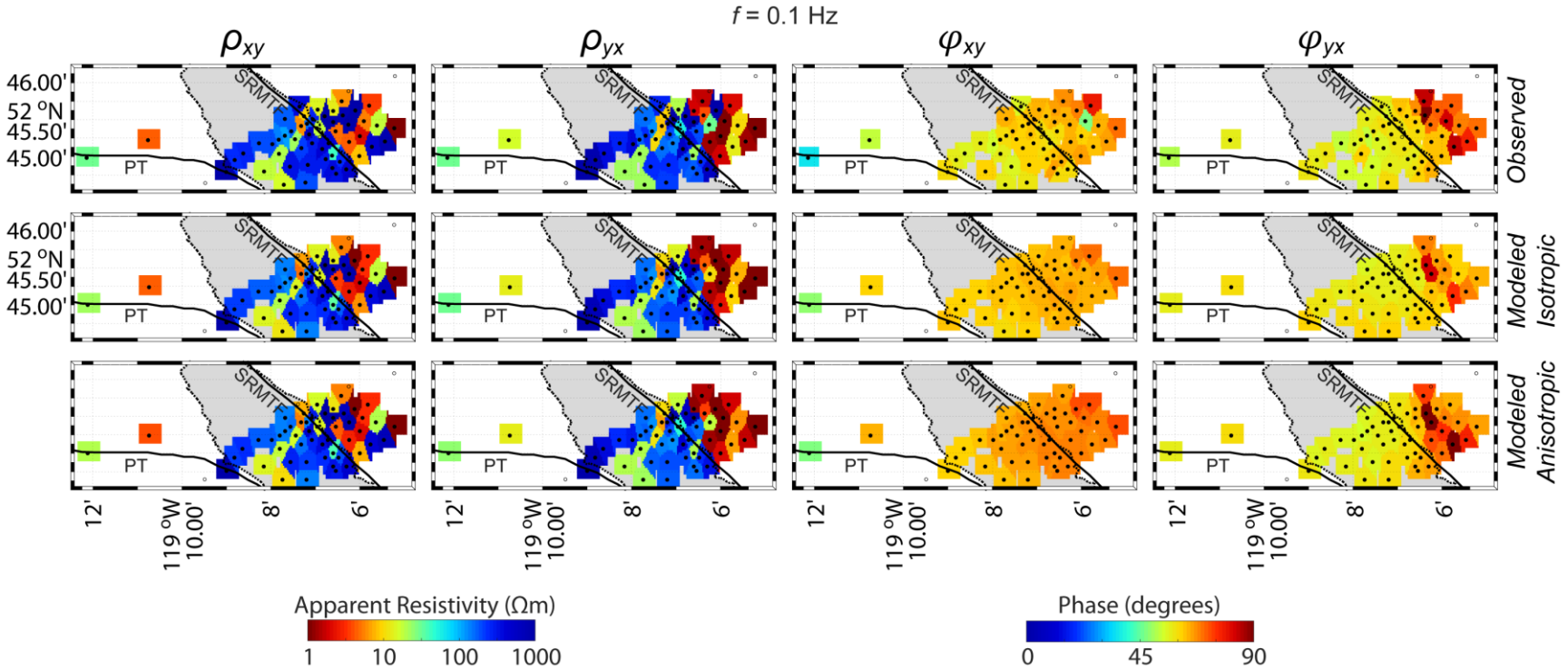


Figure B.6: Maps of Canoe Reach North observed and modeled apparent resistivity ($\rho$) and phase ($\varphi$) data at a frequency of 0.1 Hz. Modeled data are from isotropic and anisotropic 3-D inversions of the Canoe Reach North data set. *xy* (*yx*) = data from electric field polarized to geographic north (east). Black points show locations of MT stations. Grey shading = Kinbasket Lake. SRMTF = Southern Rocky Mountain Trench Fault; PT = Purcell Thrust.

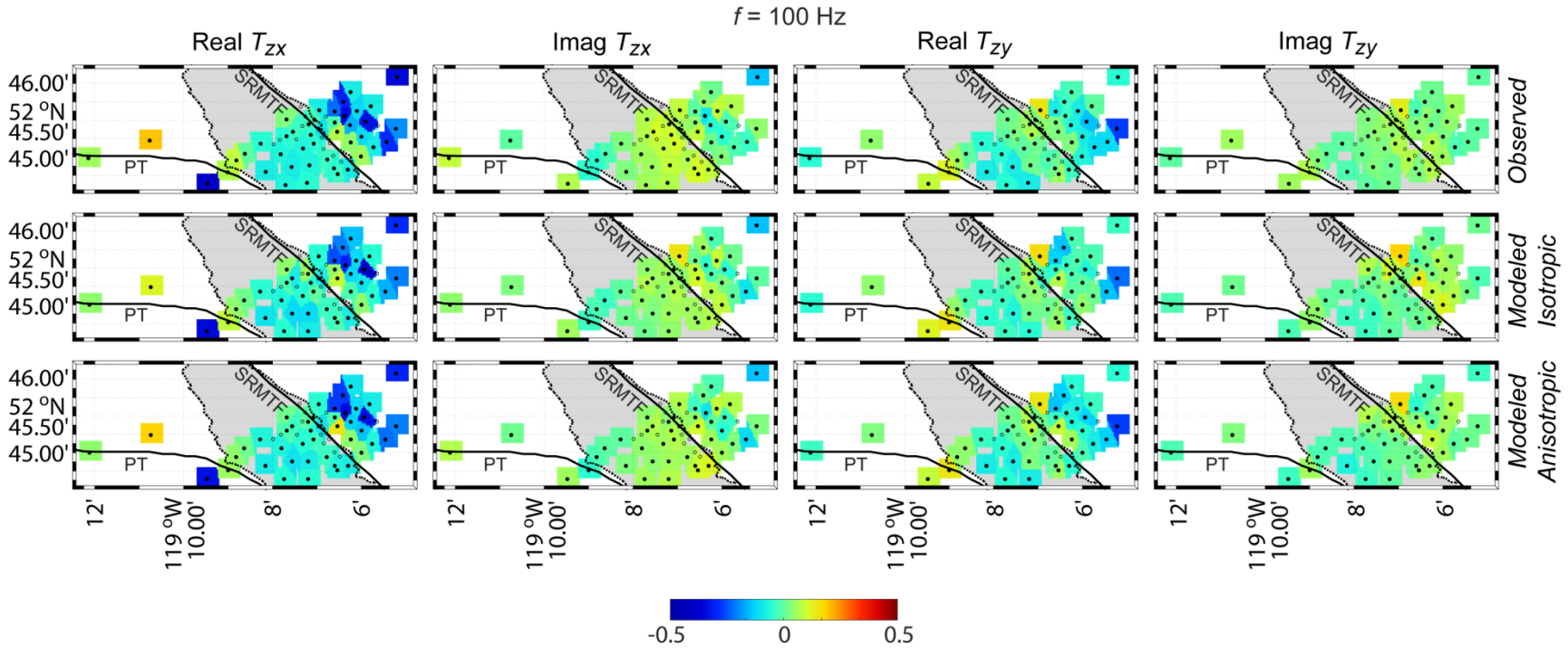


Figure B.7: Maps of Canoe Reach North observed and modeled tipper (*T*) data at a frequency of 100 Hz. Real and imaginary (Imag) parts of the tipper components are shown. Modeled data are from isotropic and anisotropic 3-D inversions of the Canoe Reach North data set. *zx* (*zy*) = data from magnetic field polarized to geographic north (east). Black points show locations of MT stations. Grey shading = Kinbasket Lake. SRMTF = Southern Rocky Mountain Trench Fault; PT = Purcell Thrust.

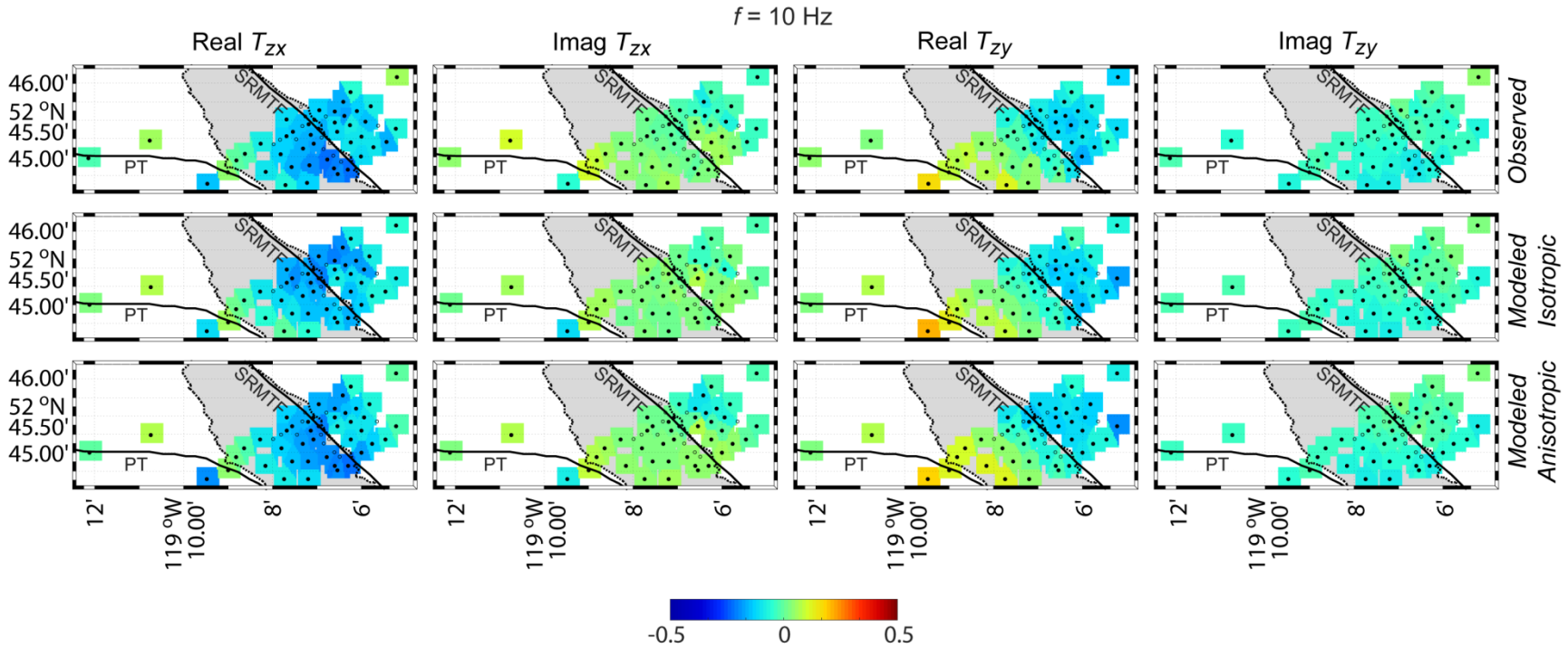


Figure B.8: Maps of Canoe Reach North observed and modeled tipper (*T*) data at a frequency of 10 Hz. Real and imaginary (Imag) parts of the tipper components are shown. Modeled data are from isotropic and anisotropic 3-D inversions of the Canoe Reach North data set. *zx* (*zy*) = data from magnetic field polarized to geographic north (east). Black points show locations of MT stations. Grey shading = Kinbasket Lake. SRMTF = Southern Rocky Mountain Trench Fault; PT = Purcell Thrust.

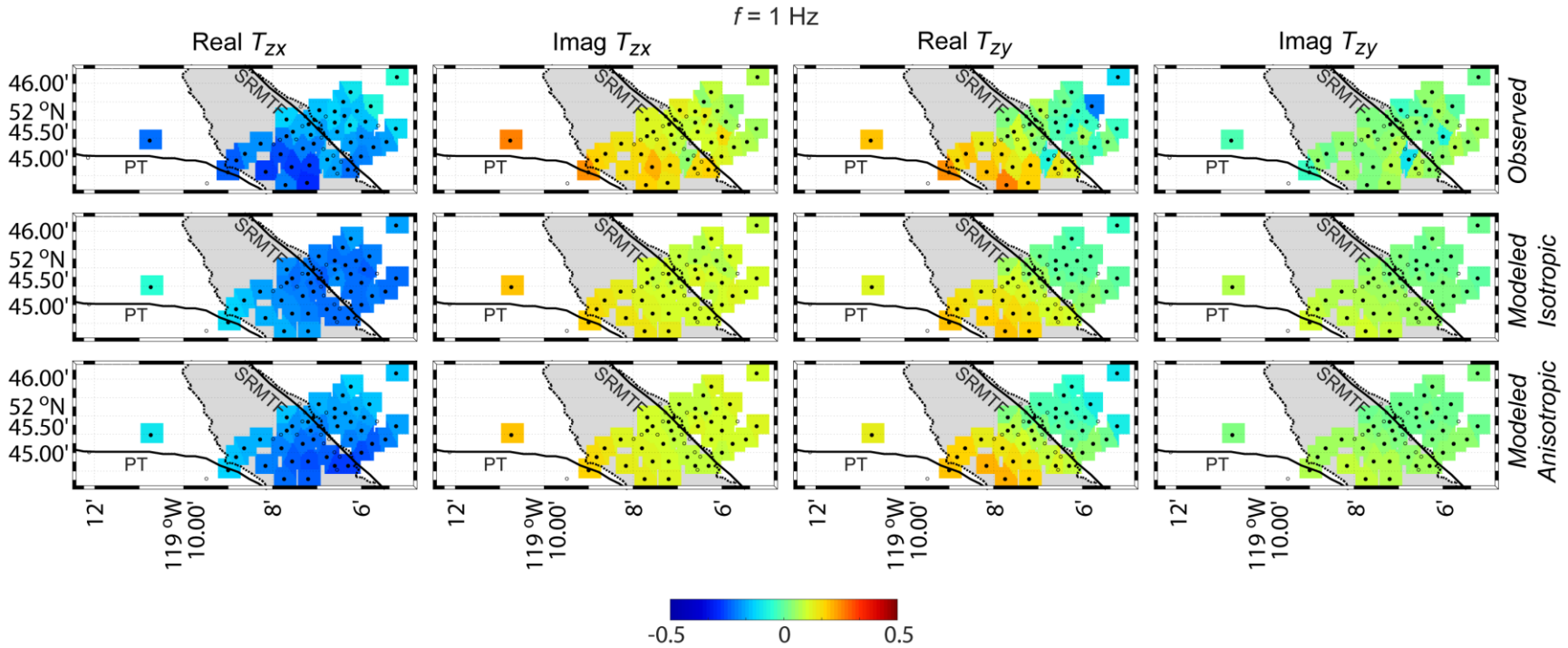


Figure B.9: Maps of Canoe Reach North observed and modeled tipper (*T*) data at a frequency of 1 Hz. Real and imaginary (Imag) parts of the tipper components are shown. Modeled data are from isotropic and anisotropic 3-D inversions of the Canoe Reach North data set. *zx* (*zy*) = data from magnetic field polarized to geographic north (east). Black points show locations of MT stations. Grey shading = Kinbasket Lake. SRMTF = Southern Rocky Mountain Trench Fault; PT = Purcell Thrust.

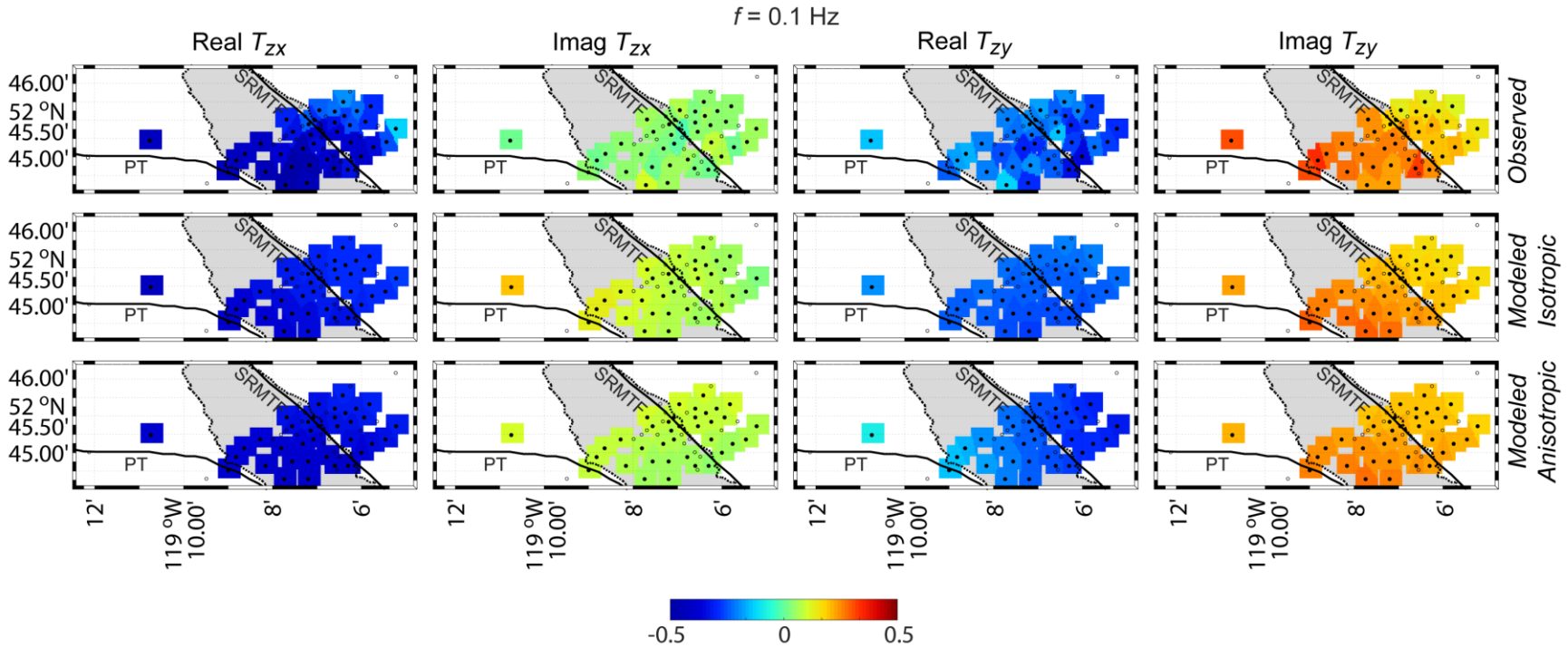


Figure B.10: Maps of Canoe Reach North observed and modeled tipper (*T*) data at a frequency of 0.1 Hz. Real and imaginary (Imag) parts of the tipper components are shown. Modeled data are from isotropic and anisotropic 3-D inversions of the Canoe Reach North data set. *zx* (*zy*) = data from magnetic field polarized to geographic north (east). Black points show locations of MT stations. Grey shading = Kinbasket Lake. SRMTF = Southern Rocky Mountain Trench Fault; PT = Purcell Thrust.

## Appendix B.3 :Observed and modeled data from the Lines A and B 3-D inversions

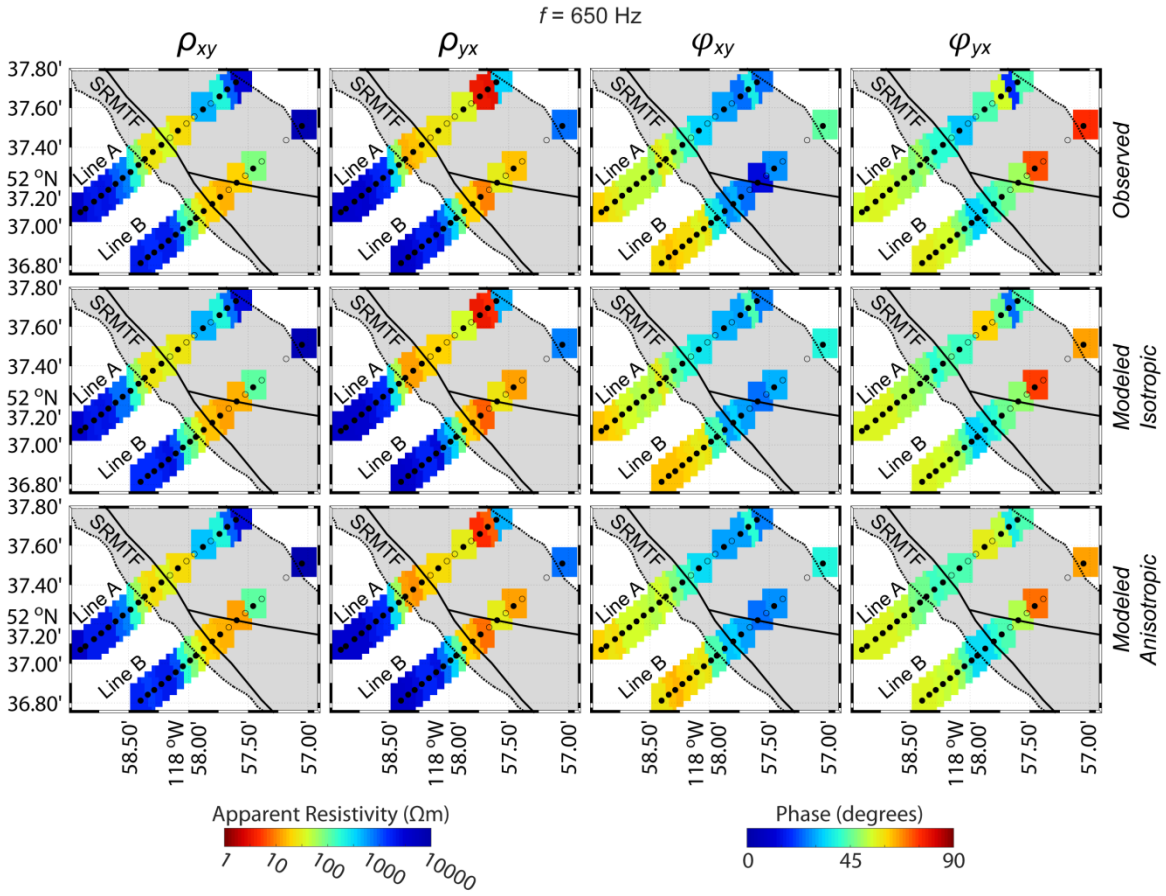


Figure B.11: Maps of the Lines A and B observed and modeled apparent resistivity ($\rho$) and phase ($\varphi$) data at a frequency of 650 Hz. Modeled data are from isotropic and anisotropic 3-D inversions of the Lines A and B data. *xy* (*yx*) = data from electric field polarized to geographic north (east). Black points show locations of MT stations. Grey shading = Kinbasket Lake. SRMTF = Southern Rocky Mountain Trench Fault.

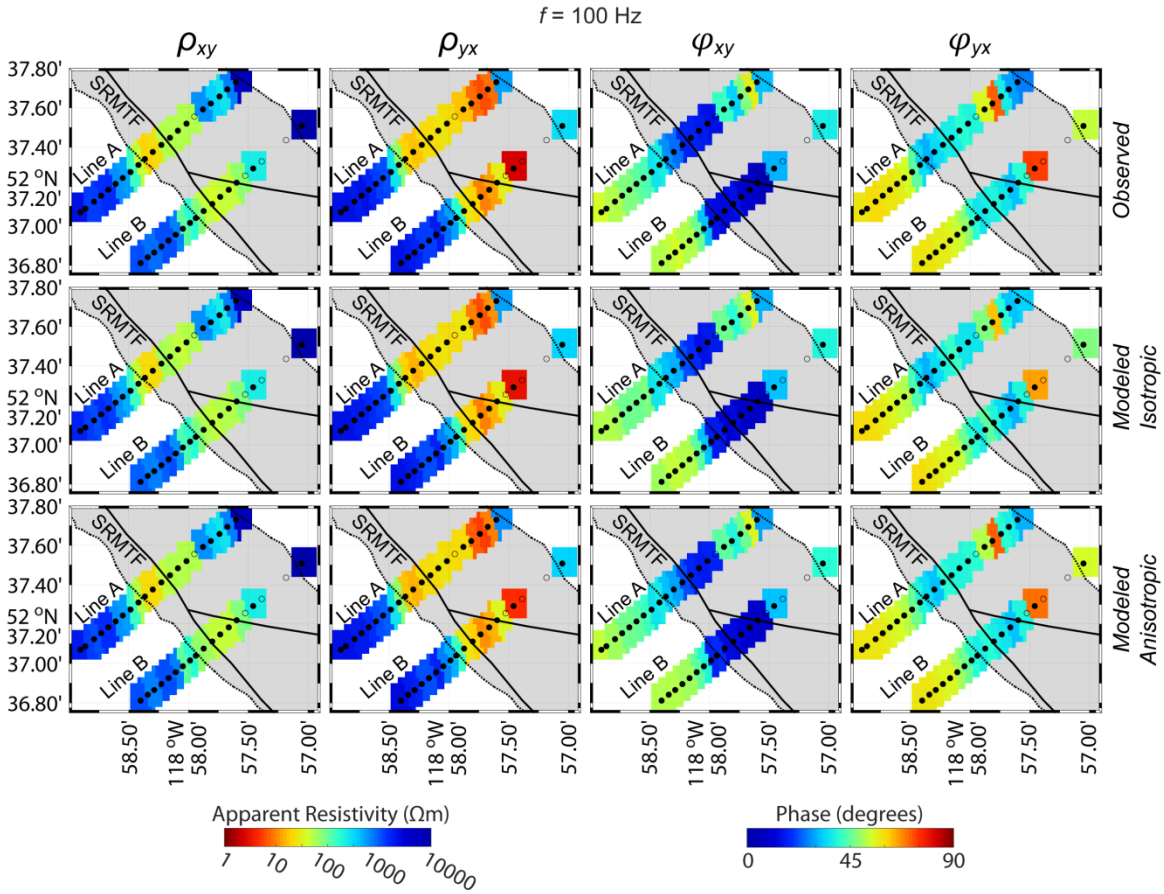


Figure B.12: Maps of the Lines A and B observed and modeled apparent resistivity ($\rho$) and phase ($\varphi$) data at a frequency of 100 Hz. Modeled data are from isotropic and anisotropic 3-D inversions of the Lines A and B data. *xy* (*yx*) = data from electric field polarized to geographic north (east). Black points show locations of MT stations. Grey shading = Kinbasket Lake. SRMTF = Southern Rocky Mountain Trench Fault.

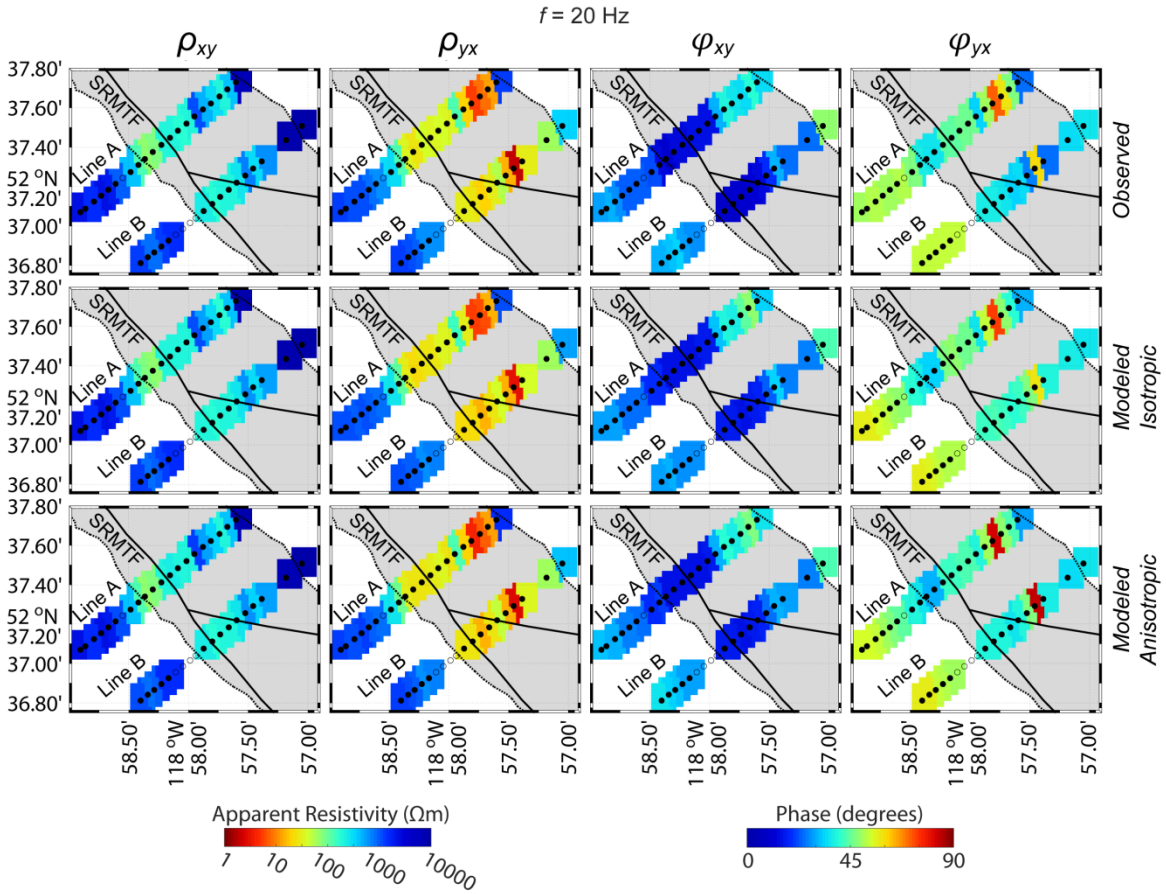


Figure B.13: Maps of the Lines A and B observed and modeled apparent resistivity ($\rho$) and phase ($\varphi$) data at a frequency of 20 Hz. Modeled data are from isotropic and anisotropic 3-D inversions of the Lines A and B data. *xy* (*yx*) = data from electric field polarized to geographic north (east). Black points show locations of MT stations. Grey shading = Kinbasket Lake. SRMTF = Southern Rocky Mountain Trench Fault.

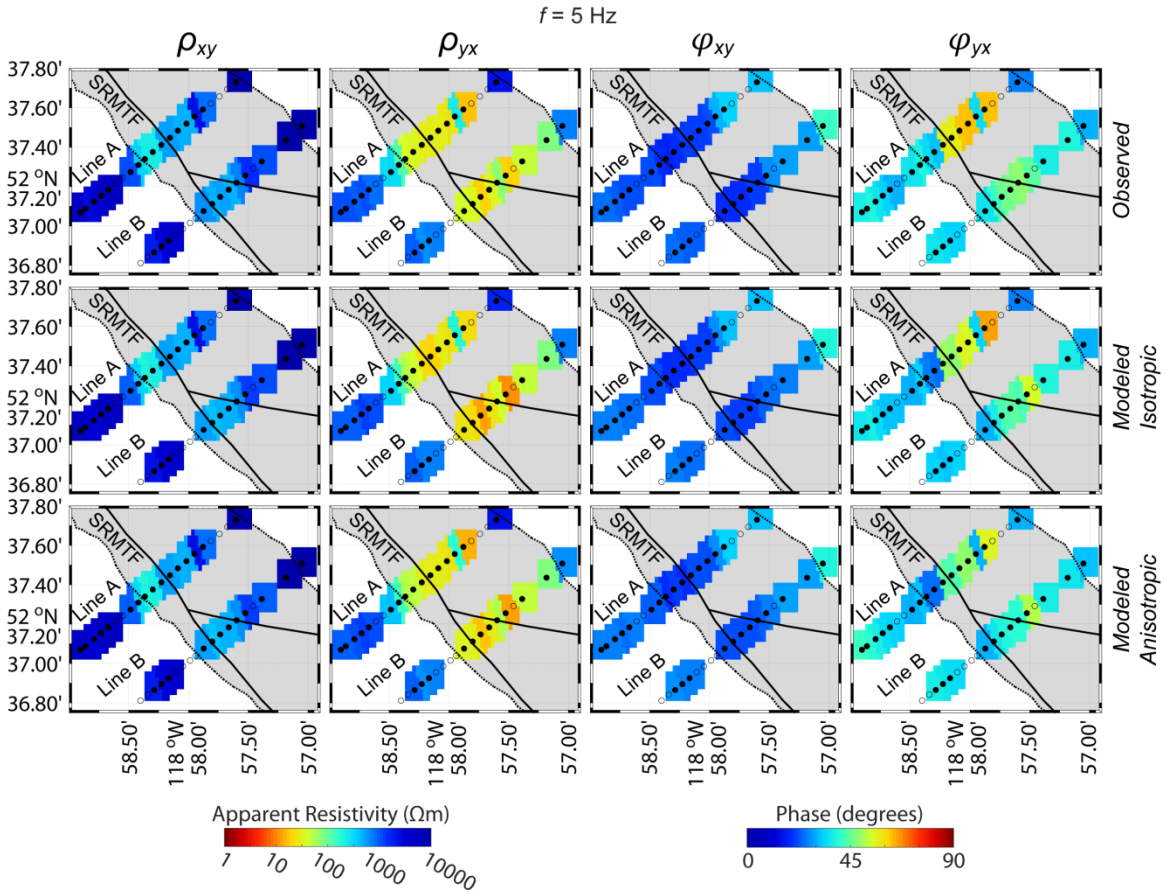


Figure B.14: Maps of the Lines A and B observed and modeled apparent resistivity ($\rho$) and phase ($\varphi$) data at a frequency of 5 Hz. Modeled data are from isotropic and anisotropic 3-D inversions of the Lines A and B data. *xy* (*yx*) = data from electric field polarized to geographic north (east). Black points show locations of MT stations. Grey shading = Kinbasket Lake. SRMTF = Southern Rocky Mountain Trench Fault.

## Appendix B.4 : Observed and modeled data from the Lines C and D 3-D inversions

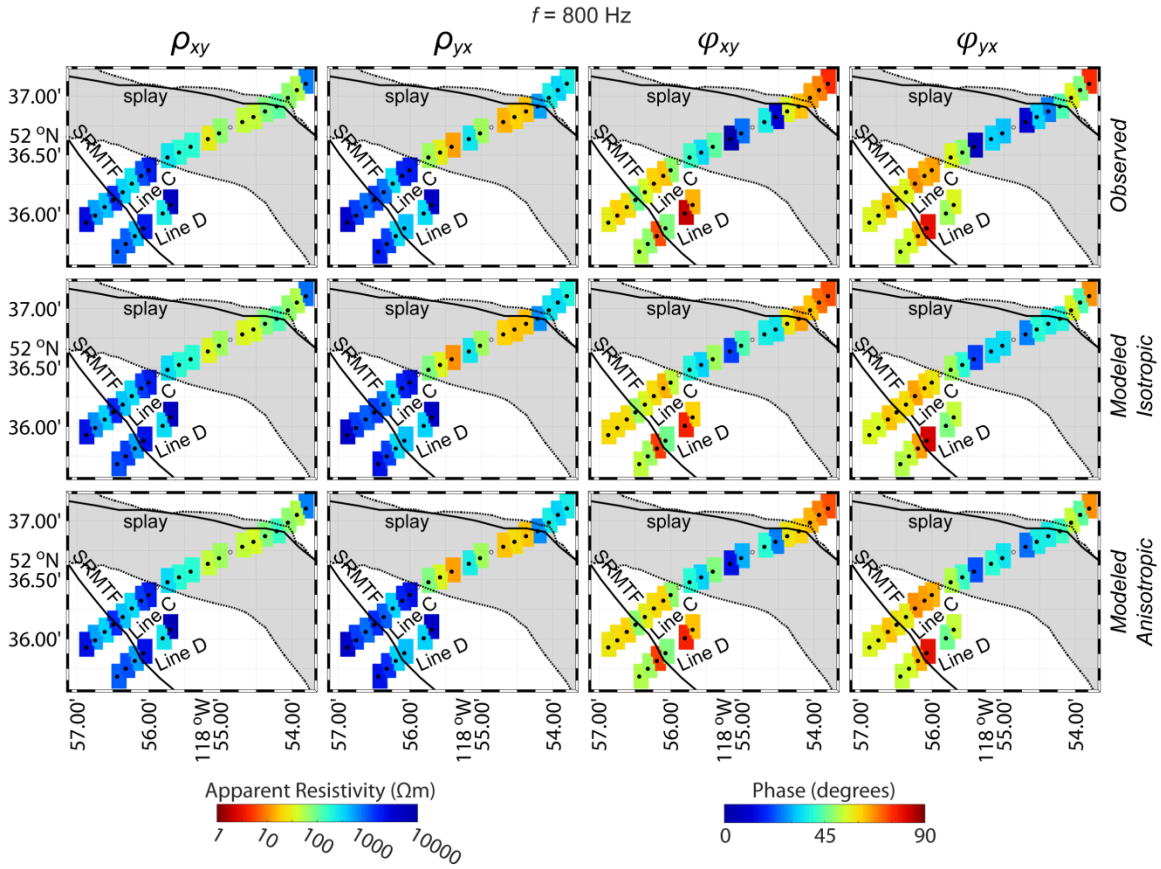


Figure B.15: Maps of the Lines C and D observed and modeled apparent resistivity ($\rho$) and phase ($\varphi$) data at a frequency of 800 Hz. Modeled data are from isotropic and anisotropic 3-D inversions of the Lines C and D data. *xy* (*yx*) = data from electric field polarized to geographic north (east). Black points show locations of MT stations. Grey shading = Kinbasket Lake. SRMTF = Southern Rocky Mountain Trench Fault; splay = mapped splay of the SRMTF.

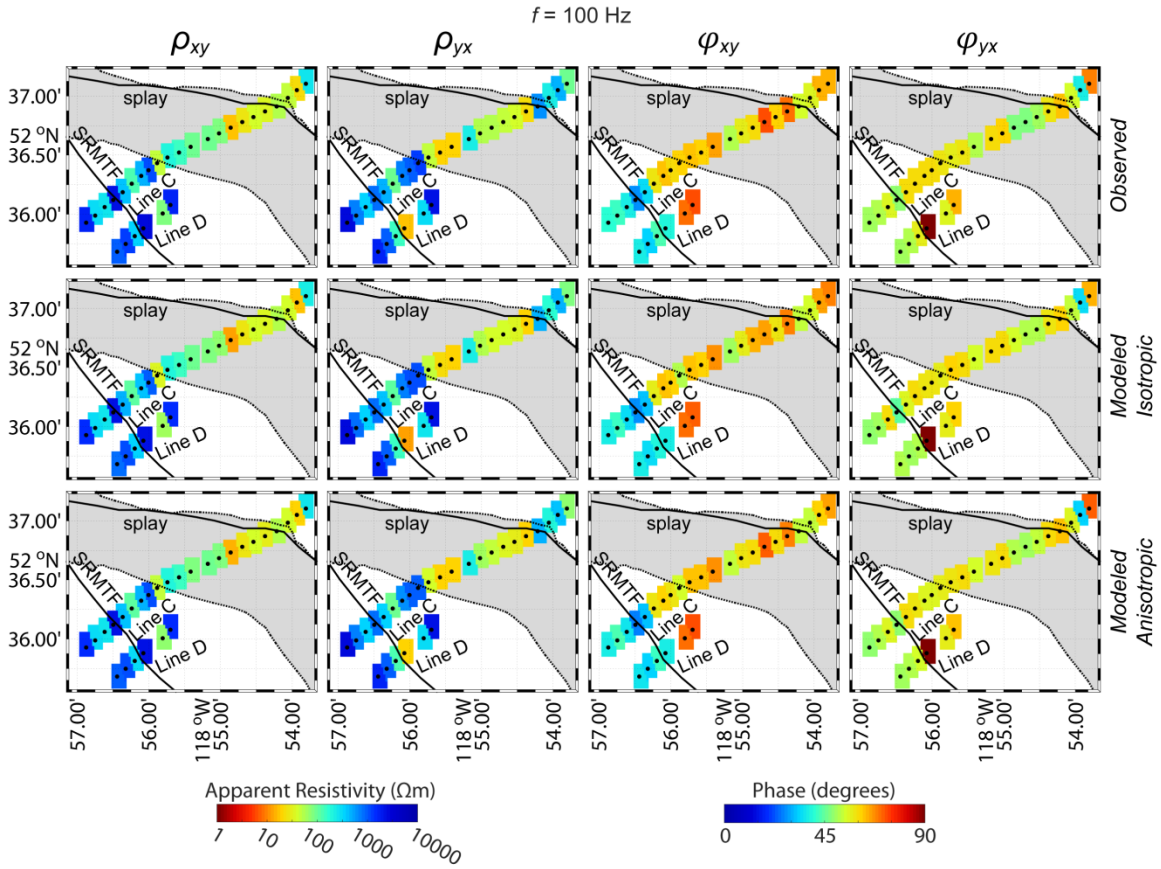


Figure B.16: Maps of the Lines C and D observed and modeled apparent resistivity ($\rho$) and phase ($\varphi$) data at a frequency of 100 Hz. Modeled data are from isotropic and anisotropic 3-D inversions of the Lines C and D data. *xy* (*yx*) = data from electric field polarized to geographic north (east). Black points show locations of MT stations. Grey shading = Kinbasket Lake. SRMTF = Southern Rocky Mountain Trench Fault; splay = mapped splay of the SRMTF.

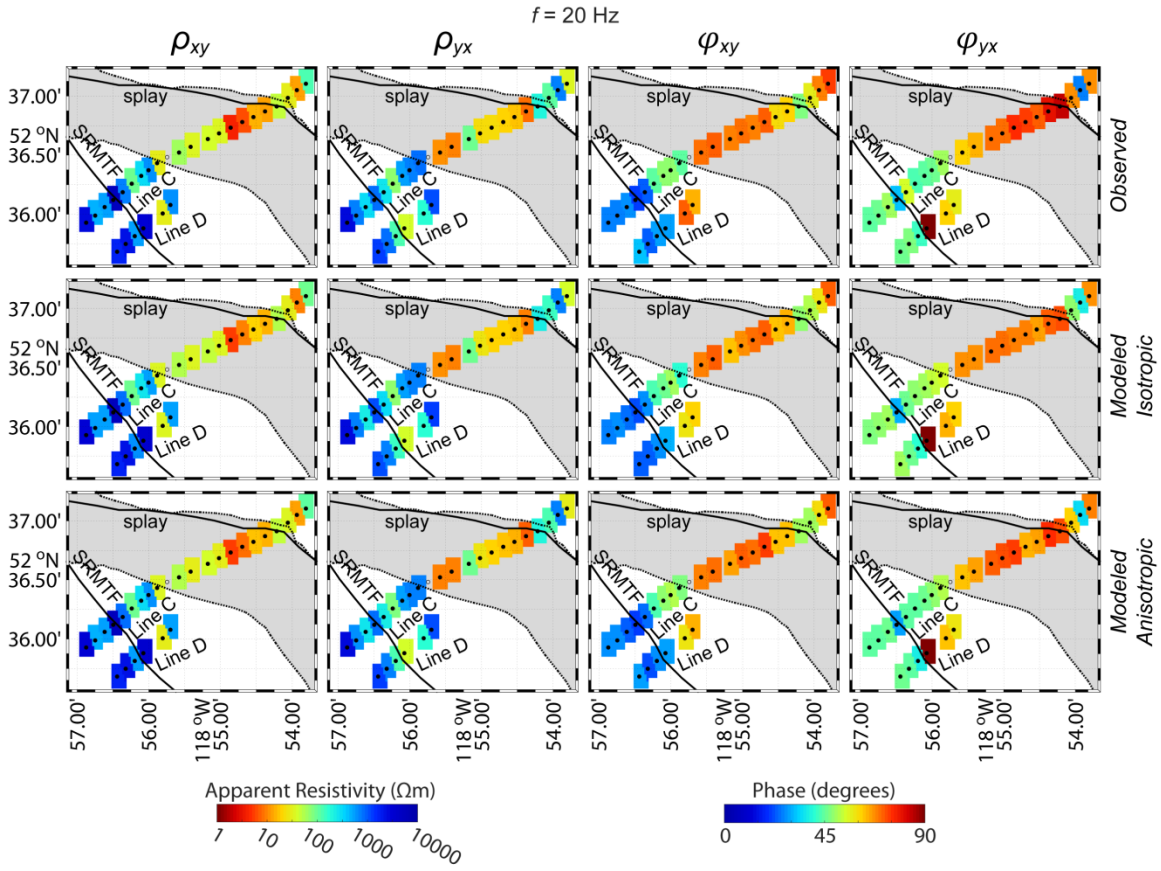


Figure B.17: Maps of the Lines C and D observed and modeled apparent resistivity ($\rho$) and phase ($\varphi$) data at a frequency of 20 Hz. Modeled data are from isotropic and anisotropic 3-D inversions of the Lines C and D data. *xy* (*yx*) = data from electric field polarized to geographic north (east). Black points show locations of MT stations. Grey shading = Kinbasket Lake. SRMTF = Southern Rocky Mountain Trench Fault; splay = mapped splay of the SRMTF.

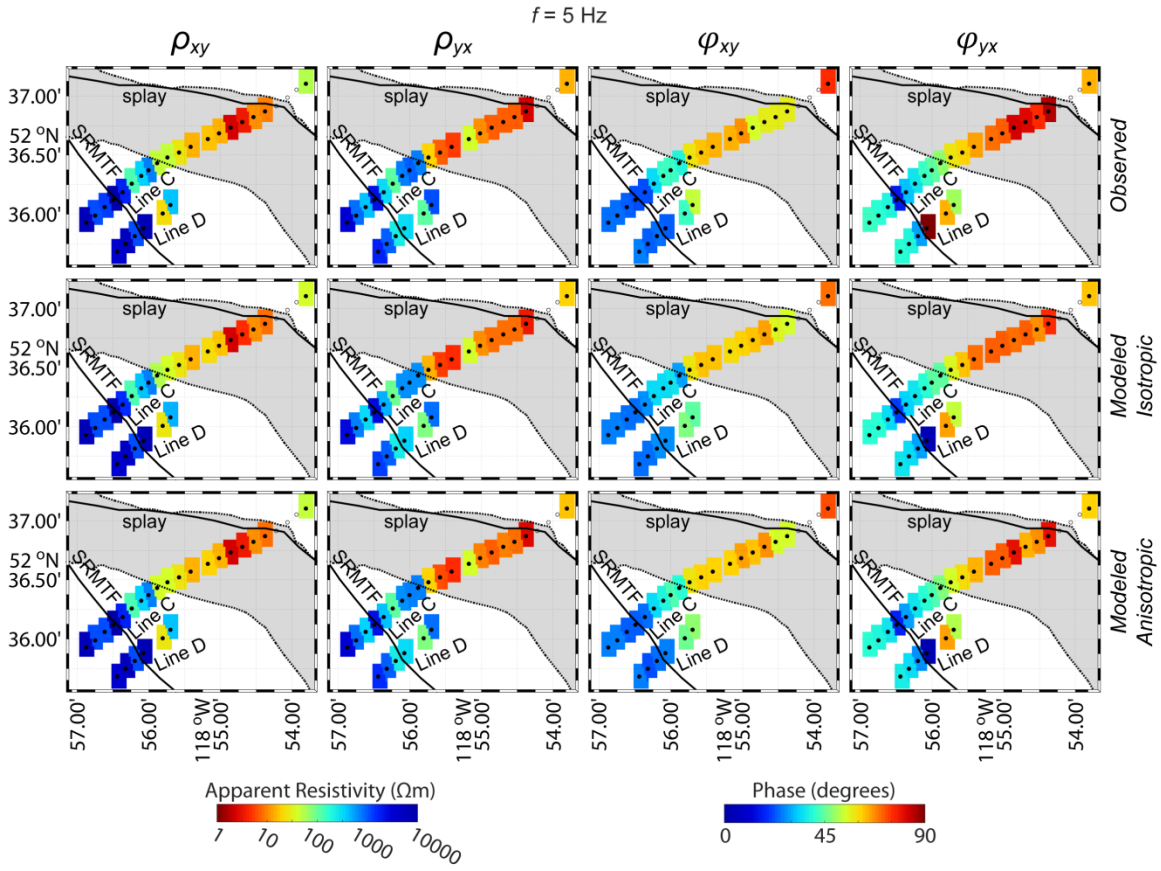


Figure B.18: Maps of the Lines C and D observed and modeled apparent resistivity ($\rho$) and phase ($\varphi$) data at a frequency of 5 Hz. Modeled data are from isotropic and anisotropic 3-D inversions of the Lines C and D data. *xy* (*yx*) = data from electric field polarized to geographic north (east). Black points show locations of MT stations. Grey shading = Kinbasket Lake. SRMTF = Southern Rocky Mountain Trench Fault; splay = mapped splay of the SRMTF.

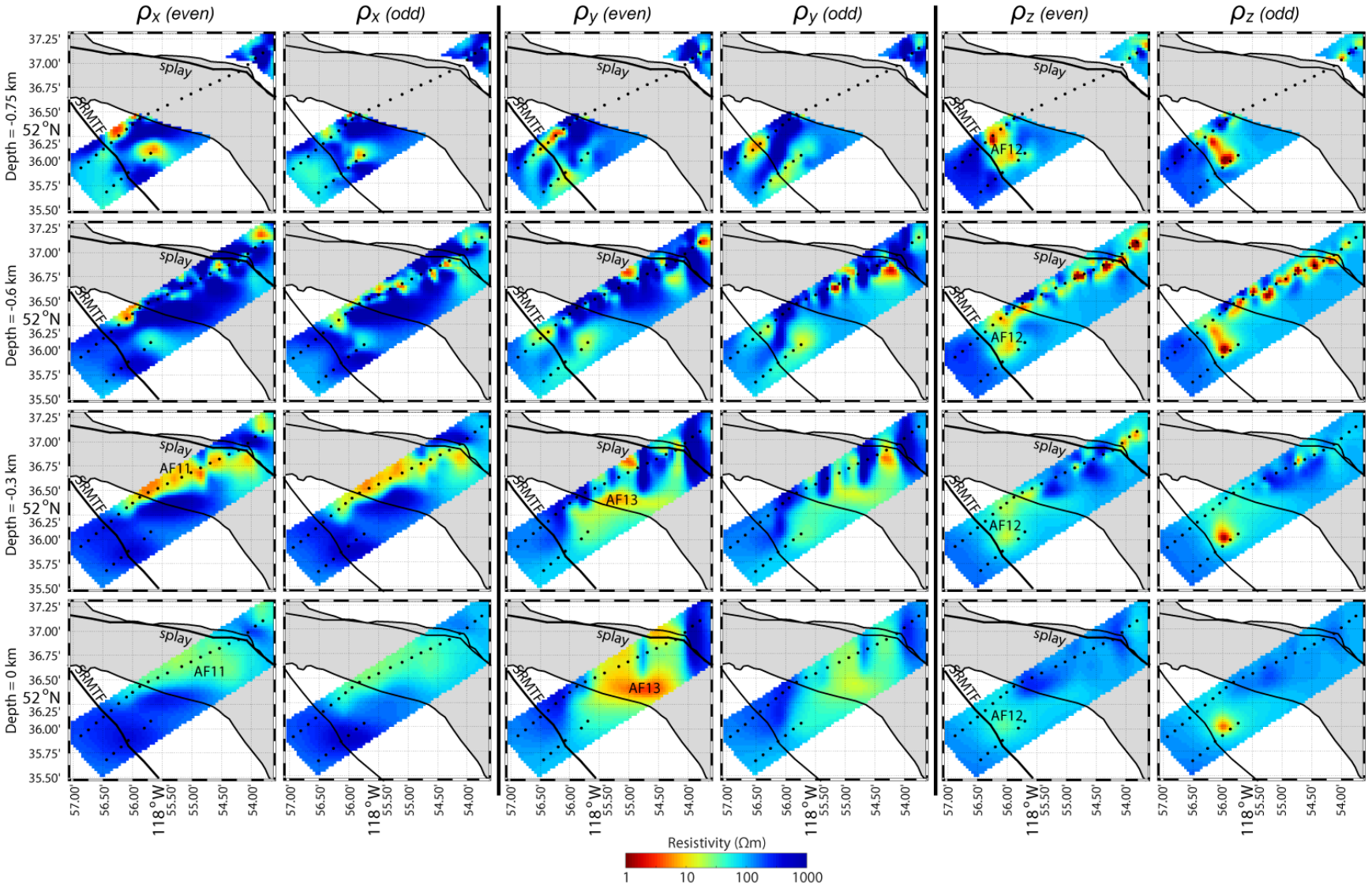
ρx (even)
ρx (odd)
ρy (even)
ρy (odd)
ρz (even)
ρz (odd)
Depth = -0.75 km
Depth = -0.6 km
Depth = -0.3 km
Depth = 0 km
splay
SRMTF
AF11
AF12
AF13
52°N
118°W
Resistivity (Ωm)
1
10
100
1000

Figure B.19: Comparison of horizontal slices from the Canoe Reach South Lines C and D anisotropic 3-D resistivity models. The "even" inversion used every second even-numbered MT station and the "odd" inversion used every second odd-numbered MT station. The resistivity model from the even-numbered inversion is interpreted in the text. The principal anisotropic resistivities $\rho_x$, $\rho_y$, and $\rho_z$ are measured in the N-S, E-W, and vertical directions, respectively. Model areas poorly constrained by the MT data are shown as white. The lake surface is at -0.73 km depth, and is therefore plotted as white in the first row. Grey shading = Kinbasket Lake. Black filled circles show locations of MT stations. SRMTF = Southern Rocky Mountain Trench Fault; splay = mapped splay of the SRMTF. AF11, AF12, and AF13 are features described in the text. Positive *x* direction = north, positive *y* direction = east, positive *z* direction = downward.